UNIVERSITY OF CALIFORNIA SAN DIEGO

# Fibroblast mechanosignaling and extracellular matrix remodeling in pulmonary arterial hypertension

A Dissertation submitted in partial satisfaction of the requirements
for the degree Doctor of Philosophy

in

Bioengineering

by

Ariel Wang

Committee in charge:

Professor Daniela Valdez-Jasso, Chair
Professor Andrew McCulloch, Co-Chair
Professor Adam Engler
Professor Jeffrey Omens
Professor Jason Yuan

2022

The Dissertation of Ariel Wang is approved, and it is acceptable in quality and form for publication on microfilm and electronically.

University of California San Diego

2022

# DEDICATION

To my friends and family, I could not have done any of this without you.

TABLE OF CONTENTS

LIST OF FIGURES

LIST OF TABLES

# LIST OF ABBREVIATIONS

| | |
|---|---|
| PAH | Pulmonary Arterial Hypertension |
| PAEC | Pulmonary Arterial Endothelial Cells |
| PASMC | Pulmonary Arterial Smooth Muscle Cells |
| PAAF | Pulmonary Arterial Adventitial Fibroblasts |
| NO | Nitric Oxide |
| TGFβ | Transforming Growth Factor Beta |
| ECM | Extracellular Matrix |
| PA | Pulmonary Artery (L = Left, M = Main, R = Right) |
| GPCR | G protein-coupled receptors |
| BMPR2 | Bone morphogenic protein receptor type 2 |
| EndoMT | Endothelial-to-mesenchymal transition |
| mPAP | Mean Pulmonary Arterial Pressure |
| ET-1 | Endothelin-1 |
| PDGF | Platelet-derived Growth Factor |
| MCT | Monocrotaline |
| CH | Chronic hypoxia |
| SuHx | Sugen-hypoxia |
| PTEN | phosphatase and tensin homolog |
| PI3K | Phosphoinositide-3-kinase |
| eNOS | Endothelial nitric oxide synthase |
| miR | MicroRNA |
| SRSF1 | Serine and Arginine-rich Splicing Factor 1 |

| | |
|---|---|
| PKCδ | Protein Kinase C delta |
| NFAT | Nuclear Factor of Activated T-cells |
| EUGR | Extrauterine Growth Restriction |
| TRPV | Transient Receptor Potential Vanilloid |
| MICAL2 | Molecule Interacting with CasL 2 |
| lncRNA | Long Noncoding RNA |
| CTGF | Connective Tissue Growth Factor |
| MAPK | Mitogen-Activated Protein Kinases |
| ROS | Reactive Oxygen Species |
| PLCγ1 | Phospholipase C |
| RT-PCR | Reverse Transcription Polymerase Chain Reaction |
| BrdU | Bromodeoxyuridine |
| UQ | Uncertainty Quantification |
| CFB | Cardiac Fibroblasts |
| LV | Left Ventricular |
| RV | Right Ventricular |
| TNFα | Tumor Necrosis Factor alpha |
| ERK | Extracellular Signal-related Kinases |
| IL6 | Interleukin 6 |
| Col | Collagen mRNA |
| Acta2 | Alpha Smooth Muscle Actin mRNA |
| αSMA | Alpha Smooth Muscle Actin Protein |
| Loxl1 | Lysyl oxidase-like 1 mRNA |

| | |
|---|---|
| Eln | Elastin mRNA |
| Fn1 | Fibronectin mRNA |
| FGF | Fibroblast Growth Factor |
| VEGF | Vascular Endothelial Growth Factor |
| Ang II | Angiotensin II |
| AT1R | Angiotension II Receptor Type 1 |
| MST1/2 | Macrophage Stimulating 1 or 2 |
| TRP | Transient Receptor Potential Ion Channel |
| ANOVA | Analysis of variance |
| JNK1/2 | c-Jun N-terminal Kinases |
| PKCα | Protein Kinase C Alpha |
| ASK1 | Apoptosis Signal-regulating Kinase 1 |
| TAK1 | TGF-β–Activated Kinase 1 |
| PDMS | Polydimethylsiloxane |
| FBS | Fetal Bovine Serum |
| DMEM | Dulbecco's Modified Eagle Media |
| vWF | von Willebrand Factor |
| MYH11 | Myosin-11 |
| CTCF | Corrected Total Cell Fluorescence |
| clOPN | Cleaved Osteopontin |
| OVX | Ovariectomized |

# ACKNOWLEDGEMENTS

I would like to acknowledge the great help of all of my advisors, labmates, fellow graduate students, and family and all of their invaluable support in the last five years, without whom this never would have been possible.

Chapter 1, in part, is a reprint of the material as it appears in Biophysical Review 2021. Wang, Ariel; Valdez-Jasso, Daniela. The dissertation author was the primary investigator and author of this paper.

Chapter 2, in full, is a reprint of the materials as it appears in the following publications: Philosophical Transactions of the Royal Society A 2020. Wang, Ariel; Cao, Shulin; Aboelkassam Yasser; Valdez-Jasso Daniela. The thesis author was the primary investigator and author of this paper.

Chapter 3, in part, is a reprint of the materials as it appears in the following publications: Cells 2021. Wang, Ariel; Cao, Shulin; Stowe Jennifer C.; Valdez-Jasso Daniela. The thesis author was the primary investigator and author of this paper.

Chapter 4 contains unpublished material coauthored with Wang, Ariel and Valdez-Jasso, Daniela. The dissertation author was the primary author of this chapter.

Chapter 5 contains unpublished material coauthored with Wang, Ariel and Valdez-Jasso, Daniela. The dissertation author was the primary author of this chapter.

# VITA

2015 Bachelor of Science in Bioengineering, University of California, Berkeley

2022 Doctor of Philosophy in Bioengineering, University of California San Diego

# PUBLICATIONS

**Wang, A.**, Valdez-Jasso, D. Cellular mechanosignaling in pulmonary arterial hypertension. Biophys Rev. 2021 Sep 2;13(5):747-756. doi: 10.1007/s12551-021-00828-3. PMID: 34765048; PMCID: PMC8555029.

**Wang, A.**, Cao, S., Stowe, J.C. and Valdez-Jasso, D. 2021. Substrate Stiffness and Stretch Regulate Profibrotic Mechanosignaling in Pulmonary Arterial Adventitial Fibroblasts. Cells, 10(5), p.1000.

**Wang, A.**, Cao, S., Aboelkassem, Y. and Valdez-Jasso, D. 2020. Quantification of uncertainty in a new network model of pulmonary arterial adventitial fibroblast pro-fibrotic signalling. Philosophical Transactions of the Royal Society A, 378(2173), 20190338.

Cao, S., Aboelkassem, Y., **Wang, A.**, Valdez-Jasso, D., Saucerman, J.J., Omens, J.H., McCulloch, A.D. 2020 Quantification of model and data uncertainty in a network analysis of cardiac myocyte mechanosignalling. Proc Roy Soc A; 378: 20190336.

Herum, K.M., Romaine, A., **Wang, A.**, Melleby, A.O., Strand, M.E., Pacheco, J., Braathen, B., Dunér, P., Tønnessen, T., Lunde, I.G., Sjaastad, I., Brakebusch, C., McCulloch, A.D., Gomez, M.F., Carlson, C.R., and Christensen, G. 2020 Syndecan-4 Protects the Heart From the Profibrotic Effects of Thrombin-Cleaved Osteopontin. J Am Heart Assoc. January; 9(3): e013518

Hoepker, A.C., **Wang, A.**, Le Marois, A., Suhling, K., Yan, Y., Marriott, G. Genetically encoded sensors of protein hydrodynamics and molecular proximity. Proc Natl Acad Sci U S A. 2015 May 19;112(20):E2569-74. doi: 10.1073/pnas.1424021112. Epub 2015 Apr 30. PMID: 25931526; PMCID: PMC4443326.

ABSTRACT OF THE DISSERTATION

Fibroblast mechanosignaling and extracellular matrix remodeling in pulmonary arterial hypertension

by

Ariel Wang

Doctor of Philosophy in Bioengineering

University of California San Diego, 2022

Professor Daniela Valdez-Jasso, Chair
Professor Andrew McCulloch, Co-Chair

Pulmonary arterial hypertension (PAH) is a vasculopathy characterized by sustained elevated pulmonary arterial pressures in which the pulmonary vasculature and right ventricle undergo significant structural and functional remodeling. To understand the mechanisms of this disease, we use a multiscale approach to quantify the relationship between cellular signaling and tissue biomechanics, specifically fibrotic cell signals arising due to stretch and changes in substrate stiffness. Since sex differences are well-established in PAH patients, where the prevalence of PAH in women is much higher but their survival rate is better, we also want to examine how biological

sex plays a role in how fibroblasts respond to stretch and stiffness. Given the upregulation of profibrotic gene expression of pulmonary arterial adventitial fibroblasts (PAAFs) and right ventricular cardiac fibroblasts in PAH, *in-silico* models were made of cell signaling, *in-vitro* experiments with cultured fibroblasts were conducted, and pulmonary artery tissue from *in-vivo* rat models of pulmonary arterial hypertension were analyzed.

We studied crosstalk of profibrotic pathways in PAAFs as well as teased apart the effects of stretch and substrate stiffness in mechanical activation of these cells. By conducting *in-vitro* inhibition studies that the model was able to recapitulate, we demonstrated the usefulness of a computational model that was 80% accurate in simulating experimental designs and robust to parameter and epistemic uncertainty. We used this model to propose crucial experiments on the effects of AngII and TGFβ blockade based on the sensitivity analysis determining that those two cytokines along with stiffness and stretch were the most crucial to PAH pathology. The model was able to qualitatively predict 70% of the *in-vitro* AngII and TGFβ inhibition experiments, and areas of quantitative mismatch were used to propose differential regulation, missing pathways, and determine the relative importance of specific pathways. Pathways determined to be important in more than one gene's regulation of expression were stiffness and stretch upregulating TGFβ, AngII and the Hippo pathway, stretch activation of TRP, AngII activating MAPK and AP1 to latent TGFβ, and TGFβ activation of smad2/3 phosphorylation and TAK1 activation of p38. This has led to a model that can be used for predictive high-throughput screening of which target species in the PAAF signaling network can be inhibited to reverse adverse remodeling in PAH.

By combining *in-vitro* and *in-silico* data, we were able to tease apart profibrotic responses to individual mechanical stimuli and individual inhibitors. Reducing variables have allowed us to come to important conclusions about the importance of genes at varying time points of the disease

due to stretch or stiffness, which is important since marked differences are seen at different weeks of PAH treatment. We learned that expression of *Col1a1*, *Col3a1*, and *Eln* might rise early *in-vivo* as the increased mPAP in PAH increases vascular wall strain and stays elevated, but *Loxl1* and *Acta2* expression may rise at first but eventually returns to baseline as wall stiffening becomes severe, while *Fn1* may be induced after the ECM stiffens. By varying stretch time from 0, 4, 8, and 24 hours, we were able to find that *Col1a1* expression increases progressively while other genes increased at 4 or 8 hours but went back down to baseline, indicating profibrotic responses to stretch may be more transient in some genes.

Isolating cells and tissue from both the pulmonary artery and right ventricle have allowed us to tackle the vascular remodeling in PAH in two different organ systems, which is important to understanding the interplay which leads to RV dysfunction. Ultimate failure of the RV shows survival rate sexual dimorphism in PAH, a sex paradox which has not yet been explained. Our studying of male and female-derived fibroblasts in both the pulmonary artery and right ventricle as well as male and female pulmonary artery and right ventricular tissue has led us to conclude that profibrotic genes are more likely to be activated in male-derived cells and tissue. In PAAFs, female-derived fibroblasts require a higher threshold of stiffness before activation and the profibrotic genes primarily only respond to changes in stiffness not stretch while ovariectomized-derived cells had a higher baseline expression. In RV CFBs, male-derived cells primarily respond to stretch, which given there is demonstrated greater end diastolic pressure in male RVs, means this induction by stretch may lead to adverse remodeling via increased ECM remodeling. There is significant upregulation of all six genes in male-derived PA tissue in sugen-hypoxia animal model of PAH, with only four genes upregulated in female-derived PA tissue and one in ovariectomized-derived PA tissue. The observed variability in response of fibroblasts from male, female, and

ovariectomized rats and tissue to PAH conditions exhibits why it is so important to consider sexual dimorphism in disease to explain differences in outcome and is crucial headway into why male patients are less likely to survive PAH due to pressure overload in the remodeled pulmonary arteries leading to pressure overload in the right ventricle.

We used our *in-silico* model to determine that mechanical stimuli were a main driver of PAH, then iterated upon it to separately probe what pathways affected stretch and stiffness separately. *In-vivo* data in PAs from male rats demonstrated profibrotic activation in all six genes, while *in-vitro* data in male-derived PAAFs analyzing those same six genes demonstrated their response to both stiffness and stretch. Adding the variable of sex led to conclusions that mechanoregulation in the cells themselves are responsible for changes in response to stretch and stiffness as PAAFs from female rats were less likely to be activated by stretch and PAs from female rats were overall less induced, while PAAFs and PAs from ovariectomized rats had a high baseline expression and were much less likely to be induced. The variable of time in male PAAF response to stretch demonstrates that not all profibrotic genes respond equally, such as *Col1a1* increasing while the other genes have a more transient response. By isolating variables of stretch, stiffness, and sex, we can break down PAH into its important pathways in different sexes.

# CHAPTER 1: INTRODUCTION

## 1.1 Cellular Mechanosignaling in Pulmonary Arterial Hypertension

Pulmonary arterial hypertension (PAH) is a complex vasculopathy characterized by sustained elevated pulmonary arterial pressures in which the pulmonary vasculature and right ventricle undergo significant structural and functional remodeling. To better understand disease mechanisms, in this thesis we highlight recent insights into the regulation of pulmonary arterial cells by mechanical cues associated with PAH. Specifically, the mechanobiology of pulmonary arterial endothelial cells (PAECs), smooth muscle cells (PASMCs) and adventitial fibroblasts (PAAFs) has been investigated *in-vivo*, *in-vitro*, and *in-silico*. Increased pulmonary arterial pressure increases vessel wall stress and strain and endothelial fluid shear stress. These mechanical cues promote vasoconstriction and fibrosis that contribute further to hypertension and alter the mechanical milieu and regulation of pulmonary arterial cells.

### 1.1.1 Clinical Indications and Treatments for PAH

Pulmonary arterial hypertension is a vasculopathy that is manifested by sustained elevation of pulmonary arterial pressures and irreversible vascular remodeling. In PAH, the pulmonary vasculature undergoes significant structural and functional remodeling, including thrombus formation, endothelial dysfunction, cell proliferation, migration, and hypertrophy, and accumulation of extracellular matrix (ECM) proteins, leading to the formation of complex lesions known as plexiform lesions [1]. Consequently, there is thickening of the vascular wall, persistent vasoconstriction, arterial stiffening, and vascular rarefaction that further exacerbate pressure overload and adversely impairs pulmonary artery (PA) perfusion and hemodynamics.

Therapeutics targeting different cell types involved in this cascade of events have been developed to ameliorate the symptoms or progression of PAH. Vasodilators targeting smooth muscle cells by stimulating nitric oxide (NO) release have shown to reduce pulmonary arterial pressure, but do not reverse adverse vascular remodeling [2]. Other therapeutic targets include G protein-coupled receptors (GPCRs), ion channels, metabolic pathways, transcription factors, and growth factor receptors [3,4]. NO release is stimulated by phosphodiesterase type 5 (PDE5) inhibitors Tadalafil and Sildenafil, and endothelin receptor antagonists Ambrisentan and Macitentan also lead to smooth muscle cell relaxation. Bone morphogenic protein receptor type 2 (BMPR2) antagonists like chloroquine and Smad2/3 antagonists like Sotatercept are used to target the BMP and transforming growth factor beta (TGF-β1) pathways, respectively [4,5]. Since the structural and cellular remodeling of the pulmonary arteries is still largely irreversible, the prognosis of PAH is poor, and the underlying causes remain untreatable. Existing drugs do not reduce the progression of vascular remodeling, and patients deteriorate over time. Fewer than 60% of patients survive more than five years after diagnosis [6] and lung transplantation remains the only cure [4]. Since PAH therapeutics have had limited efficacy in reversing the pathological mechanisms that drive vascular remodeling, there is a need for more research into the pathology and crosstalk between biochemical and mechanosensitive signaling pathways in pulmonary arterial cells [5].

### 1.1.2 Cellular Mechanical Regulation

In response to the rise in mean pulmonary arterial pressure, the pulmonary artery wall thickens due to increased proliferation and hypertrophy of PA smooth muscle cells (PASMCs) [7,8]. This is accompanied by increased proliferation of PA endothelial cells (PAECs) and adventitial

fibroblasts (PAAFs) as well as inhibited apoptosis of PAECs and PASMCs, and an endothelial-to-mesenchymal-transition (EndoMT), that transforms PAECs to myofibroblasts, leading to overproduction of ECM proteins and fibrosis [9]. The mechanical stresses that trigger vascular cell remodeling in PAH result from the effect of increased blood pressure on the wall and increased blood flow on the endothelium [10,11]. Increases in arterial pressure leads to vessel thickening, while increased PA flow due to PAH also increases PAEC fluid shear stress which promotes EndoMT and further accumulation of PAAFs [9]. Increased vessel loading also promotes PAAF proliferation and activates increased ECM expression resulting in matrix stiffening that in turn activates myofibroblasts to produce more ECM, further decreasing vascular compliance [11]. This cascade of events exacerbates adverse structural remodeling and vascular dysfunction (**Fig. 1.1**).

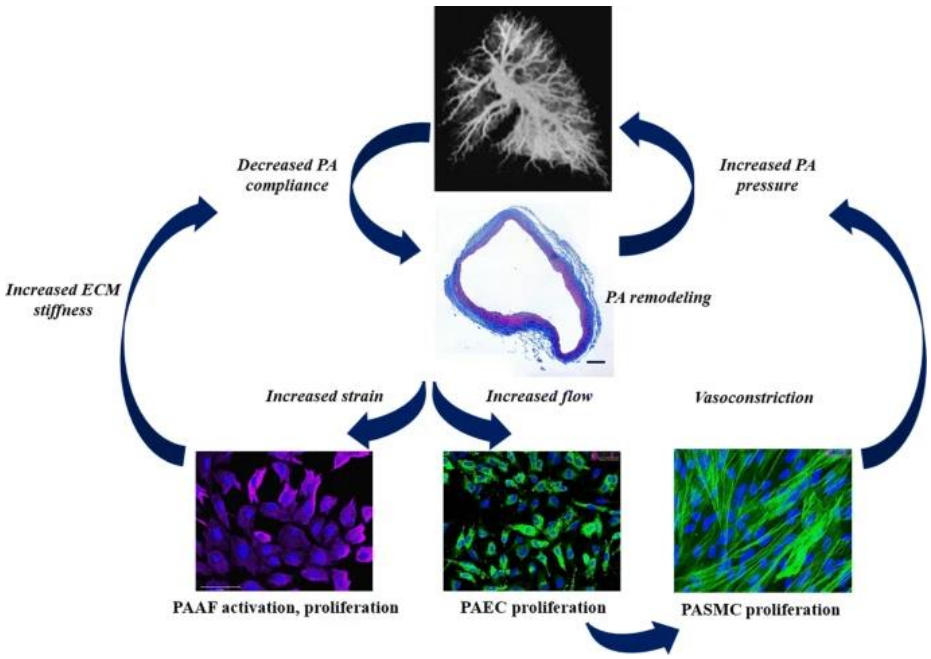


**Figure 1.1: Schematic of mechanical feedback in pulmonary arterial cells.** Vascular remodeling in pulmonary arterial hypertension is manifested by increased pulmonary arterial pressures, decreased arterial compliance, and pruning of the vasculature. At the cellular level, pulmonary arterial adventitial fibroblasts (PAAFs) respond to increased strain, endothelial cells (PAECs) respond to increased flow, and smooth muscle cells (PASMCs) are activated to contract causing vasoconstriction. These cellular responses feedback into the system by increasing extracellular matrix (ECM) stiffness, releasing paracrine factors, and increasing PA pressure, respectively.

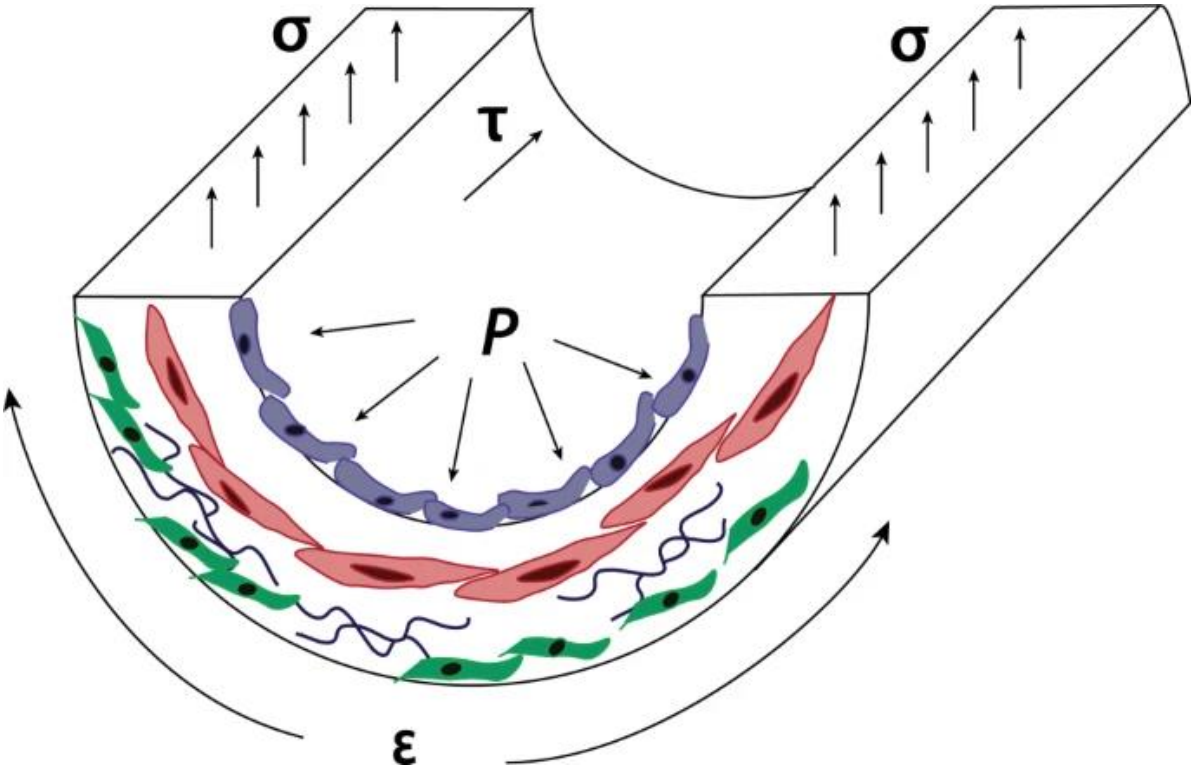


**Figure 1.2**: **Diagram of how pressure, stress, strain, and blood flow affect pulmonary artery cells.** Increased pulmonary arterial pressure (P) increases vessel wall stress (σ) and strain (ε). Pressure gradients increase blood flow, which increases shear fluid shear stress (τ) on the endothelium. The main cell types affected by these mechanical stimuli are PAECs — blue which experience shear stress, PASMCs — red which thicken in response to wall strain, and PAAFs — green which proliferate and increase pulmonary artery stiffness.

Increased pulmonary arterial pressure induces an increase in vessel wall stress and strain and drives an increase in blood flow that increases fluid shear stress on the endothelium (**Fig. 1.2**). Changes in stiffness at the tissue scale of the pulmonary vasculature results in cellular mechanotransduction responses leading to activation of signaling pathways that feed back to induce more remodeling [12]. For example, ECM gene expression by PAAFs can be activated by mechanical strain, leading to the overproduction of collagen. The resulting increase in ECM stiffness activates PAAFs to transition to myofibroblasts and can also stimulate PASMC and PAEC proliferation [13]. Here we summarize the mechanobiological responses to wall stress and strain, fluid shear stress and ECM stiffening in these three cell types and the crosstalk between

them in the context of vessel remodeling in response to mechanical overload in the pathogenesis of PAH (**Fig. 1.3**).

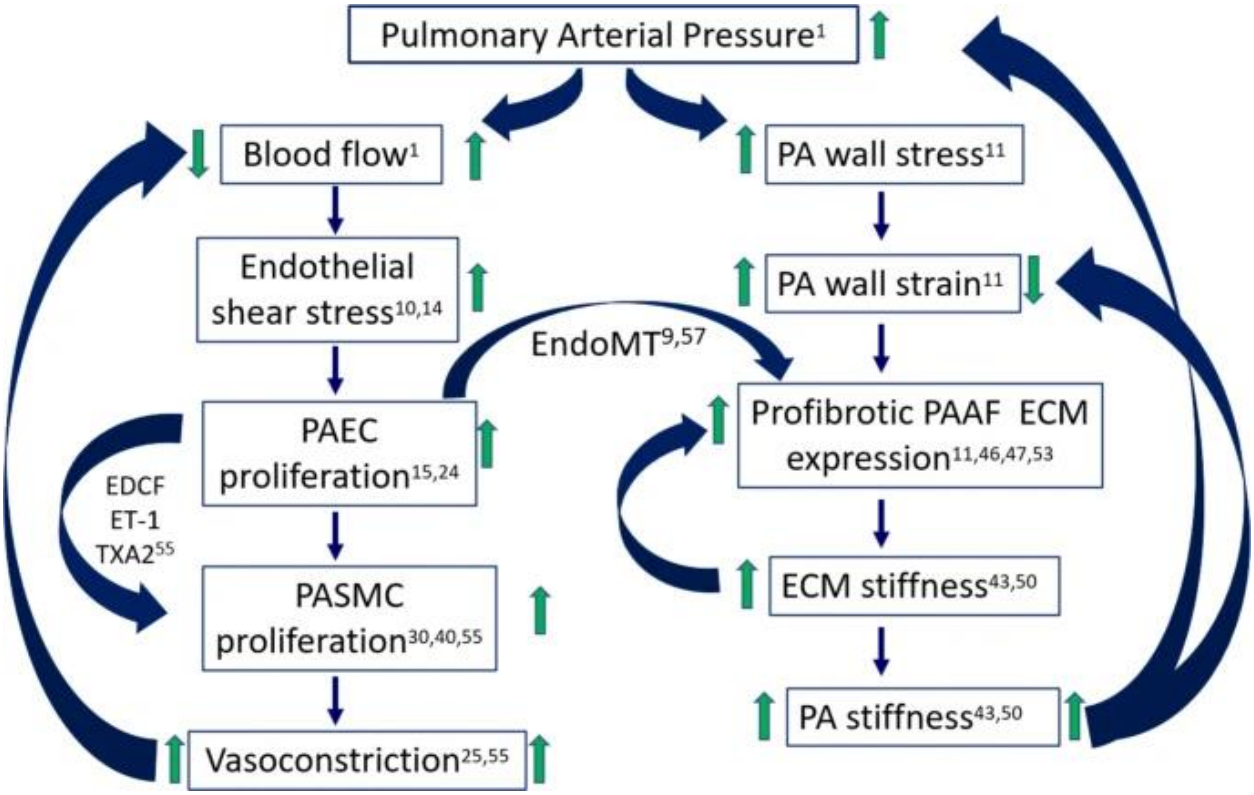


**Figure 1.3: Effect of an increased mean pulmonary arterial pressure on pulmonary artery stiffness**. The effect of an increase of mean pulmonary arterial pressure (mPAP) on increasing blood flow results in increased shear stress experienced by pulmonary arterial endothelial cells (PAECs) which increases their proliferation. This and other cytokines mediate the PAEC transition into activated fibroblasts and release of paracrine factors that induce smooth muscle cell (PASMC) proliferation and vasoconstriction that in turn reduces blood flow. An increase in mPAP also increases PA wall stress and strain, which increases profibrotic adventitial fibroblast (PAAF) expression, increasing ECM stiffness and overall PA stiffness leading to decreased PA wall strain.

### 1.1.3 *In-vivo* Models of Pulmonary Arterial Hypertension

Most experimental studies of vascular remodeling in PAH use one of three animal models: monocrotaline (MCT), chronic hypoxia (CH), and sugen-hypoxia (SuHx). MCT is a poisonous pyrolizidine alkaloid found in the leguminous plant Crotalaria spectabilis, that produces a massive

inflammatory response in the lung, damaging pulmonary endothelial cells, leading to pathologically elevated pulmonary arterial pressures [14]. Four weeks post-MCT injection in rodents is a well-established animal model of end-stage PAH. MCT is however toxic to the liver and other tissues [14,15], and commonly results in sudden cardiac death [16]. Exposure to chronic hypoxia (10% oxygen) for few weeks induces pathologic elevation in pulmonary arterial pressure via PA medial hypertrophy and sustained pulmonary vasoconstriction [17]. SuHx in rats, an animal model developed by Taraseviciene-Stewart *et al*. [18], is the model of PAH that most closely recapitulates the pulmonary arterial lesions found in lung tissues from human PAH patients [19] and the progressive hemodynamic sequelae. With a single injection of 20 mg/kg of vascular endothelial growth receptor factor inhibitor sugen SU5416 and exposure to chronic hypoxia (10% oxygen) for three weeks, rats show significant pulmonary arterial medial hypertrophy, pulmonary arterial wall thickening and sustained pulmonary vasoconstriction that results in progressively elevated pressures [19,20].

### 1.1.4 Pulmonary Arterial Endothelial Cells

PAECs form the permeable barrier between blood and vascular tissue and respond to circulating cytokines such as endothelin-1 (ET-1), a vasoconstrictor, and platelet-derived growth factor (PDGF), which increases cell proliferation [21,22]. PAEC signaling is also regulated by mechanical cues associated with altered fluid shear stress on the vascular endothelium due to increased blood pressure and flow, increases in matrix stiffness, and hypoxia. Dysregulation of pathways such as the vascular endothelial growth factor (VEGF), Notch, and bone morphogenetic protein (BMP) signaling pathways leads to disordered formation of new vessels [21].

In both chronic hypoxia and MCT rats, hyper-proliferation of PAECs and increased levels of VEGF *in-vivo* mediated vessel growth and disordered angiogenesis [17]. Chronic hypoxia induces expression of PDGF, increasing PAEC proliferation and inhibiting apoptosis. This indicates that hypoxia-induced angiogenesis in PAECs stimulates elevated expression of PDGF and VEGF, growth factors that are well known to regulate vascular remodeling.

In the MCT rat model of PAH, downregulation of miR-371b-5p was shown to increase apoptosis of PAECs via phosphatase and tensin homolog (PTEN)/ phosphoinositide 3-kinase (PI3K)/Akt signaling and to suppress endothelial nitric oxide synthase (eNOS) synthesis of nitric oxide which is a vasodilator [15]. This miRNA could thus be an important regulator of proliferation of PAECs and vasoconstriction in PAH.

An important pathway that is dysregulated in PAH is BMP signaling. In SuHx rats and cultured lung samples from human patients, an elastase inhibitor Elafin was used to rescue BMP signaling, which is important in vasculogenesis, improving PAEC survival and normal angiogenesis and thereby reversing adverse remodeling [20].

In a recent study by Woodcock *et al*., SuHx rats and lungs from PAH patients showed decreased miR-7 expression [19]. miR-7 has been reported to regulate serine and arginine-rich splicing factor 1 (SRSF1), which promotes PAEC migration [19]. Therefore, this may be a novel mechanism by which changes in ECM stiffness in PAH regulates pathologic endothelial dysfunction and cell migration.

*In-vitro experiments*. Increased fluid shear stress on PAECs *in-vitro* has been shown to decrease Protein Kinase C delta (PKCδ) activity, which leads to increases in phosphorylation of eNOS and consequent generation of NO in primary ovine cell cultures [10].

In primary human PAECs isolated from PAH patients, increased production of ET-1 was observed, which leads to PAEC dysfunction and excessive proliferation [23]. Stimulation with peroxisome proliferator–activated receptor gamma (PPARγ) was able to reduce this ET-1 overexpression, demonstrating the potential for PPARγ agonists as therapeutics for PAH.

*In-vitro*, increased extracellular matrix stiffness from 1 kilopascal (kPa), representing control arterioles, to 50 kPa, representing diseased pulmonary arterioles, led to increased glycolysis via the YAP/TAZ mechanotransducers in the Hippo signaling pathway [24]. A shift from oxidative phosphorylation to glycolysis is a driver of PAEC proliferation and migration early in PH, as glycolysis is needed to meet the metabolic demands of proliferating cells. When PAECs were grown on the 50-kilopascal (kPa) matrix representative of tissue stiffness in PAH compared with a soft 1-kPa matrix representative of control lungs by Woodcock *et al*., miR-7 was downregulated, which led to increased migration [19].

*Summary*. PAECs respond to the elevated ECM stiffness, fluid shear stress, and hypoxia associated with PAH via dysregulated PI3K and BMP signaling, which trigger hyper-proliferation and migration. This in turn mediates pathogenic angiogenesis and vascular remodeling.

### 1.1.5 Pulmonary Arterial Smooth Muscle Cells

PASMCs are the primary cell type in the medial layer of the pulmonary artery. They contain contractile proteins which are regulated by calcium and control vascular tone [25]. When dysregulated, abnormal SMC contractility can cause persistent vasoconstriction, a disease marker of PAH. In PAH we also observe neointimal hyperplasia due to proliferation, hypertrophy, and migration of PASMCs to the intimal layer of the PA. Under PAH conditions, SMCs also produce

more pro-inflammatory cytokines, deposit increased elastin and collagen, and grow thereby thickening the medial layer [26]. SMCs respond to increases in matrix stiffness and hypoxia by remodeling the ECM and proliferating abnormally.

*In-vivo experiments.* Signaling pathways such as NFAT and Notch signaling become overactive in PAH conditions. In MCT rats, calcineurin/nuclear factor of activated T-cells (NFAT) signaling was reported to be activated and shown to increase PASMC proliferation and migration and inhibit apoptosis [27]. Notch signaling is another important pathway that upregulates proliferation and differentiation of PASMCs. The γ-secretase inhibitor DAPT blocks Notch3 and successfully reduced mean pulmonary arterial pressure in extrauterine growth restriction (EUGR) rats [28,29].

Transient receptor potential vanilloid-3 (TRPV3) channel expression was also found to be increased in hypoxic rats and is thought to mediate pulmonary vascular remodeling via the proliferation of PASMCs by activating PI3K/Akt signaling [30].

There is evidence of regulation of PAH by noncoding RNAs. Upregulation of the newly found microRNA miR-205-5p was observed to reduce PASMC proliferation in a hypoxia-induced PAH mouse model, inhibiting molecule interacting with CasL 2 (MICAL2) expression by targeting the 3′ untranslated region, which activates the ERK1/2 pathway [31]. miRNAs were also found to be important in PASMC synthesis of collagen, particularly miR-29b, which physically binds Smad3 downstream of TGFβ1 as found by chromatin immunoprecipitation [32]. TGF-β1 is an important cytokine because chronic activation *in-vivo* leads to spontaneous PAH in mice [33]). TGF-β1 also downregulates miR-29b through Smad3 [34]. PASMCs isolated from PAH patients by Lei *et al*. demonstrated an increase in a long noncoding RNA (lncRNA), which reduces the expression of miR-141 [35]. miR-141 normally downregulates expression of RhoA, suppressing

the RhoA/ROCK pathway, but when miR-141 is not highly expressed the ROCK pathway is upregulated, which increases vasoconstriction and remodeling of the arterial wall.

*In-vitro experiments*. Rat PASMCs showed higher expression of collagen III protein and fibronectin mRNA when stimulated with connective tissue growth factor (CTGF), upstream of PI3K [36]. This increase in ECM protein deposition promotes pulmonary vascular remodeling under PAH conditions.

Different pathways are upregulated by hypoxia in PASMCs. Huang *et al*. showed that the mitogen-activated protein kinases (MAPK) signal pathway is crucial in the proliferative response of PASMCs to hypoxia [37]. Hypoxia induces pulmonary vasoconstriction, mediated by increased intracellular calcium in PASMCs [38]. Vasoconstriction causes reactive oxygen species (ROS)-dependent phospholipase C (PLCγ1) activation and contraction in mouse PASMCs.

BMP signaling is important to normal function of PASMCs but can be disrupted by disease. Wang *et al*. found in rat primary PASMCs that BMP signaling is suppressed in hypoxia-induced PH [39]. Dysfunctional BMP signaling causes proliferation of PASMCs in PAH, and PDGF-BB can activate Rho kinase and enhance proliferation of rat SMCs [32].

NFAT signaling can also be dysregulated in PAH. PASMCs isolated from PAH patients and control subjects showed upregulated STIM2 in PAH-PASMCs, which raises resting cytosolic calcium and increases PASMC proliferation via, among others, the Akt and NFAT signaling pathways [40]. Upregulation of the matricellular protein osteopontin by Sphingosine-1-phosphate (S1P) via calcineurin/NFAT signaling is observed in rat cell cultures [41]. S1P induces a vasoconstrictive response, and via osteopontin, directly promotes PASMC proliferation.

Regulation of PAH by noncoding RNAs has also been shown *in-vitro*, particularly miR-17-92 has been shown to regulate the PASMC contractile phenotype and increase proliferation in cells isolated from PAH patients [42].

*Summary*. PASMCs respond to increases in pulmonary arterial pressure by increasing vasoconstriction via the NFAT signaling pathway, increases in stiffness through proliferation mediated by miRNAs and dysregulated BMP and TGFβ1 signaling, and hypoxic conditions by depositing ECM proteins which remodels the pulmonary vasculature.

### 1.1.6 Pulmonary Arterial Adventitial Fibroblasts

PAAF cells are important for vascular ECM homeostasis and remodeling [13,43]. There is evidence that PAAFs are regulated by matrix stiffness [2,12,44], stretch [45], and hypoxia [43]. In the presence of injury, PAAFs are activated and differentiate into myofibroblast subtypes that remodel vascular wall properties by altering the expression, degradation or cross-linking of ECM proteins including collagen, fibronectin, and elastin [43]. Given that the ECM also serves as a substrate for cell adhesion and sends physical and chemical cues that determine cell phenotype, it has recently been suggested that matrix remodeling and stiffening may themselves signal tissue remodeling and drive the disease process [11].

*In-vivo experiments*. Balloon overstretch has been a useful way to study *in-vivo* activation of PAAFs in injury. Juvenile swine had a high number of proliferating cells in the adventitia, and increased expression of PDGF, showing that adventitial myofibroblasts aid in lesion formation by synthesizing growth factors and alpha-smooth muscle actin [46]. Another balloon overstretch

experiment conducted by Mallawaarachchi *et al*. demonstrated that PAAFs are activated to myofibroblasts by stretch in PAH, migrate towards the lumen to form the neointima, and synthesize ECM after vascular injury mediated by the TGF-β1 pathway [47].

Hypoxia is also a critical regulator of matrix gene expression by activating ROS signaling that stimulates increased alpha smooth muscle actin (α-SMA) production, a marker of activated fibroblasts [48]. Work by Chai *et al*. [49] showed that hypoxia induces PAAF proliferation, migration, and vascular remodeling via the PI3K/Akt pathway, inducing medial and adventitial thickening and excessive fibronectin and collagen deposition in pulmonary artery walls of hypoxic rats *in-vivo*.

*In-vivo* studies have shown an overexpression of transient receptor potential vanilloid 4 (TRPV4), a calcium-permeable channel that is activated by mechanical stimulation, in chronic hypoxia and MCT rats [50]. In their study, Cussac *et al*. showed how upregulation of the TRPV4 channel leads to PAAF activation and adverse adventitial remodeling in PAH, increasing collagen I and fibronectin expression. Targeting TRPV4 could potentially ameliorate disease progression in PAH by reducing PAAF activation.

*In-vitro experiments*. *In-vitro* experiments have shown the effect of altered substrate stiffness on PAAFs. Bertero *et al*. studied the YAP/TAZ and miR-130/301 vascular matrix feedback loop using cultured primary human PAAFs. They conducted quantitative RT-PCR of PAAFs on 1-kPa and 12-kPa stiffness matrices and found that stiffer matrices created a positive feedback loop, suggesting that matrix remodeling and stiffening may themselves signal tissue remodeling and drive the disease process [11]. The group also showed that YAP/TAZ signaling was activated by ECM stiffening from as low as 0.4 kPa to 1 kPa [51]. As part of the Hippo pathway, YAP/TAZ

and the role of miRNA 130/301 have also been suggested to promote PAAF proliferation, collagen deposition and cross-linking [12]. As the matrix stiffens due to fibrosis, angiotensin II is released by PAAFs activating pathways, such as the MAPK signaling cascade, that stimulate further ECM deposition [52].

Recently, TRPV4 has been shown to mediate PAAF proliferation and migration *in-vitro* using BrdU and wound scratch assays in PAAFs isolated from rats [50]. Cussac *et al*. showed how upregulation of TRPV4 activates PAAFs to transition to myofibroblasts. This work suggests a role for TRPV4 in excessive adventitial remodeling in PH.

Our group has shown how PAAFs respond to stretch and changes in extracellular matrix stiffness associated with PAH remodeling [53]. PAAFs were differentially regulated by stretch and stiffness in expressing collagen I (*Col1a1*), collagen III (*Col3a1*), fibronectin (*Fn1*), α-SMA (*Acta2*), Lysyl oxidase-like 1 (*Loxl1*), and elastin (*Eln*) mRNA, but there were no interaction effects between stretch and stiffness for these genes. Increasing substrate stiffness resulted in an increase in collagen III and myofibroblast marker protein α-SMA, confirming the important role of PAAFs in PA stiffening and vascular remodeling. In addition, *Fn1* expression was significantly upregulated when PAAFs were stretched for 4 h but returned to baseline if cells were stretched for 24 h. However, *Col1a1* expression was only upregulated after PAAFs were stretched for 24 h. This faster response to stretch of *Fn1* than *Col1a1* suggests that more detailed time-courses of PA cell responses to stretch may be needed.

We used a sensitivity analysis of the computational model to predict which receptors would have the largest impact on downstream phenotypic outputs when inhibited. Based on this, we tested the effects of using losartan, an angiotensin II type I receptor inhibitor, on the relative expression of *Fn1*. Losartan inhibited the upregulation of *Fn1* by an increase in matrix stiffness

and revealed an angiotensin receptor-independent activation of *Fn1* expression by stretch in PAAFs grown on stiffer substrates.

*In-silico experiments.* We developed a computational model of PAAFs mechanosignaling that included TGFβ, MAPK, PDGF, tumor necrosis factor α (TNFα), hypoxia, fibroblast growth factor (FGF), angiotensin II, and Hippo signaling pathways, which are upregulated by PAH, and phenotypic outputs to investigate mechanical regulation of fibrosis in PAH [54]. The model predicted 80% of the results from 20 independent papers not used for the original formulation. Sensitivity analysis showed PAAFs to be most sensitive to TGF-β1, MAPK and hypoxia signaling. *In-vitro,* PAAF cells were cultured on hydrogel substrates having stiffnesses representing normal, mild and severe PAH vessels, and were subjected to biaxial cell stretch [53]. Based on increasing the stimulus of the input "stiffness", we ran experiments and verified the model-predicted upregulation of five profibrotic genes including *Col1a1*, *Col3a1*, and *Eln* mRNA in response to biaxial stretch, while six profibrotic genes including *Fn1* and *Acta2* were upregulated by increases in matrix stiffness in PAAFs. This computational framework allowed us to incorporate experimental findings, to predict how PAAFs would respond to inhibition of the angiotensin II and TGFβ receptors, and design new experiments. By using the model, we were able to successfully test our hypothesis of the differential effects of stretch and substrate stiffness in which stretch activates integrin-β3, Macrophage Stimulating 1 or 2 (MST1/2) kinases, angiotensin II, and the TRP pathways and stiffness activates integrin β3, MST1/2, angiotensin II, TGF-β1, and syndecan-4 signaling. Even though the model identified candidate pathways based on the available literature, this model was not able to replicate the observed inhibition of *Fn1* expression by losartan or the transient response of *Fn1* at 4 h that was demonstrated in our *in-vitro* experiments published in

Wang *et al.* [53]. In addition, while this model can accurately predict many independent experiments, it only predicts qualitative increases and decreases of expression. With more data, the predictive and quantitative power of this model should increase greatly.

*Summary*. PAAFs respond to hypoxia, stretch and stiffness by activating to myofibroblasts that produce more α-SMA, proliferate, and overproduce ECM proteins causing adventitial remodeling via YAP/TAZ and MAPK signaling *in-vitro* and *in-vivo*.

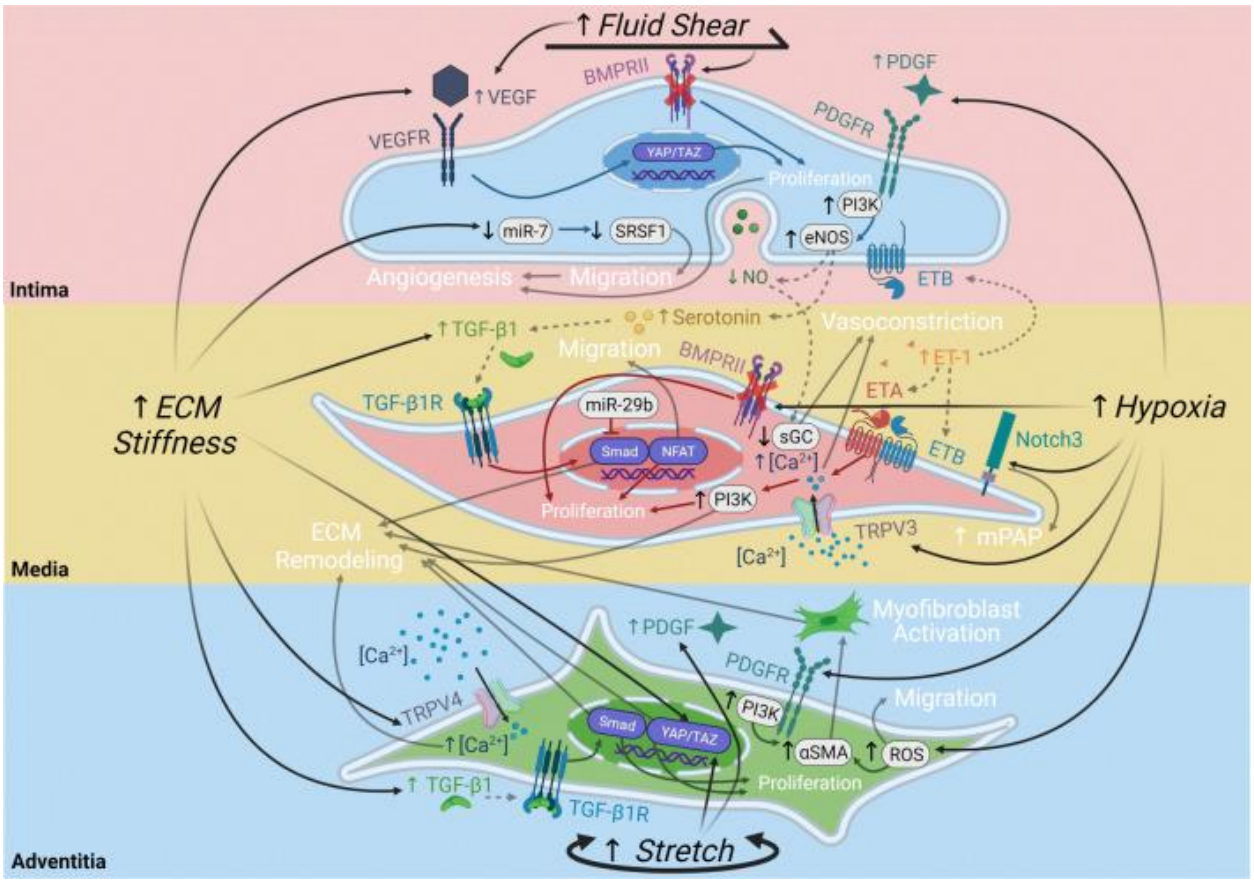


**Figure 1.4: Intracellular and intercellular signaling pathways in pulmonary arterial cells regulated by fluid shear stress, stretch, hypoxia and extracellular matrix stiffening**. PAECs respond to fluid shear stress via vascular endothelial growth factor (VEGF) signaling and bone morphogenic protein (BMP) signaling to ECM stiffness via VEGF signaling and miR-7, and to hypoxia via platelet-derived growth factor (PDGF) signaling. PASMCs respond to paracrine signals released by the PAEC and ECM stiffness via transforming growth factor beta 1 (TGF-β1), soluble guanylate cyclase (sGC), and endothelin (ET) signaling while responding to hypoxia via dysregulated BMP signaling and increased Notch signaling and transient receptor potential (TRP) channel calcium influx. PAAFs respond to ECM stiffness via TRP influx of calcium, TGF-β1 signaling, and activation of the Hippo pathway via YAP/TAZ transcription factors, to stretch via YAP/TAZ and PDGF signaling, and to hypoxia via reactive oxygen species (ROS) signaling. The four physical stimuli (black) lead to intercellular reactions (gray dashed arrows) and intracellular reactions (solid arrows matching cell color), resulting in phenotypic outputs (white). Illustration created with Biorender.com

### 1.1.7 Cellular Crosstalk

In addition to the intracellular signaling via VEGF, BMP, PDGF, TGF-β1, Notch, endothelin and

TRP channel signaling, mechanical crosstalk and paracrine signaling mediate interactions between

PAECs, PASMCs, and PAAFs in response to physical stimuli caused by PAH, including altered fluid shear stress, stretch, ECM stiffness and hypoxia (**Fig. 1.4**).

Constriction of the pulmonary artery, regulated by PASMC contraction and relaxation, can be regulated by PAEC released paracrine factors. ECs release endothelium-derived constricting factors (EDCF), endothelin-1 (ET-1) and thromboxane A2 (TXA2), which lead to vasoconstriction via PASMCs [55]. On the other hand, ECs can also release endothelium-derived relaxing factors (EDRF), NO and prostacyclin (PGI2), and the endothelium-derived hyperpolarizing factors (EDHF), which cause vasodilatation via PASMCs. This response between cell types is due to a connection of myoendothelial gap junctions, which transfer electric signals [55]. Serotonin synthesized by PAECs is transferred through these gap junctions into PASMCs, where it activates TGF-β1 signaling and induces a more differentiated phenotype. As TGF-β1 is a crucial regulator of fibrosis, this is an important way PAECs and PASMCs respond to PAH [56,57].

A crucial way endothelium responds to stressors such as increased levels of TGF-β1, tumor necrosis factor-α (TNF-α), or interleukin-1β (IL-1β), is to undergo endothelial-to-mesenchymal transition (EndoMT). This cellular transdifferentiation results in some PAECs losing their endothelial markers, for example von Willebrand factor (vWF), and tight gap junctions between cells. The PAECs then express α-smooth muscle actin (α-SMA) and vimentin, fibronectin, and other markers of myofibroblasts. These transformed PAECs then go on to overproduce collagen I and other ECM proteins that remodel the matrix, inducing a profibrotic phenotype and increasing PA stiffness [9]. This then decreases vascular wall strain and further exacerbates ECM remodeling (**Fig. 1.3**).

*In-silico experiments.* Recently, there has been published a computational model of the EndoMT transition integrating boolean equations, feedback mechanisms, and fixed patterns of activation which simulates cell behaviors and predicts effects of mutations. This allows them to explore conditions that cause EC activation, the transition, and reverse-transitions for future possible pharmacological control of the endothelial to mesenchymal transition [58].

There is currently no computational model of the crosstalk between PAECs, PASMCs, and PAAFs, or indeed any network models of PAECs or PASMCs individually, but a theoretical framework would allow us to synthesize experimental findings from different cell types and understand how their interactions contribute to pathological vascular remodeling.

*Summary*. PAECs release paracrine factors that can affect the level of vasoconstriction and TGF-β1 signaling as mediated by PASMCs through gap junctions. Increased levels of TGF-β1 and TNF-α can lead to EndoMT wherein PAECs transform into activated PAAFs, or myofibroblasts, which increases deposition and accumulation of collagen and other ECM proteins (**Fig. 4**). This matrix remodeling can in turn increase ECM stiffness, which regulates PAEC migration and angiogenesis, matrix expression by PASMCs and PAAFs, and PAAF proliferation.

### 1.1.8 Discussion

There is now compelling evidence that mechanical cues caused by pulmonary arterial hypertension and subsequent disease remodeling regulate the responses of endothelial cells, smooth muscle cells, and adventitial fibroblasts in the pulmonary vasculature. As we continue to map the signaling pathways, paracrine interactions, and mechanical crosstalk in these cells, we can build predictive network models and use them to identify new therapeutic targets specifically to the mechanical

milieu during different stages of the disease. It is likely that customized combination therapies could prove more effective than single targets in this context.

### 1.2 Network Models of Cell Signaling

*In-silico* network models of cell signaling help to integrate the function of many pathways together to better understand their crosstalk and effects without having to do many combinatorial experiments. These network models of specific cell types also help one to better probe effects of stimuli such as stretch, stiffness, or hypoxia and their ultimate effect on phenotypic outputs such as cell proliferation or extracellular matrix deposition. By using experimental data to construct these network models, and other literature data to serve as validation, the model can be used to propose new experiments that feed back into the model and vice versa. In the subsections below, model formulations and uncertainty quantification of these models will be discussed, as well as schematized models for pulmonary artery cells.

#### 1.2.1 Normalized Hill-Type Differential Equations

Work has been done by the Saucerman group to develop normalized Hill-type ordinary differential equations to create a biochemical model of cell signaling across different pathways in a cardiac beta-adrenergic signaling context that can be adapted to other cell types [59]. The cell signaling networks use normalized functions based on the Hill equation that incorporate the parameters $n$ as the Hill coefficient, the $EC_{50}$ which represents half maximal activation, $\omega$ the weight of the reaction, $\tau$ the time constant, and a $y_{initial}$ and $y_{max}$ that are by default 0 and 1 respectively for every reaction. The reaction logic is created by doing a literature review and determining if nodes are controlled by logical AND and OR operators that represent the crosstalk in signaling. The use of

normalized Hill-type differential equations allows for quantitative predictions of cell network outputs even with a scarcity of biochemical data. Sensitivity analysis of these network models also allows for identification of the most important inputs and nodes to the cell types analyzed, such as the significance of PKA negative feedback and integrin-mediated mechanotransduction on cardiac beta-adrenergic signaling.

### 1.2.2 Uncertainty Quantification

There are, however, many sources of uncertainty present in computational networks of cell signaling that can be quantified such as parameter uncertainty and epistemic uncertainty [60]. Parameter uncertainty in the parameters discussed above in Section 1.2.1 ($n$, $EC_{50}$, $\omega$, $\tau$, $y_{initial}$ and $y_{max}$) can arise due to default parameters being used when the actual value is not known. Within a reasonable range, these parameters can be sampled and the change in accuracy of the model in predicting activity of nodes can be evaluated to determine which parameter is most sensitive to uncertainty. Epistemic uncertainty arises when the structure or logic of a reaction is not made clear by literature, as there can be errors of interpretation, or the logic-based ordinary differential equation cannot accurately reflect the real biochemical reaction. Indeed, in cases where there are not enough experiments on the specific cell type in the literature, models can be filled in with other cell types which may not perfectly reflect how this cell type will respond.

A more detailed discussion of how uncertainty quantification (UQ) in parameter uncertainty and epistemic uncertainty was applied to a specific pulmonary arterial fibroblast model will be examined in Chapter 2.

### 1.2.3 Pulmonary Arterial Smooth Muscle Cell Model

Schematics of how pulmonary arterial smooth muscle cells use ion channels and membrane receptors to respond to external stimuli such as mechanical stimuli and hypoxia that we have made can be used to construct a network model as shown below (**Fig 1.5**).

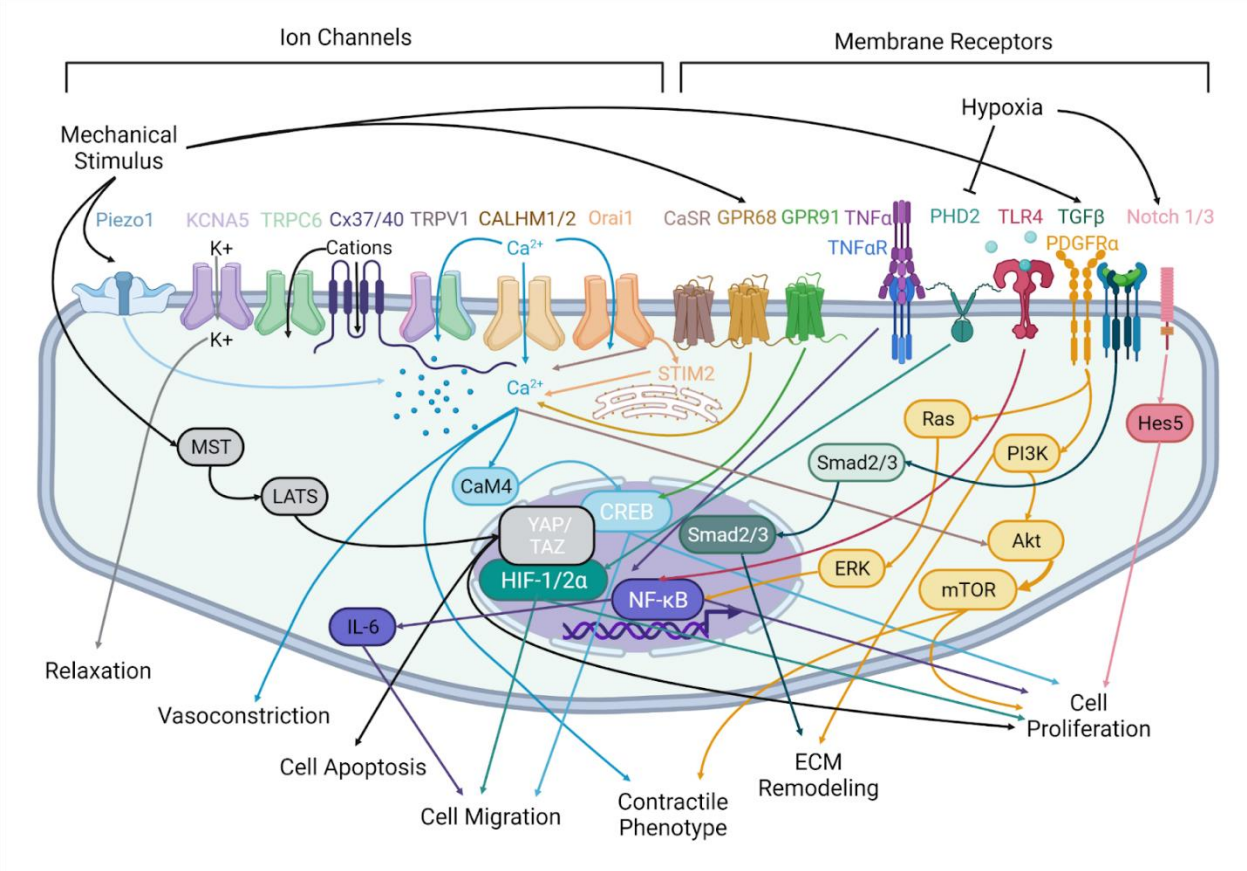


**Figure 1.5: Pulmonary arterial smooth muscle cell model with diagrammed ion channels and membrane receptors.** External inputs of mechanical stimuli and hypoxia lead to cytokines, nodes of signaling proteins, transcription factors, and functional outputs such as cell migration and proliferation. Made on Biorender.com

The flow of cations such as $Ca^{2+}$ and $K^{+}$ through ion channels and binding of cytokines such as transforming growth factor beta (TGFβ) and platelet-derived growth factor (PDGF) to their respective membrane receptors leads to signaling cascades such as Smad3 [33] and phosphoinositide 3-kinase (PI3K)/Akt signaling [30] that can ultimately lead to activation of

transcription factors and phenotypic outputs such as extracellular matrix remodeling, increased smooth muscle cell contractility, or cell proliferation. Combining the effects of these pathways can lead to predictions such as which cations would increase vasoconstriction, and inhibition of which pathways could reduce smooth muscle cell proliferation.

### 1.2.4 Pulmonary Arterial Adventitial Fibroblast Modeling

A pulmonary arterial adventitial fibroblast network model was constructed using 56 research papers with 20 papers that included only human, rat or mouse data set aside for independent validation. The resulting network has 69 nodes and 97 reactions, with input nodes specifically found to be important in PAH. These inputs include the mechanical stimuli of stiffness and stretch, TGFβ, tumor necrosis factor alpha (TNFα), PDGF, angiotensin II (AngII), fibroblast growth factor (FGF) and hypoxia. These then lead to signaling modules PI3K, TGFβ, Notch, reactive oxygen species (ROS), mitogen-activated protein kinase (MAPK), calcineurin, and Hippo signaling. Pathways activate or inhibit seven transcriptional regulators, and crosstalk to affect eight phenotypic outputs crucial to PAH disease progression, including collagen I, collagen III, alpha smooth muscle actin (αSMA), lysyl oxidase like 1 (Loxl1), fibronectin, elastin, cell proliferation, and cell migration.

The model schematic and formulation, as well as iterations and improvements, will be discussed in detail in Chapters 2 and 3.

## 1.3 *In-vitro* Methods to Study PAAFs

To iterate upon the network model of pulmonary arterial adventitial fibroblasts, *in-vitro* experiments teasing apart the effects of stretch and stiffness, as well as inhibition of specific nodes

suggested by sensitivity analysis of the model were done. This led to improvements of the model and in turn suggested future *in-vitro* experiments. These following subsections will discuss the methods by which these *in-vitro* PAAF studies were conducted.

### 1.3.1 PAAF Isolation and Characterization

The pulmonary artery is dissected from the heart and lungs of a Sprague-Dawley rat, then the outer adventitial layer is stripped off and enzymatically digested with 1 mg/mL Type 2 collagenase for 1.5 hours at 37 ◦C (**Fig. 1.6**).

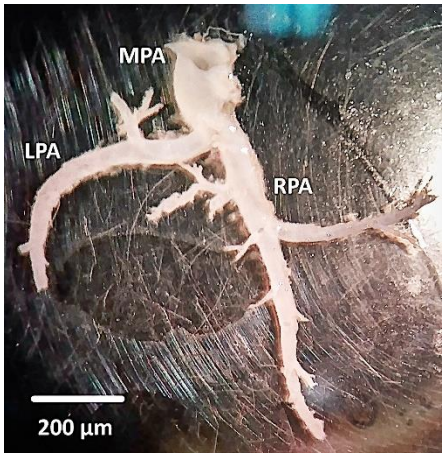


**Figure 1.6: Isolated pulmonary artery.** The pleura is carefully removed from the harvested lungs to identify and isolate the left pulmonary artery (LPA), main pulmonary artery (MPA), and right pulmonary artery (RPA).

Samples of the PAAF culture were taken as labeling controls to estimate purity. Cells were stained for DAPI (nucleus), vimentin (mesenchymal lineage cells), von Willebrand factor (vWF) which is a pulmonary arterial endothelial cell marker, and myosin heavy chain 11 (MYH11) which is a pulmonary arterial smooth muscle cell marker. Images were all acquired at 40× magnification, with representative images shown below (**Fig. 1.7**). Cells were characterized as pulmonary arterial adventitial fibroblasts if they expressed vimentin and not vWF or MYH11, and only 3% were

positive for vWF and 0.2% were positive for MYH11 suggesting high enrichment of PAAFs [53]. Intact pulmonary artery tissue sections were stained and imaged with the same antibodies and imaging settings as positive controls for these markers.

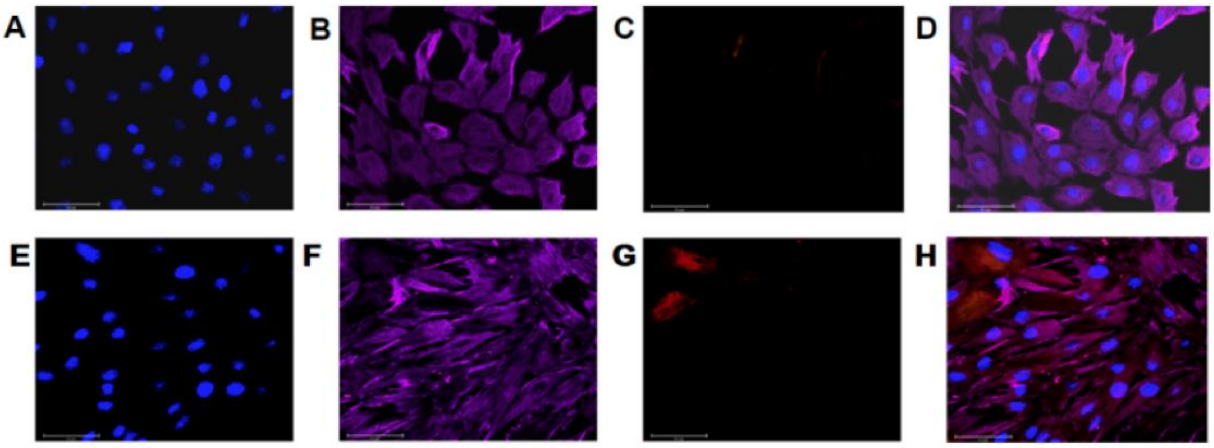


**Figure 1.7: Immunofluorescent staining of cells isolated from pulmonary arterial adventitia**. The cell culture showed positive labeling for (**A**, **E**) DAPI, (**B**, **F**) vimentin, (**C**) vWF, and (**G**) MYH11 with (**D**,**H**) overlays. Out of 425 isolated cells, 3% expressed vWF, a PAEC marker, and out of 888 cells, 0.2% expressed MYH11, a PASMC marker, and 100% expressed vimentin (**A**–**H**). Due to the exclusion of PAEC and PASMC marker expressing cells, the culture was determined to be primarily PAAFs.

### 1.3.2 PAAFs Cultured on Varying Stiffness Hydrogels

Based on work by Liu *et al*. using atomic force microscopy (AFM), pulmonary arteries (PAs) from Sprague Dawley rats were determined to have stiffnesses of roughly 0.5 kPa for normotensive controls, 3 kPa for mild PAH, and 10 kPa for severe PAH conditions [61]. Corresponding stiffness polyacrylamide hydrogels with the same modulus of elasticity were formulated according to formulas by Tse *et al* [62]. PAAFs when cultured on plastic transition into myofibroblasts, which exhibit higher collagen I (*Col1a1*), collagen III (*Col3a1*), and αSMA (*Acta2*) expression (Fig 1.8). To validate that culture for three days on a softer matrix of 0.5 kPa was enough to revert PAAFs back to fibroblasts, PAAFs were trypsinized from plastic and cultured at 0.5 and 8 kPa. To validate

the comparison of *in-vitro* isolated PAAF data to *in-vivo* isolated pulmonary artery data, relative expressions of six profibrotic genes (*Col1a1, Col3a1, Acta2, Loxl1, Fn1, Eln*) were compared to RNA isolated from a normotensive pulmonary artery and no significant difference was found [53]. These six genes were used due to their inclusion in the PAAF mechanosignaling model discussed in Section 1.2.4 as mRNA important in PAAF response to many different crucial pathways upregulated by PAH such as the mechanosignaling TGFβ and Hippo pathways.

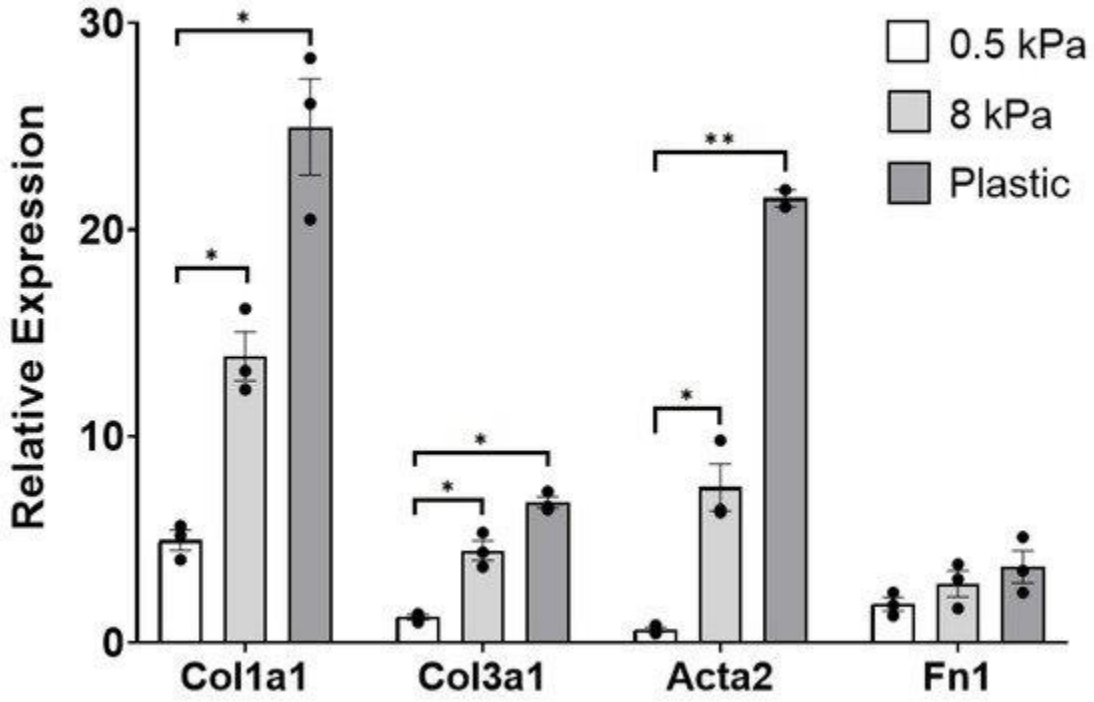


**Figure 1.8: Relative expression of PAAFs cultured on 0.5 kPa and 8 kPa substrates and plastic.** Mean ± standard errors of the mean of *Col1a1*, *Col3a1*, *Acta2*, and *Fn1* gene expression of cells seeded on Cytosoft® plates. Effects of stiffness on PAAF gene expression relative to 18S ribosomal RNA. Induction of *Col1a1*, *Col3a1*, and *Acta2* were significant at both 8 kPa and the stiffness of tissue culture plastic, while induction of *Fn1* was not significant. This experiment demonstrates the response of PAAFs to induction by stiffness in 4 profibrotic genes. Significant effect of stiffness (* $p < 0.05$ and ** $p < 0.0001$) by one-way analysis of variance (ANOVA) is compared with gene expression at 0.5 kPa.

### 1.3.3 PAAFs Cultured on Equibiaxial Stretchers

To apply 10% equibiaxial stretch to PAAFs cultured onto varying stiffness gels (0.5 kPa, 3 kPa, 10 kPa), custom-machined circular stretchers made of polycarbonate were designed using computer-aided design (**Fig. 1.9**). Polydimethylsiloxane (PDMS) membranes are made and treated with benzophenone for polyacrylamide gel adherence [63]. Polyacrylamide gels were made to be 25 mm in diameter and ringed with silicone grease, then coated with collagen I for cell adherence. 100,000 – 140,000 PAAFs are platted and cultured onto the polyacrylamide gels for three days at 37 °C, 5% $CO_2$, 100% humidity, changed to serum-free media, then stretched via two full turns of the stretcher equivalent to 10% static stretch for 24 hours before RNA isolation.

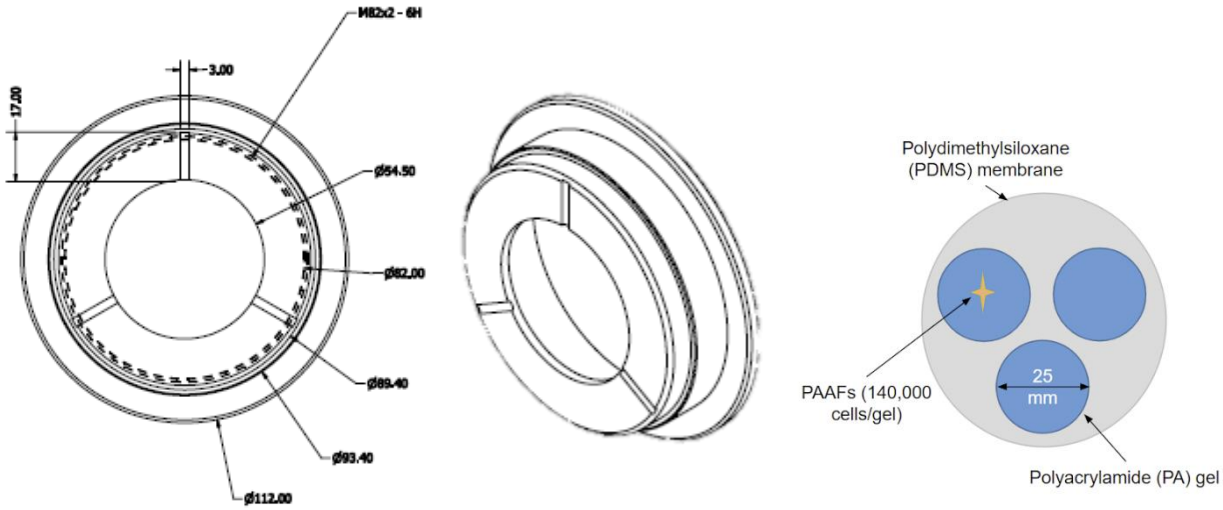


**Figure 1.9: Equibiaxial stretcher design and cell seeding schematic**. On the left, the stretcher CAD file with design specifications and measurements**.** On the right, a schematic of the tunable stiffness polyacrylamide gel arrangement on polydimethylsiloxane (PDMS) membrane to be placed into stretcher for cell culture in separate wells.

## 1.4 Sex Differences in Pulmonary Arterial Hypertension

The incidence of PAH is two to four times higher in women than men, but their prognosis is better with higher rates of survival than men if the women are pre-menopausal [64]. Estrogens are elevated in men and postmenopausal PAH patients, and sex differences largely dissipate after

women are 45 years of age or post-menopause, indicating a possible role for estrogen in the pathophysiology of PAH. Cardiovascular diseases show a great deal of sexual dimorphism in incidence and outcome as well, and studies by the Aguado lab show the importance of considering the sex of cardiac cells in *in-vitro* disease models [180]. Left ventricular cardiac fibroblasts particularly secrete factors that affect heart function and display a differential fibrotic response in male-derived *versus* female-derived cells. This suggests an underlying sex difference in the disease that is not well-understood that could be present at the cellular and tissue scales.

### 1.5 Current Open Questions and Motivation for this Dissertation

Pulmonary arterial hypertension is a complex and often fatal disease that ultimately results in right heart failure [65, 66]. PAH is a very complex disease, and the molecular pathways that lead to its pathogenesis are not fully elucidated. A multitude of pathways have been identified but their crosstalk and response to stimuli are not well-understood [3,43]. Dysregulation of this cell signaling is critical to understanding how PAH develops, but there is a scarcity of available literature data to characterize this dysregulation.

The underlying molecular mechanisms and the time course of the disease are also not well-characterized. Since our model showed high sensitivity to the interplay of important pathways like AngII, TGFβ and hypoxia, we built a network signaling model of the PAAF, using it to generate experimentally testable hypotheses about *in-vitro* inhibition experiments utilizing hydrogels of tunable stiffness and custom machined equibiaxial stretchers. This allows for examination of the model to suggest areas where experiments are necessary, and the results of the experiments feed in to and improve the computational model. While there is literature data on individual pathways that regulate the fibrotic responses of PAAFs *in-vitro* and *in-vivo*, such as the Angiotensin and

TGFβ pathways, how these different pathways respond to physical stimuli and interact with each other remains unknown. [3] There are also limited treatment options, only vasodilators or whole lung transplants or but no treatments that reverse the maladaptive vascular remodeling [2]. Our hypothesis is that we can use this model to identify important drivers of PAH and predict inhibitors for the fibrosis that occurs as the disease progresses.

No such computational model of PAAFs existed beforehand, nor did experiments that separated the variables of stretch and stiffness and their interplay in PAH progression. PAH introduces many mechanical stimuli including fluid shear, vessel wall stress and vessel wall strain, but the effect of these on the cells and phenotype are still unknown [26] The idea of stretch and stiffness as separate mechanical signals which separately regulate disease response had also not yet been explored and how different profibrotic genes respond to different stimuli is important to understand in the context of PAH disease complexity. We are studying the activation of crucial ECM proteins collagen I (*Col1a1),* collagen III (*Col3a1*), fibronectin (*Fn1*) as the model has identified these as candidate genes for how PAAFs remodel the matrix. We are also studying smooth muscle actin (*Acta2*) for its role in transitioning fibroblasts to myofibroblasts, elastin (*Eln*) which determines PAAF response to stretch, and lysyl-oxidase like 1 (*Loxl1*) due to its role in stiffening the matrix independent of increases in collagen through crosslinking [53]. We aim to identify the pathways that regulate differential responses of PAAFs to altered stiffness and stretch at different stages of PAH because in PAH, there is an increase of pressure in the vessels that increases strain as well of deposition of ECM proteins leading to an increase of stiffness [43]. We hypothesize that combinations of altered substrate stretch and stiffness give rise to different PAAF responses than altered stretch or stiffness alone, that changes in ECM stiffness and strain are regulated by a combination of different pathways and those mechanical stimuli occur at different

timepoints in PAH. Using the model's inhibition predictions of the effect of the most important inputs of angiotensin and TGFβ, we can identify combinations of receptor blockers that inhibit disease phenotypes arising from stretch and stiffness to test *in-vitro*. By iterating the model using conclusions from *in-vitro* experiments, we can make better predictions of PAAF responses to PAH conditions that tease apart which pathways are the most important in activation of the profibrotic genes we are studying and hypothesize about regulation and other pathways that may be involved in this regulation.

Sex differences in PAH at the cellular and tissue level have also not been examined this in-depth, which is a crucial need to be addressed. This sex difference on the patient scale has been demonstrated [64], but the underlying cause has yet to be determined. In sugen-hypoxia rats, female rats have demonstrated improved hemodynamics, demonstrating a significantly lower mean pulmonary arterial pressure than male and ovariectomized rats, and Rafikova *et al.* have also shown significantly more collagen accumulation in PAs from sugen-hypoxia male rats compared to PAs from female rats [179]. In the RV, we have observed higher end diastolic pressure in male rats, profibrotic gene upregulation in male RV tissue, and increased collagen in histology and end diastolic elastance as a measure of RV stiffness in RVs isolated from male rats. Studies on the sex differences in left ventricular cardiac fibroblasts suggest the importance of cellular level responses to microenvironment in determining cardiovascular disease sexual dimorphism [180]. Tissue-level sex differences could arise due to differential activation of PAAFs and RV CFBs in response to stiffness and stretch due to sex of the cells alone as the Aguado lab has observed in LV CFBs. This suggests hypothetical differences in activation of profibrotic genes by stretch and stiffness in pulmonary arterial and cardiac fibroblasts and changes in vascular remodeling due to sugen-hypoxia treatment in pulmonary arteries could give rise to the sex paradox differences in PAH

since increased fibrosis in the PAs and RVs could lead to increases in pressure and reduction in cardiac function. This work would go a long way to elucidating if female-derived, ovariectomized-derived, and male-derived cells and tissue are fundamentally different at baseline or in their response to stretch and stiffness *in-vitro* and to sugen-hypoxia *in-vivo* models of PAH.

**Acknowledgements**

Chapter 1, in part, is a reprint of the material as it appears in Biophysical Review 2021. Wang, Ariel; Valdez-Jasso, Daniela. The dissertation author was the primary investigator and author of this paper.

# CHAPTER 2: QUANTIFICATION OF UNCERTAINTY IN A NEW NETWORK MODEL OF PULMONARY ARTERIAL ADVENTITIAL FIBROBLAST PROFIBROTIC SIGNALING

## 2.1 Abstract

Here, we present a novel network model of the pulmonary arterial adventitial fibroblast (PAAF) that represents seven signaling pathways, confirmed to be important in pulmonary arterial fibrosis, as 92 reactions and 64 state variables. Without optimizing parameters, the model correctly predicted 80% of 39 results of input–output and inhibition experiments reported in 20 independent papers not used to formulate the original network. Parameter uncertainty quantification (UQ) showed that this measure of model accuracy is robust to changes in input weights and half-maximal activation levels ($EC_{50}$) but is more affected by uncertainty in the Hill coefficient ($n$), which governs the biochemical cooperativity or steepness of the sigmoidal activation function of each state variable. Epistemic uncertainty in model structure, due to the reliance of some network components and interactions on experiments using non-PAAF cell types, suggested that this source of uncertainty had a smaller impact on model accuracy than the alternative of reducing the network to only those interactions reported in PAAFs. UQ highlighted model parameters that can be optimized to improve prediction accuracy and network modules where there is the greatest need for new experiments.

### 2.1.1 Computational Models of Cell Signaling

Cell signaling networks are cascades of biochemical reactions that regulate cellular responses to external cues, and their dysregulation is important in the progression of disease. PAH involves pathological remodeling of the vascular wall mediated in part by PAAFs in response to

pathological strain and stresses such as mechanical overload and hypoxia. PAAFs residing in the adventitial layer of the arterial wall regulate vascular extracellular matrix (ECM) and mechanical properties [43]. Studying the interplay between the effects of signaling cytokines, hypoxia and the mechanical stimuli that are activated in PAH will help to elucidate signaling pathway interactions and may aid in developing novel therapies to reverse vascular fibrosis and disease progression.

Mathematical modelling of cell signaling networks is a useful tool for synthesizing available experimental data and investigating interactions between pathways that are difficult to study experimentally. Here, we introduce a new logic-based ordinary differential equation model [59] of the major biochemical networks known to regulate pro-fibrotic cell responses such as ECM expression, proliferation and myofibroblast transformation in PAAFs [63]. The network model was derived from published cell biological experiments and transcriptional measurements in primary PAAFs supplemented, where necessary, with information on canonical pathway structure from better studied fibroblast types, mainly cardiac fibroblasts (CFBs). Inputs to the PAAF signaling network model were based on reported stimuli upregulated in PAH [43].

While the signaling pathways included in this model have been identified in PAAFs, their interplay is not well understood, and there is a paucity of experimental data in the literature specific to these fibroblast cells. Therefore, after constructing a PAAF signaling network model, we carried out a sensitivity analysis to identify the important nodes in the network.

Creating a cell signaling model inherently introduces parameter uncertainty, since experimental studies rarely report quantitative biochemical reaction properties. There are also epistemic uncertainties in the structure and logic of the network, which depend on published experiments from a variety of cell types and conditions that are occasionally inconsistent or ambiguous [67]. Therefore, to analyze the robustness of the developed model and identify how small perturbations in the parameters leads to changes in model predictions, we have carried out uncertainty quantification (UQ) analysis of the model parameters. Using a separate set of data not used in the model formulation, we determined the prediction capabilities of the model and its qualitative accuracy. We also used this method to determine if adding pathways from other fibroblast cell types impacts model accuracy.

Since the model parameters were not optimized, we do not expect a close quantitative agreement between model predictions and experimental data. Rather, objective qualitative comparison criteria were used, and we used UQ to assess the robustness of model prediction accuracy and to identify the modules and parameters that are most affected by incomplete or noisy data [68]. Analysis of parameter and structural uncertainty showed that the PAAF model is robust to most parameter uncertainty and identified new experiments that are needed to improve model confidence and accuracy.

Here, we present a novel network model of the pulmonary arterial adventitial fibroblast (PAAF) that represents seven signaling pathways, confirmed to be important in pulmonary arterial fibrosis, as 92 reactions and 64 state variables. Without optimizing parameters, the model correctly predicted 80% of 39 results of input–output and inhibition experiments reported in 20 independent papers not used to formulate the original network. Parameter uncertainty quantification (UQ) showed that this measure of model accuracy is robust to changes in input weights and half-maximal

activation levels ($EC_{50}$) but is more affected by uncertainty in the Hill coefficient ($n$), which governs the biochemical cooperativity or steepness of the sigmoidal activation function of each state variable. Epistemic uncertainty in model structure, due to the reliance of some network components and interactions on experiments using non-PAAF cell types, suggested that this source of uncertainty had a smaller impact on model accuracy than the alternative of reducing the network to only those interactions reported in PAAFs. UQ highlighted model parameters that can be optimized to improve prediction accuracy and network modules where there is the greatest need for new experiments.

### 2.1.2 Materials and Methods

#### 2.1.2.1 Computational Model of Pro-Fibrotic PAAF Cell Signaling

The PAAF signaling model was manually constructed with the same default parameters and model file structures as the one developed by Zeigler *et al.* for cardiac fibroblasts [69]. Out of the 92 reactions in our model, 52 reactions are unique to PAAFs. The model construction was based on results reported in 52 published papers describing experimental studies in PAAFs or other fibroblast types [3, 48-49, 51-52, 70-117] when necessary to complete 18 intermediate reactions not described in the comparatively sparse literature on PAAF signaling. In addition, 20 independent papers documenting *in-vitro* or *in-vivo* experiments in rat or human PAAFs and not used in the original model formulation were set aside to measure the predictive capability of the model.

The resulting PAAF signaling network (**Fig. 2.1**) integrates seven input stimuli that are implicated in PAH pathogenesis: mechanical loading, transforming growth factor-$\beta$ (TGF $\beta$),

tumor necrosis factor- $\alpha$ (TNF $\alpha$), platelet-derived growth factor (PDGF), angiotensin II (AngII), fibroblast growth factor (FGF), and hypoxia. These activate seven receptors and signaling modules, namely the phosphoinositide 3-kinase (PI3K), TGF $\beta$, Notch, reactive oxygen species (ROS), mitogen-activated protein kinase (MAPK), calcineurin and Hippo pathways. Downstream

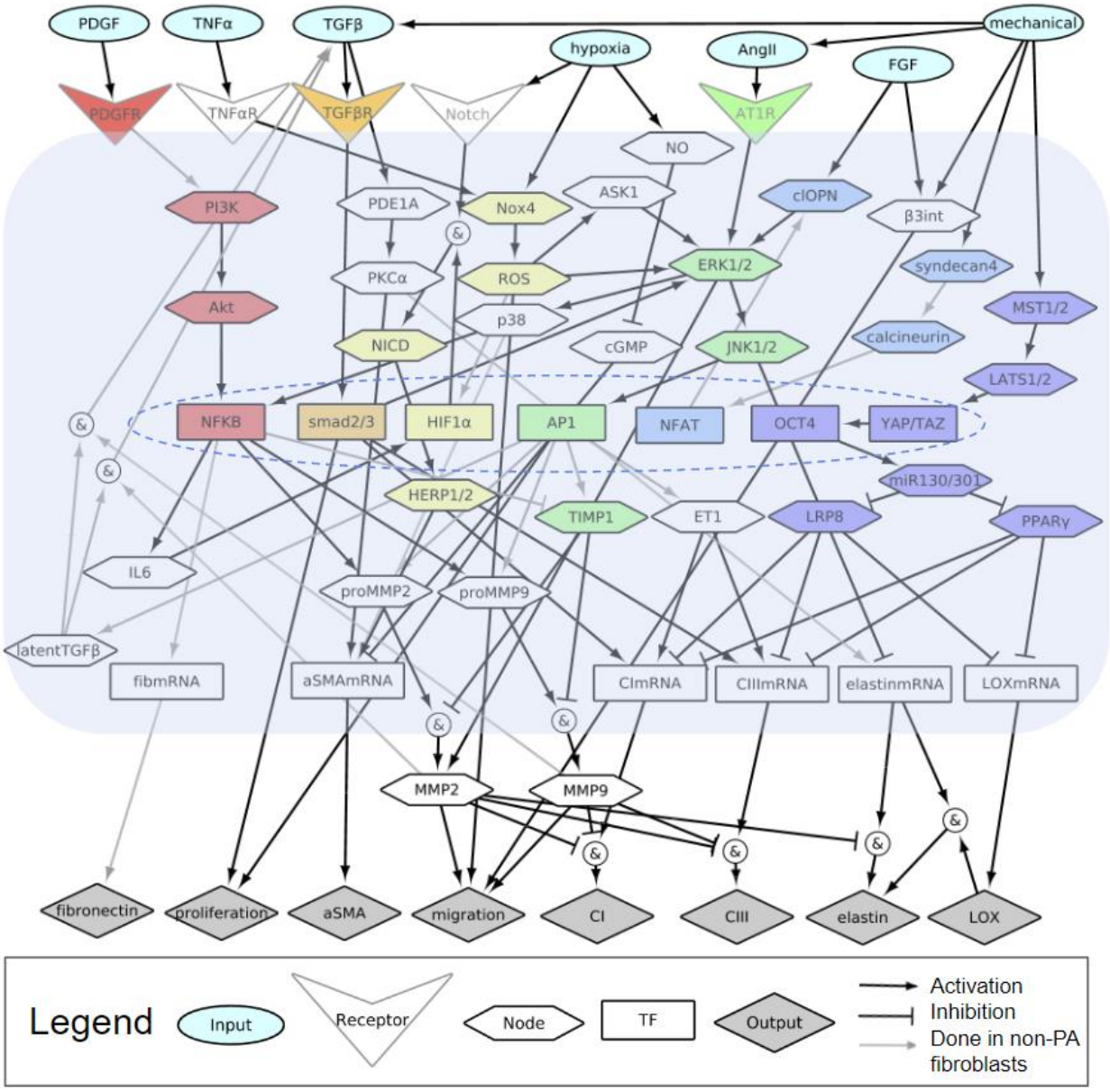


**Figure 2.1: A schematic of pro-fibrotic PAAF cell signaling network comprised of 64 nodes.** This network is comprised of 64 nodes with input stimuli (blue ovals), receptors (triangles), signaling molecules (hexagons), transcription factors (colored rectangles), messenger RNA (rectangles) and phenotypic outputs (grey diamonds). The colors represent the recognized signaling modules including phosphoinositide 3-kinase (PI3K) (red), TGFβ (orange), Notch, reactive oxygen species (ROS, yellow), mitogen-activated protein kinase (MAPK, green), calcineurin (blue) and Hippo (purple). The arrows indicate the 92 activation or inhibition reactions, with the grey arrows denoting reactions based only on experiments in non-PA fibroblasts. Converging reactions denoted by & indicate 'AND' gate logic, while other combinations imply 'OR' gate logic.

transcription factors regulate the expression of eight outputs important in the pro-fibrotic cell

phenotype and ECM remodeling [3]. Overall, there are 64 nodes that represent physical stimuli, ligands, receptors, signaling molecules, transcription factors, messenger RNA (mRNA), proteins, and cell phenotypes interconnected via 92 reactions. The publications used to justify each individual reaction and interaction are listed below in **Fig. 2.2**.

**Reaction Information**

| module | ID | Rule | Weight | n | EC50 | PMID | Secondary Reference |
|---|---|---|---|---|---|---|---|
| input | i1 | => AngII | 0.25 | 1.4 | 0.6 | 23737168 | 21949113 |
| input | i2 | => TGFB | 0.25 | 1.4 | 0.6 | 24966928 | 9102158 |
| input | i3 | => mechanical | 0.25 | 1.4 | 0.6 | 12003855 | 15894533 |
| input | i4 | => TNFa | 0.25 | 1.4 | 0.6 | 20098355 | |
| input | i5 | => PDGF | 0.25 | 1.4 | 0.6 | 22735370 | |
| input | i6 | => FGF | 0.25 | 1.4 | 0.6 | 11500961 | |
| input | i7 | => hypoxia | 0.25 | 1.4 | 0.6 | 22735370 | 20202975 |
| fback | r1 | MMP9 & latentTGFB => TGFB | 1 | 1.4 | 0.6 | 10652271 | 12226090 |
| fback | r2 | MMP2 & latentTGFB => TGFB | 1 | 1.4 | 0.6 | 10652271 | 12226090 |
| middle | r3 | AngII => AT1R | 1 | 1.4 | 0.6 | 21660462 | 27012211 |
| middle | r4 | AT1R => ERK1_2 | 1 | 1.4 | 0.6 | 21660462 | 24343777 |
| middle | r5 | ROS => ERK1_2 | 1 | 1.4 | 0.6 | 21660462 | |
| middle | r6 | FGF => B3int | 1 | 1.4 | 0.6 | 11500961 | |
| middle | r7 | B3int => migration | 1 | 1.4 | 0.6 | 11500961 | 10869268 |
| middle | r8 | mechanical => B3int | 1 | 1.4 | 0.6 | 22582113 | |
| middle | r9 | mechanical => syndecan4 | 1 | 1.4 | 0.6 | 23178899 | |
| middle | r10 | mechanical => MST1_2 | 1 | 1.4 | 0.6 | 21654799 | 26565914 |
| middle | r11 | syndecan4 => calcineurin | 1 | 1.4 | 0.6 | 23178899 | |
| middle | r12 | calcineurin => NFAT | 1 | 1.4 | 0.6 | 23178899 | |
| middle | r13 | NFAT => clOPN | 1 | 1.4 | 0.6 | 23178899 | |
| middle | r14 | clOPN => ERK1_2 | 1 | 1.4 | 0.6 | 22582113 | 10869268 |
| middle | r15 | ERK1_2 => MMP2 | 1 | 1.4 | 0.6 | 24343777 | |
| middle | r16 | MST1_2 => LATS1_2 | 1 | 1.4 | 0.6 | 26565914 | |
| middle | r17 | LATS1_2 => YAP_TAZ | 1 | 1.4 | 0.6 | 26565914 | |
| middle | r18 | YAP_TAZ => OCT4 | 1 | 1.4 | 0.6 | 26565914 | |
| middle | r19 | OCT4 => miR130_301 | 1 | 1.4 | 0.6 | 26565914 | |
| middle | r20 | !miR130_301 => PPARg | 1 | 1.4 | 0.6 | 26565914 | |
| middle | r21 | !miR130_301 => LRP8 | 1 | 1.4 | 0.6 | 26565914 | |
| middle | r22 | !PPARg => CImRNA | 1 | 1.4 | 0.6 | 26565914 | |
| middle | r23 | !LRP8 => CImRNA | 1 | 1.4 | 0.6 | 26565914 | |
| middle | r24 | !PPARg => CIIImRNA | 1 | 1.4 | 0.6 | 26565914 | |
| middle | r25 | !LRP8 => CIIImRNA | 1 | 1.4 | 0.6 | 26565914 | |
| middle | r26 | !PPARg => LOXmRNA | 1 | 1.4 | 0.6 | 26565914 | |

**Figure 2.2: Reaction List with References.** Reactions are listed as input or middle, where *!* indicates inhibition and default parameters of input weight = 0.25, middle weight = 1**,** Hill coefficient = 1.4, $EC_{50}$ = 0.6

| | | | | | | | |
|---|---|---|---|---|---|---|---|
| middle | r27 | !LRP8 => LOXmRNA | 1 | 1.4 | 0.6 | 26565914 | |
| middle | r28 | hypoxia => NO | 1 | 1.4 | 0.6 | 24719876 | |
| middle | r29 | !NO => cGMP | 1 | 1.4 | 0.6 | 19672103 | |
| middle | r30 | hypoxia => Nox4 | 1 | 1.4 | 0.6 | 24947524 | 19628034 |
| middle | r31 | Nox4 => ROS | 1 | 1.4 | 0.6 | 24947524 | |
| middle | r32 | ROS => migration | 1 | 1.4 | 0.6 | 24947524 | |
| middle | r33 | ROS => ASK1 | 1 | 1.4 | 0.6 | 28910144 | |
| middle | r34 | ASK1 => ERK1_2 | 1 | 1.4 | 0.6 | 28910144 | |
| middle | r35 | ERK1_2 => JNK1_2 | 1 | 1.4 | 0.6 | 28910144 | 27012211 |
| middle | r36 | JNK1_2 => AP1 | 1 | 1.4 | 0.6 | 21949681 | 14561589 |
| middle | r37 | AP1 => TIMP1 | 1 | 1.4 | 0.6 | 12525489 | |
| middle | r38 | proMMP9 & !TIMP1 => MMP9 | 1 | 1.4 | 0.6 | 20434368 | 16709900 |
| middle | r39 | proMMP2 & !TIMP1 => MMP2 | 1 | 1.4 | 0.6 | 20434368 | 10323763 |
| middle | r40 | AP1 => proliferation | 1 | 1.4 | 0.6 | 21949681 | |
| middle | r41 | AP1 => ET1 | 1 | 1.4 | 0.6 | 10807739 | |
| middle | r42 | ET1 => CImRNA | 1 | 1.4 | 0.6 | 16113066 | 17391658 |
| middle | r43 | ET1 => CIImRNA | 1 | 1.4 | 0.6 | 16113066 | |
| middle | r44 | ERK1_2 => p38 | 1 | 1.4 | 0.6 | 28910144 | 16298339 |
| middle | r45 | p38 => NFKB | 1 | 1.4 | 0.6 | 19959167 | |
| middle | r46 | NFKB => IL6 | 1 | 1.4 | 0.6 | 19959167 | 20202975 |
| middle | r47 | IL6 => HIF1a | 1 | 1.4 | 0.6 | 24928992 | |
| middle | r48 | !NFKB => TIMP1 | 1 | 1.4 | 0.6 | 15710627 | |
| middle | r49 | NFKB => proMMP2 | 1 | 1.4 | 0.6 | 17692316 | |
| middle | r50 | NFKB => proMMP9 | 1 | 1.4 | 0.6 | 17692316 | |
| middle | r51 | Notch1_3 & HIF1a => NICD | 1 | 1.4 | 0.6 | 23251561 | |
| middle | r52 | NICD => HERP1_2 | 1 | 1.4 | 0.6 | 23251561 | |
| middle | r53 | HERP1_2 => aSMAmRNA | 1 | 1.4 | 0.6 | 23251561 | |
| middle | r54 | TNFaR => Nox4 | 1 | 1.4 | 0.6 | 19628034 | |
| middle | r55 | MMP9 => migration | 1 | 1.4 | 0.6 | 11739275 | 10323763 |
| middle | r56 | MMP2 => migration | 1 | 1.4 | 0.6 | 11739275 | 10323763 |
| middle | r57 | TNFa => TNFaR | 1 | 1.4 | 0.6 | 20098355 | |
| middle | r58 | PI3K => Akt | 1 | 1.4 | 0.6 | 15501927 | 29436587 |
| middle | r59 | Akt => NFKB | 1 | 1.4 | 0.6 | 17692316 | |
| middle | r60 | TGFB => PDE1A | 1 | 1.4 | 0.6 | 19672103 | |
| middle | r61 | PDE1A => PKCa | 1 | 1.4 | 0.6 | 19672103 | |

**Figure 2.2: Reaction List with References.** Reactions are listed as input or middle, where *!* indicates inhibition and default parameters of input weight = 0.25, middle weight = 1**,** Hill coefficient = 1.4, $EC_{50}$ = 0.6

| | | | | | | | |
|---|---|---|---|---|---|---|---|
| middle | r62 | PKCa => aSMAmRNA | 1 | 1.4 | 0.6 | 19672103 | |
| middle | r63 | !cGMP => aSMAmRNA | 1 | 1.4 | 0.6 | 19672103 | |
| middle | r64 | TGFB => TGFBR | 1 | 1.4 | 0.6 | 24966928 | 31219429 |
| middle | r65 | TGFBR => smad2_3 | 1 | 1.4 | 0.6 | 18187669 | |
| middle | r66 | smad2_3 => ERK1_2 | 1 | 1.4 | 0.6 | 18187669 | 16246848 |
| middle | r67 | smad2_3 => proliferation | 1 | 1.4 | 0.6 | 18187669 | |
| middle | r68 | PDGF => PDGFR | 1 | 1.4 | 0.6 | 22735370 | |
| middle | r69 | PDGFR => PI3K | 1 | 1.4 | 0.6 | 25628782 | 17290308 |
| middle | r70 | NFKB => fibmRNA | 1 | 1.4 | 0.6 | 18064631 | 7640666 |
| middle | r71 | !MMP2 & CImRNA => CI | 1 | 1.4 | 0.6 | 11739275 | 10323763 |
| middle | r72 | !MMP2 & CIIImRNA => CIII | 1 | 1.4 | 0.6 | 11739275 | 10323763 |
| middle | r73 | !MMP9 & CImRNA => CI | 1 | 1.4 | 0.6 | 11739275 | 10323763 |
| middle | r74 | !MMP9 & CIIImRNA => CIII | 1 | 1.4 | 0.6 | 11739275 | 10323763 |
| middle | r75 | mechanical => AngII | 1 | 1.4 | 0.6 | 21099231 | 21949113 |
| middle | r76 | mechanical => TGFB | 1 | 1.4 | 0.6 | 19672103 | 24966928 |
| middle | r77 | FGF => clOPN | 1 | 1.4 | 0.6 | 12176960 | |
| middle | r78 | smad2_3 => CImRNA | 1 | 1.4 | 0.6 | 21468608 | 17513491 |
| middle | r79 | smad2_3 => CIIImRNA | 1 | 1.4 | 0.6 | 21468608 | 17513491 |
| middle | r80 | LOXmRNA => LOX | 1 | 1.4 | 0.6 | 26565914 | |
| middle | r81 | LOX & elastinmRNA => elastin | 1 | 1.4 | 0.6 | 20807791 | 21615773 |
| middle | r82 | !MMP2 & elastinmRNA => elastin | 1 | 1.4 | 0.6 | 20807791 | 24347665 |
| middle | r83 | !JNK1_2 => elastinmRNA | 1 | 1.4 | 0.6 | 24347665 | |
| middle | r84 | PKCa => elastinmRNA | 1 | 1.4 | 0.6 | 11804868 | |
| middle | r85 | ROS => HIF1a | 1 | 1.4 | 0.6 | 10833514 | |
| middle | r86 | hypoxia => Notch1_3 | 1 | 1.4 | 0.6 | 23251561 | |
| middle | r87 | AP1 => proMMP2 | 1 | 1.4 | 0.6 | 17921324 | 12371906 |
| middle | r88 | AP1 => proMMP9 | 1 | 1.4 | 0.6 | 17560598 | 9755853 |
| middle | r89 | AP1 => latentTGFB | 1 | 1.4 | 0.6 | 20141610 | 21367774 |
| middle | r90 | aSMAmRNA => aSMA | 1 | 1.4 | 0.6 | 19672103 | |
| middle | r91 | fibmRNA => fibronectin | 1 | 1.4 | 0.6 | 18064631 | 7640666 |
| middle | r92 | p38 => aSMAmRNA | 1 | 1.4 | 0.6 | 21630215 | |

**Figure 2.2: Reaction List with References.** Reactions are listed as input or middle, where *!* indicates inhibition and default parameters of input weight = 0.25, middle weight = 1**,** Hill coefficient = 1.4, $EC_{50}$ = 0.6

Using previously described methods [69, 118], the PAAF signaling network model was implemented as a system of logic-based ordinary differential equations that were integrated numerically using the explicit fourth Runge–Kutta method. Each state variable is normalized to a value between 0 and 1 and follows a Hill-type activation function [59]. This approach allows a Boolean system to be translated into a continuous time system with parameters that are representative of biochemical reactions [59]. Logical operators are used to represent signaling interactions with 'NOT' representing inhibition, 'OR' a reaction in which the node can be activated by multiple inputs, and 'AND' representing where the activation requires the activity of more than one upstream node.

The system of differential equations is formulated for each node $y_i$ in the network, i = 1…64 as in Equation 2.1.

$$\frac{d_{y_i}}{dt} = \frac{1}{\tau_{y_i}}\left[\omega_{y_i} f_j y_i^{max} - y_i\right] \quad (2.1)$$

with a general reaction weight ω and Hill function $f_j$, where *j* can be an activation (*act*) as in Equation 2.2 or inhibition (*inhib*) reaction as in Equation 2.3.

$$f_{act}(y_i) = \frac{By_i^n}{K^n + y_i^n} \quad (2.2) \quad \text{and} \quad f_{inhib}(y_i) = 1 - \frac{By_i^n}{K^n + y_i^n} \quad (2.3)$$

where *B* is a function of the half-maximal activation $EC_{50}$ and the Hill coefficient *n* (Equation 2.4), which is a measure of nonlinear cooperative activation and *K* is a function of *B* and Hill coefficient *n* (Equation 2.5) [59].

$$B = \frac{EC_{50}^n - 1}{2EC_{50}^n - 1} \quad (2.4) \qquad \text{and} \quad K = (B-1)^{1/n} \quad (2.5)$$

In the case where $y_j$ is an input, $f_j = 1$ and the input reaction weight is denoted $\omega$.

To represent 'OR' logic interactions, Equation 2.1 is modified to represent the sum of the reactions with respective weights for each node and subtracting the intersection of $f_j(y_k)$ and $f_j(y_l)$ as shown in Equation 2.6.

$$\frac{d_{y_i}}{dt} = \frac{1}{\tau_{y_i}}\left[\left(\omega_{y_k} f_j(y_k) + \omega_{y_l} f_j(y_l) + \omega_{y_k} f_j(y_k)\omega_{y_l} f_j(y_l)\right) y_i^{max} - y_i\right] \quad (2.6)$$

where $y_k$ and $y_l$ are upstream nodes that activate or inhibit $y_i$.

For 'AND' logic interactions, equation (2.1) is modified to be the product of the general reaction weight ω, $f_j(y_k)$ and $f_j(y_l)$ as shown in Equation 2.7.

$$\frac{d_{y_i}}{dt} = \frac{1}{\tau_{y_i}}\left[\omega_{y_k} f_j(y_k) f_j(y_l) y_i^{max} - y_i\right] \quad (2.7)$$

The baseline model solution was obtained using a default Hill coefficient of $n = 1.4$ and $EC_{50}$ of 0.6 for every node. The time constants τ for each different reaction type in the network followed those used previously [69]: 0.1 h for signaling reactions; 1 h for transcription; and 10 h for translation. Timepoints chosen were run at steady state. Input weights ($\omega$) were initialized to 0.25 to represent baseline activity. Reaction weights for the rest of the system ($\omega$) were set to a default value of 1. The system of ODEs was generated from a tabular representation of the network using custom software available on Github at https://github.com/saucermanlab/Netflux.

#### 2.1.2.2 Model Validation

To validate the model predictions, 39 input-output experiments in rat or human PAAF cells (reported in 20 papers [11, 22, 47, 119-135]) were classified as observing a significant increase or decrease, or no significant change in activity of an output quantity that is a node in the model in response to a stimulus, that was also an input to the model. The threshold for considering a response in the model to represent a significant change in output activity was chosen to be 0.05. *In-vivo* data were used when there were no *in-vitro* data reported in the literature on PAAFs. The time-course of the model for each comparison was matched to that of the corresponding experimental measurement. Citations to the publications used for each model comparison experiment are given in **Fig. 2.3** below.

| ID | Input | Input Code | Output | 'prediction' | Measurement | in-out | 'match' | Reference |
|---|---|---|---|---|---|---|---|---|
| v1 | TGFB | w(2) = 1; | aSMA | Increase | Increase | in-out | 1 | 22166643 |
| v2 | TGFB | w(2) = 1; | proliferation | Increase | Increase | in-out | 1 | 24966928 |
| v3 | TGFB | w(2) = 1; | migration | Increase | Increase | in-out | 1 | 24966928 |
| v4 | TGFB | w(2) = 1; | CI | Increase | Increase | in-out | 1 | 23982954 |
| v5 | TGFB | w(2) = 1; | CIII | Increase | Increase | in-out | 1 | 10347096 |
| v6 | TGFB | w(2) = 1; | clOPN | No change | No change | in-out | 1 | 10347096 |
| v7 | TGFB | w(2) = 1; | fibronectin | Increase | No change | in-out | 0 | 23982954 |
| v8 | TGFB | w(2) = 1; | p38 | Increase | Increase | in-out | 1 | 23982954 |
| v9 | TGFB | w(2) = 1; | ERK1_2 | Increase | Increase | in-out | 1 | 23982954 |
| v10 | TGFB | w(2) = 1; | elastin | Decrease | Increase | In-out | 0 | 9426317 |
| v11 | AngII | w(1) = 1; | migration | Increase | Increase | in-out | 1 | 25766526 |
| v12 | AngII | w(1) = 1; | proliferation | Increase | Increase | in-out | 1 | 25766526 |
| v13 | AngII | w(1) = 1; | ET1 | Increase | Increase | in-out | 1 | 25766526 |
| v14 | AngII | w(1) = 1; | CI | Increase | Increase | in-out | 1 | 25766526 |
| v15 | AngII | w(1) = 1; | Nox4 | No change | Decrease | in-out | 0 | 18474828 |
| v16 | mechanical | w(3) = 1; | proliferation | Increase | Increase | in-out | 1 | 22374788 |
| v17 | mechanical | w(3) = 1; | aSMA | Increase | Decrease | in-out | 0 | 28527302 |
| v18 | mechanical | w(3) = 1; | MMP2 | Increase | Increase | In-out | 1 | 28527302 |
| v19 | mechanical | w(3) = 1; | MMP9 | Increase | No change | In-out | 0 | 28527302 |
| v20 | mechanical | w(3) = 1; | miR130_301 | Increase | Increase | in-out | 1 | 30081553 |
| v21 | TNFa | w(4) = 1; | IL6 | Increase | Increase | in-out | 1 | 28477980 |
| v22 | TNFa | w(4) = 1; | ROS | Increase | Increase | in-out | 1 | 28477980 |
| v23 | TNFa | w(4) = 1; | Akt | No change | No change | in-out | 1 | 28477980 |
| v24 | hypoxia | w(7) = 1; | Nox4 | Increase | Increase | in-out | 1 | 18593227 |
| v25 | hypoxia | w(7) = 1; | proliferation | Increase | Increase | in-out | 1 | 18593227 |
| v26 | hypoxia | w(7) = 1; | ROS | Increase | Increase | in-out | 1 | 18593227 |
| v27 | hypoxia | w(7) = 1; | CI | Increase | Increase | in-out | 1 | 23982954 |
| v28 | hypoxia | w(7) = 1; | fibronectin | Increase | Increase | in-out | 1 | 23982954 |
| v29 | hypoxia | w(7) = 1; | LOX | Decrease | Increase | in-out | 0 | 24833797 |
| v30 | hypoxia | w(7) = 1; | MMP2 | Increase | Increase | in-out | 1 | 25623089 |
| v31 | hypoxia | w(7) = 1; | aSMA | Increase | No change | in-out | 0 | 16263938 |
| v32 | hypoxia | w(7) = 1; | HIF1a | Increase | Increase | in-out | 1 | 15970449 |
| v33 | FGF | w(6) = 1; | aSMA | Increase | Increase | in-out | 1 | 26729053 |
| v34 | FGF | w(6) = 1; | TGFb | Increase | Increase | in-out | 1 | 26729053 |
| v35 | FGF | w(6) = 1; | proliferation | Increase | Increase | in-out | 1 | 26729053 |
| v36 | PDGF | w(5) = 1; | migration | Increase | Increase | in-out | 1 | 16790526 |
| v37 | PDGF | w(5) = 1; | MMP2 | Increase | Increase | in-out | 1 | 16790526 |
| v38 | PDGF | w(5) = 1; | TIMP1 | Decrease | Decrease | in-out | 1 | 16790526 |
| v39 | PDGF | w(5) = 1; | CI | Decrease | Increase | in-out | 0 | 16790526 |
| | | | | | | | 31 | |
| | | | | | | | 0.79487 | |

**Figure 2.3: Validation Data with References.** The input is listed, and then the weight (w) of the input is set to 1, and the change in the output is determined by a threshold value of 0.1. The 1 indicates there is a match with the model prediction and the experimental measurement.

### 2.1.2.3 Sensitivity Analysis

A model baseline was calculated by setting all input weights to 0.25 and the initial values of all state variables to 0. They were then integrated until a steady state was achieved for all nodes at 200 minutes. 100% knockdown of each node was simulated by reducing $y_{max}$ from 1 to 0, and the subsequent effect at every node was calculated as knockdown activity minus baseline activity. Sensitivity analysis was performed under baseline conditions and under conditions of high

mechanical stretch (mechanical input weight set to 0.9) to represent the effects of mechanical overload and matrix stiffening associated with PAH.

#### 2.1.2.4 Uncertainty Quantification

The model system of ordinary differential equations (Equation 2.1) can be represented as $\dot{\mathbf{y}} = f(\mathbf{y},\boldsymbol{\theta})$, $\mathbf{y} \in \mathbb{R}^i$, where $\dot{\mathbf{y}}$ is a vector representing the time rate of the change of the nodal network states $y$. The index $i$ represents the problem dimension, which in this case is equal to the number of nodes in the network (**Fig. 2.1**). The vector $\boldsymbol{\theta}$ contains the parameters that can be represented as $\boldsymbol{\theta} \in \mathbb{R}^k$, where $k$ is the number of uncertain model parameters that we intend to investigate.

To propagate parameter uncertainties in the network, we followed the approach described by Marino *et al.* [136], in which each parameter in $\theta$ is assumed to be a uniform random variable from the uniform distribution ~$U$(min, max). Herein, we propagate three uncertain independent parameters: $n$, $EC_{50}$, and $\omega$ ($\boldsymbol{\theta} = \{n, \mathrm{EC}_{50}, \omega\}$). These parameters were sampled randomly from uniform distributions. The ranges chosen for the model parameters vary roughly 30% around their mean when carrying out UQ analysis. For example, $n$ was chosen to be a uniform random variable such that $n \sim U(1.36, 2.36)$. It should be noted that the range of $n$ was set from 1.36 to 2.36 as guided by the equation in Section 2.2.3.1, since a default value of $EC_{50} = 0.6$ gives a minimum of $n$ to be 1.36 or else $B$ would be negative and thus $K$ would not produce a viable value. When $n$ is set to 1.4, the $EC_{50}$ can only vary slightly around the default value of 0.6, so the UQ analysis was run with $n$ set to 2, in order to perturb a wider range of $EC_{50}$ from 0.4 to 0.7, $EC_{50} \sim U(0.4,0.7)$. Similarly, the input weight $\omega$ was also run with $n$ set to 2 to keep the results consistent, and was set to vary from 0.1 to 0.4, around the default value (0.25), $\omega \sim U(0.1,0.4)$.

The uncertainty quantification simulations were performed using the package Uncertainty 1.2.1 in Python [137]. The package was run to quantify the change in model accuracy when varying the three model parameters: $n$, $EC_{50}$, and $\omega$. Since there are only 7 locations in the network that depend on the input weight $\omega$, we used the polynomial chaos expansion approach with order-4 approximation to non-intrusively propagate uncertainty. This is generally less computationally expensive than Monte Carlo simulations, however for systems with over 20 uncertain parameters, the required number of model evaluations scales worse than the Monte Carlo method [137]. Because of this, the (quasi-) MC method was used with 5,000 model evaluations for UQ analysis of $n$ and $EC_{50}$ due to there being 99 reactions each with individual $n$ and $EC_{50}$ values being perturbed in the network. The ranges of parameter values that are noted in the UQ results are identified by examining the output file and sorting by accuracy, then analyzing the combinations of parameters that led to notable changes in accuracy. The code used for uncertainty analysis is available on Github at https://uncertainty-toolbox.github.io/

Moreover, to compare the baseline model results with a model derived only from experiments in PAAFs or cardiac fibroblasts, we ran UQ analysis using the (quasi-)Monte Carlo approach varying all 3 parameters where $n \sim U(2, 2.4)$, $EC_{50} \sim U(0.4, 0.6)$, and $\omega \sim U(0.1, 0.4)$, and with 10,000 model evaluations. The effects on model accuracy of changing parameters and the network structure were evaluated by classifying input-output model results as increased, decreased, or unchanged using a threshold change of 0.05 and determining the percentage of model results in agreement with the published experimental findings.

### 2.1.3 Results

#### 2.1.3.1 Model Validation

The model accurately predicted 31 out of 39 (80%) of the qualitative experimental results, including 4 out of 5 of the *in-vivo* (bolded) and 27/34 of the *in-vitro* experimental findings (**Fig. 2.4A**). Model accuracy went down to 35% when not using PAAF-specific pathways and using only reactions from the cardiac fibroblast model by Zeigler *et al.* (**Fig. 2.8B**) [69]. The model was also able to predict results from *in-vitro* experiments in rat PAAFs in which TGF$\beta$, TNF$\alpha$ or ROS were inhibited pharmacologically [131, 132]. Each node in the model was first initialized with a default baseline value of 0.25, and the control activity of collagen I, $\alpha$-SMA, fibronectin, and IL6 were computed. Next, stimulation with TGF$\beta$ and TNF$\alpha$ was simulated by increasing the input weights corresponding to those nodes to 0.475 and 0.375, respectively. These two values were chosen to best match the increase in relative level of $\alpha$-SMA as reported by Zhang *et al.* and IL6 as reported by He *et al.* [131, 132] experiment. Experiments using 10 $\mu$M of the ERK inhibitor U0126 (T+U) reduced its activity to 30% [138]. Similarly, 10 $\mu$M of the p38 inhibitor SB203580 (T+SB) reduced p38 activity to 5% [139], the ROS scavenger N-acetyl-L-cysteine (NAC) completely blocked ROS activity [132]. Hence, after stimulation of the baseline model with TGF$\beta$, the effects inhibiting the ERK1/2 and p38 nodes were simulated in the model by reducing $y_{max}$ from 1.0 to 0.3 and 0.05, respectively (**Fig. 2.4B-D**). Similarly, the effects of NAC on TNF $\alpha$ were simulated by reducing the ROS node from 1.0 to 0.0 (**Fig. 2.4E**). Simulations ran for 24 hours [131] and 8 hours [132] to match the time-course of the corresponding experimental measurements, as depicted in **Fig. 2.4 B-E**.

Percent errors between model-predicted and experimental results for collagen I expression stimulated by TGF$\beta$ and with TGF$\beta$ in the presence of the ERK1/2 and p38 inhibitors were 109%,

218%, and 283%, respectively [131]. Although these errors were high, the model did qualitatively predict the observed increase in collagen I stimulated by TGF$\beta$ but not the observed inhibitory effects of either inhibitor. This may be because of incomplete or inaccurate interaction logic in the module of the network regulating collagen I expression. On the other hand, the model did correctly predict observed trends for fibronectin with % errors of 66%, -95%, and -99%, though predicted inhibition was greater than observed, perhaps because only MAPK signaling regulates fibronectin in the model. Because the model simulation was matched to the $\alpha$-SMA experimental results, the error for TGF$\beta$ stimulation was only -0.4%, and there was a good match with the inhibition results with % errors of 16.7% for T+U (ERK1/2 $y_{max}$ to 0.3) and 8.4% T+SB (p38 $y_{max}$ to 0.05) [131]. This shows that the model was able to closely predict the trends in $\alpha$-SMA and fibronectin activity. Changes in the model structure may be required before collagen I expression can be predicted.

We compared the model to experiments in which TNF$\alpha$ was added to rat PAAFs [132] by increasing the TNF$\alpha$ node from 0.25 to 0.375. The error in the predicted increase in IL6 expression was only -1.1%, and the predicted effect of adding the ROS scavenger was qualitatively as measured, with an error of 128% (**Fig 2.4E**).

All model results were significantly different ($p < 0.05$) than experimental means except those for $\alpha$-SMA (**Fig. 2.4D)**. A Student's heteroscedastic t-Test produced p-values of 0.06 for $\alpha$-SMA stimulation and ERK inhibitor (T+U) and 0.16 for $\alpha$-SMA stimulation and p38 inhibitor (T+SB) given the sample size (n=3) and standard deviation reported in the original experimental paper [131].

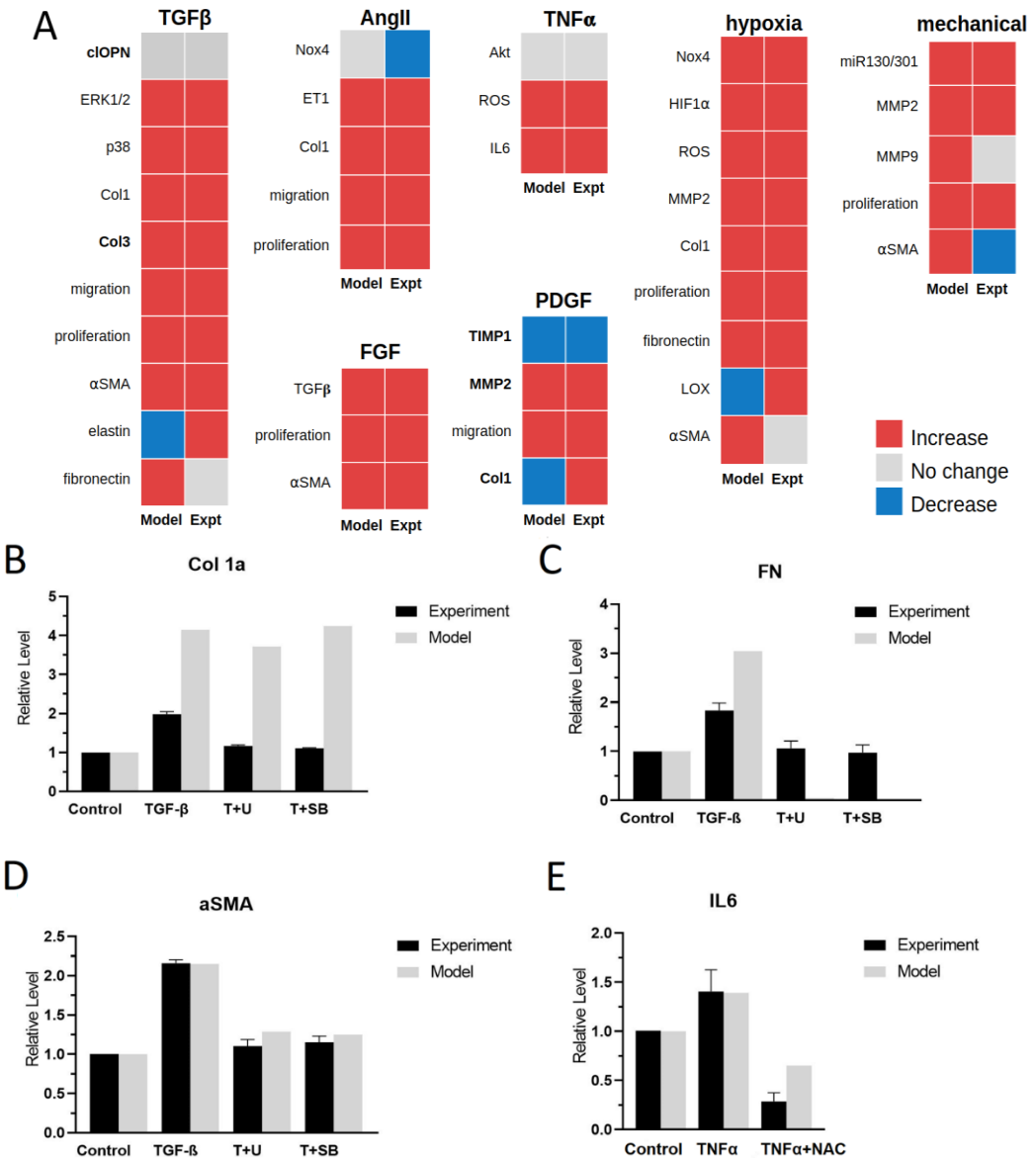


**Figure 2.4: Model prediction of qualitative input-output experiments and inhibition results signaling.** (**A**) Input–output validation: model predictions agreed with published experimental observations for 31 out of 39 (80%) of the input–output responses measured in rat or human PAAFs. Intermediate and phenotypic output results are organized by input stimulus, where the bolded node names indicate experimental results that were measured *in-vivo*. (**B–E**) Inhibition validation: results of the PAAF model are compared with the results of inhibition experiments in cultured rat PAAFs reported by Zhang *et al*. (**B–D**) [131] and He *et al*. (**E**) [132]. Each model prediction was normalized to the baseline condition obtained when all inputs were 0.25. Stimulation with TGFβ and TNFα were simulated by increasing these inputs to 0.475 and 0.375, respectively, to be consistent with the experimental protocol. The effects of the ERK inhibitor (T+U), p38 inhibitor (T+SB) and ROS scavenger (NAC) were simulated by decreasing $y_{max}$ for those nodes from 1.0 to 0.3, 0.05 and 0, respectively, consistent with the published reports [131].

#### 2.1.3.2 Sensitivity Analysis

A sensitivity analysis was used to identify the nodes that are the most influential determinants of network state under baseline conditions and conditions of high-mechanical stimulation as occurs in PAH. The change in the steady-state (200 min) response of each node in the network (columns) to 100% knockout of each node individually (rows) is displayed as a heat map in **Fig 2.5.** The analysis shows that mechanical stimulation, hypoxia, AngII, and TGF$\beta$ are the most important inputs. Important intermediate regulators include the mitogen-activated protein kinases (ERK1/2, JNK1/2 and p38), calcineurin, the Smads 2 and 3, cleaved osteopontin (clOPN), reactive oxygen species (ROS), notch intracellular domain (NICD), nitric oxide (NO), and NADPH oxidase 4 (Nox4). This sensitivity analysis has thus revealed the larger influence of hypoxia and FGF in the PAAF model than in the model of cardiac fibroblasts [69].

Given the importance of mechanical loading and vessel stiffening in the pathogenesis of pulmonary arterial fibrosis, we repeated the sensitivity analysis in the context of high-mechanical load by increasing the input weight of the mechanical stimulation input node from the baseline value of 0.25 to 0.9 (**Fig. 2.6)**. Under these conditions, the most influential unique nodes were found to be $\alpha$-SMA, cGMP, ET1, proteins in the Hippo pathway, and syndecan-4. These nodes are highly active in mechanotransduction, proliferation, vasoconstriction, and activation of fibroblasts into the myofibroblast phenotype [63]. Knocking out these nodes generally resulted in a decrease in matrix proteins including collagen III and fibronectin. This global sensitivity analysis is also a way to elucidate the likely determinants of greatest structural and parameter uncertainty in the model. In the following sections we investigated the effects of parameter and network uncertainty in the model.

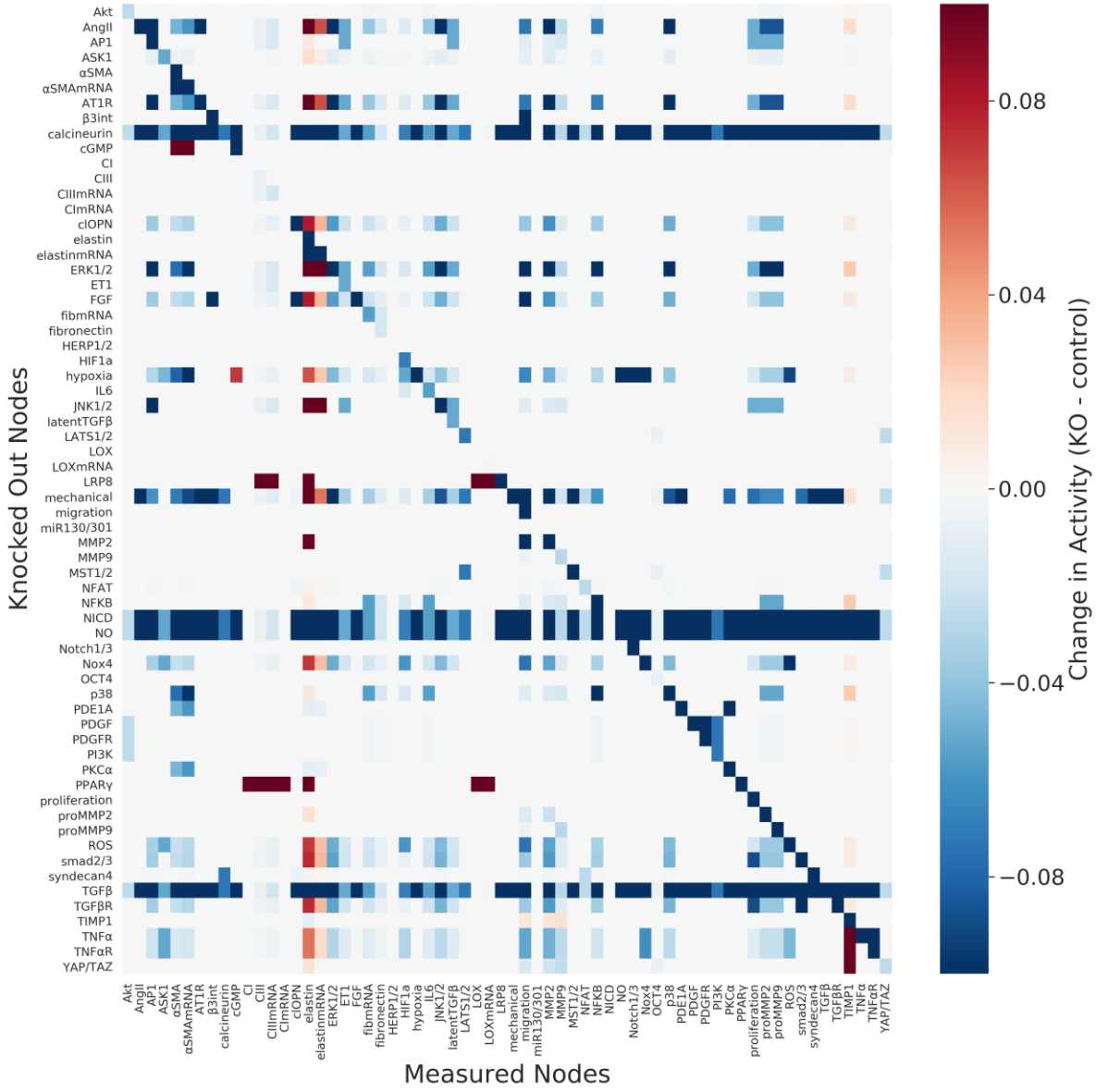


**Figure 2.5: Heatmap of the baseline sensitivity analysis for pulmonary arterial adventitial fibroblasts.** Heatmap of the baseline sensitivity analysis showing changes in activity of all the nodes in the model (columns) in response to knocking out each node (rows), where red indicates an increase in activity over baseline and blue shades indicate a decrease in activity in response to the knockout. This indicates the most important nodes are mechanical stimulation, TGFβ, AngII, and hypoxia.

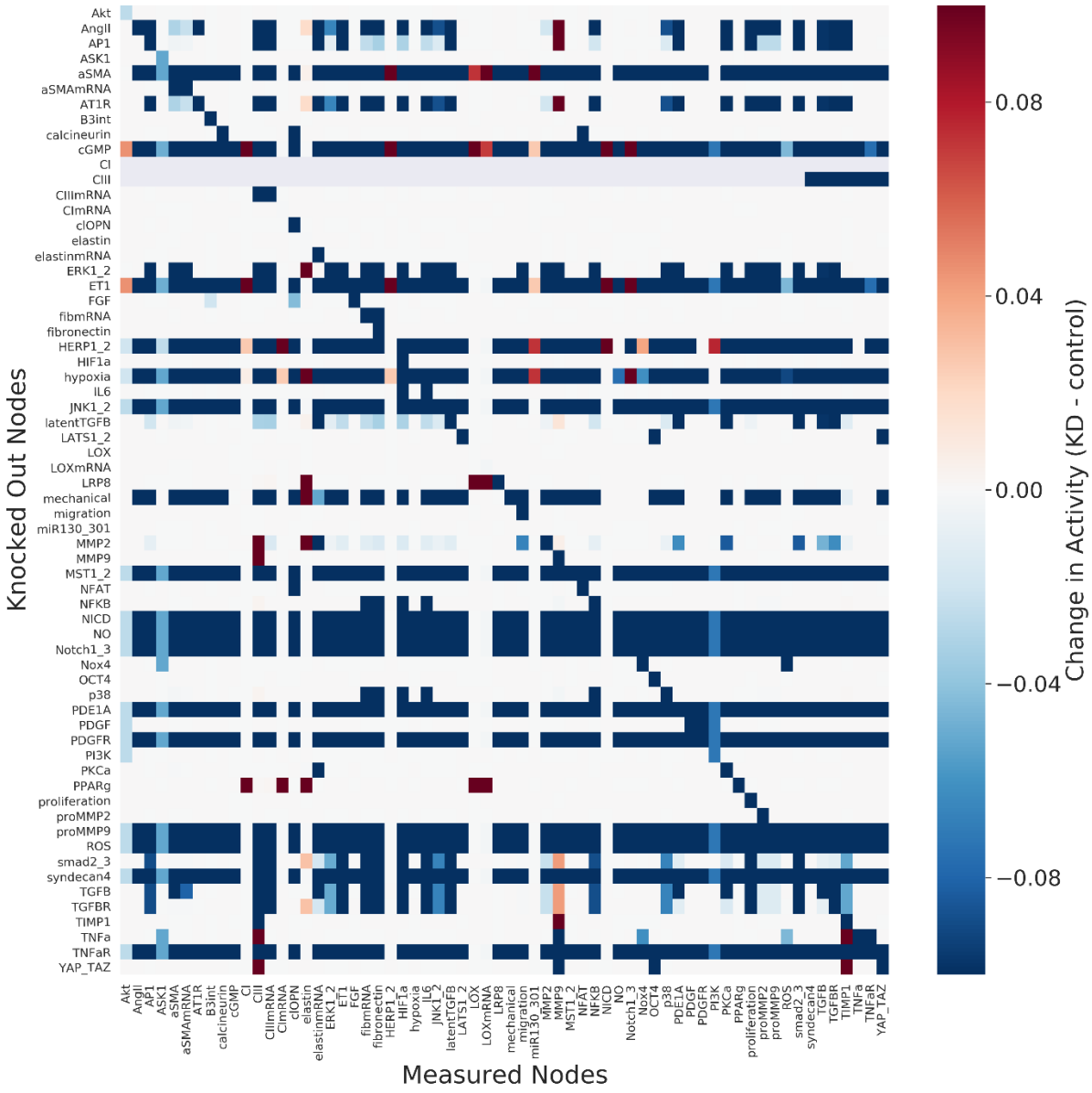


**Figure 2.6: Sensitivity Analysis Under High Mechanical Stimulation.** Heatmap of sensitivity analysis with the weight of the mechanical input increased from a default of 0.25 to 0.9, showing changes in activity of all the nodes in the model (columns) in response to knocking out each node (rows), where red indicates an increase in activity over baseline and blue shades indicate a decrease in activity in response to the knockout. This indicates the most important input nodes are mechanical stimulation, Notch1/3, TGFβ, AngII, and hypoxia.

#### 2.1.3.3 Quantification of Parameter Uncertainty

To examine the effect of propagated uncertainty of model parameters on the accuracy of the model, a table of the 39 experimental results was coded to compare results against. The accuracy was compared with the baseline 80% accuracy achieved with default model parameters.

Each parameter was varied independently using a uniform distribution $n$ ~ (1.36-2.36), $EC_{50}$ ~ (0.4-0.7), $\omega$ ~ (0.1-0.4). A (quasi-)Monte Carlo method with 5,000 model evaluations was used for UQ analysis of $n$ and $EC_{50}$ to cover the 99 uncertain reactions, and an order-4 polynomial chaos expansion was used for the weight $\omega$ of the 7 model inputs. As seen in Figure 2.4, the distribution of model accuracy for input weight has a mean of 70.4%, standard deviation of 5.3%, a minimum accuracy of 66.67%, and a maximum accuracy of 79.5%. For $EC_{50}$, the mean of the distribution is 65.4% with a standard deviation of 19.2% and a minimum accuracy of 20.5% and maximum accuracy of 82%. For the Hill coefficient, the mean accuracy of the distribution was 63.9% with a standard deviation of 13.3%, a minimum accuracy of 20.5%, and a maximum accuracy of 79.5%. This indicates that network model accuracy was most vulnerable to uncertainty in n, somewhat vulnerable to uncertainty in $EC_{50}$ and relatively robust to input weight uncertainty.

A subset of specific combinations of input weights over the range of 0.1-0.4 did result in a decrease in accuracy including a combination of low mechanical and low hypoxia or a combination of low AngII, TGF$\beta$ and FGF, but these did not decrease the model accuracy more than 13% (**Fig 2.7A**).

There was a wide range of changes in model accuracy as shown in **Fig 2.7B**, over the relatively large range of $n$ of 1.36-2.36, showing increased uncertainty propagation. Lower model accuracy (<40%) was observed when more than 30% of the 99 reactions had Hill coefficients $n$

exceeding 2.2. To allow $EC_{50}$ to vary, $n$ was set to 2 as stated in the Methods to avoid numerical errors [59].

Model accuracy was generally high and robust to varying $EC_{50}$ from 0.4-0.7, but there was a secondary peak at 20% as seen in **Fig 2.7C**. The low peak occurred when the reactions of MST1/2 activating LATS1/2 and miR130/301 inhibiting LRP8 both had $EC_{50}$ values greater than 0.68. Both reactions are involved in the Hippo pathway, which is activated by mechanical stimulus.

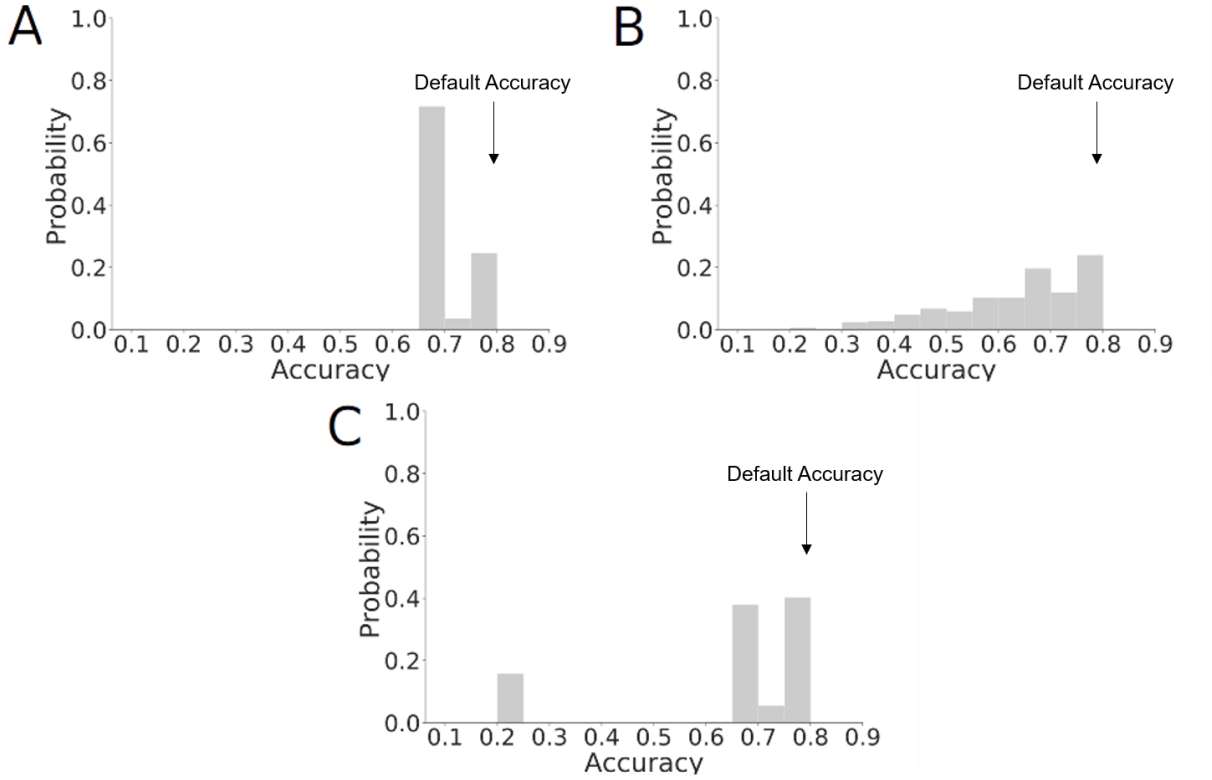


**Figure 2.7: Uncertainty quantification of parameters in Pulmonary Arterial Adventitial Fibroblasts.** Quantification of the effects of model parameter uncertainty on the probability of qualitative model prediction accuracy assuming uniform random distributions of input weights $\omega$ (**A**), Hill coefficients $n$ (**B**), and half-maximal activations $EC_{50}$ (**C**). Accuracy with using default parameters is annotated. Varying input weight $\omega$ randomly between 0.1 and 0.4 for seven inputs using polynomial chaos expansion with a fourth order produced accuracies between 70% and 80%, whereas varying the Hill coefficient $n$ from 1.36 to 2.36 for all 99 reactions using the (quasi-)Monte Carlo method resulted in a much wider distribution of model accuracies ranging from 20% to 80%. Varying $EC_{50}$ randomly between 0.4 and 0.7 for all 99 reactions using the (quasi-)Monte Carlo method resulted in peaks in accuracy at around 20% and at 70–80%.

Finally, there was a set of $EC_{50}$ values that led to an increased model accuracy of 82%. When compared with thousands of combinations that produced an 80% accuracy. This result is unique in that all of the inputs and hypoxia -> Nox4 were not extreme values ($0.42 < EC_{50} < 0.68$) combined with a high $EC_{50}$ (>0.68) for the reaction: MMP9 and latent TGF$\beta$ activating TGF$\beta$ and a low $EC_{50}$ (<0.42) for the reaction: proMMP9 activating MMP9 and TIMP1 inhibiting MMP9. This finding demonstrates how further tuning can be done by optimizing model parameters.

The 11 inhibition results seen in **Fig 2.4B-E** (activation by TGF$\beta$ and TNF$\alpha$ then inhibition of p38, ERK1/2 or ROS) were coded with a threshold of 0.05, and UQ was repeated using polynomial chaos expansion with an order-4 varying the 7 input weights from 0.1-0.4. **Fig. 2.9** shows that the predicted results of inhibition experiments were relatively robust to this change, accurately predicting 9/11 (82%) or 8/11 (73%) of the activation by TGF$\beta$ and TNF$\alpha$ and inhibition of p38, ERK1/2, and ROS. However, the model was not able to capture the inhibition of collagen I by p38 or ERK1/2.

#### 2.1.3.4 Quantification of Epistemic Uncertainty

To use UQ to evaluate the level of uncertainty associated with the cell type used in the model construction, a reduced version of the model was created with only experimental data reported for fibroblast cells from the cardiovascular system, specifically PAAFs and cardiac fibroblasts (CFBs). This new criterion led to a reduced model with 82 reactions and 62 nodes, due to the removal of ET1 and latent TGF$\beta$, versus the 92 reactions and 64 nodes in the original model. The reduced model was qualitatively compared against the same independent set of data as the full model. Here the accuracy went down to 24/38 (63%) from the accuracy of 31/39 (80%) for the

original model. The number of experiments compared against drops down from 39 to 38 as a result of ET1 being a node in the input-output comparison.

We ran a (quasi-)Monte Carlo simulation with 10,000 model evaluations where $n$ was given a uniform distribution from 2 to 2.4, $EC_{50}$ was given a uniform distribution of 0.4 to 0.7 (default value of 0.6), and the input weight $\omega$ was given a uniform distribution of 0.1 to 0.4 (default value of 0.25) as depicted in **Fig. 2.8A.**

We further compared the two models by varying all three parameters at once: $n \sim U(2, 2.4)$, $EC_{50} \sim U(0.4, 0.6)$, and $\omega \sim U(0.1, 0.4)$ (**Fig. 2.8**). The mean accuracy of the baseline model (Fig 2.5A) was 35.7% with a standard deviation of 18% and reaches a maximum accuracy of 80%, while the mean accuracy of the reduced model (**Fig 2.8B**) was 38.4% with a standard deviation of 12% and a maximum accuracy of 63%. Overall, this result suggests that while using data from non-cardiovascular cell types is a source of epistemic uncertainty, the additional model components and reactions deduced from these other cell types can improve prediction accuracy without significantly compromising robustness. These results may help to prioritize new *in-vitro*

experiments in PAAFs that are not in the literature but are important to the accuracy of the model.

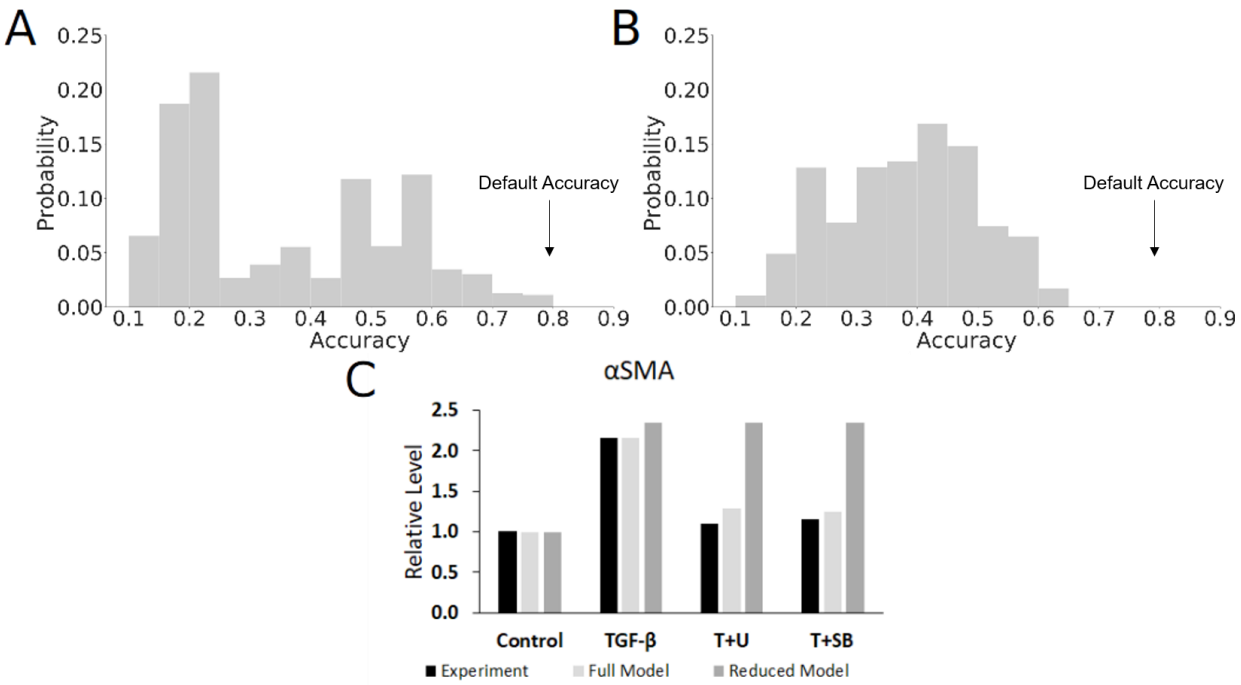


**Figure 2.8: Quantification of epistemic uncertainty in network structure.** Results of a 10000 model evaluation runs using the (quasi-)Monte Carlo simulation where the Hill coefficient *n* was a uniform random variate between 2 and 2.4, $EC_{50}$ was given a uniform distribution of 0.4 to 0.6, and $\omega$ was varied according to a uniform random distribution of 0.1 to 0.4. The two models being compared are the UQ results for the full model (**A**) versus the reduced model (**B**) based only on literature data from cardiovascular cells (PAAFs and CFBs) with accuracy using default parameters annotated. Inhibition results for α-SMA using the reduced model were run under the same conditions used to produce figure 2.4D (**C**). Results remained unchanged for the other outputs (collagen I, fibronectin, IL6).

This includes experiments on the feedback from and activation of latent TGF$\beta$, activation of TIMP1 and ET1 by AP1, activation of *Eln* by PKC$\alpha$, activation of HIF1$\alpha$ by ROS, and activation of $\alpha$-SMA (*Acta2*) by p38.

To examine the effects of only including cardiovascular fibroblast data (PAAFs and CFBs) on the inhibition results, simulations were rerun with the same conditions as in **Fig. 2.4B-E**. Briefly, input TGF$\beta$ = 0.475, and TNF$\alpha$ = 0.375, ERK1/2 $y_{max}$ = 0.3, p38 $y_{max}$ = 0.05, ROS $y_{max}$ = 0, and at 24 hours and 8 hours, respectively. While other trends remained the same, the reduced

model resulted in a qualitative reversal of the accuracy for $\alpha$-SMA predicted by the full PAAF model. As shown in **Fig 2.5C**, there was no longer a decrease in activity in $\alpha$-SMA due to ERK and p38 inhibitors as originally observed. The reduced form of the model only agrees with the increase in $\alpha$-SMA due to TGF$\beta$ stimulation. The results also no longer match the experiment, producing p values that were less than 0.05 with a heteroscedastic Student's t-Test, rejecting the null hypothesis that the model results lie in the same distribution as the experimental ones [131]. Thus, the full model, despite including some information from non-cardiovascular fibroblasts, better captures the complex regulation of $\alpha$-SMA expression.

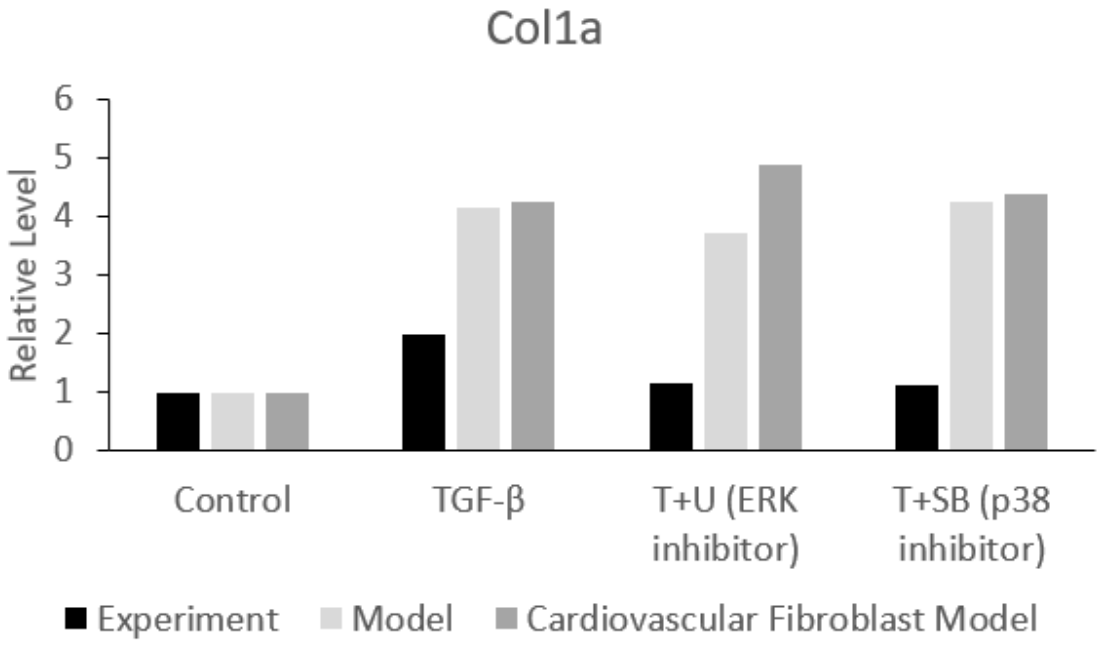


**Figure 2.9: Dynamic Inhibition Results using the Cardiovascular Fibroblast Model for *Col1a1*.** The reduced model with only cardiovascular fibroblast data was not able to predict inhibition of *Col1a1* by ERK or p38 inhibitor. Model prediction results for the other inhibition predictions when using the reduced cardiovascular fibroblast model (fibronectin, alpha smooth muscle actin, and IL6) were unchanged from results shown in **Fig. 2.4 B-E**.

### 2.1.4 Conclusion

We created a novel network model of cell signaling in PAAFs that integrates seven signaling modules known to be involved in pulmonary arterial fibrosis. This model was qualitatively consistent with experimentally measured input–output relationships and was able to match results from inhibition experiments not used to formulate the model originally. To determine the specificity of the model to fibroblasts from the pulmonary arterial adventitia, we ran a simulation using only nodes also included in the CFB model developed by Zeigler *et al*. Here, the CFB model with 40 reactions significantly underpredicted by almost threefold the PAAF input–output experiments. This indicates the important role played by the 52 added reactions in our fibroblast model to describe the signaling pathway representing PAAF properties in PAH. Sensitivity analysis showed that the model predicted PAAF network state was most sensitive to TGFβ, MAPK and hypoxia signaling pathways. The sensitivity analysis for the CFB model showed similar importance of TGFβ pathways and MAPK pathways, but mechanical stimulus had a higher impact. By using UQ, we determined the robustness of the model with respect to input weight and $EC_{50}$, but found that parameter uncertainty propagation was increased significantly with increased $n$.

This work takes similar approaches to those previously undertaken in other logic-based network models including those done by Zeigler *et al*. [69] and Kraeutler *et al*. [59]. The Zeigler model has been shown to be similarly robust to this PAAF model, with an accuracy of 80% and similarly predicts a strong influence of TGFβ [69]. Our model uses the same default parameters and includes analysis of variation in baseline input. This contrasts with the Kraeutler model, where the model is fully parameterized and the authors carried out a sensitivity analysis on the Hill coefficient, $EC_{50}$, and $y_{max}$ [59]. We have further varied the Hill coefficient and $EC_{50}$ using a uniform distribution via UQ.

We also identified the areas of epistemic uncertainty inherent in network construction that will need further confirmation, revision and comparison with future experiments done specifically in PAAFs by running a three parameter UQ analysis on the model with and without the pathways derived from non-cardiovascular fibroblasts. In some cases, information from non-cardiovascular cell types were shown not to highly affect input–output prediction accuracy but did improve the accuracy of predictions on the effects of inhibitors as seen in the predictions of how α-SMA responds to TGFβ when ERK or ROS were inhibited. Thus, the full model, despite including some information from non-cardiovascular fibroblasts, better recapitulated the regulation of α-SMA expression. In this way, UQ was able to capture the levels to which the output of model accuracy could vary given changes in large ranges of parameters and in the absence of pathways elucidated by non-cardiovascular fibroblasts. This analysis was crucial to a system that has so little certainty in model construction and literature data such as in PAAFs. With directions for optimization given by UQ, this model can be improved to help the scientific community understand the complex interplay of pathways in pulmonary arterial remodeling to identify treatments that can better target adventitial fibrosis.

### 2.1.5. Limitations and Future Directions

There is very little literature from which to determine specific model parameters, so we have not attempted to identify individual parameters and instead used constant values for every node and explored parameter uncertainty over a wide range of values. For example, all reactions are at a default weight of 1; however, the literature data could suggest that some reactions are more important than others in determining fibrosis. These findings are consistent with the conclusion that capturing the molecular interactions within the network topology is more important for

reproducing the qualitative features revealed by typical cell biological experiments than the choice of parameters. This property explains why this class of network model is often preferred to more biochemically detailed models with fewer interacting pathways for interpreting the frequently more qualitative conclusions of many cell-biological studies. The analyses suggested that the model is quite robust to parameter uncertainty at least when using qualitative experimental criteria. When varying input weight ($\omega$) the model accuracy ranged from 67% to 80%, when varying half-maximal effective concentration ($EC_{50}$) the accuracy generally ranged from 60% to 80% though the model accuracy was highly affected by changes in the Hill coefficient ($n$). Given that the UQ results depend on the ranges chosen for the model parameters, in this case $n$, $EC_{50}$ and $\omega$, caution should be taken in making too many biological conclusions based on this analysis.

A critical next step identified by UQ is to fill in the areas where there are no *in-vitro* experiments in PAAFs both to refine the model and acquire more validation data so one can be more confident in the results. For example, there are no literature data on how stimulation of PAAFs with TNFα affect phenotypic outputs, only on intermediates in the model. There is some data uncertainty in the literature, as a low sample size and power in typical cell biology experiments means there is less confidence in experimental findings concluding no significant change versus those reporting significant changes.

The model is currently only shown to be qualitatively consistent with input–output experiments and normalized from 0 to 1 as the range is unknown and many reported experimental results are not quantitative. In the future, we can implement mass-action equations with kinetic rates to create a more quantitative and realistic measure of matrix remodeling that we can validate through experimentation. We can also integrate paracrine signaling with other cell types, as PAAFs are known to activate macrophages and smooth muscle cells surrounding them in the pulmonary

arterial wall [3] Another future direction is to reformulate the model by adding exogenous stimulation for ET1 and IL6 and feedback, which could increase model accuracy.

**Acknowledgements**

Chapter 2, in full, is a reprint of the materials as it appears in the following publications: Philosophical Transactions of the Royal Society A 2020. Wang, Ariel; Cao, Shulin; Aboelkassam Yasser; Valdez-Jasso Daniela. The thesis author was the primary investigator and author of this paper.

# CHAPTER 3: SUBSTRATE STIFFNESS AND STRETCH REGULATE PROFIBROTIC MECHANOSIGNALING IN PULMONARY ARTERIAL ADVENTITIAL FIBROBLASTS

## 3.1 Abstract

PAAFs are important regulators of fibrotic vascular remodeling during the progression of PAH, a disease that currently has no effective anti-fibrotic treatments. We conducted *in-vitro* experiments in PAAFs cultured on hydrogels attached to custom-made equibiaxial stretchers at 10% stretch and substrate stiffnesses representing the mechanical conditions of mild and severe stages of PAH. The expression of collagens α(1)I and α(1)III and elastin messenger RNAs (*Col1a1*, *Col3a1*, *Eln*) were upregulated by increased stretch and substrate stiffness, while lysyl oxidase-like 1 and α-smooth muscle actin messenger RNAs (*Loxl1*, *Acta2*) were only significantly upregulated when the cells were grown on matrices with an elevated stiffness representative of mild PAH but not on a stiffness representative of severe PAH.

Fibronectin messenger RNA (*Fn1*) levels were significantly elevated by increased substrate stiffness and transiently upregulated by a 4h stretch, but was not significantly altered by a 24h stretch while *Col3a1*, *Acta2*, *Loxl1*, and *Eln* were significantly altered/up-regulated at both 8h and 24h, where the 8h groups show a higher response level. We modified our published computational network model of the signaling pathways that regulate profibrotic gene expression in PAAFs to allow for differential regulation of mechanically-sensitive nodes by stretch and stiffness. When the model was modified so that stiffness activated integrin $\beta_3$, the Macrophage Stimulating 1 or 2 (MST1\2) kinases, angiotensin II (Ang II), transforming growth factor-β (TGF-β), and syndecan-4, and stretch-regulated integrin $\beta_3$, MST1\2, Ang II, and the transient receptor potential (TRP) channel, the model correctly predicted the upregulation of all six genes by

increased stiffness and the observed responses to stretch in five out of six genes, although it could not replicate the non-monotonic effects of stiffness on *Loxl1* and *Acta2* expression.

Blocking Transforming Growth Factor β (TGFβ) and Ang II Receptor Type 1 ($AT_1R$) *in-vitro* uncovered previously unknown pathway interactions in regulation of *Col1a1, Col3a1,* and *Acta2,* as well as novel pathways that could be in PAAFs that regulate *Fn1*. This novel combination of *in-vitro* and *in-silico* models of PAAF profibrotic cell signaling in response to altered mechanical and biochemical conditions may help identify regulators of vascular adventitial remodeling due to changes in stretch and matrix stiffness that occur during the progression of PAH *in-vivo*.

### 3.1.1 Importance of PAAFs in PAH

PAH is a vasculopathy manifested by sustained elevation of pulmonary arterial pressures, vascular constriction, and irreversible vascular remodeling [43]. The fibrosis that occurs in PAH is an important vascular pathology that is not well-studied, and there are currently no anti-fibrotic treatments for PAH [131]. PAAFs are important for vascular extracellular matrix (ECM) homeostasis and remodeling [13, 43] and fibrosis [131], and there is evidence that PAAFs are regulated by stretch [141, 142] or overstretch injury [47, 152], matrix stiffness [12, 44, 140], and hypoxia [43]. During injury, PAAFs are activated and differentiate into myofibroblast subtypes that remodel the pulmonary arterial wall by modifying the expression, synthesis, degradation, and cross-linking of ECM proteins including collagen, fibronectin, and elastin [80,73,82]. Since elevated pulmonary artery pressure in PAH results in increased arterial wall strain [11], increased stretch of PAAFs may be a primary driver of fibrosis in the adventitia and resultant stiffening of the PA ECM [46, 47]. Given that the ECM also serves as a substrate for cell adhesion and sends

physical and chemical cues that can regulate cell phenotype [153], matrix stiffening may also regulate subsequent tissue remodeling as PAH progresses [11].

While fibroblast activation induces changes in the composition and structure of the vascular adventitial matrix, it is unclear how PAAFs are regulated by the combination of altered vessel stretch due to increased loading during PAH and the matrix stiffening that occurs, what signaling pathways regulate these phenotypic responses to physical stimuli, and the extent to which these mechanically-stimulated pathways overlap and interact.

We previously constructed a mechanosignaling model of PAAFs as described in Chapter 2 [54]. The computational model incorporated major pathways such as Ang II and TGFβ profibrotic signaling pathways reported in the literature and included a single input representing all types of mechanical stimulation [54]. Here we used a new iteration of this model together with *in vitro* experiments in PAAFs cultured on different stiffness gels and subjected to different stretch conditions to focus on how six important profibrotic gene outputs of the model respond to stretch and changes in stiffness that mimic the mild and severe stages of PAH (compared with healthy conditions). The analysis suggests pathways that are differentially activated by changes in cell stretch and ECM stiffness that help elucidate how PAAFs respond to mild and severe PAH.

Therefore, the goal of this study was to investigate how increased stretch and matrix stiffness affect the expression of profibrotic genes in PAAFs and whether there is an interaction effect between these stimuli. We stretched PAAFs grown on different substrates for 4, 8 and 24 hours and measured the expression of the six profibrotic genes in the model to test the hypothesis that responses to stretch and stiffness in PAAFs are regulated by different but overlapping and potentially interacting pathways. We also used the model to identify nodal regulators of

mechanoregulation of profibrotic gene expression in PAAFs and investigated the yet unknown effects of inhibiting these pathways on responses to stretch and matrix stiffness.

### 3.1.2 Materials and Methods

#### 3.1.2.1 Cell Isolation

Pulmonary arteries (PAs) were harvested and isolated from six- to eight-week-old normotensive male Sprague–Dawley rats (Charles River Laboratories, Wilmington, MA, USA) under advisement of the Animal Care and Use Committee at the University of California San Diego (Protocol #S17237). The adventitial layer was stripped off and segments were cut into pieces, enzymatically digested with 1 mg/mL Type 2 collagenase (#LS004176, Worthington, Lakewood, NJ, USA) in Dulbecco's Modified Eagle Media (DMEM, D5030, Gibco Thermo Fisher Scientific, Waltham, MA, USA) and agitated for 1.5 h at 37 °C, following the protocol by Liu *et al*. [105]. Fibroblast media was prepared by combining DMEM and 10% (v/v) fetal bovine serum (FBS) (#16140, Sigma Aldrich, St. Louis, MO, USA) and 1% antibiotic-antimycotic solution (#15240062, Gibco Thermo Fisher Scientific, Waltham, MA, USA). Isolated PAAFs were expanded on T75 tissue culture plastic (#25-209, Genesee Scientific, El Cajon, CA, USA) at 5% CO2, 37 °C, 100% humidity. To characterize PAAF cultures and compare their phenotypes to PAAFs *in-vivo*, 10 mm segments of fixed, intact normotensive pulmonary artery were cryosectioned to 10µm and immunolabeled with antibodies against von Willebrand Factor (vWF) (#SC-365712, 1:50, Santa Cruz Biotechnology, Santa Cruz, CA, USA) as a marker for pulmonary arterial endothelial cells, myosin-11 (MYH11) (#SC-6956, 1:50, Santa Cruz Biotechnology, Santa Cruz, CA, USA) as a marker of pulmonary arterial smooth muscle cells, and vimentin (#AB-

92547, 1:250, AbCam, Cambridge, UK) as a marker in all pulmonary artery cells that is also highly expressed in pulmonary arterial myofibroblasts, with appropriately matched secondary antibodies (Life Technologies, Carlsbad, CA, USA) (1:500) (Goat anti-Mouse Texas Red (#T862), Goat anti-Rabbit AlexaFluor700 (#A21038) with Wheat Germ Agglutinin-488 for membrane (#W6748, 10 μg/mL) and DAPI (#P36941) using standard immunofluorescence protocols with images taken at 40× magnification on a ThermoFisher Scientific EVOS FL-Auto 2 fluorescent microscope. The same staining protocol and imaging settings were also used to image isolated PAAFs that were expanded on plastic to characterize the culture. Cells were freshly isolated or used at a maximum passage number of 3 for these experiments. Data on Cytosoft® 6-well plates (#5140 and #5142, Sigma Aldrich, St. Louis, MO, USA) were from seeding 100,000 frozen PAAFs per well, where 2 wells were pooled for RNA isolation after 3 days.

#### 3.1.2.2 Stretcher Preparation

Polyacrylamide gels were prepared using stiffnesses corresponding to a normotensive pulmonary artery (0.5 kPa), mild PAH (3 kPa), and severe PAH (10 kPa), based on work by Liu *et al*. [61]. Gel stiffness was modulated by the percentage of acrylamide and bis-acrylamide (#A9099 and #146072, Sigma Aldrich, St. Louis, MO, USA): 3% acrylamide and 0.06% bis-acrylamide were used for the construction of 0.5 kPa gels; 4% acrylamide and 0.3% bis-acrylamide were used for the constructions of 3 kPa gels; and 10% acrylamide and 0.1% bis-acrylamide were used for the construction of 10 kPa gels [62].

Custom-made circular stretchers were designed using computer-aided design and constructed with polycarbonate. Polydimethylsiloxane (PDMS) membranes were built by mixing the Sylgard 186 elastomer kit (#4026144, Dow, Midland, MI, USA), extruding onto a wafer,

degassing in a vacuum chamber then curing in the oven. The PDMS membranes were treated with 10% benzophenone (#A10739, Alfa Aesar Thermo Scientific, Haverhill, MA, USA) for polyacrylamide gel adherence, as previously described by Herum *et al*. [63]. The polyacrylamide gels were constructed to be 25 mm in diameter, cross-linked through exposure to ultraviolet light for 25 min, attached to PDMS membranes, and surrounded by silicone grease to prevent cell migration and media leakage. The gels were equilibrated in 1× Phosphate Buffered Saline (PBS, # 10010023, Gibco Thermo Fisher Scientific, Waltham, MA, USA) overnight, then Corning® collagen I (100 g/mL, #354236, Sigma Aldrich, St. Louis, MO, USA) was attached with 1-Ethyl-3-(3-dimethylaminopropyl) carbodiimide (#00050, Chemplex, Mahwah, MJ, USA) and N-hydroxysuccinimide (#A10312, Alfa Aesar Thermo Scientific, Haverhill, MA, USA) to facilitate cell adherence. The stretcher was assembled so that two full turns were equivalent to 10% static stretch, as previously done [144, 145]. PAAFs were trypsinized from the tissue culture plates using 0.25% Trypsin-EDTA (#25200056, Gibco Thermo Fisher Scientific, Waltham, MA, USA) and seeded onto the gels at a density of 140,000 cells per gel. Cells were cultured at 37 °C, 5% CO2, 100% humidity for three days. Cells were changed into serum-free media for 24 h before being stretched. The stretch condition was applied for 24 h (and 4h and 8h) based on the increase in gene expression shown by Herum *et al*. in left ventricular cardiac fibroblasts [63].

#### 3.1.2.3 Inhibition Studies

For the inhibition experiments, PAAFs were seeded onto 0.5 kPa and 3 kPa gels at a density of 40,000 cells per gel and cultured for three days as described above. The media was changed to serum-free media, and each gel slated for inhibition was pre-incubated for 4 h with 1 M losartan (#3798, Tocris Bioscience, Minneapolis, MN, USA) or with 30 min of 10 µM SB 431542 (#1614,

Tocris Bioscience, Minneapolis, MN, USA). The dose of losartan was delivered according to work by Kim *et al*. in adventitial fibroblasts from 6-week-old Sprague–Dawley rats [146] and dose of SB 431542 was determined by work with Herum *et al*. done in cardiac fibroblasts [109]. The cells were then stretched for 24 h as previously described in the Stretcher Preparation subsection. RNA isolation of these cells was conducted as described below.

#### 3.1.2.4 RNA Isolation

For RNA extraction of the normotensive pulmonary artery, the adventitial layer was sectioned into 6 pieces and submerged in TRIzol reagent (Invitrogen #15596026, Thermo Fisher Scientific, Waltham, MA, USA). Tissue was homogenized using a BeadBug homogenizer with 1.5 mm zirconium beads. (Benchmark Scientific, Sayreville, NJ, USA). For PAAF experiments, RNA isolation was carried out using TRIzol and 5PRIME Phase Lock Gel Heavy tubes (#2302830, Quantabio, Beverly, MA, USA) and RNA was extracted using either a standard TRIzol total RNA isolation protocol or the RNeasy® Mini kit (#74104, Qiagen®, Hilden, Germany), which was then reverse transcribed into cDNA using the NEB cDNA ProtoScript First Strand Kit (#E6300L, New England Biolabs, Ipswich, MA, USA) and then RNA was extracted using the RNeasy Mini kit (#74104, Qiagen, Hilden, Germany). Quantitative real-time PCR was performed using the StepOnePlusTM Real-time PCR machine (Thermo Fisher Scientific, Waltham, MA, USA) and KAPA SYBR Fast Universal qPCR kit (#KK4601, Roche, Basel, Switzerland) using primers targeting genes of interest listed in Supplementary Table S1 (produced by Integrated DNA Technologies, San Diego, CA, USA). Relative gene expressions were compared against housekeeping gene 18S ribosomal RNA unless otherwise noted.

#### 3.1.2.5 Imaging

Thirty thousand PAAFs were plated onto 35 mm cell culture dishes with #0 coverglass bottom (#D35-20-0-N, CellVis, Sunnyvale, CA, USA) onto 0.5 kPa or 3 kPa polyacrylamide gels, or directly onto plastic for 3 days at 37 °C and 5% CO2. Images were taken on an EVOS FL Auto 2 microscope, running software v2.0.1732.0 (Thermo Fisher Scientific, Waltham, MA, USA). Antibodies against Smooth Muscle alpha-Actin (mouse #A5228 1:100, Sigma, St. Louis, MO, USA) with secondary Goat anti-Mouse Texas Red (#T862, 1:250, Life Technologies, Carlsbad, CA, USA), Wheat Germ Agglutinin-488 for membrane (#W6748, 10 g/mL, Life Technologies, Carlsbad, CA, USA) and DAPI for nuclei in mounting media with Prolong Gold Antifade Reagent with DAPI (#P36941, Life Technologies, Carlsbad, CA, USA). Images were processed using DeconvolutionLab2 (EPFL, Lausanne, Switzerland) in ImageJ v1.53g4 developed by the National Institutes of Health (Bethesda, MD, USA).

#### 3.1.2.6 Protein Quantification

Ten thousand PAAFs per gel were plated on 12 mm polyacrylamide gels at 0.5 kPa, 3 kPa, and 10 kPa stiffnesses formulated as described above and cultured for 3 days and fixed. Antibodies against Collagen 3a1 Rabbit (#13548-1-AP, 1:50, Proteintech, Wuhan, China) with secondary Goat anti-Rabbit AF700 (#A21038, 1:250, Life Technologies, Carlsbad, CA, USA) and against Smooth Muscle alpha-Actin (SMA) Mouse (#A5228, 1:100, Sigma, St. Louis, MO, USA) with secondary Goat anti-Mouse Texas Red (#T862, 1:250, Life Technologies, Carlsbad, CA, USA) were used to stain the PAAFs. The same imaging settings were used across cells cultured on different stiffnesses and fluorescence intensity was quantified using ImageJ v1.53g4 developed by the National

Institutes of Health (Bethesda, MD, USA) and displayed as corrected total cell fluorescence (CTCF).

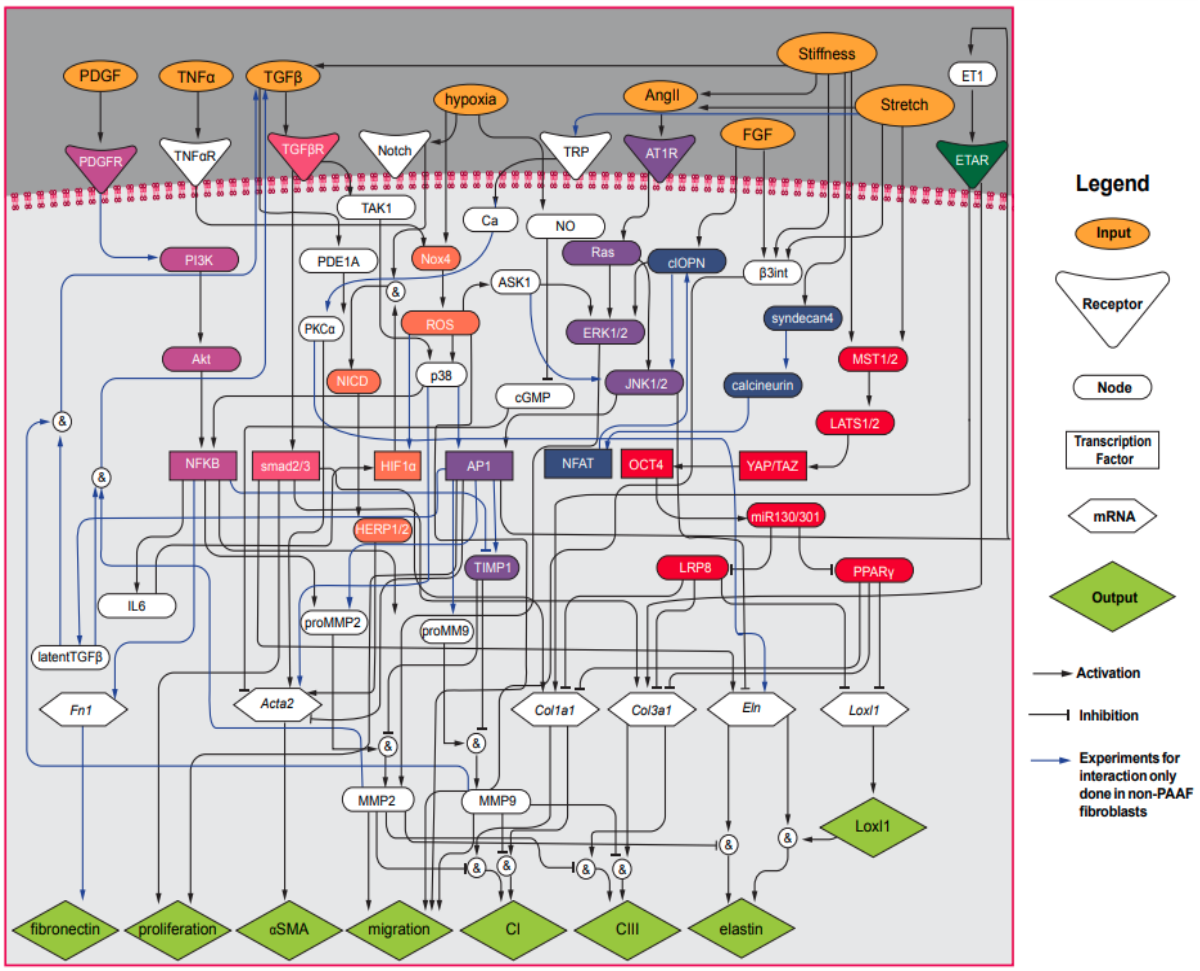


**Figure 3.1: Revised PAAF signaling network model with 70 nodes**. PAAF mechanosignaling network with 8 input stimuli (orange ovals), 7 receptors (triangles), 34 nodes (ovals), 7 transcription factors (rectangles), 6 messenger RNAs (hexagons), and 8 phenotypic outputs (green diamonds), modified from our previous work [54]. Activation is shown with arrows and inhibition is shown with blunt head arrows. Blue arrows indicate non-PAAF-based experiments. Magenta nodes indicate the Phosphoinositide 3-kinase (PI3K) pathway, orange nodes indicate the Reactive Oxygen Species (ROS) pathway, purple nodes indicate the mitogen-activated protein kinase (MAPK) pathway, blue nodes indicate the calcineurin pathway, and red nodes indicate the Hippo signaling pathway.

### 3.1.2.7 Computational PAAF Network Model

We used our recently published PAAF network model [54] to investigate how substrate stiffness and stretch regulate profibrotic gene expression in PAAFs. The mechanical stimulus input was divided into substrate stiffness and stretch inputs, where stretch activated integrin $\beta_3$, AngII, MST1/2, and TRP; and stiffness activated integrin $\beta_3$, Ang II, MST1/2, TGF-$\beta$, and Syndecan-4 [51, 107, 109,112, 147-149]. We also added details to the activation of mitogen activated protein kinases (MAPKs) to allow independent regulation of JNK1/2, p38, and ERK1/2 [69, 150-157]. In this refined model, ASK1 regulates JNK1/2 as well as ERK1/2 [150-151]. Ras was added downstream of AT1R to mediate regulation of ERK1/2 and JNK1/2 [152-153]. Based on studies by Xie *et al.* [154] in adult rat cardiac fibroblasts, activation of JNK1/2 by cleaved osteopontin (clOPN) was included. The TGFβ receptor now also activates p38 via the TGFβ-activated kinase (TAK1) [155] and TGFβ receptor also activates *Eln* through smad2/3 based on work in PAAFs by Rabinovitch *et al.* [158]. Based on a model of cardiac fibroblasts by Zeigler *et al.* [69] and papers on MAPK signaling [156, 157], we included ROS activation of p38. Finally, we incorporated the activation of TRP channels TRPC6 and TRPC1/C5 by stretch, which allows calcium to activate Protein Kinase C alpha (PKC$\alpha$) [159-161]. We also updated endothelin-1 and its receptor to be outside of the PAAFs due to secreted endothelin feeding back into the model and have thusly updated the model to reflect this [162]. Given the scarcity of PAAF studies, the network includes reactions from fibroblasts not derived from pulmonary arteries, such as cardiac and lung fibroblasts. The updated network is displayed in **Fig. 3.1.**

The PAAF signaling network model was implemented as a system of logic-based ordinary differential equations that were integrated numerically using an explicit Runge–Kutta method. Briefly, each state variable $y_i$ that represents each of the species in the network is normalized to a

value between 0 and 1 and follows a Hill-type activation function. The system of equations for the 69 nodes in the model takes the form of Equation 3.1:

$$\frac{d_{y_i}}{dt} = \frac{1}{\tau_{y_i}}[(\omega_i y_i f(EC_{50}, n, B) y_i^{max} - y_i] \quad (3.1)$$

where $\omega_i$ represents the weight for each node, τ is the time constant, and *f* is the sigmoidal Hill function of $y_i$, where *f*($EC_{50}$, *n*, B) is a function of half-maximal activation $EC_{50}$, cooperativity *n*, and constant *B*. The form of biochemical interactions between two or more species is specified by 'AND' or 'OR' Boolean operators that represent the biochemical interactions between upstream nodes expressed as continuous functions as described in Wang *et al*. [54] in Chapter 2 of this thesis.

Inputs of the model (PDGF, TNF, TGF-β, hypoxia, AngII, FGF, stiffness, stretch) were initialized at 0.25. Default reaction weights $\omega$, Hill coefficient *n*, and half-maximal activation $EC_{50}$ were set to 1, 1.4, and 0.6, respectively. The time constants τ for each different reaction followed those used previously [54]: 0.1 h for signaling reactions; 1 h for transcription; and 10 h for translation. Similar to the network model analysis by Tan *et al*., (2017), we chose a change in normalized model output values of 0.1 as the threshold for considering the output to have changed significantly by mechanical stimulation or for a significant response to have been significantly inhibited [118]. While Tan *et al*., (2017) used a threshold of 0.05, we chose a more stringent threshold of 0.1, but our conclusions were not affected by this difference. Parameters in the model were not optimized or fitted. Rather we chose equal parameters for all reactions using values from Zeigler *et al*. [69]. While the parameters $EC_{50}$, weight, and Hill coefficient were set to be the same value across all reactions, the time constant τ was chosen according to the type of reaction. Furthermore, parameter values were tested for consistency with the mathematical constraints

described in Cao *et al*. for this class of model [159]. In a previous comprehensive analysis of parameter uncertainty, we verified that model accuracy was robust to the choices of these parameter values [54].

The input weights of stretch and stiffness were both set to 0.25 to represent the softest matrix, 0.5-kPa, and no applied stretch. We increased the stiffness input weight to 0.7 and 0.9 to represent the effects of 3-kPa and 10-kPa substrates, respectively, and evaluated the model at t=72 hours to mimic the *in-vitro* experimental time course.

To numerically simulate the effects of stretch on PAAFs after 24 h and the changes in substrate stiffness for 72 h when inhibiting nodes, the model was evaluated at those time points (i.e., *yi* (t = 24) and *yi* (t = 72)) after the corresponding input weights of stiffness and stretch were increased from 0.25 to 0.7. To simulate the effects of inhibition, $y_i^{max}$ corresponding to blocked nodes were set to 0, while the other parameters remained the same. The change for each gene was calculated with respect to each condition's control group.

To simulate the different conditions under which losartan inhibited AT1R or SB 431542 inhibited TGFβR, we conducted eight sets of simulations. Four sets of these simulations were evaluated on 0.5 kPa substrate stiffness for 72 h with parameters at baseline, and input weights stiffness and stretch set to 0.25. For simulations involving stretch but no inhibition, the input weight of stretch was increased from 0.25 to 0.7 and the model was evaluated at t = 24 h. For the unstretched and stretched inhibited conditions, $y_i^{max}$ corresponding to the AT1R node or TGFβR node was set to 0 before applying changes to the stretch input weight and was evaluated at t = 24 h. The same combinations were used for the other four set of simulations on 3 kPa substrate conditions, but with a stiffness input weight of 0.6.

The implementation of the model in Python 3.9.0 along with simulation data are available on Github at https://github.com/dvaldezjasso/DVJ-LAB/tree/main/PAAF.

#### 3.1.2.8 Statistics

Descriptive statistics were performed using JMP Pro Statistical software (version 14, SAS Institute Inc., NC, USA) for group comparisons of relative gene expression. For normally distributed data, one-way analysis of variance (ANOVA) was used to test for differences in means of three different stiffnesses and gene expression of the normotensive pulmonary artery adventitial layer for all six genes, followed by the Dunnett's *post-hoc* test. Otherwise, the non-parametric Wilcoxon–Kruskal–Wallis statistic was used followed by Dunnett's *post-hoc* test. Effects of stiffness and stretch were tested using two-way ANOVA with stiffness and stretch as fixed factors. For normally distributed data, the Dunnett's *post-hoc* test was used. Otherwise, the non-parametric Wilcoxon–Kruskal–Wallis statistic was used followed by Dunnett's *post-hoc* test. For the inhibition studies, three-way ANOVA was used to compare the effects of stiffness, stretch, and inhibition, followed by Sidak's *post-hoc* test. Data are expressed as means ± standard error of the mean, unless otherwise specified. Statistical significance was determined at a level of 0.05. Data were graphed in GraphPad Prism software (v8.4.3.686, San Diego, CA, USA) and Illustrator (Adobe, San Diego, CA, USA, v24.2.3).

### 3.1.3 Results

#### 3.1.3.1 PAAFs Upregulate Profibrotic Genes in Response to Increased Substrate Stiffness and Stretch

The immunostained cultures for markers of endothelial cells (vWF), smooth muscle cells (MYH11), and myofibroblasts (vimentin) (**Fig. 3.2A-H**) were only 3% were positive for vWF and 0.2% positive for MYH11, suggesting high enrichment of PAAFs in our cell cultures. Intact PA tissue sections were stained and imaged with the same antibodies and imaging settings as positive controls for these markers (**Fig. 3.2I-R**).

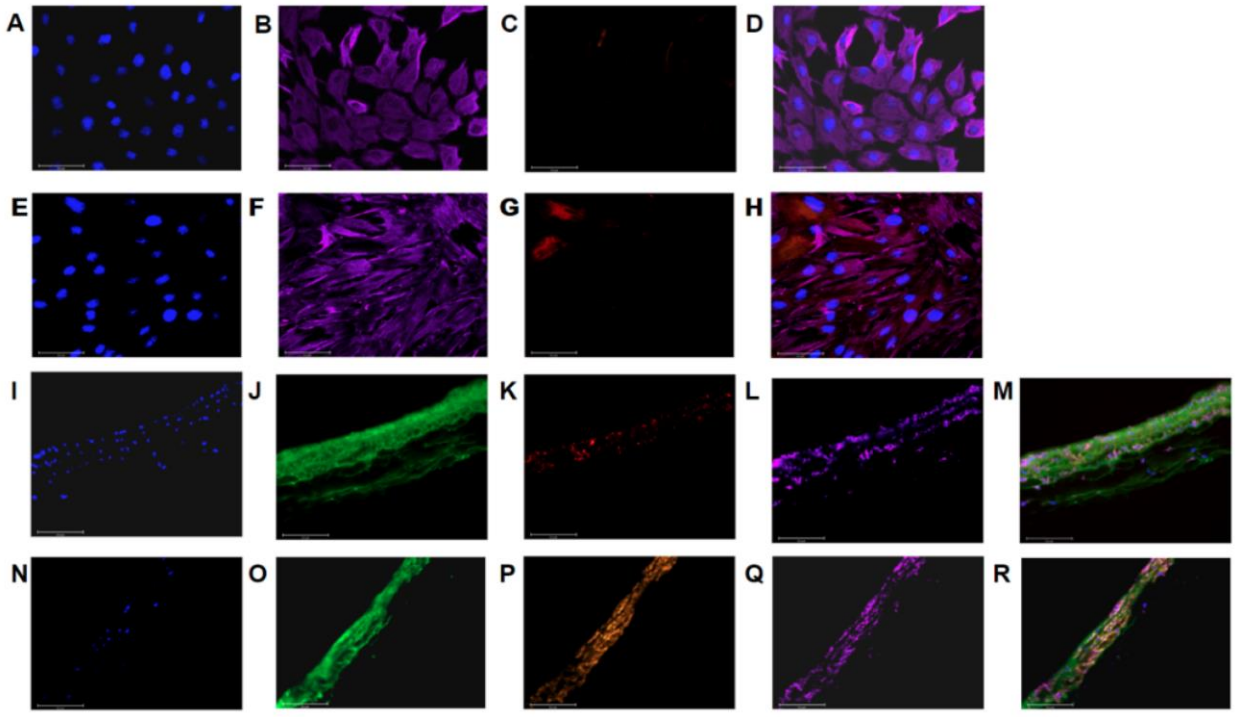


**Figure 3.2: Characterization of cells isolated from pulmonary arterial adventitia.** The cell culture showed positive labeling for (**A, E**) DAPI, (**B,F**) vimentin, (**C**) vWF, and (**G**) MYH11 with (**D,H**) overlays. Out of 425 isolated cells, 3% expressed vWF, and out of 888 cells 0.2% expressed MYH11 and 100% expressed vimentin with representative images shown in (**A–H**). Immunostained PA tissue sections showed positive labeling for: (**I**) DAPI, (**J**) WGA, (**K**) vWF, (red), and (**L**) vimentin(magenta) with an (**M**) overlay. Separate immunostained PA tissue sections showed positive labeling for: (**N**) DAPI, (**O**) WGA, (**P**) MYH11 (orange), and (**Q**) vimentin (magenta) with an (**R**) overlay. These samples were used as labeling controls to estimate purity of a cell culture expanded on plastic. Images were all acquired at 40× magnification, scale bar 50 µm.

PAAFs expanded on plastic reverted from a myofibroblast to a fibroblast phenotype after three days of culture on 0.5-kPa stiffness 6-well plates, as assessed by their low expression of *Acta2* (**Fig. 3.4**) and their rounded appearance in culture (**Fig. 3.3B**) compared with the more

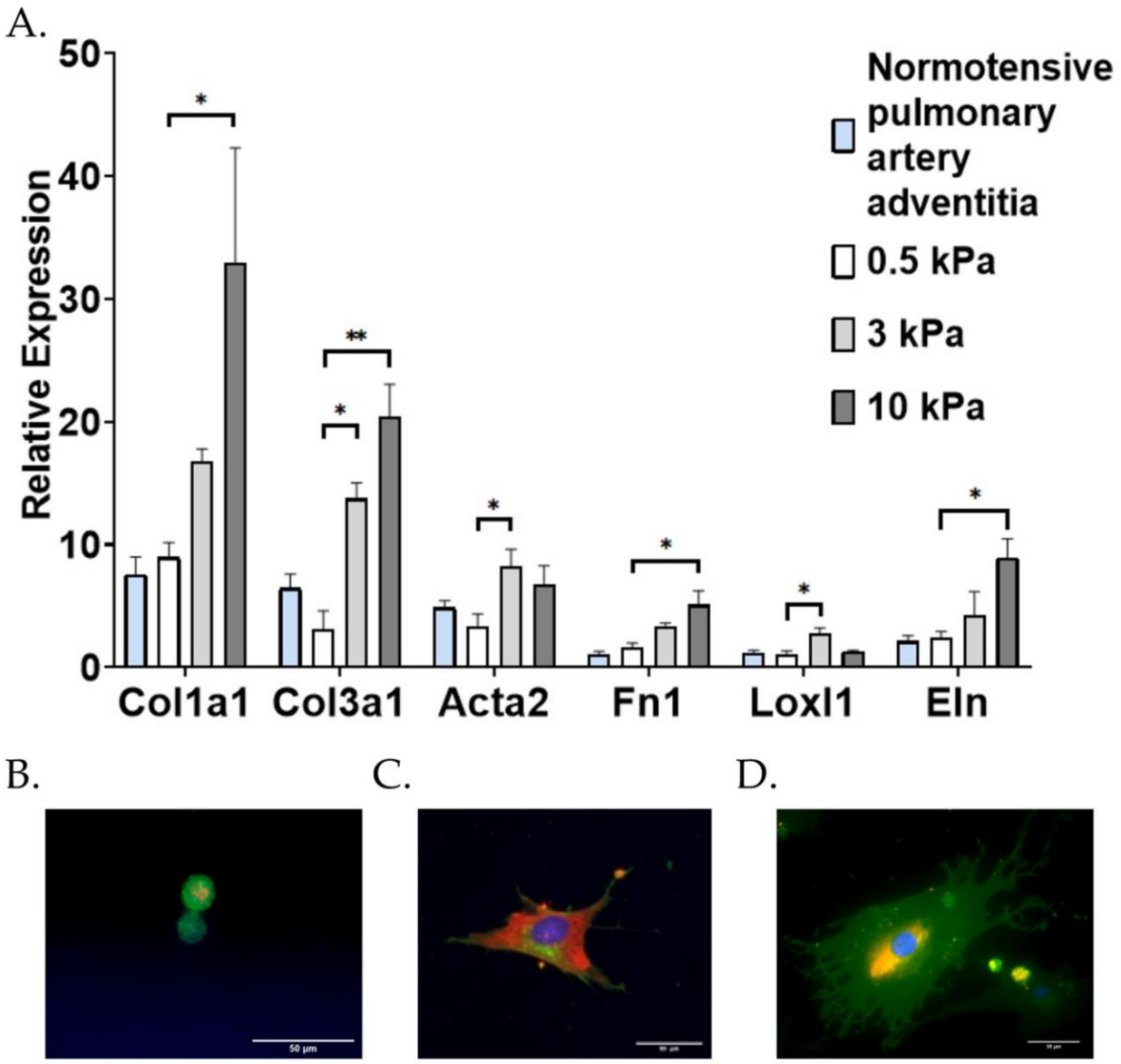


**Figure 3.3: Effect of substrate stiffness on PAAF differentiation.** (**A**) Mean ± standard errors of the mean relative to housekeeping gene 18S ribosomal RNA of PAAFs cultured at different stiffness (n = 9) compared with gene expression of sections in a normotensive pulmonary artery adventitia (n = 6). Effect of stiffness (* $p < 0.05$ and ** $p < 0.0001$) by one-way analysis of variance (ANOVA) compared with control 0.5 kPa with a *post-hoc* Dunnett's test. (**B**–**D**) PAAFs plated on (**B**) 0.5 kPa (40×), (**C**) 3 kPa (20×) polyacrylamide gel and (**D**) plastic (40×), scale bar 50 µm. Cells were stained with DAPI, which stains the nucleus (blue), wheat germ agglutinin stains the membrane (green), and α-SMA filaments (orange).

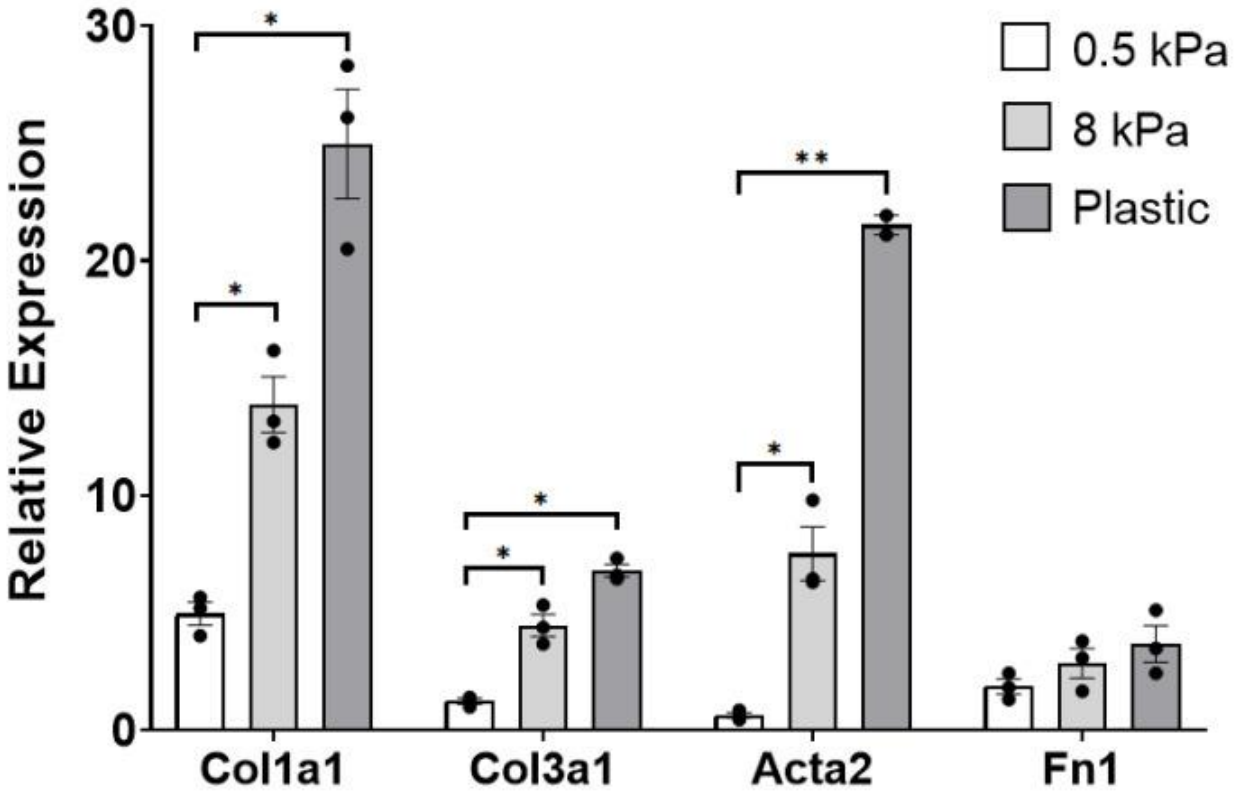


**Figure 3.4: Mean ± standard errors of the mean of Col1a1, Col3a1, Acta2, and Fn1 gene expression of cells seeded on Cytosoft® plates.** Effects of stiffness on PAAF gene expression relative to 18S ribosomal RNA. Genes *Col1a1*, *Col3a1*, and *Acta2* were significantly induced by an increased stiffness of 8 kPa and plastic relative to a control stiffness of 0.5 kPa. *Fn1* was not significantly upregulated at 24 hours. Significant effect of stiffness (* $p < 0.05$ and ** $p < 0.0001$) by one-way analysis of variance (ANOVA) compared with gene expression at 0.5 kPa.

stellate shapes and higher *Acta2* expression in cells grown on stiffer substrates (**Fig. 3.3 C-D**).

Messenger RNA levels of *Col1a1*, *Col3a1*, *Eln*, *Fn1*, *Loxl1*, and *Acta2* genes in fibroblasts

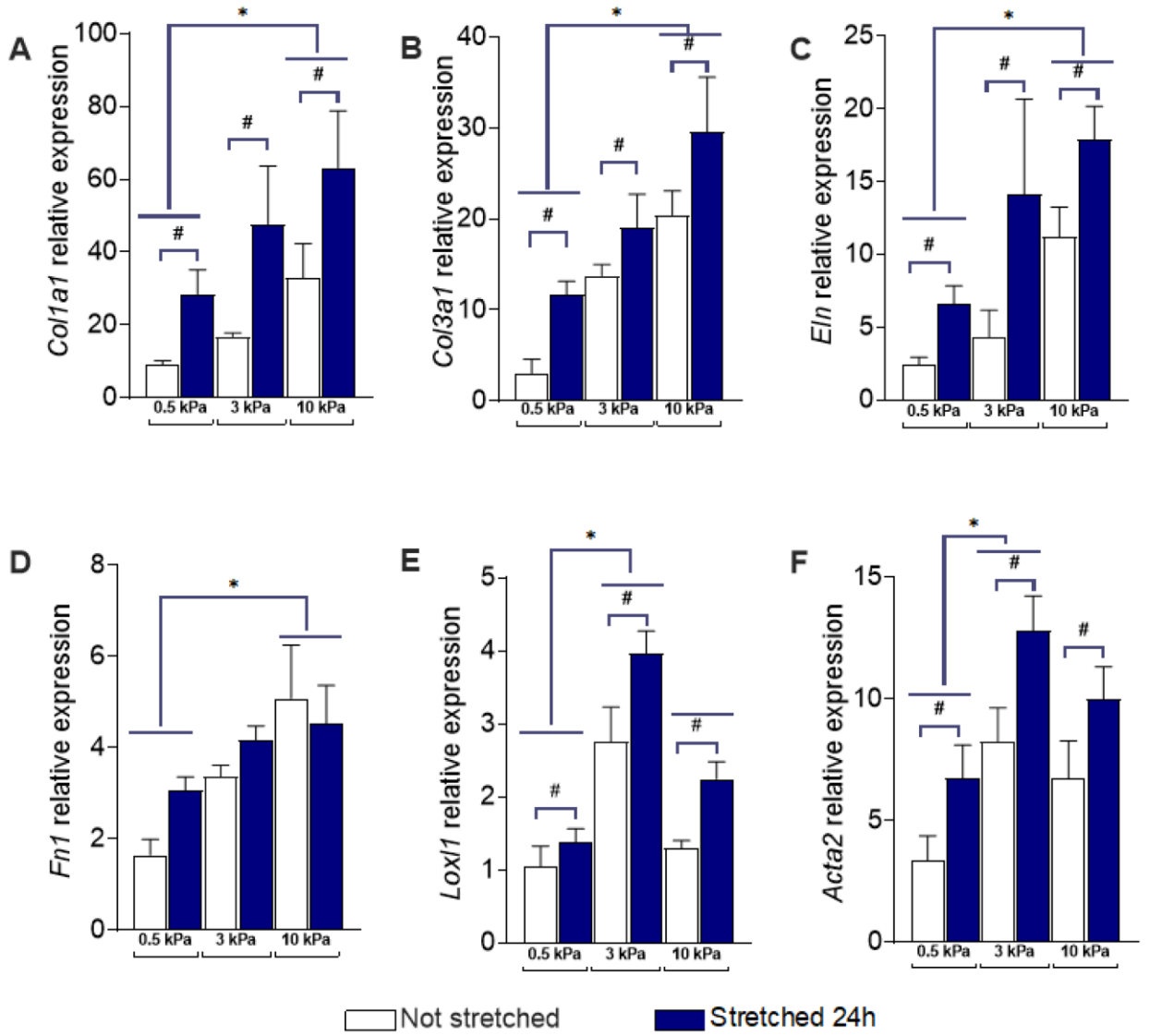


**Figure 3.5: Effect of stiffness and stretch on gene expression in PAAFs.** Mean ± standard errors of the mean of mRNA levels relative to housekeeping control gene 18S ribosomal RNA in unstretched cells (n = 9, white bars) and after 24 h 10% equibiaxial stretch (n = 12, blue bars). *Significant pairwise effect of stiffness ($p < 0.05$) by a *post-hoc* Dunnett's multiple comparisons test and # significant effect of stretch ($p < 0.05$) based on group comparisons made using a two-way analysis of variance (ANOVA) for: (**A**) Collagen I (*Col1a1*) (**B**) Collagen III (*Col3a1*) (C) Elastin (*Eln*) (**D**) Fibronectin (*Fn1*) (**E**) Lysyl oxidase-like 1 (*Loxl1*) (**F**) Smooth Muscle Actin (*Acta2*).

cultured on 0.5-kPa substrates were not significantly different from those in the pulmonary artery adventitia of a normotensive rat ($p>0.05$ by one-way ANOVA, **Fig. 3.3A**). This finding suggests

that cells cultured on a 0.5-kPa substrate may mimic expression of PAAFs *in-vivo* with respect to the six genes studied in this thesis.

Compared with mRNA levels in PAAFs cultured on 0.5-kPa substrates (as control), all six genes were significantly upregulated in response to increased matrix stiffness ($p<0.05$ by one-way ANOVA and Dunnett's *post-hoc* test). The expression of *Acta2* and *Loxl1* was significantly up-regulated on cells grown on 3-kPa matrices but not significantly altered on cells grown on 10-kPa matrices, while *Col1a1*, *Col3a1*, *Eln*, and *Fn1* were only significantly upregulated on 10-kPa substrates (comparable to arterial stiffness in advanced PAH [61]), all compared with PAAFs cultured on 0.5-kPa matrices (Figure 3.3A). Interestingly, *Acta2* and *Loxl1* expression exhibited non-monotonic responses, with significant upregulation of gene expression on 3-kPa matrices compared with the 0.5-kPa matrices, but no significant difference between cells cultured on 0.5-kPa and 10-kPa matrices.

Examining the transcriptional responses of the six genes to 10% equibiaxial stretch for 24h in PAAFs (**Fig. 3.5A-F**), we observed that *Col1a1*, *Col3a1*, *Eln*, *Loxl1* and *Acta2* were significantly upregulated compared with unstretched cells independent of the substrate stiffness ($p<0.05$ based on group comparisons made using a two-way ANOVA).

As described in Section 3.1.2.3, stretchers apply 10% equibiaxial stretch with two full rotations. RNA is isolated at 4, 8, and 24 hours post application of stretch. In the case of *Col1a1*, relative expression increased the most 24 hours after stretch, while *Col3a1, Acta2, Loxl1* and *Eln* expression increased at 8 hours and partially returned to baseline at 24 hours, and *Fn1* expression increased at 4 and 8 hours after stretch and returned to baseline by 24 hours (**Fig. 3.6**). *Col3a1* demonstrated the highest increase in relative expression at 8 hours of stretch, while *Acta2, Fn1*, and *Eln* showed the greatest increase with stretch on the stiffest matrices. *Loxl1*, which is

responsible for crosslinking collagens, increased greatly at 8 hours in cells grown on all substrates. This suggests *Fn1* is transiently induced by a short period of stretch, while the *Col1a1* response to stretch is much slower. This finding is consistent with reports identifying *Fn1* as an early response gene [164]. No significant interaction effects between substrate stiffness and stretch were found in the expression of any of the six genes (**Table 3.1**).

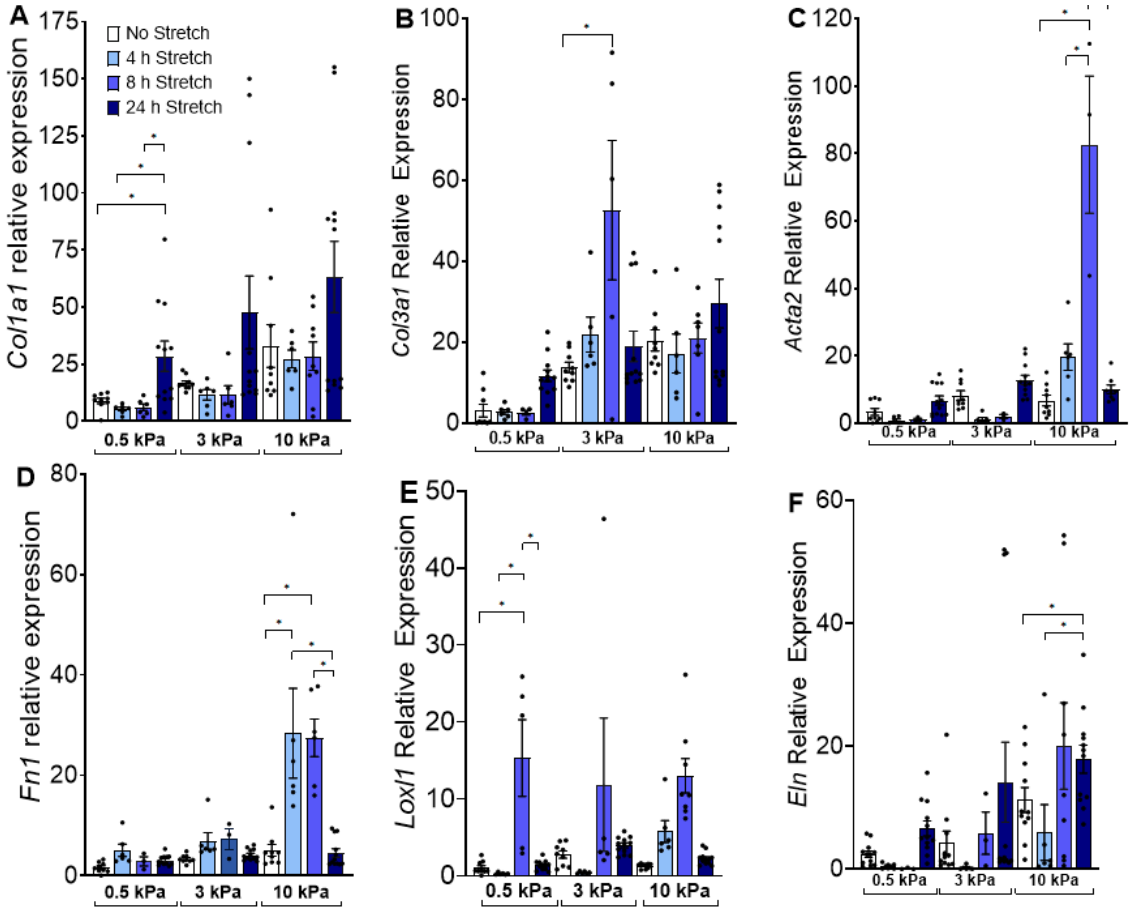


**Figure 3.6: Time course of PAAF profibrotic gene expression evaluated after at 4, 8 and 24 hours of applied stretch.** For genes: (**A**) *Col1a1* (**B**) *Col3a1* (**C**) *Acta2* (**D**) *Fn1* (**E**) *Loxl1* (**F**) *Eln.* For *Col1a1*, the largest increase occurs when stretched for 24 hours, while for *Col3a1*, *Acta2*, *Loxl1* and *Eln* the largest increase occurs when stretched for 8 hours. *Fn1* gene expression is largest at both 4- and 8-hour timepoints. *Col3a1*, *Acta2*, *Loxl1* and *Eln* thus may have the most induction after 8 hours of stretch, and *Fn1* is transiently induced by a short period of stretch but returns to baseline at 24 hours, while the *Col1a1* is most induced at 24 hours. Data is graphed as means ± standard errors of the mean of cells undergoing no stretch (n=9), stretch for 4h (n=6), 8h (n=9), and 24h (n=12). Significant differences ($p<0.05$) are marked by an asterisk * via 2-way ANOVA and *post-hoc* Dunnett's test.

**Table 3.1: p-values from a two-way ANOVA testing for the effects of substrate stiffness and stretch on the expression of six genes in cultured PAAFs.** Bolded values indicate $p<0.05$. All genes responded to changes in stiffness and all but fibronectin to stretch. No gene was found to be $p<0.05$ in the interaction term, suggesting stiffness and stretch are independent of each other with regards to these six genes.

| Genes | Effects of Stiffness | Effect of Stretch | Interaction Term |
|---|---|---|---|
| *Col1a1* | **0.046** | **0.006** | 0.86 |
| *Col3a1* | **<0.0001** | **0.012** | 0.69 |
| *Eln* | **0.009** | **0.009** | 0.66 |
| *Fn1* | **0.001** | 0.27 | 0.28 |
| *Loxl1* | **<0.0001** | **0.0007** | 0.30 |
| *Acta2* | **0.0007** | **0.002** | 0.88 |

Increased ECM stiffness significantly upregulated protein expression of Collagen III and Smooth Muscle Actin (SMA) from a baseline of 0.5-kPa at both 3-kPa and 10 kPa based on a *post-hoc* test (**Fig. 3.7**). There was no significant difference between 3-kPa and 10-kPa protein expression for either Collagen III or SMA. This is consistent with the changes in relative expression of RNA for Collagen III (*Col3a1*) and SMA (*Acta2*) (**Fig. 3.5 B**, **F)**, where there was a significant increase in gene expression from 0.5-kPa to 3-kPa, and no further significant increase in gene expression from 3-kPa and 10-kPa substrates.

### 3.1.3.2 PAAF Network Model Simulates Gene Expression Activated by Stiffness and Stretch

A threshold change of 0.1 in the normalized variable representing each of the six genes was used to classify the change in each gene as significant. The model predicted significant upregulation of five genes in response to an increase in substrate stiffness from 0.5-kPa to 3- or 10-kPa but not for *Eln*, and the data showed a non-monotonic decrease from 3- to 10-kPa in *Acta2* and *Loxl1* that the

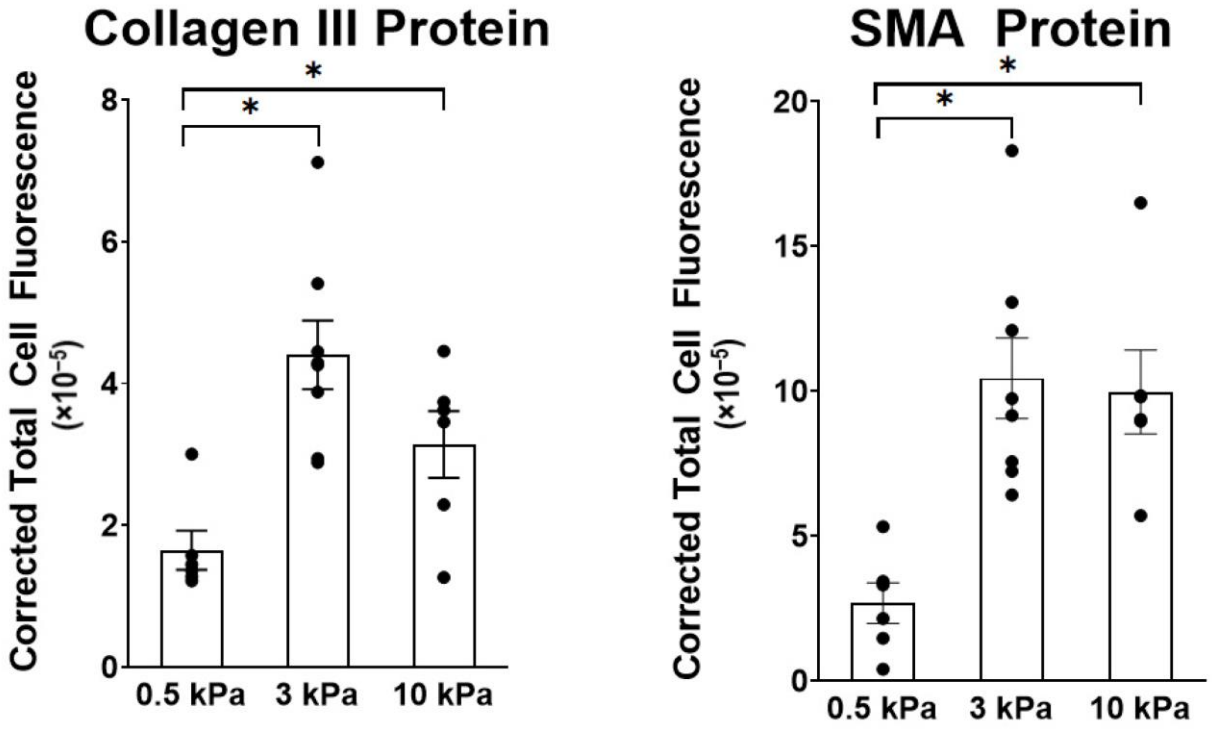


**Figure 3.7: Effect of stiffness on PAAF protein expression of Collagen III and SMA.** Mean ± standard errors of the mean of Corrected Total Cell Fluorescence (CTCF) for 6–8 replicate hydrogels cultured with PAAFs. Collagen III and SMA protein results match the trends in the relative expression mRNA results in *Col3a1* and *Acta2* respectively, suggesting mRNA trends are a good predictor of protein activity for Collagen III and SMA. *Significant pairwise effect of stiffness ($p < 0.05$) determined by one-way analysis of variance (ANOVA).

model was not able to capture, while stretch data matched except for predicting a decrease in *Eln* (**Fig. 3.8**). These model predictions matched our experimental observation that five genes were significantly upregulated in cells grown on stiffer matrices and increased due to stretch except for no change in *Fn1* and an increase in *Eln* in experimental data but decrease in model prediction.

The model also predicted upregulation of the gene expression of *Col1a1*, *Col3a1*, *Loxl1*,

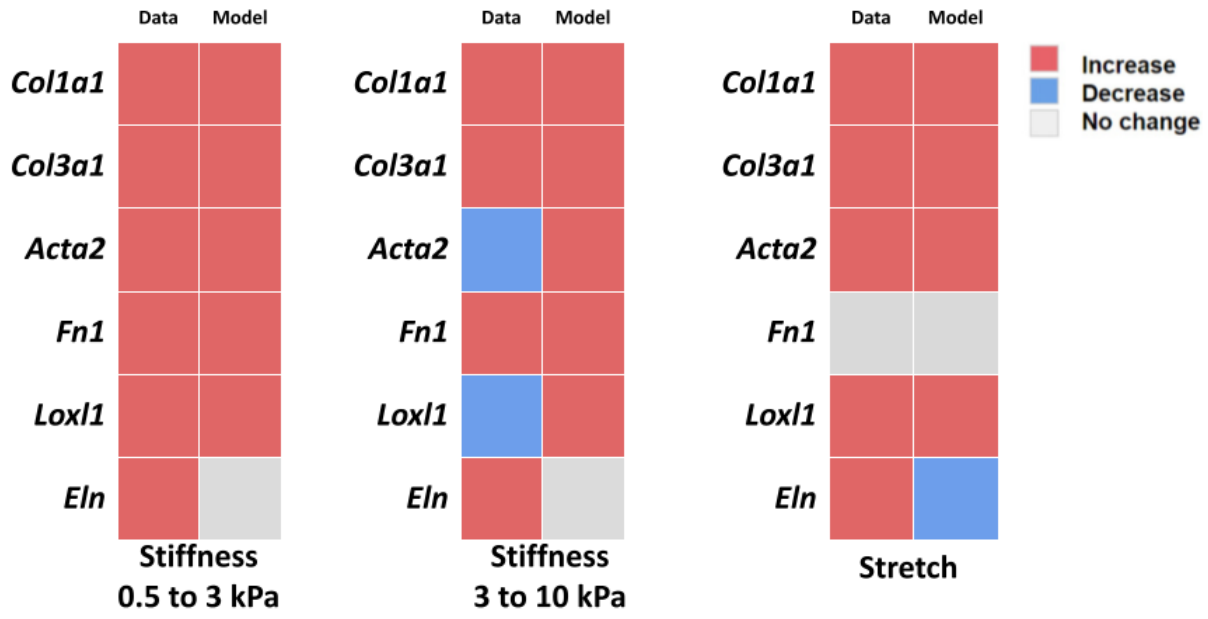


**Figure 3.8: Comparison of the experimental observations (Data) with model predictions (Model) of gene activity due to stretch and stiffness**. Increase (red), decrease (blue), and no change (grey) in gene predicted by the model is based on a threshold of 0.1 and experimental observations that reached a significant difference 24h after stretch ($p < 0.05$). Model results match well with stiffness increases from 0.5 to 3 kPa except for in *Eln* where the model predicts no change. The model was not able to predict the non-monotonic response of *Acta2* and *Loxl1* where a stiffness increase from 3 to 10 kPa led to a decrease in induction of *Acta2* and *Loxl1* experimentally. With regards to stretch, the model was well able to predict the lack of induction of *Fn1* by stretch but did not predict an increase in *Eln* induction by stretch, instead predicting a decrease. This suggests the model does not predict *Eln* induction nor non-monotonic responses with accuracy.

and *Acta2* and the return to baseline of *Fn1* expression 24 hours after induction by 10% equibiaxial stretch. However, the model predicted *Eln* expression to be downregulated with stretch while experimental results showed upregulation. We investigated whether the inhibitory effect of JNK1/2 on *Eln* may have outweighed the activating effect of PKC$\alpha$ and found that decreasing the weight of the inhibition of JNK1/2 on *Eln* [173] by 50% allowed the model to predict the observed upregulation of *Eln* (**Fig. 3.5**). While the model was in qualitative agreement with the data, it did not recapitulate the non-monotonic responses of *Loxl1* and *Acta2* (**Fig. 3.3A**), which were

significantly upregulated by 3-kPa matrix stiffness (compared with 0.5-kPa) but not by 10-kPa substrates.

### 3.1.3.3 Transforming Growth Factor β Receptor Inhibition and Angiotensin II Receptor Inhibition Unmasks New Pathway Interactions

Based on a sensitivity analysis done in Chapter 2 [54], we simulated the effects of stretch and increased stiffness in the presence of inhibitors of three mechanosensitive nodes in the model (AT1, and TGF-$\beta$, and MST1/2). Table 3.2 shows the effects of inhibiting AT1, TGF-$\beta$, and MST1/2 on changes in gene expression due to an increase in substrate stiffness from 0.5 and 3-kPa and due to stretch on 0.5 kPa stiffness matrices. Here, model-predicted differences in the normalized mRNA variable due to inhibitor treatments were considered significant if they exceeded a threshold of 0.1.

From the model simulations, the induction of *Loxl1* expression by increased substrate stiffness is specifically regulated by MST1/2 signaling, whereas the responses of the other five genes to stiffness were all significantly inhibited by blocking TGF$\beta$ receptor. AT1 receptor

**Table 3.2: Model-predicted changes in gene expression due to inhibition of AT1, TGFβ, MST1/2 receptors in response to stiffness and stretch in cultured PAAFs.** Numbers in bold indicate activity changes greater than a threshold of 0.1. The model predicts significant changes in the output six genes upon inhibition of AT1, TGFβ, and MST1/2 with AT1 and TGFβ significantly reducing effects of stiffness, and AT1 inhibition more crucial in affecting response to stretch.

| Genes | Effects of Stiffness on 3kPa | | | Effect of Stretch on 0.5 kPa | | |
|---|---|---|---|---|---|---|
| | AT1 (-) | TGF-$\beta$ (-) | MST1/2 (-) | AT1 (-) | TGF-$\beta$ (-) | MST1/2 (-) |
| *Col1a1* | **-0.16** | **-0.24** | **-0.10** | **-0.14** | -0.06 | **-0.26** |
| *Col3a1* | **-0.16** | **-0.24** | **-0.10** | **-0.14** | -0.06 | **-0.26** |
| *Eln* | -0.04 | **-0.46** | 0 | **0.20** | -0.08 | 0 |
| *Fn1* | **-0.15** | **-0.39** | 0 | -0.01 | -0.03 | 0 |
| *Loxl1* | 0 | 0 | **-0.37** | 0 | 0 | **-0.37** |
| *Acta2* | **-0.14** | **-0.70** | 0 | -0.04 | **-0.14** | 0 |

inhibition significantly attenuated the stiffness-dependent induction of *Col1a1*, *Col3a1*, *Fn1* and *Acta2*, but had no significant effect on *Eln* or *Loxl1*, and the magnitude of inhibition was noticeably less than when TGF$\beta$ receptors were blocked. Blocking angiotensin signaling in the model with increased substrate stiffness downregulated the collagens by 16% and blocking TGF$\beta$ signaling downregulated the collagens by 24%, while blocking angiotensin downregulated *Acta2* by 14% and blocking TGF$\beta$ downregulated it by 70% (**Table 3.2**).

Blocking TGF$\beta$ signaling in the model while applying stretch stimulation suppressed the upregulation of *Acta2* by 14% and reduced the downregulation of *Eln* by 8%. Stretch induction of *Col1a1* and *Col3a1* was shown to be reduced by inhibition of MST1/2 (by 26%) and angiotensin II signaling (by 14%), while *Loxl1* regulation by stretch was affected only by inhibiting MST1/2 (by 37%). *Fn1* expression, which was not significantly altered by stretch, remained unchanged in the presence of all three inhibitors. This contrasts with its response to substrate stiffness, where inhibiting AT1 and TGF$\beta$ receptors had a significant effect (**Table 3.2**).

Since inhibiting AT1 or TGF$\beta$ receptors were predicted to have the largest effect on the induction by increased stiffness and stretch of the profibrotic genes we are studying, we treated cells with losartan (AT1R inhibitor) or SB 431542 (TGF$\beta$RI inhibitor) as described in Methods Section 3.1.2.3. *In-vitro* experimental results were normalized and plotted against normalized *in-silico* modeling results carried out according to the protocol described in Methods Section 3.1.2.7 in **Fig. 3.9** below.

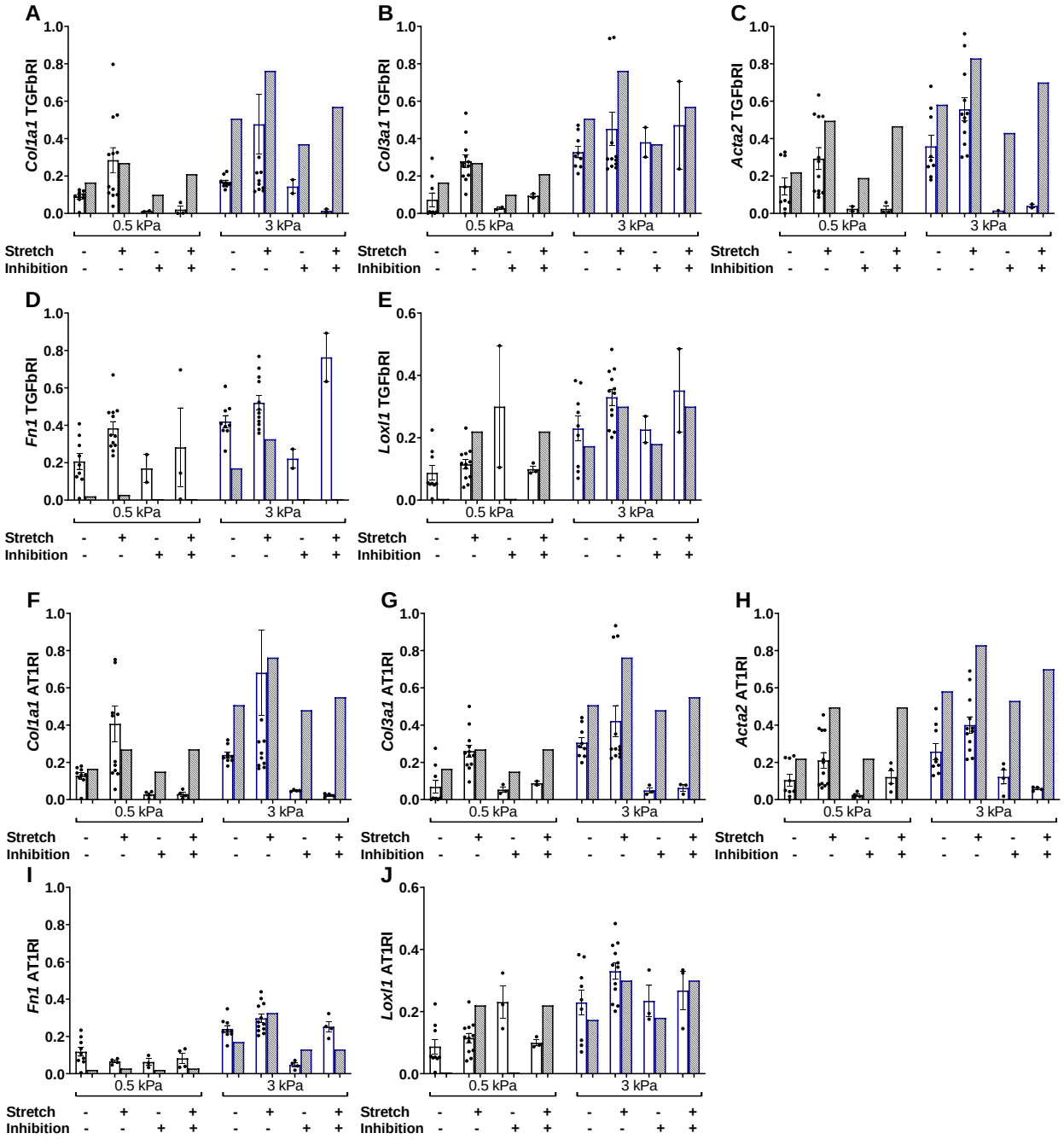


**Figure 3.9: PAAF inhibition experimental data (solid) compared with model predictions (shaded)**. Effects of inhibiting TGFβ receptor on: (**A**) *Col1a1* (**B**) *Col3a1* (**C**) *Acta2* (**D**) *Fn1* and (**E**) *Loxl1* and AT1 receptor on: (**F**) *Col1a1* (**G**) *Col3a1* (**H**) *Acta2* (**I**) *Fn1* and (**J**) *Loxl1* in five out of the six profibrotic genes. Experimental data (solid white) with mean ± SEM and n=3 independent gels cultured with PAAFs are normalized and graphed against model simulations (shaded) of 72 hours of stiffness plus 24 hours of no stretch, stretch, or inhibition. Since the model did not predict the effects of stiffness or stretch for *Eln*, this gene expression is not included in this comparison. Model predictions qualitatively match experimental results in stiffness for *Col1a1* (**A, F**) and *Fn1* (**D, I**); both stretch and stiffness for *Col3a1* (**B, G**), and *Loxl1* (**E, I**), but model predictions do not match for *Acta2* (**C, H),** detailed tabulation is given below in **Fig. 3.11**.

*In-vitro* inhibition data in shades of grey are compared with model predictions, both normalized from 0 to 1. The model was not able to predict stiffness or stretch measures for *Eln*, so its gene expression was not included in the comparison. *Col3a1* response to TGFβRI, the *Loxl1* response to TGFβR, and AT1R inhibition show the best qualitative agreement between the model and the experimental data. On both soft and stiff substrates, the induction of *Col1a1* and *Acta2 in* response to stretch was completely blocked by either TGFβ receptor or AT1 receptor inhibition, but the model predicted little or no inhibition. This may be because while either pathway was sufficient for stretch activation in the model, both may be required to upregulate *Col1a1* and *Acta2* signaling following stretch. *Fn1* expression, on the other hand, was not affected by TGFβ receptor or AT1 receptor inhibition in the experiments, but the model did predict attenuated stretch responses by both inhibitions. *Loxl1* expression generally agreed well, though baseline expression was too low in the model.

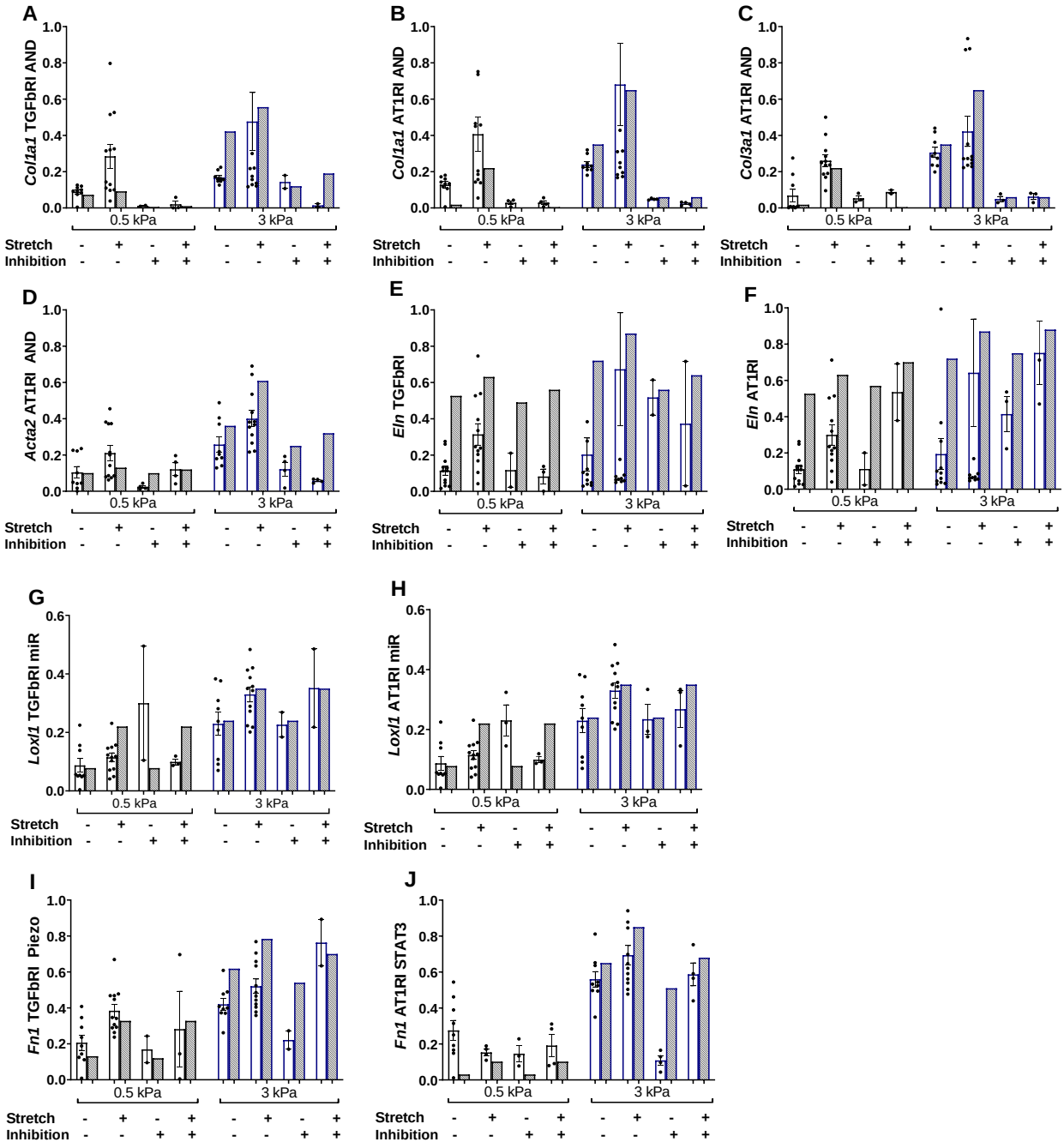


**Figure 3.10: Model modifications made to improve agreement with experiments.** White bars indicate experimental data and shaded bars indicate model simulation results. (**A-D**) *Col1a1*, *Col3a1* and *Acta2* modifications involve adding an AND reaction, (**E, F**) *Eln* the reduction of weight of the JNK reaction, (**G, H**) *Loxl1* a reduction of weight of the miR node, and for (**I, J**) *Fn1* the addition of a Piezo1 pathway for TGFβRI and addition of a STAT3 pathway for AT1RI.

**Figure 3.10A** shows the effects of inhibiting the TGFβ receptor on *Col1a1* expression when the model was modified by changing the OR logic coupling ET1 and PPARγ signaling to an AND. This change resulted in the model being able to better match experimental results by correctly predicting a larger effect of TGFβ receptor inhibitor. **Figure 3.10B** and **3.10C** illustrates how changing reactions upstream of *Col1a1* and *Col3a1* to allow for coregulation with smad2/3 and YAP/TAZ better predicts the inhibition response to AT1RI since the model now predicts a larger effect of AT1RI as shown by the experimental results. **Figure 3.10D** is *Acta2* AT1R in response to changing to coregulation of p38 and PKCα, TGFβRI is not shown since results were the same. This similarly demonstrates a larger effect of AT1RI on *Acta2* induction as demonstrated in the experiment. **Figures 3.10E** and **3.10F** are *Eln* response to decreasing the weight of the JNK1/2 inhibiting *Eln* reaction to 0.5 which allowed for prediction of *Eln* in response to stiffness, stretch, and inhibition whereas before the model was not able to predict *Eln* response at all. Figures **3.10 G** and **3.10 H** are model predictions of *Loxl1* in relation to decreasing the weight of the miR130/301 reaction by 5%, this allows the model to better capture the lack of *Loxl1* response to inhibition of AT1R and TGFβR that is predicted by experiments. **Figures 3.10 I** and **3.10 J** are *Fn1* in response to adding the Piezo1 and STAT3 pathways, which allows for *Fn1* to still be induced while AT1R and TGFβR are inhibited where before the *Fn1* gene in the model was only regulated by AT1R and TGFβR. Alternate pathways allow for the model to better predict *Fn1* induction by stretch and stiffness.

Based on observations of differences between the *in-vitro* experiments and model predictions, modifications were made to the model to generate new hypotheses. The model was used to investigate possible mechanisms of differential regulation of *Col1a1* and *Col3a1* signaling in response to TGFβRI. Assuming that ET1 and PPARγ signaling are both required upstream of

*Col1a1* better recapitulated the observed inhibition of *Col1a1* expression by TGFβRI without affecting *Col3a1* expression (data is not shown as it matches the **Fig. 3.9** *Col3a1* response to TGFβRI). In human PAECs both ET1 and PPARγ signaling were required for response to hypoxia, and Kang *et al.* [181] reported that this was mediated by miR-27a reduction of the expression of PPARγ and increase in ET1 protein levels. In response to AT1R block, both *Col1a1* and *Col3a1* signaling were significantly more inhibited in the experiment than in the model, suggesting that smad2/3 and YAP/TAZ may both be required for angiotensin mediated induction of these genes during in induction by increased stiffness and stretch. smad3 and YAP/TAZ have been reported to act as transcriptional co-factors in the mouse lung endothelial cell endothelial-to-mesenchymal transition process mentioned in **Chapter 1** as mediated by TGFβ signaling [182]. Based on experimental data, TGFβ and AngII were necessary for stiffness and stretch induction of *Col1a1* expression, while only AngII was necessary for *Col3a1* since AT1R blockade was sufficient to block *Col3a1* response to stiffness and stretch.

Block of TGFβR and AT1R receptors highly inhibited *Acta2* expression in response to stretch and stiffness but the model only predicted a slight decrease (**Fig. 3.9**). Modifying the model to change the OR reactions of PKCα and p38 to PKCα AND p38 improved the model agreement with observations as shown in panel 4 (**Fig. 3.10**).

*Fn1* was, on the other hand, not upregulated enough in the model. Comparison between experimental and modeling data revealed an angiotensin-independent stretch-activated pathway that was not explained by the model, so we modified the model to add regulation of *Fn1* via stretch activating integrins which activate c-Src which then activate signal transducer and transcription factor 3 (STAT3) which then increases active TGFβ expression outside of the membrane, that then induces *Fn1* via smad2/3 as reported in renal epithelial cells [183]. In response to TGFβR block,

*Fn1* expression induction by stiffness and stretch still occurs. To test whether the stiffness activated Piezo1 pathway that increases *Fn1* expression as observed in cardiac fibroblasts by Braidotti *et al.* [184] may explain this discrepancy, the model was modified to include Piezo1 *Fn1* induction via calcium signaling and PKCα and the predictions showed better agreement with experimental results (**Fig. 3.10**).

*Loxl1* is not activated without stiffness or stretch in the model as it is only regulated by one pathway, stiffness or stretch activating the Hippo pathway which upregulates the transcription factor YAP/TAZ. In the model, decreasing the weight of miR130/301 inhibiting PPARγ from 1 to 0.95 allows us to predict levels of *Loxl1* even at 0.5 kPa without stretch with and without inhibition to a level that follows closely to experimental data.

*Eln* expression was not able to be predicted by the model as neither stretch nor stiffness were activated enough to match experimental results where both stretch and stiffness significantly increased *Eln* expression in experiments. In the model, *Eln* is regulated by TGFβ via smad2/3 signaling, hypoxia via ROS and JNK1/2 inhibiting *Eln* and stretch via TRP. Reducing the weight of the hypoxia to JNK1/2 inhibition of *Eln* allows for correct prediction of inhibition results and prediction of stiffness and stretch effects.

Important pathways in the model needed to explain much of the profibrotic upregulation in the six genes examined: *Col1a1, Col3a1, Acta2, Fn1, Loxl1,* and *Eln* were determined to be stiffness and stretch upregulating TGFβ, AngII and the Hippo pathway. Another important pathway was stretch activating the TRP channel then activating PKCα. The important pathways for angiotensin II signaling were MAPK and the path through AP1 to latent TGFβ which is important for crosstalk between AngII and TGFβ. For TGFβ, induction through smad2/3 phosphorylation as well as the pathway involving TAK1 and p38 were the most crucial.

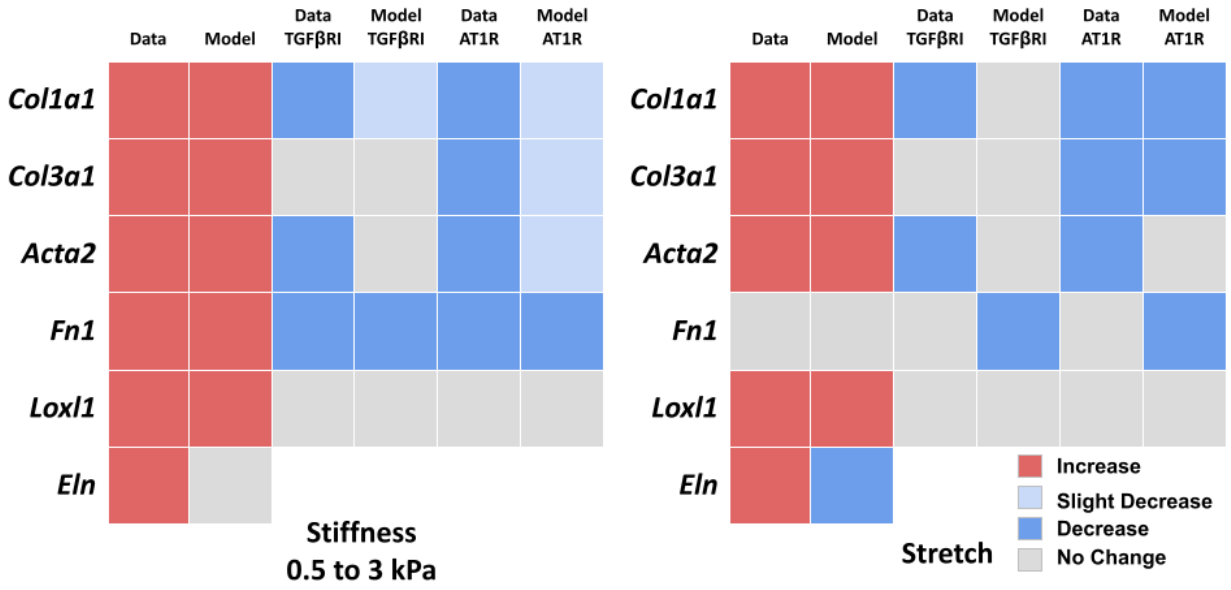


**Figure 3.11 Model predictions vs. experimental results from the inhibition of angiotensin signaling via Losartan (AT1R) and inhibition of TGFβ signaling via SB431542 (TGFβRI) in PAAFs**. Colors represent if stiffness or stretch responses were fully inhibited (blue), there was a significant model decrease over the threshold of 0.1 but the simulation response was not as fully inhibited as in the experimental data (light blue) or if the response stayed the same (grey), or if the response was increased (red). *Eln* gene expression is not included in this comparison because the model was not able to predict its increase in stiffness or response to stretch. Experimental conditions were considered significantly changed if $p < 0.05$ while model predictions used a normalized threshold of 0.1 to indicate significant change.

Through the model described in Chapter 3 and the Chapter 2 sensitivity analysis identifying the importance of AngII, TGFβ and mechanical signaling, it was determined that the pathways driving PAH were those downstream of AngII, TGFβ, and the signals of stiffness and stretch can be separated through *in-vitro* experiments. PAAFs were plated onto gels and then pre-incubated with 10 μM TGFβR inhibitor SB451342 or 1 M AT1R inhibitor losartan as described in Section 4.1.2.5 and then isolated for RT-PCR. Model simulations of inhibition were run for each condition by using the corresponding stiffness input ($\omega = 0.25$ for 0.5 kPa, $\omega = 0.6$ for 3 kPa) and according to the methods detailed in Section 3.1.2.7 where the $y_{max}$ of the inhibited species (AT1R or TGFβR)

were set to 0. Time scales in the model were set to match the experiment of first 72 hours of the corresponding stiffness, then 24 hours of no stretch or stretch ($\omega$ = 0.7 for the stretch input) and inhibition or no inhibition. **Fig. 3.11** displays an "increase" in red if the inhibited condition is higher than the non-inhibited control in response to stiffness or stretch, "no change" if there is no significant difference ($p > 0.05$) or the difference in model prediction is < 0.1, "slight decrease" if the difference in model prediction is ≥ 0.1 but the response was not fully blocked, and "decrease" if the inhibition attenuated the gene response to stiffness or stretch. The model was able to predict 70% of the inhibition results without any modifications.

### 3.1.4 Discussion

*In-vitro* experiments in PAAFs were used to investigate the differential effects of equibiaxial stretch and increased substrate stiffness on six genes of a new mathematical model of PAAF cell signaling [54]. While both physical stimuli occur in PAH, these stimuli may occur at different stages of the disease, in part because increased vascular fibrosis leads to ECM stiffening that in turn opposes the increase in arterial wall strain caused by increased wall stress. In this study, we used a novel combination of *in-vitro* and *in-silico* models to investigate how PAAFs respond to changes in ECM stiffness and strains representative of those associated with adventitial remodeling in PAH. While PAAFs are exposed to cyclic loading *in-vivo*, we used static stretch as a model of the strain increase from the mean pulmonary arterial pressure increase [63] during PAH rather than fluctuations in the cardiac cycle [63, 163]. Although there are no existing studies examining how PAAFs respond to cyclic stretch, Wu *et al*. [102] reported that 10% cyclic stretch for 36 h led to 2- to 3-fold increases in *Col1a1* and *Col3a1* expression in mouse aortic fibroblasts, which are comparable to the 3-fold increase in *Col1a1* and 2- to 4-fold increase in *Col3a1* that we

observed after 24 h of static stretch [164]. While the cells were maintained at a 10% static stretch for 24 h, measurements of cell area in cardiac fibroblasts using the same circular custom stretchers showed that after cell area initially increased during static stretch, they returned to their original size within 1 h, well before the 24-h time point at which gene expression was measured [63].

#### 3.1.4.1 Stiffness and Stretch Differentially Affect Expression of Six Profibrotic Genes

Stretch and increased substrate stiffness were both able to upregulate five out of the six profibrotic genes we investigated. However, while increasing stiffness from 0.5 kPa significantly induced all six genes, fibronectin expression was transiently upregulated by stretch at 4 h but was not significantly altered by stretch at 24 h. There was also a non-monotonic response to the two levels of increased substrate stiffness in the expression of *Loxl1* and *Acta2*, which were both upregulated compared with 0.5 kPa substrates on 3 kPa matrices (mimicking vessel stiffness walls during mild PAH), but the expression of both was not significantly altered compared with 0.5 kPa substrates on 10 kPa matrices (which are comparable to vessel stiffness walls in severe PAH). Unlike observations in cardiac fibroblasts [63], we found no statistical interaction effects between the stretch and stiffness conditions in these six genes. These results suggest that the expression of *Col1a1*, *Col3a1*, and *Eln* could be expected to rise early *in-vivo* as elevated pulmonary arterial pressure increases vascular wall strain and remain elevated as fibrosis increases adventitial ECM stiffness, even though this stiffening would also reduce arterial strain. In contrast, *Loxl1* and *Acta2* expression may initially rise but eventually return to baseline as wall stiffening becomes severe, and *Fn1* mRNA may be induced only after the ECM has remodeled and stiffened.

### 3.1.4.2 Model Modifications to Investigate Differential Regulation by Stretch and Stiffness

By allowing stiffness and stretch to be separate inputs to the model, we investigated the pathways regulating the expression of six mechanosensitive genes (*Col1a1, Col3a1, Eln, Fn1, Loxl1, Acta2*) in response to each stimulus. While there is published evidence that TGF-β is activated by stretch in cardiac [63] and lung [165] fibroblasts, we only found experimental evidence of TGF-β activation by substrate stiffness in PAAFs [148, 149]. Based on ample published data in other cell types, we refined the model of the MAPK signaling cascade in the original version of our model so that ERK1/2, p38, and JNK1/2 could be independently activated, and we updated the model to include the effects of stretch activated TRP channels observed by Yue and Suzuma *et al*. [160, 161].

Comparing the predictions of this revised model against the same independent experimental data from rat and human PAAFs that we used to test our original implementation [54], we found no significant changes in model validation accuracy from what we reported previously [54]. Comparing predictions of the revised model with *in-vitro* PAAF experiments conducted here on the effects of stretch and stiffness on gene expression, the model correctly predicted the upregulation of all six ECM genes by increased stiffness though not the subsequent return to baseline levels on the stiffest matrices for *Loxl1* and Acta2. The model also correctly predicted the observed upregulation of four ECM genes and the lack of response to stretch in *Fn1* expression at 24 hrs. However, while we observed an increase in *Eln* mRNA after stretch, the model incorrectly predicted a decrease. Examining the regulation of elastin gene expression in the network, we found that halving the weight of JNK1/2 inhibition on *Eln* mRNA while leaving the activating weight of PKC on *Eln* the same reversed this result. Hence it is possible that the

activating effect of PKC dominates the inhibiting effect of JNK1/2 in the regulation of elastin gene expression by stretch.

Since we were curious if there was a transient response to stretch in some genes, we collected RNA from stretched PAAFs after 4, 8, and 24 hours. We found that *Col1a1* monotonically increases and has the highest expression at 24 hours, *Fn1* is most induced by stretch at 4 hours then returns to baseline, and the other four genes are transiently upregulated at 8 hours. This indicates that stretch may induce *Col1a1* due to stretch associated with increased pulmonary arterial pressure, causing PAAFs to deposit more matrix that leads to fibrosis and arterial stiffening. On the other hand, *Fn1* may be induced transiently by stretch, but primarily respond to longer term changes in stiffness *in-vivo*.

The equations in the model were formulated using studies from both *in-vivo* and *in-vitro* experiments. While we used the rat PAAFs to validate the gene expression in response to stimuli such as mechanical stretch or substrate stiffness, this approach allows us to predict how phenotypic outputs respond to mechanical load. It is reported that mechanical stretch may increase the stiffness of the substrate, which in turn decreases the stretch. However, the interactions between them have not yet been classified. Through this work, we can model the interactions by adjusting time parameters and the activated reactions to represent beneficial versus maladaptive remodeling in fibrosis. Furthermore, the model can simulate a high number of experimental designs and make corresponding predictions that would be difficult to reproduce experimentally. This feature also enables the model to predict effects of specific drugs through simulating the activation or inhibition of any target species in the network.

### 3.1.4.3 Blocking TGFβ Receptor and Angiotensin II Receptor Unveil New Possible Mechanisms of Regulation

We did *in-vitro* experiments to inhibit the AngII receptor AT1R and the TGFβ receptor TGFβR using losartan and SB 431542 respectively to determine the important pathways regulating induction by stiffness and stretch. Based on quantitative differences between the model and experimental inhibition data, we were able to posit many novel areas of regulation which could be responsible for these differences.

The differential responses in *Col1a1* and *Col3a1* in response to TGFβRI are consistent with the hypothesis that both ET1 and PPARγ signaling are required to induce *Col1a1* response to stretch and stiffness but either pathway may be sufficient to induce *Col3a1* in response to these stimuli. There is a known mechanism by which ET1 and PPARγ signaling are both regulated by miR-27a in PAECs found by Kang *et al* [181]. Wolf *et al.* have discovered that ET1 production decreases PPARγ signaling which impairs tube formation *in-vitro* also in PAECs [185]. While Montezano *et al.* posits that PPARγ activators may prevent ET1 dependent proinflammatory vascular effects in vascular smooth muscle cells in hypertension [186]. These papers suggest this mechanism may be well-supported, but possibly only in regulation of *Col1a1*. Currently, every pathway in the model that regulates *Col1a1* also regulates *Col3a1*, but this improvement in matching experimental data indicates this should not be the case. This suggests differential regulation of the collagens that Tang *et al.* has observed through MAPK signaling in cardiac fibroblasts, and Millar *et al.* has seen this differential effect via miR-29a in human tendon-specific fibroblasts [187, 188]. On the other hand, experimentally, AT1R inhibition exhibited a great effect on both *Col1a1* and *Col3a1* so the proposed hypothesis is that smad2/3 and YAP/TAZ may act as

co-transcriptional regulators. Savorani *et al.* have demonstrated that smad3 may combine with YAP/TAZ in the nucleus during endothelial to mesenchymal transitions in lung endothelial cells from mice in response to TGFβ signaling [182]. The ability of the model modification to improve predictions and evidence for smad3 and YAP/TAZ as transcriptional co-factors outside of PAAFs leads us to conclude this is a possible mechanism by which collagens are regulated in response to AngII signaling. Our work was able to determine that TGFβ and AngII are needed for *Col1a1* response to stretch and stiffness, but only AngII is needed for *Col3a1* response.

Inhibition of *Acta2* by TGFβRI and AT1RI revealed that p38 and PKCα could both be required for *Acta2* induction. By blocking PKCα signaling, which is not crucial to adaptive fibrosis, we could then reduce the fibroblast to myofibroblast transition as the induction of *Acta2* leads to this phenotypic change [63]. Evidence for p38 and PKCα both being activated by the same receptor for advanced glycation end products in response to angiotensin signaling has been shown in human umbilical vein endothelial cells [189]. We have concluded that both TGFβ and AngII are needed for *Acta2* response to stretch and stiffness.

*Fn1* inhibition reveals possible regulation by STAT3 and Piezo1 pathways not yet implicated in PAAFs but there is evidence in literature of the STAT3 pathway in renal epithelial cells [183] and Piezo1 induction of fibronectin in cardiac fibroblasts via calcium signaling and PKCα [184]. AngII is responsible for the stiffness response in *Fn1* Since *Fn1* is primarily induced by stiffness, we have accurately identified these important regulators but the transient induction of *Fn1* by stretch through AngII independent pathways would need to be targeted to reduce fibrotic fibronectin deposition due to stretch induction [53]. Since PKCα signaling may be important in both *Fn1* induction by TGFβ signaling in stiffness and in *Acta2* induction by TGFβ and AngII signaling in response to stiffness and stretch, PKCα signaling could be a novel target to target to

reduce *Fn1* ECM deposition and fibroblast to myofibroblast transitions that lead to excess ECM deposition. Since PKC isoforms have been implicated in regulating AngII-mediated fibrosis through p38 in RV fibrosis in pulmonary hypertension, targeting PKC could potentially reduce fibrosis in both the PA and the RV [190].

Differences in induction of *Loxl1* also led us to conclude that miR130/301 could be an important regulator of *Loxl1* expression and increasing the weight of TGFβ and stretch regulation on *Eln* allows for significantly improved model predictions in response to stretch, stiffness and inhibition though neither *Loxl1* nor *Eln* require TGFβ or AngII for stretch and stiffness response [11, 163]. This use of the model to compare against *in-vitro* data and propose mechanisms and pathways not previously implicated in PAAFs is a useful tool to discover which pathways are necessary to upregulate the profibrotic genes we are studying, and which mechanical signals are responsible for this upregulation. *Col1a1, Col3a1,* and *Acta2* are all induced by at least AngII in stretch and stiffness, while *Fn1* is induced by AngII in stiffness alone, and the genes *Loxl1* and *Eln* are not regulated by AngII or TGFβ. By identifying the importance of AngII and TGFβ cytokines, we can hypothesize targets to reverse PAH fibrosis through inhibiting nodes downstream of these pathways such as MAPK or smad2/3 signaling, or introducing PPARγ agonists, since the inhibition of PPARγ induces *Col1a1* expression in response to stretch and stiffness, which have been proposed as a vasodilator treatment of PAH [191].

#### 3.1.4.4 Limitations

We used rat PAAFs because of the detailed biomechanical measurements of ECM stiffness pulmonary arterial strain in the sugen-hypoxia rat model of PAH and normotensive control rats. However, human PAAF cell lines have been used to study fibrotic signaling in response to

increased ECM stiffness [11], where they showed that ten out of twelve genes studied were differentially expressed when stiffness increased from 1 to 12 kPa. Their analysis identified an miR-130/301-PPARγ signaling network regulated by ECM stiffness and associated with ECM remodeling in human PAH. Studies of mechanosignaling in human PAAF cell lines would enable us to generate a similar model of profibrotic mechanosignaling in human cells that could include these networks. ECM remodeling depends on protein synthesis, post-translational modifications, and cell-mediated matrix assembly [13]. One limitation of this study is that we focused primarily on gene expression, but we did find that changes in collagen III and smooth muscle actin protein abundances in response to increased ECM stiffness were consistent with changes in their mRNA expression. Finally, while the model was able to predict many TGFβR and AT1R inhibition results, it was not able to predict many profibrotic gene responses to stretch. These model limitations can nevertheless be used to identify candidate pathways and reactions that need to be added to the network.

### 3.1.5 Conclusions

*In-vitro* experiments using hydrogel substrates of various stiffnesses coating elastic membranes in cell-stretch devices showed that expression of profibrotic genes by PAAFs is differentially regulated by cell stretch and extracellular matrix stiffness. No interaction effects between stretch and stiffness were observed for the six genes studied here; however, the blockade of TGFβR and AT1R did reveal possible mechanisms upstream of stiffness and stretch regulation and the need for inclusion of pathways not previously implicated in PAAFs. A novel combination of *in-vitro* and *in-silico* models of PAAF profibrotic cell signaling in response to altered mechanical

conditions has helped to identify regulators of the vascular adventitial remodeling that results from the changes in stretch and matrix stiffness occurring during the progression of PAH.

**Acknowledgements**

Chapter 3, in part, is a reprint of the materials as it appears in the following publications: Cells 2021. Wang, Ariel; Cao, Shulin; Stowe Jennifer C.; Valdez-Jasso Daniela. The thesis author was the primary investigator and author of this paper.

# CHAPTER 4: SEX DIFFERENCES IN MECHANOREGULATION IN PAAFS INDUCE SIGNIFICANT DIFFERENCES IN REMODELING AT THE TISSUE LEVEL

## 4.1 Abstract

Pulmonary arterial hypertension results in changes in arterial wall stiffness and strain due to increased mean pulmonary arterial pressure that results in vascular remodeling. The incidence of PAH is much higher in women, but women do better with treatment and are less likely to die from the disease. We have demonstrated significant upregulation of six profibrotic genes (*Col1a1, Col3a1, Acta2, Fn1, Loxl1,* and *Eln*) in pulmonary arteries isolated from male rat models of PAH compared to normotensive male PAs, that is not observed in PAs from female or ovariectomized rats.

Having examined the variables of stretch and stiffness, we wanted to know if differences at the cellular level were responsible for the sex differences in the PA tissue. Studying PAAFs from female rats demonstrated that female-derived PAAFs have a higher threshold to effects of stiffness and less sensitivity to stretch than male-derived cells, a possible explanation for female PAH patients not doing as poorly as male patients in response to mild PAH. Cells from ovariectomized rats also had less sensitivity to stretch but were activated even at lower stiffnesses representing normotensive and mild PAH. This demonstrates that sex differences already exist in mechanoregulation at the cellular level, an important finding that may point towards mechanisms leading to why male patient outcomes are so much worse.

### 4.1.1 Remodeling Process of the PA Vasculature in PAH and Sex Differences

As we mentioned in Chapter 1, there are significant sex differences in PAH. There is evidence that sex chromosomes themselves may modify sexual dimorphism in pulmonary arterial hypertension rather than just the contribution of sex hormones, positing foundational differences may result in inherent genetic differences [192]. The role of sex hormones in decreased arterial stiffness in women compared to increased arterial stiffness in males has been examined by Dupont *et al.* [193]. The removal of ovaries, or ovariectomy, in rats can somewhat elucidate the effect of having less sex hormones while still isolating cells from biologically female animals [194]. These differences indicate a need to study the sex differences in profibrotic induction of the pulmonary artery *in-vivo* to determine if sex was an independent predictor of outcome in the sugen-hypoxia rat model of PAH as well.

Experiments we have done using sugen-hypoxia rats have demonstrated that, although mPAPs are still significantly increased by sugen-hypoxia treatment in all groups, female rat mPAP is significantly lower than that of male or ovariectomized rats, and studies by Rafikova *et al*. have shown increased fibrosis in male rat PAs with no significant increased fibrosis in female rat PAs [179]. Treatment of sugen-hypoxia rats with exogenous estrogen also reduced PA vasoconstriction and remodeling as demonstrated by Phillip *et al* [195]. This sexual dimorphism in the sugen-hypoxia model of PAH makes it a useful tool to study what is causing this difference in profibrotic response and ultimately increased fibrosis in male rat PAs [196]. Because of this, we hypothesize that PAs from male rats will have significantly increased profibrotic induction in response to sugen-hypoxia treatment compared to PAs from female and ovariectomized rats. Since PAAFs are the cells in the adventitial layer of PAs primarily responsible for mechanosignaling in response to vascular wall stiffening and stretch due to changes in mPAP, we speculate that they could play a

role in this increased fibrosis and vascular remodeling in male rats compared to female rats [43]. What is unknown is if differences in PA stretch and stiffening between sugen-hypoxia male and female rats can explain differences in PA remodeling or if the differences are a result of PAAF response to stretch and stiffness differing between PAAFs from male and female rats.

While studies by Aguado *et al*. have shown that sex differences in left ventricular cardiac fibroblasts are crucial to sexual dimorphism in cardiac disease outcome, no study exists addressing sex differences in PAAFs [180]. Our hypothesis is that since PAAFs respond to changes in wall strain in the pulmonary artery because of increased mean pulmonary arterial pressure, PAAFs derived from male rats will exhibit more profibrotic gene induction in response to stretch.

We believe that the significant difference in magnitude of mPAP between sugen-hypoxia male rats and sugen-hypoxia female rats, which induces stretch on PAs, alone is not enough to explain the significantly increased fibrosis in male rat PAs. Do sex differences in PAAF mechanosignaling explain this difference in PA fibrosis? Could this be due to differences in male versus female PAAF cells by themselves, or could this be due to differences in male and female PAAF induction by stretch?

### 4.1.2 Materials and Methods

#### 4.1.2.1 PAAF Stretch and Stiffness

Cells are isolated according to the same procedure as in Section 3.1.2.1, PAAF isolation from female and ovariectomized Sprague-Dawley normotensive rats follows the same protocol as the isolation from male Sprague-Dawley rats. For the sex difference data, 100-150,000 female-derived

and ovariectomized female-derived PAAFs were seeded onto equibiaxial stretchers with gels at 0.5, 3 and 10 kPa stiffnesses and subjected to stretch for 24 hours

#### 4.1.2.2 Ovariectomization

Ovariectomization of rats are done at Charles River Lab, Wilmington, MA. Ovaries are removed from five-week-old female Sprague-Dawley rats weighing 140-170 grams and shipped UC San Diego. After a week of recovery, the animals are randomized into different treatment groups.

#### 4.1.2.3 Sugen-Hypoxia (SuHx) Rat Model of PAH

The sugen-hypoxia (SuHx) rat model of PAH was used because combining the vascular endothelial growth factor (VEGF) receptor antagonist Sugen 5416 and hypoxia, one can prevent vascular remodeling and adaptation via small vessel angiogenesis of the pulmonary vasculature when exposed to low levels of oxygen. Hence, when the rats return to normoxia, the vessels do not adapt and the animals develop similar lesions found in human PAH patients. This is the most specific and localized model of PAH as it develops vascular lesions resembling those found during autopsy in patients with PAH [18]. Animal care, housing, and food were approved by the Institutional Animal Care and Use Committees at the University of California San Diego. The inducement of PAH occurs via a single subcutaneous injection (20 mg/kg) of sugen (S8442 MilliporeSigma, CAS Number 204005-46-9, PubChem Substance ID 24278606 Sigma-Aldrich, MO) followed by exposure to chronic hypoxia (10% O2) for three weeks, then a return to normoxia for up to 10 weeks post-injection (**Fig. 4.1**). The disease phenotype is verified by measuring the mean pulmonary arterial pressure invasively with catheter (>20 mmHg). Age-matched normotensive control rats are kept in normoxia throughout the duration of the study.

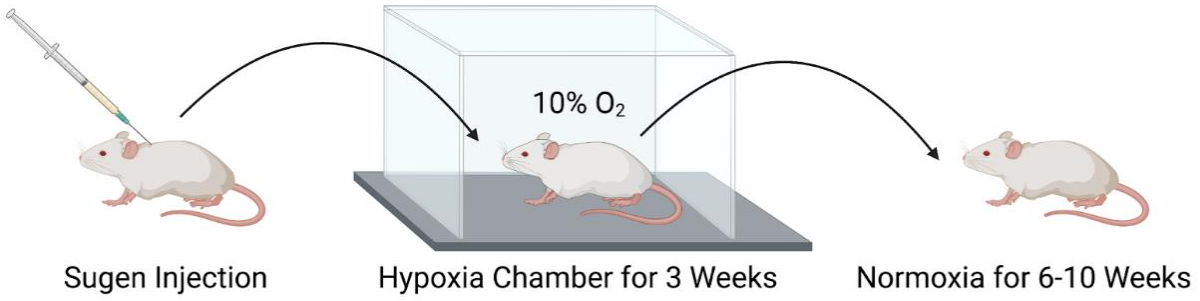


**Figure 4.1: Schematic of inducing PAH in rats with Sugen-Hypoxia (SuHx)**. Timeline of the sugen-hypoxia animal model, which after a single injection of sugen, the animals are kept for three weeks in a hypoxic chamber, and then kept in normoxia for 6-10 weeks. Control groups are aged-matched and kept for the same duration in normoxia. Figure created using Biorender.com

#### 4.1.2.4 Homogenization of Tissue

Pulmonary arteries were isolated as described in Chapter 3 Methods Section 3.1.2.1. BeadBug Microtube Homogenizer (Benchmark Scientific #D1030 Sayreville, NJ, USA), 3.0 mm High Impact Zirconium beads TriplePure M-Bio Grade (Benchmark Scientific, Sayreville, NJ, USA) at 1800 rpm for 3-6 minutes until sections of pulmonary artery tissue and right ventricle chunks were visually confirmed to be broken down in TRIzol by Invitrogen (#15596026, Thermo Fisher Scientific, Waltham, MA, USA). The sugen-hypoxia procedure is as described in Section 4.1.2.3 for rats from which pulmonary artery tissue was taken. Pulmonary artery tissues from (n=3) normotensive male rats, (n=6) normotensive female rats, (n=7) normotensive ovariectomized rats, (n=10) male SuHx rats, (n=10) female SuHx rats, and (n=9) ovariectomized SuHx rats were homogenized and processed via the RNA isolation methods described in Section 3.1.2.4. The relative expression of six profibrotic genes (*Col1a1, Col3a1, Acta2, Fn1, Eln, Loxl1*) were analyzed for each pulmonary artery tissue type and analyzed using RT-PCR as described in Section 3.1.2.4.

#### 4.1.2.5 Statistics

Descriptive statistics were performed using JMP Pro Statistical software (version 14, SAS Institute Inc., NC, USA) for group comparisons of relative gene expression. For normally distributed data, one-way analysis of variance (ANOVA) was used to test for differences in means of three different stiffnesses and for all six genes, followed by the Dunnett's *post-hoc* test. Otherwise, the non-parametric Wilcoxon–Kruskal–Wallis statistic was used followed by Dunnett's *post-hoc* test. Effects of stiffness and stretch were tested using two-way ANOVA with stiffness and stretch as fixed factors. For normally distributed data, the Dunnett's *post-hoc* test was used. Otherwise, the non-parametric Wilcoxon–Kruskal–Wallis statistic was used followed by Dunnett's *post-hoc* test. Data are expressed as means ± standard error of the mean relative to housekeeping gene 18S, unless otherwise specified. Statistical significance was determined at a level of 0.05. Data were graphed in GraphPad Prism software (v8.4.3.686, San Diego, CA, USA).

### 4.1.3 Results

#### 4.1.3.1 Profibrotic Gene Expressions Measured at the Tissue Level

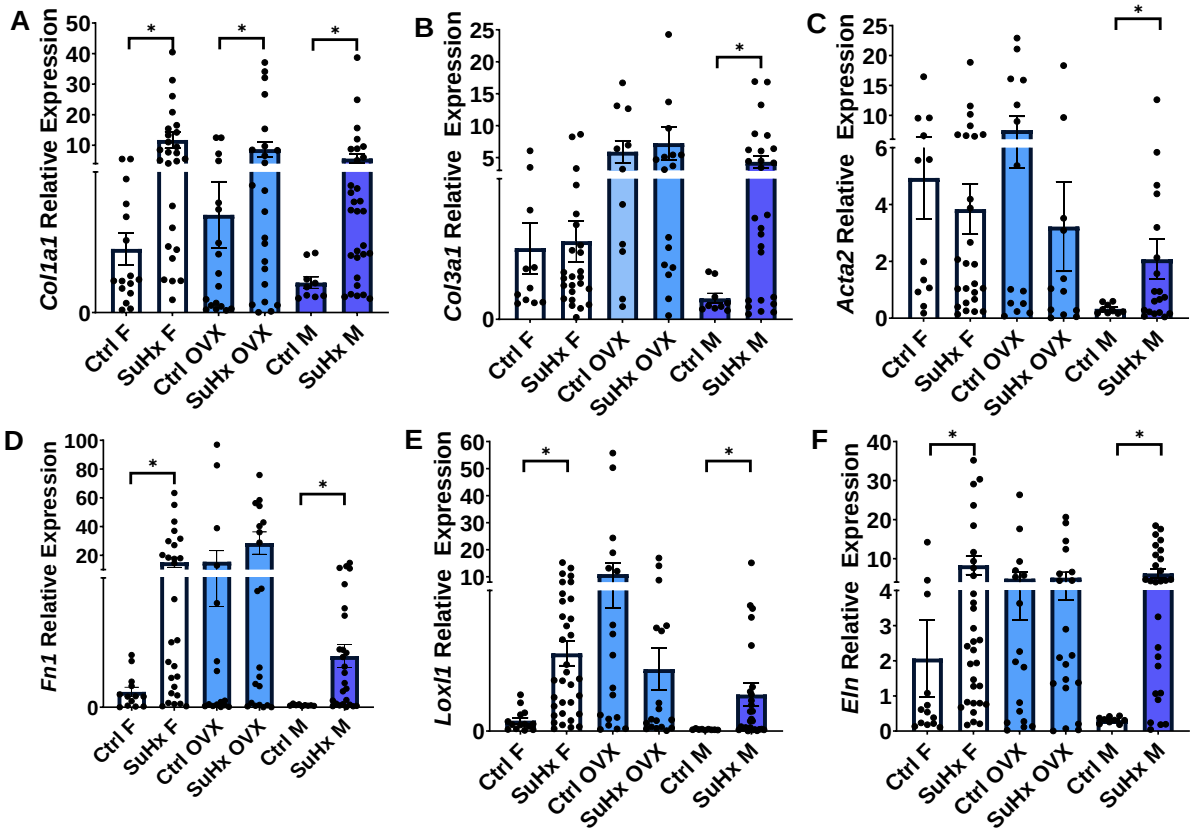


**Figure 4.2: Combined pulmonary artery tissue data separated by sex and SuHx treatment**. Pulmonary artery tissues from (n=3) normotensive male rats, (n=6) normotensive female rats, (n=7) normotensive ovariectomized rats, (n=10) male SuHx rats, (n=10) female SuHx rats, and (n=9) ovariectomized SuHx rats are homogenized and RNA from isolated tissue is analyzed with RT-PCR. Mean ± standard errors of the mean of mRNA levels relative to housekeeping gene 18S with white bars for female data, light blue bars for ovariectomized data and dark blue bars for male data. * indicates significance between control and SuHx conditions by two-way ANOVA and *post-hoc* Tukey test for female, ovariectomized, and male rats. Significant induction by SuHx in all six genes: (**A**) *Col1a1* (**B**) *Col3a1* (**C**) *Acta2* (**D**) *Fn1* (**E**) *Loxl1* and (**F**) *Eln* is observed in male rats, while significant induction in fewer genes by SuHx (*Col1a1, Fn1, Loxl1,* and *Eln*) is observed in female rats, and only significant induction by SuHx in *Col1a1* in ovariectomized rats is observed. This suggests more profibrotic genes are upregulated in male rats than female rats, while a higher baseline expression of genes at control is observed in ovariectomized rats.

Pulmonary artery tissues were isolated from rats that underwent sugen-hypoxia treatment as described in Section 4.1.2.3 and were then homogenized as described in Section 4.1.2.4. Pulmonary artery tissue from male rats shows significant upregulation by sugen-hypoxia treatment for all six genes, tissue from female rats shows significant upregulation in *Col1a1, Fn1, Loxl1,* and

*Eln*, and tissue from ovariectomized females displays a significant upregulation only in *Col1a1* and a generally higher relative expression of the six genes at baseline when taken from normotensive rats that did not undergo sugen-hypoxia treatment (**Fig. 4.2**)

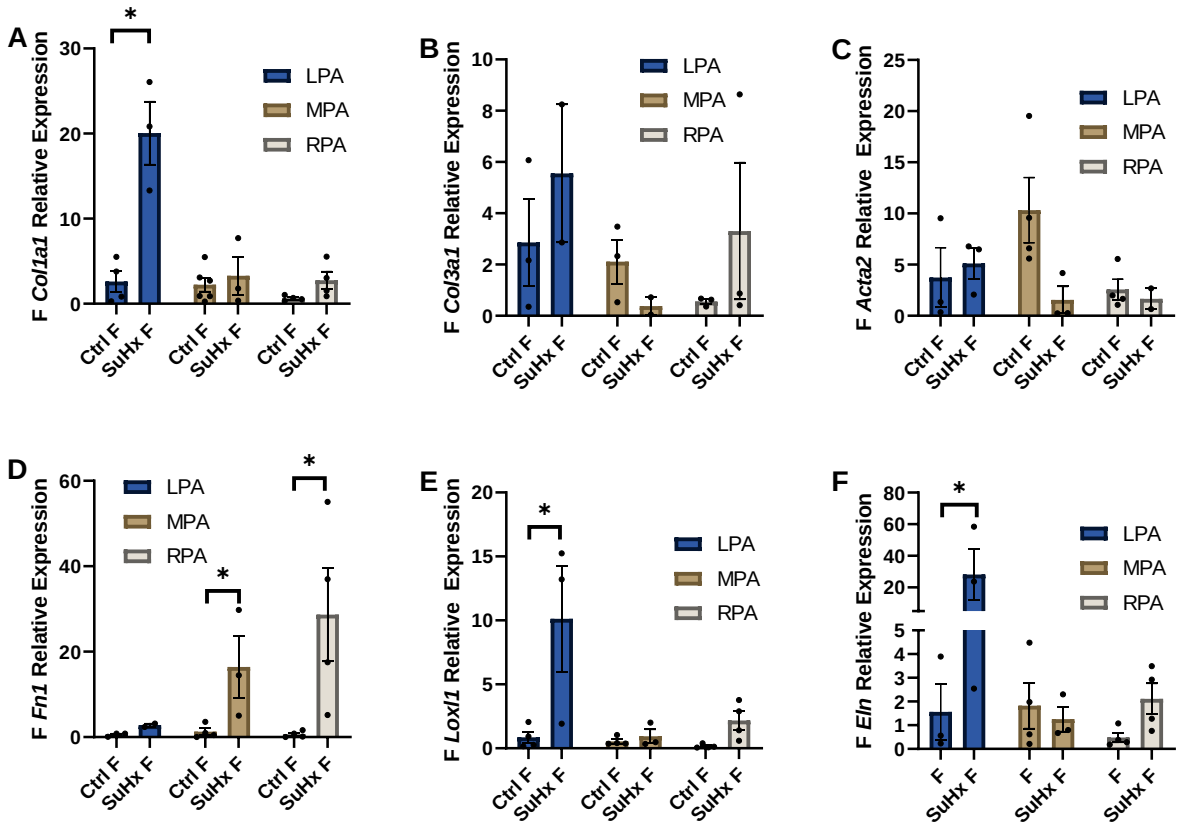


**Figure 4.3: Gene expression of pulmonary arterial sections clustered into sex and treatment**. Messenger RNA relative expression derived tissue from the main, left and right pulmonary artery (MPA, LPA, RPA) from normotensive male (n=3), female (n=6), and ovariectomized rats (n=7) were compared with relative expression of PA tissue from male (n=10), female (n=10), and ovariectomized (n=9) SuHx rats. Across sexes, there was a more significant effect of SuHx treatment in increasing the induction of profibrotic genes in the LPA and RPA as opposed to the MPA. There was significant induction of profibrotic genes in sections of pulmonary artery from male rats (**M-R**) in all six genes (*Col1a1, Col3a1, Acta2, Fn1, Loxl1, Eln*), and in 4 genes (*Col1a1, Fn1, Loxl1, Eln*) in pulmonary artery sections from female rats (**A-F**) and 2 genes (*Col1a1, Fn1*) in ovariectomized rats (**G-L**). Ovariectomized rat MPA sections demonstrated a high baseline expression of *Acta2* and *Loxl1* in the control rats and a significantly lower expression in SuHx ovariectomized rats. Statistical analysis done by two-way ANOVA and a *post-hoc* Tukey test. Mean ± standard errors of the mean of mRNA levels relative to housekeeping gene 18S with blue bars for left pulmonary artery data, gold bars for main pulmonary artery data, and white bars for right pulmonary artery data.

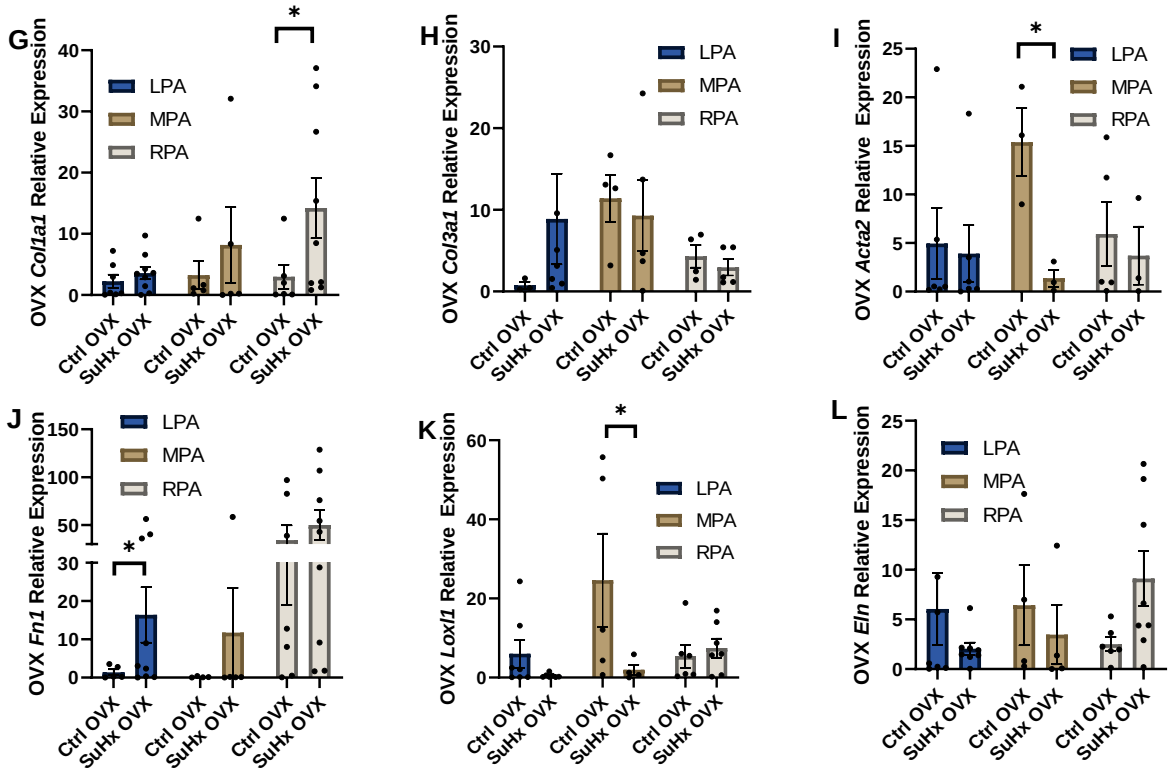


**Figure 4.3: Gene expression of pulmonary arterial sections clustered into sex and treatment**. Messenger RNA relative expression derived tissue from the main, left and right pulmonary artery (MPA, LPA, RPA) from normotensive male (n=3), female (n=6), and ovariectomized rats (n=7) were compared with relative expression of PA tissue from male (n=10), female (n=10), and ovariectomized (n=9) SuHx rats. Across sexes, there was a more significant effect of SuHx treatment in increasing the induction of profibrotic genes in the LPA and RPA as opposed to the MPA. There was significant induction of profibrotic genes in sections of pulmonary artery from male rats (**M-R**) in all six genes (*Col1a1, Col3a1, Acta2, Fn1, Loxl1, Eln*), and in 4 genes (*Col1a1, Fn1, Loxl1, Eln*) in pulmonary artery sections from female rats (**A-F**) and 2 genes (*Col1a1, Fn1*) in ovariectomized rats (**G-L**). Ovariectomized rat MPA sections demonstrated a high baseline expression of *Acta2* and *Loxl1* in the control rats and a significantly lower expression in SuHx ovariectomized rats. Statistical analysis done by two-way ANOVA and a *post-hoc* Tukey test. Mean ± standard errors of the mean of mRNA levels relative to housekeeping gene 18S with blue bars for left pulmonary artery data, gold bars for main pulmonary artery data, and white bars for right pulmonary artery data.

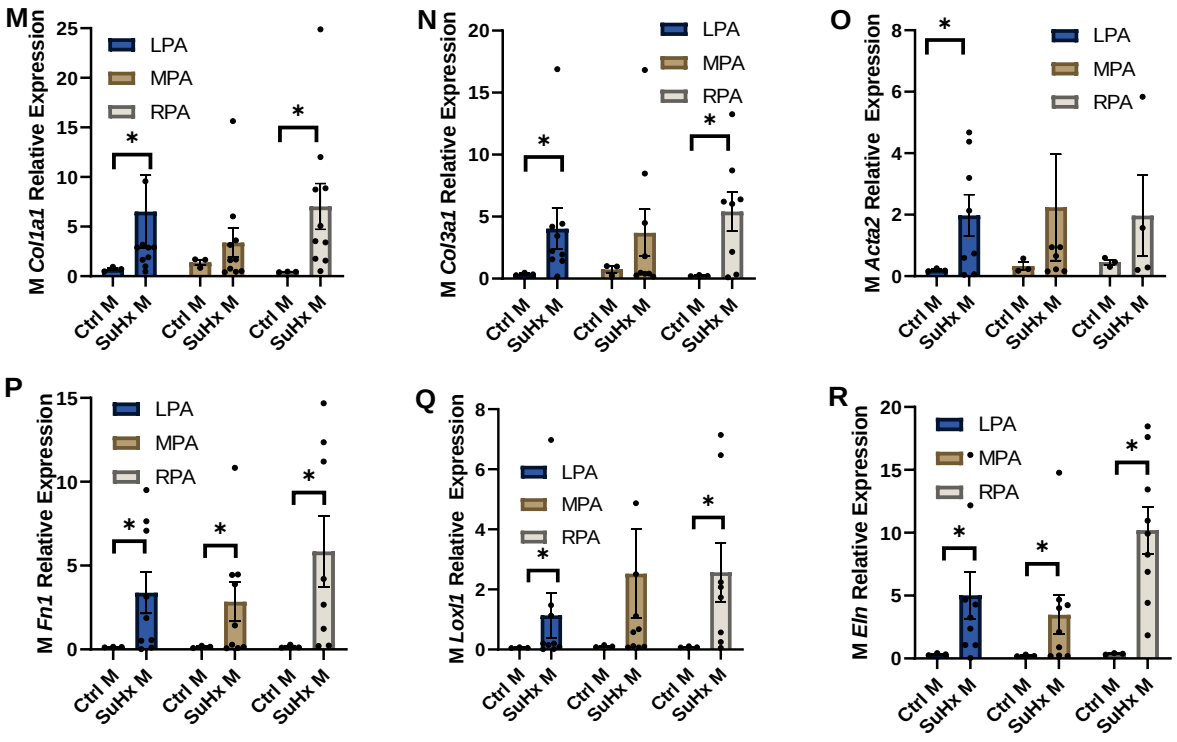


**Figure 4.3: Gene expression of pulmonary arterial sections clustered into sex and treatment**. Messenger RNA relative expression derived tissue from the main, left and right pulmonary artery (MPA, LPA, RPA) from normotensive male (n=3), female (n=6), and ovariectomized rats (n=7) were compared with relative expression of PA tissue from male (n=10), female (n=10), and ovariectomized (n=9) SuHx rats. Across sexes, there was a more significant effect of SuHx treatment in increasing the induction of profibrotic genes in the LPA and RPA as opposed to the MPA. There was significant induction of profibrotic genes in sections of pulmonary artery from male rats (**M-R**) in all six genes (*Col1a1, Col3a1, Acta2, Fn1, Loxl1, Eln*), and in 4 genes (*Col1a1, Fn1, Loxl1, Eln*) in pulmonary artery sections from female rats (**A-F**) and 2 genes (*Col1a1, Fn1*) in ovariectomized rats (**G-L**). Ovariectomized rat MPA sections demonstrated a high baseline expression of *Acta2* and *Loxl1* in the control rats and a significantly lower expression in SuHx ovariectomized rats. Statistical analysis done by two-way ANOVA and a *post-hoc* Tukey test. Mean ± standard errors of the mean of mRNA levels relative to housekeeping gene 18S with blue bars for left pulmonary artery data, gold bars for main pulmonary artery data, and white bars for right pulmonary artery data.

Pulmonary artery tissue data is separated by sex and pulmonary arterial segments: left pulmonary artery (LPA), main pulmonary artery (MPA) and right pulmonary artery (RPA). These trends show that the MPA generally has a lower relative expression in the six genes, except for the pulmonary arteries derived from ovariectomized control and sugen-hypoxia treated animals (**Fig.**

**4.3**). The left and right pulmonary artery sections show similar trends for increase by SuHx treatment, though overall as seen in the combined pulmonary artery tissue data, arteries from male animals are more induced in the left and right pulmonary arteries than ovariectomized and female rats. Significant induction by SuHx is demonstrated in all six genes in the pulmonary artery sections from male rats compared to only four genes in the pulmonary artery sections in female rats (*Col1a1, Fn1, Loxl1, Eln*) in pulmonary artery sections from female rats and two genes (*Col1a1, Fn1*) in ovariectomized rats. The MPA in control ovariectomized rats have higher *Loxl1* and *Acta2* expression than the MPAs in SuHx ovariectomized rats, demonstrating higher baseline gene expression in control ovariectomized rat PA tissue.

#### 4.1.3.2 Sex Differences in PAAFs

PAAFs derived from male rats are significantly upregulated by stiffness and stretch in all six (targeted) genes except for *Fn1*, while PAAFs from female rats are upregulated by only stiffness in all six genes except for *Acta2* which is regulated only by stretch (**Fig. 4.4**). PAAFs derived from ovariectomized animals are significantly upregulated by stiffness in *Col1a1* and *Eln*, and by stretch for *Acta2* but not any of the other genes. PAAFs from female rats show a higher stiffness induction threshold before upregulation of relative gene expression for all profibrotic genes, only significantly increasing under stiffnesses representing severe PAH. PAAFs from ovariectomized female rats, on the other hand, already show a higher relative expression than ones from male and female rats even at stiffnesses representing normotensive and mild PAH conditions in genes *Fn1*, *Loxl1* and *Eln*.

**Figure 4.4: Effect of stiffness and stretch on gene expression in PAAFs derived from male rats (blue), ovariectomized rats (red) and female rats (green).** Mean ± standard errors of the mean of mRNA levels relative to housekeeping gene 18S in unstretched cells (striped bars) and after 24 h 10% equibiaxial stretch (solid bars). No interaction effects were found between stretch and stiffness for either male, ovariectomized, or female derived cells. Unstretched male (n=9), stretched male (n=12), unstretched female (n=7), stretched female (n=6), unstretched ovariectomized (n=8), stretched ovariectomized (n=9). (**A**) *Col1a1* (**B**) *Col3a1* (**C**) *Acta2* (**D**) *Fn1* (**E**) *Loxl1* and (**F**) *Eln.* Annotations of significance in blue refer to male data, in green refer to female data, and in red refer to ovariectomized data as to whether cells are significantly affected by stiffness or *stretch* via 2-way ANOVA and *post-hoc* Dunnett's multiple comparisons test. PAAFs derived from male rats are significantly upregulated by stiffness and stretch in all six genes except for *Fn1* which is only upregulated by stiffness, while PAAFs from female rats are upregulated by only stiffness in all six genes except for *Acta2* which is regulated only by stretch. PAAFs derived from ovariectomized animals are significantly upregulated by stiffness in *Col1a1* and *Eln*, and by stretch for *Acta2* but not any of the other genes. PAAFs from female rats have a higher threshold before upregulation of relative gene expression due to stiffness for all profibrotic genes, only significantly increasing when subjected to 10 kPa stiffnesses representing severe PAH.

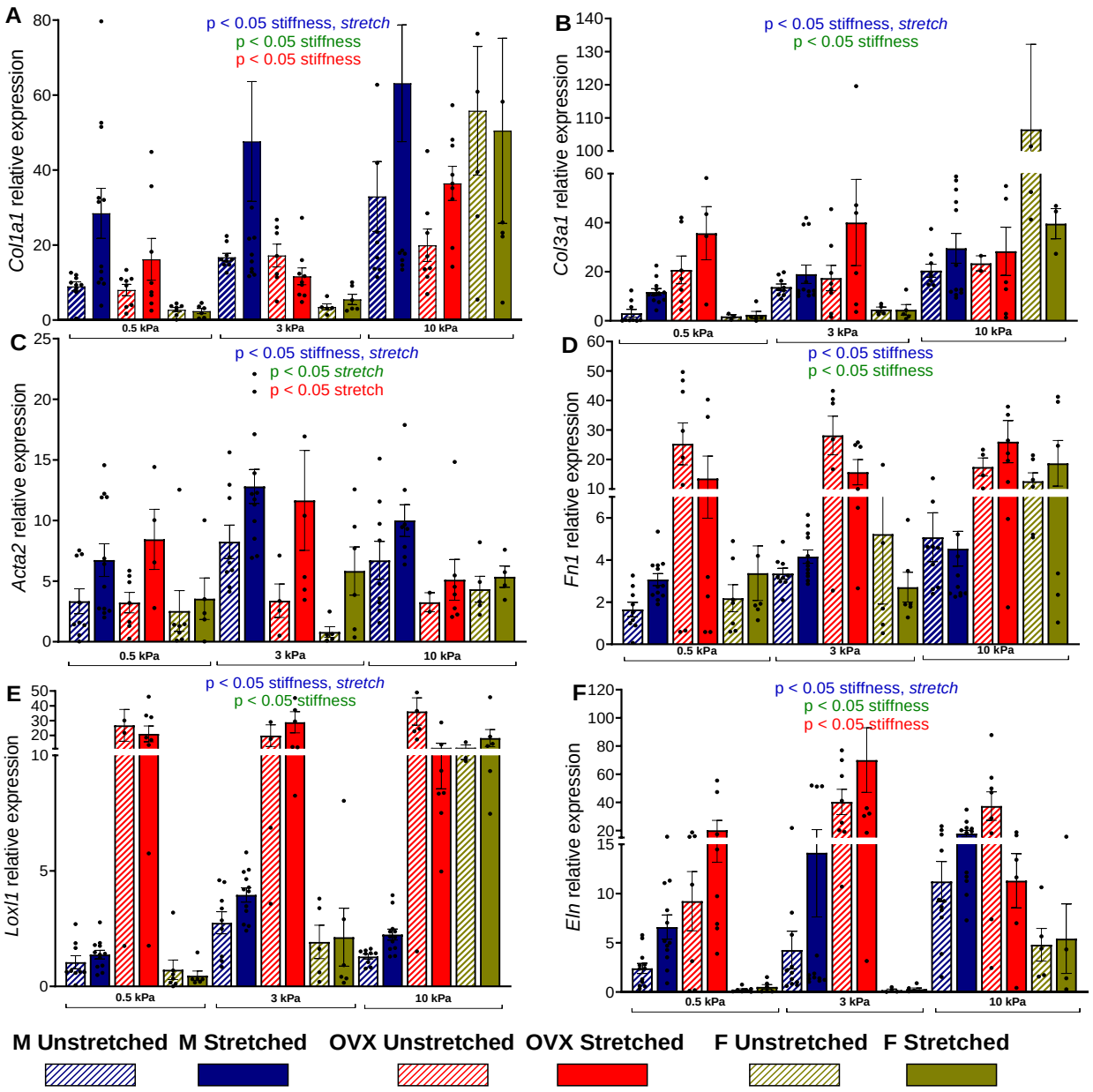
A
Col1a1 relative expression
p < 0.05 stiffness, stretch
p < 0.05 stiffness
p < 0.05 stiffness
0.5 kPa
3 kPa
10 kPa
B
Col3a1 relative expression
p < 0.05 stiffness, stretch
p < 0.05 stiffness
C
Acta2 relative expression
p < 0.05 stiffness, stretch
p < 0.05 stretch
p < 0.05 stretch
D
Fn1 relative expression
p < 0.05 stiffness
p < 0.05 stiffness
E
Loxl1 relative expression
p < 0.05 stiffness, stretch
p < 0.05 stiffness
F
Eln relative expression
p < 0.05 stiffness, stretch
p < 0.05 stiffness
p < 0.05 stiffness
M Unstretched
M Stretched
OVX Unstretched
OVX Stretched
F Unstretched
F Stretched

### 4.1.4 Discussion

Sexual dimorphism in PAH is a well-known phenomenon in which the incidence of the disease is much higher in female patients, but male sex is an independent predictor of death [64]. Because of this it is important to understand if these sex differences were reflected in isolated pulmonary arteries from rats subjected to PAH conditions *in-vivo*. Pooled pulmonary artery tissue data suggests that sugen-hypoxia treatment significantly increases expression of all six profibrotic genes (*Col1a1, Col3a1, Acta2, Fn1*, *Loxl1*, and *Eln*) pulmonary arteries from male rats. This suggests higher induction of male-derived PAs by sugen-hypoxia which could be a reason for the worse PAH survival rates due to increased fibrosis and PA stiffening leading to pressure overload [179]. As PAH continues to progress, the profibrotic induction of male PAs could lead to increased vascular wall stiffening which can in turn feed back into more fibrosis and ECM stiffening.

Along with increases in matrix stiffness, a significantly higher mean pulmonary arterial pressure in male rats due to sugen-hypoxia treatment compared to female rats indicates hemodynamic differences that increase the stimulus of stretch in male PAs as shown in data from our lab.

With how profibrotic genes respond to stretch, stiffness, and inhibition of these signals established, adding the variable of sex may indicate a need for personalized inhibition treatments depending on patient gender since we discovered differential induction effects of stretch in isolated fibroblasts among male, OVX, and female rats.

While male-derived cells generally exhibited a monotonic increase of gene expression from normotensive to mild PAH conditions and from mild PAH conditions to severe PAH conditions, female-derived cells had no significant difference between normotensive and mild PAH conditions but a significant increase in relative gene expression under severe PAH conditions. This is well in

line with work by Chaudhury *et al.* which has found that protective effects of female sex hormones are lost once severe PAH phenotypes are established in female patients [197]. Female-derived cells appear to have a higher threshold to the effects of stiffness than male cells and overall display less sensitivity to stretch than the male-derived cells, which could result in less induction of female PAAFs in response to mild PAH due to stretch and thus less vascular remodeling. Decreased vascular stiffening and fibrosis is indeed observed in female rat models of PAH [179].

On the other hand, ovariectomized-derived cells had an overall higher relative expression even at stiffnesses representing normotensive and mild PAH. According to work by Hussien *et al.*, ovariectomy in rats may cause fibrosis through activation of the renin-angiotensin system [198]. The higher baseline expression in profibrotic genes in cells from ovariectomized rats could be explained by this activation of the renin-angiotensin system, since we have established that angiotensin is an incredibly important cytokine in induction of four of the six profibrotic genes (*Col1a1, Col3a1, Acta2, Fn1*).

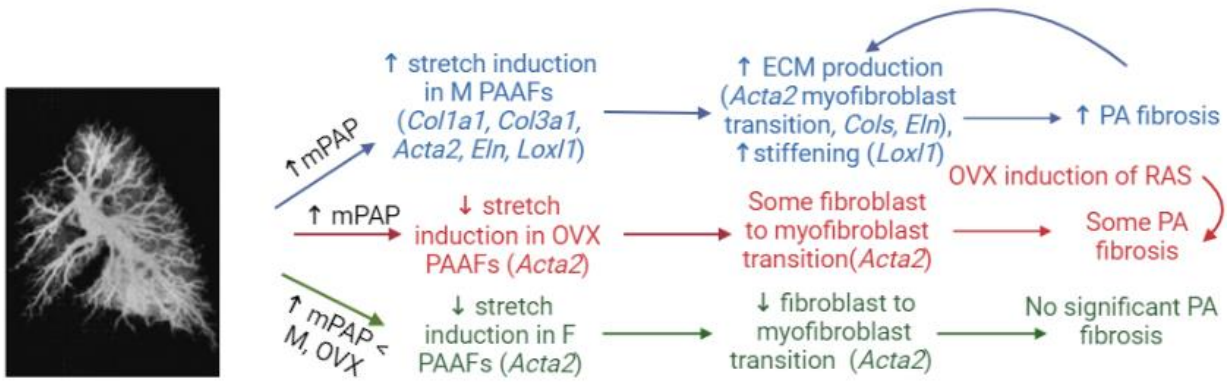


**Figure 4.5: Summary hypothesis of how PAAFs derived from male (blue), ovariectomized (red), and female (green) rats responds to changes in mean pulmonary arterial pressure in PAH.** Increases in mean pulmonary arterial pressure in PAAFs derived from male rats leads to high stretch induction and ECM production that then increases fibrosis which feeds back into higher ECM production. Lower stretch induction in PAAFs from ovariectomized and female rats leads to overall lower PA fibrosis.

In humans, women are more susceptible to PAH but demonstrate better survival and response to treatment, indicating sex differences in the pathophysiology and vascular remodeling in response to this disease. Male PA tissue and PAAFs show higher induction of profibrotic genes in response to sugen-hypoxia treatment and *in-vitro* increases in stretch, which in turn leads to more vascular remodeling and fibrosis in the PA compared to lower induction by stretch of PAAFs from female rats which can explain the lack of significant PA fibrosis in female rats (**Fig. 4.4**). The slightly higher mPAP in male rats compared to that in female rats is not enough to explain the stark differences in PA fibrosis and stiffening [179], therefore we turned to the differential induction by stretch in PAAFs from male and female rats (**Fig. 4.5**). Through this work, we have learned that sex differences already exist in mechanoregulation at the cellular level. This increased induction of profibrotic genes in PAAFs and PAs from male rats likely leads to deleterious fibrosis, an important finding that may be the mechanism leading to why male patient outcomes are so much worse.

#### 4.1.4.1 Limitations

A limitation of our work is that we have not examined if there is a threshold effect for female PAAFs in response to stretch. We have determined that PAAFs derived from female rats require a higher threshold of stiffness representing severe PAH before induction by stiffness occurs but have not determined the same for stretch. It is possible that there is a similar threshold PAAFs from female rats have in response to stretch. Another limitation is that studies were not done in human PAAFs, though work is being done to establish a human PAAF culture line with stiffness at 2 kPa and 4 kPa to represent human PA stiffnesses [61]. Another limitation is that there is no

model of the difference between male and female PAAFs, especially in stretch induction, though there is some evidence as to the mechanistic difference in estrogen response as determined by Frump *et al.* [199].

**Acknowledgements**

Chapter 4 contains unpublished material coauthored with Wang, Ariel and Valdez-Jasso, Daniela. The dissertation author was the primary author of this chapter.

# CHAPTER 5: SEX DIFFERENCES IN MECHANOREGULATION IN RV CFBS INDUCE SIGNIFICANT REMODELING AT THE TISSUE LEVEL

## 5.1 Abstract

Pulmonary arterial hypertension affects not only the pulmonary artery, but also the right ventricle. Left untreated, RV dysfunction and decompensation often lead to heart failure, and no treatment exists to reverse the matrix remodeling and stiffening of the RV. Sex differences in PAH also manifest in the RV, leading to increased end diastolic pressure, fibrosis, and stiffening in male RV tissue.

Our lab has studied the longitudinal nature of PAH, examining changes in RV end diastolic pressure, stiffness, fibrosis, and hypertrophy across many weeks of sugen-hypoxia treatment. This has led us to work comparing what is upregulated at week 4 of sugen-hypoxia representing less stiff RV and weeks 9 and 10 wherein the RV is significantly stiffened by measures of end diastolic elastance. Some genes were upregulated by sugen-hypoxia at 4 weeks representing mild PAH and then went back down at 9-10 weeks representing more severe PAH: *Col1a1*, *Fn1*, *Eln*, while some monotonically increased to be highest after 9 and 10 weeks of sugen-hypoxia: *Col3a1*, *Loxl1*, *Acta2*. In RV tissue from male rats, significant induction by six weeks of sugen-hypoxia treatment occurred while there was no significant induction in female rat RV tissue by two-way ANOVA.

The important longitudinal and sex difference factors in RV tissue led us to investigate the primary responder to changes in mechanical stimuli, cardiac fibroblasts. We isolated cardiac fibroblasts from male and female rats and determined that cells from male rats primarily respond to stretch and not stiffness, while cells from female rats did not respond as much to stretch. Since we observed a significant increase in end diastolic pressure in male rat RVs we did not see in

female rat RVs, and pressure induces stretch activation of CFBs, we hypothesize that this stretch signal is responsible for much of the RV remodeling and stiffening in male RVs. As male RV CFBs are more induced by stretch, this leads to profibrotic gene activation that increases matrix proteins and crosslinking which in turn can increase stiffening that feeds back into more ECM deposition. Through this proposed mechanism, male RVs are more likely to fail in PAH through this differential stretch response.

### 5.1.1 Sex Differences in the Remodeling of the Right Ventricle in PAH

As PAH progresses, the formation of plexiform lesions leads to a rise in mean pulmonary arterial pressure that induces a pressure overload on the right ventricle, which can then lead to right ventricular dysfunction and decompensation and ultimately heart failure [172, 173]. The right ventricle is often implicated as a large contributor to the PAH "sex paradox" since reduction in cardiac function in male patients is a predictor for death by PAH [64]. Tello *et al.* demonstrated that there is superior RV systolic function in female versus male patients, better diastolic relaxation, and lower RV mass index [200].

Our work in RVs in sugen-hypoxia male rats gives compelling evidence that there is a significant increased end diastolic pressure that is not observed in female rats, an activation in profibrotic genes in male RV tissue due to sugen-hypoxia not observed in female tissue, a higher collagen-myocyte ratio in histology, and increased RV stiffening in male rats via the measure of end diastolic elastance as proven in data from our lab. Our group has also studied the distinct time course of right ventricular hypertrophy and structural remodeling over a longitudinal 10-week period in sugen-hypoxia treated male Sprague-Dawley rats, noting significant RV hypertrophy by

week 4, then a later stage significant increase in end-systolic and end-diastolic elastance in week 5-10 animals [177].

To study how the RV adapts to changes throughout the pathobiology of the disease, RV tissue from normotensive and sugen-hypoxia [18] treated rats at week 4 and weeks 9 and 10 were analyzed. We also examined if the "sex paradox" in PAH would be exhibited in differential induction of profibrotic genes by RVs from male and female rats after six weeks of sugen-hypoxia treatment [64]. Since induction was significantly different in male and female RV tissue, and RV diastolic stiffening and dysfunction in animals and PAH patients [66, 174] is mediated by remodeling of the RV ECM by cardiac fibroblasts (CFBs), we hypothesized a difference in induction of CFBs between male and female rats.

CFBs regulate extracellular matrix remodeling in response to mechanical stress due to hypertension by activating and transforming into myofibroblasts which produce excess ECM and can exhibit increased proliferation [63, 175, 176]. Work by the Aguado lab in left ventricular cardiac fibroblasts demonstrates that sex differences in isolated male and female CFBs are crucial in determining sexual dimorphism in heart disease outcome [180]. Sex differences in mechanoregulation of RV CFBs, has not yet been established. Thus, this work will be key in determining the mechanism by which male RV tissue is stiffer and more fibrotic than female RV tissue through studying sex differences in CFB induction by stretch and stiffness.

### 5.1.2 Methods and Materials

#### 5.1.2.1 Homogenization of Tissue

BeadBug Microtube Homogenizer (Benchmark Scientific #D1030 Sayreville, NJ, USA), 3.0 mm High Impact Zirconium beads TriplePure M-Bio Grade (Benchmark Scientific, Sayreville, NJ, USA) at 1800 rpm for 3-6 minutes until RV chunks were visually confirmed to be broken down in TRIzol by Invitrogen (#15596026, Thermo Fisher Scientific, Waltham, MA, USA). The sugen-hypoxia procedure is as described in Section 4.1.2.3 for rats from which right ventricular tissue was taken.

#### 5.1.2.2 Adult Primary Cardiac Fibroblast Isolation

Animal care, housing, and feed were approved by the Institutional Animal Care and Use Committee (IACUC) at the University of California San Diego. Sprague-Dawley rat (Charles River, Wilmington, MA) right ventricles were cut into 8-12 pieces. Hearts were transferred into 0.6 mg/mL Trypsin solution (Trypsin 1:300 #2271525-GM, USB Corporation, Cleveland OH USA) in cold Hanks' Balanced Salt Solution (1X #14175-095 Gibco by Life Technologies Carlsbad, CA USA) and left to rock overnight at 4°C for pre-digestion. A solution of 1 mg/mL collagenase type 2 (#LS004176, Worthington, Lakewood NJ USA) and mechanical agitation with a 10 mL serological pipette (Nunc Cat #170356N, Thermo Fisher Scientific, Waltham, MA, USA) is used to digest the heart tissue. Dead cells and red blood cells are removed, then the solution is passed through a 100 µm cell strainer (#22363549, Fisherbrand, Hampton, NH, USA). Cells are spun down at 400g for 5 minutes in a centrifuge (5804 R, Eppendorf, Hamburg, Germany) in fibroblast media (DMEM with 10% FBS and 1% anti/anti) (DMEM 1X #10566-016, Gibco

Carlsbad, CA, USA; FBS #35-010-CV, Corning, Corning, NY, USA; antibiotic/antimycotic #15240-062 Life Technologies Grand Island NY USA), and pre-plated in a T-75 flask (#25-209, Genesee Scientific San Diego, CA USA) for 30 minutes at 37°C and 5% $CO_2$. The supernatant is transferred to a new flask and pre-plated for another 30 minutes. Cells are detached with 0.25% trypsin (1X #15050-065 Life Technologies Grand Island NY USA) and pooled to spin at 400g for 10 minutes and counted via hemacytometer and plated at a concentration of 100-150,000 cells per gel.

#### 5.1.2.3 Stiffness Determination

Polyacrylamide gels were formulated as described previously using acrylamide (#A4058100ML Sigma Aldrich St Louis, MO USA) and bis-acrylamide (#M1533-25ML Sigma Aldrich St Louis, MO USA) with the same protocol as Section 3.1.2.2 according to the stiffnesses outlined by Tse *et al*. [62]. To mimic the substrate stiffness of the cardiac fibroblasts, according to a study by Jang *et al*., normotensive rat RVs are at a stiffness of roughly 7 kPa and pulmonary artery banded rats, a model of RV dysfunction in PAH, exhibits a stiffness of roughly 40 kPa [178].

#### 5.1.2.4 Attachment Methods

The polyacrylamide gels described in the last section were then coated with collagen or fibronectin for LV or RV cardiac fibroblast attachment. Collagen (10 μg/mL) was added using the crosslinking of EDC (#00050, Chem-Impex Int'l Inc Wood Dale IL, USA) and NHS (#A10312, Alfa Aesar Ward Hill MA USA), PBS, anti-anti (#15240-062 Life Technologies Grand Island NY USA), and rat tail collagen I (#354236, Corning, Corning, NY USA). The solution was then incubated overnight at 37 °C, 5% $CO_2$, 100% humidity before cells are plated.

Fibronectin attachment is done according to the protocol by Tse *et al.* [62]. First, sulfo-SANPAH (#22589 Thermo Scientific Waltham, MA USA) is used to coat the polyacrylamide gel, then the gel is placed in a 365-nm UV light source (Black-Ray UV Bench Lamp 365 nm 115V~60Hz #XX-15L P/N 95-0042-07, UVP Upland, CA USA) for 10 minutes. The gel is then rinsed with 50 mM HEPES (Free acid #JT4018-1, Avantor Center Valley, PA USA), and fibronectin (#F1141-1MG Sigma Aldrich St Louis, MO USA) is added and incubated overnight at 37 °C, 5% $CO_2$, 100% humidity before cells are plated. RT-PCR is done as described in Chapter 4.

#### 5.1.2.5 Statistics

Descriptive statistics were performed using JMP Pro Statistical software (version 14, SAS Institute Inc., NC, USA) for group comparisons of relative gene expression. For normally distributed data, one-way analysis of variance (ANOVA) was used to test for differences in means of three different stiffnesses and for all six genes, followed by the Dunnett's *post-hoc* test. Otherwise, the non-parametric Wilcoxon–Kruskal–Wallis statistic was used followed by Dunnett's *post-hoc* test. Effects of stiffness and stretch were tested using two-way ANOVA with stiffness and stretch as fixed factors. For normally distributed data, the Dunnett's *post-hoc* test was used. Otherwise, the non-parametric Wilcoxon–Kruskal–Wallis statistic was used followed by Dunnett's *post-hoc* test. Data are expressed as means ± standard error of the mean relative to housekeeping gene 18S, unless otherwise specified. Statistical significance was determined at a level of 0.05. Data were graphed in GraphPad Prism software (v8.4.3.686, San Diego, CA, USA).

### 5.1.3 Results

#### 5.1.3.1 RV Tissue Longitudinal and Sex Difference Data

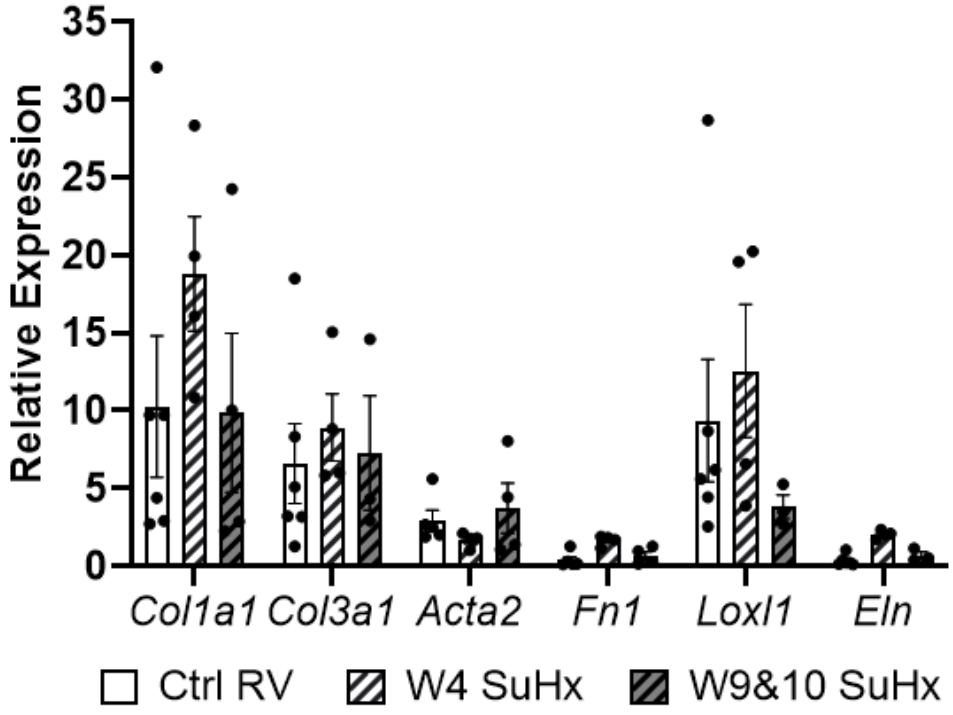


**Figure 5.1: Right-ventricular tissue gene expression derived from male control, 4 weeks and 9 and 10 weeks of SuHx**. RV tissue is extracted from male Sprague-Dawley rats and graphed as relative expression of 6 relevant genes in pulmonary arterial hypertension. *Col1a1, Fn1,* and *Eln* exhibit an increased induction at week 4 of sugen-hypoxia treatment and then a decrease at weeks 9 and 10, while *Col3a1, Acta2,* and *Loxl1* continue to increase by weeks 9 and 10 of SuHx treatment. No significant increases were found using one-way ANOVA.

RV tissue is broken down by homogenization and analyzed by RT-PCR as described in Section 5.1.2.1 and graphed as relative expression of six genes that increased at 4 weeks of SuHx treatment and went down to baseline and genes that increased until 9-10 weeks of SuHx (**Fig. 5.1**). The genes increased after 4 weeks of SuHx were *Col1a1, Eln,* and *Fn1*. The genes which kept increasing by weeks 9 and 10 of SuHx treatment were *Col3a1, Loxl1*, and *Acta2*. Based on these results, for our cellular level study in RV CFB, we chose to target three genes that increased at 4 weeks of SuHx: *Cola1, Eln, Fn1,* and three that continued to increase: *Col3a1, Loxl1, and Acta2.*

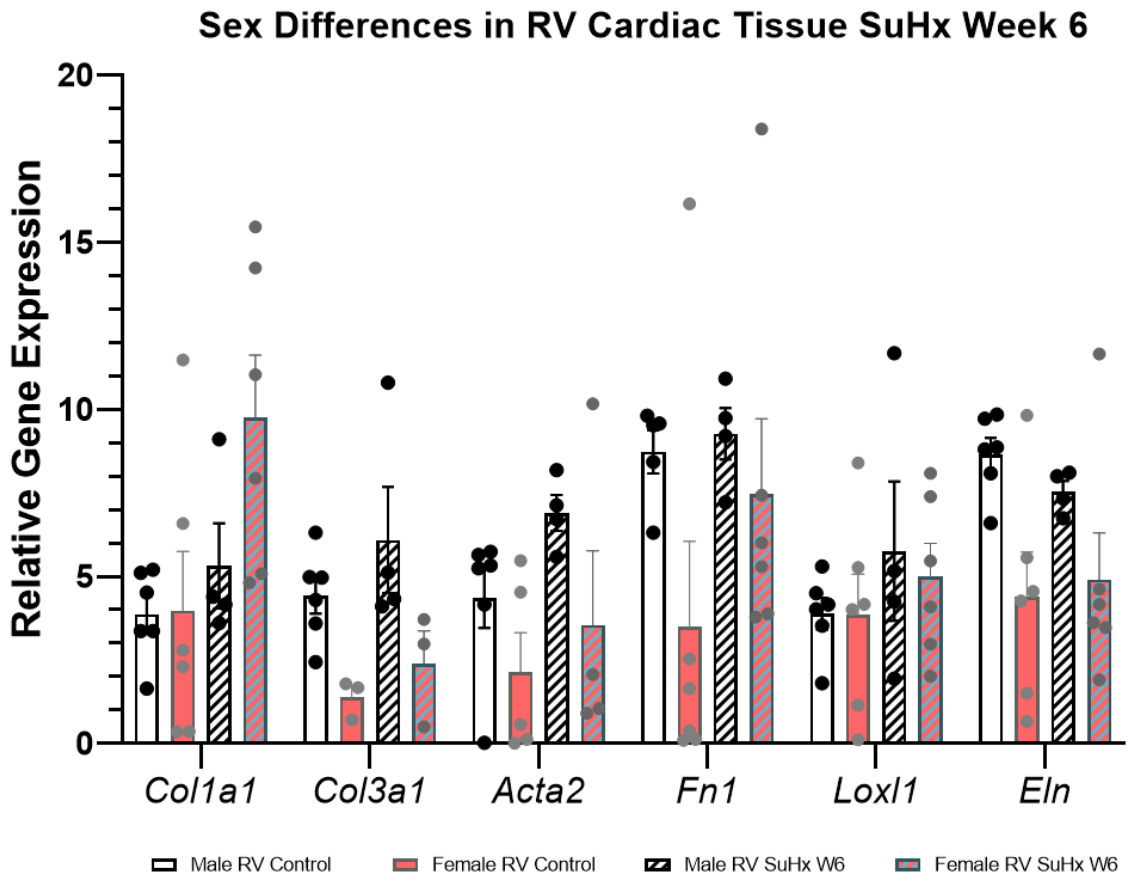


**Figure 5.2: Rat right-ventricular tissue response to 6 weeks of SuHx in male and female rats**. RV tissue is extracted from Sprague-Dawley rats and the relative expression against housekeeping gene 18S is graphed as the mean ± SEM. Age-matched normotensive male control data (n=6) is plotted against shaded male 6-week SuHx data (n=4), along with age-matched normotensive female control data in red (n=6) against shaded female 6 week SuHx data (n=6). No significant differences were found in induction of the six genes by sugen-hypoxia in RV tissue from female rats but was significant by two-way ANOVA in RV tissue from male rats.

RV tissue from week 6 male and female rats is homogenized as discussed in Section 5.1.2.1 and analyzed by RT-PCR. The six profibrotic genes examined here are the same as used to analyze isolated CFBs in the section below. Male and female RV data demonstrate some upregulation in response to sugen-hypoxia treatment used to mimic PAH in rats. Normotensive female control rat RVs had generally lower relative expression than the normotensive male control rat RVs, and

induction of the six genes by sugen-hypoxia was not significant in female RVs but was significant by two-way ANOVA in male RVs.

### 5.1.3.2 Sex Differences in Isolated RV CFBs in Response to Stiffness and Stretch

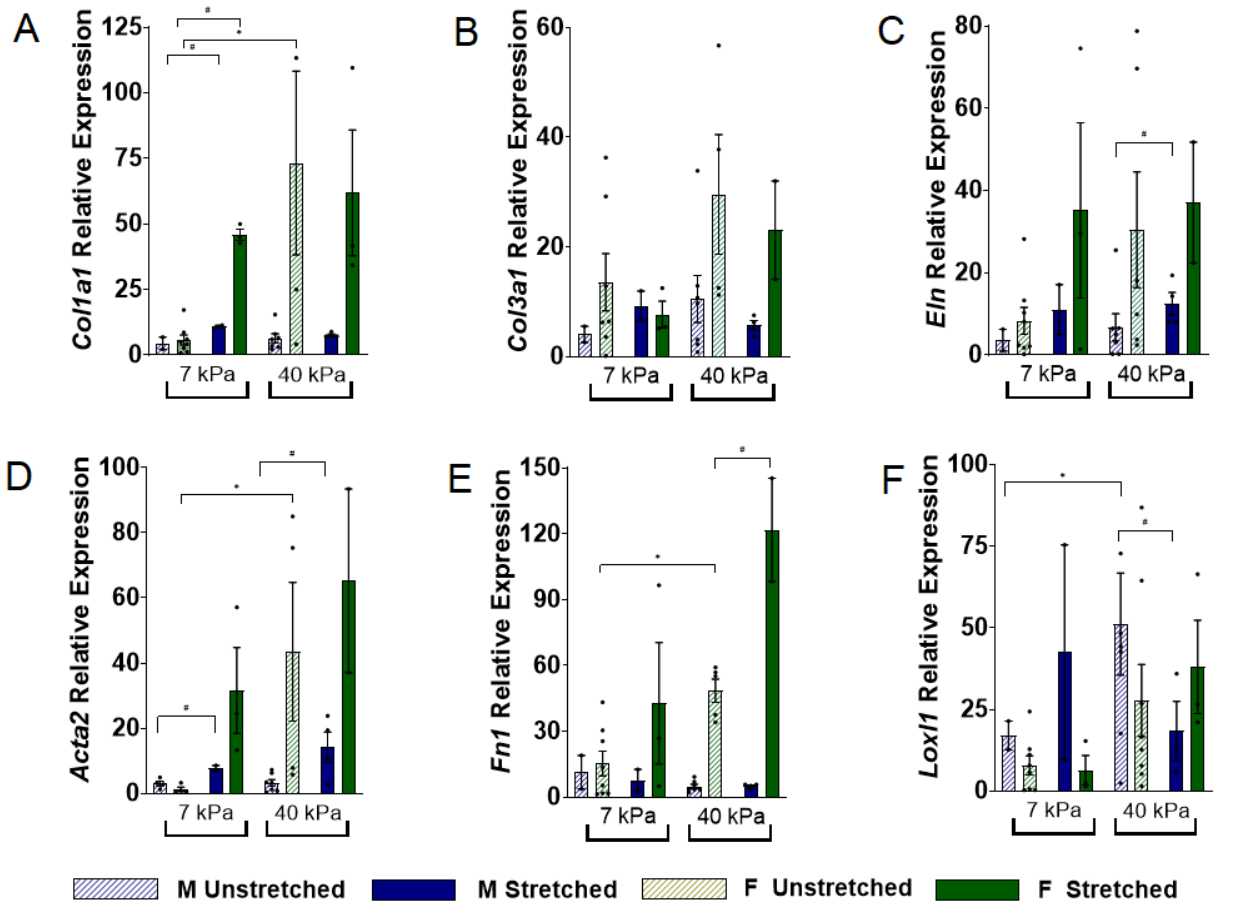


**Figure 5.3: RV cardiac fibroblasts isolated from male and female Sprague-Dawley rats shows response to stiffness and stretch**. RV cardiac fibroblasts are isolated from male and female rats and plated onto polyacrylamide gels coated with fibronectin and subjected to differences in stiffness (7 kPa for normotensive and 40 kPa representing PAH stiffness) and 10% stretch for (**A**) *Col1a1* (**B**) *Col3a1*, (**C**) *Eln*, (**D**) *Acta2*, (**E**) *Fn1*, and (**F**) *Loxl1*. Data is graphed as mean ± standard errors of the mean of mRNA levels relative to housekeeping gene 18S with blue bars male data (n=4) and green bars representing female data (n=8) with shaded data indicating no stretch and solid data indicating stretch. Asterisks (*) show data significantly affected by stiffness and # indicates data significantly affected by stretch by Students' t-test. RV CFBs from male rats were more induced by stretch in genes *Col1a1*, *Eln, Acta2*, and *Loxl1* while RV CFBs from female rats were only induced by stretch in genes *Col1a1* and *Fn1*. RV CFBs from female rats were were induced by stiffness in genes *Col1a1, Acta2,* and *Fn1* while RV CFBs from male rats were upregulated by stiffness only in gene *Loxl1*.

Control RV CFBs isolated from male and female Sprague-Dawley rats according to Section 5.1.2.2 were plated on gels of 7 kPa and 40 kPa using the same protocol and were coated in fibronectin according to Section 5.1.2.4. Significant upregulation due to stretch in CFBs from male rats were observed in *Col1a1, Eln, Acta2,* and *Loxl1*, while CFBs from female rats responded to stretch in genes *Col1a1* and *Fn1*. RV CFBs from male rats was upregulated due to stiffness in *Loxl1* while CFBs from female rats were upregulated due to stiffness in genes *Col1a1*, *Fn1*, and *Acta2*.

### 5.1.4 Conclusions

Ultimately, it is RV dysfunction that leads to the outcome of death in PAH, and since the PAH sex paradox indicates that male sex is an independent indicator of death, it is important to study sex differences in the RV.

To probe differing induction of genes depending on severity of PAH, RV tissue from normotensive and sugen-hypoxia treated male Sprague-Dawley rats was isolated and probed for gene expression that is important in cardiac fibrosis. Data showed some gene expression was upregulated by SuHx at 4 weeks and then returns to baseline by 9-10 weeks: *Col1a1*, *Fn1*, *Eln,* while some increase to their highest point after 9-10 weeks of SuHx treatment: *Col3a1*, *Loxl1*, *Acta2*. This four-week timepoint is also when our group has found a turn from the early stage of PAH significant RV hypertrophy by week 4, then the late-stage increase in end-systolic and end-diastolic elastance indicating RV stiffening after that [177]. This indicates matrix proteins *Col1a1* and *Fn1* are induced early in PAH in the RV during adaptive remodeling, while *Eln,* which is responsible for response to stretch may first be induced but there is less signal once adaptive

remodeling decreases the effect of stretch through RV wall thickening. On the other hand, *Col3a1* is induced but continues to be expressed as the RV stiffens, *Loxl1* which crosslinks collagen thereby increasing stiffening may lead to the increased RV stiffening after week 4, and *Acta2* indicating transition of fibroblasts to myofibroblasts is induced as the RV wall stress increases and excess ECM is deposited.

RV tissue from male and female rats after six weeks of sugen-hypoxia treatment compared to normotensive control demonstrated increases in profibrotic gene expression, though only male RV tissue was significantly induced by two-way ANOVA. This indicates that there are sex differences in profibrotic gene activation in RV tissue, along with increased fibrosis, and increased RV stiffening found in data from our lab. The profibrotic gene activation in tissue is likely due to the contribution of CFBs, which are the primary responder to injury in the myocardium. It is unknown, however, whether RV CFBs have sex differences in response to mechanosignaling.

We isolated RV CFBs from male and female rats and cultured them at stiffnesses representing control RV stiffness (7 kPa) and pulmonary artery banded RV stiffness (40 kPa). Overall, RV CFBs from male rats were found to primarily respond to stretch in genes *Col1a1, Acta2, Loxl1,* and *Eln* expressions, while RV CFBs from female rats only respond to stretch in genes *Col1a1 and Fn1* expressions. This sex difference in induction of RV CFBs indicates that their response to their microenvironment and effect on cardiac function [180] is varied in male versus female rats, which could be translated and explain the different rates of RV dysfunction in male versus female patients once they suffer from the disease [64].

Our lab has previously found significantly increased end-diastolic pressure in male rats undergoing SuHx treatment that is not observed in female rats, indicating that there is a strong stretch induction of RV CFBs from male rats that does not occur in RV CFBs from female rats

based on data from our lab. This stretch signal is hypothesized to lead to stretch induction of *Col1a1* and *Eln* which means RV CFBs from male rats put down more ECM in response to stretch signals, and higher induction of *Acta2* leads to fibroblast transition into myofibroblasts which in turn deposit excessive ECM (**Fig. 5.4**). This leads to increased RV stiffening, which is increased by induction of *Loxl1*, a crosslinker of collagen that increases stiffening without increasing collagen production. The higher end diastolic pressures in male rats with SuHx compared to female rats with SuHx in turn leads to differential induction of RV CFBs from male rats at the cellular level. This difference in induction of the cellular phenotype can in turn explain increased stiffness in the RV of male rats as measured by end diastolic elastance done in our lab.

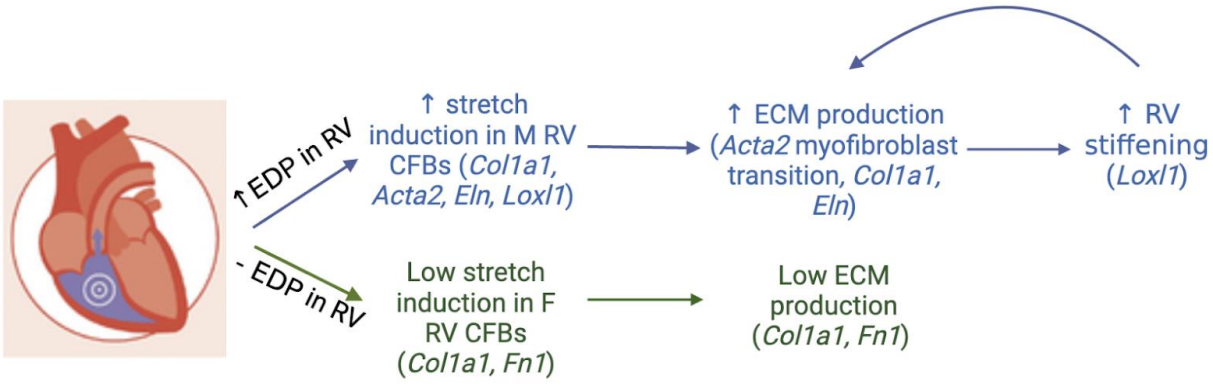


**Figure 5.4: Summary hypothesis of differential responses between male and female RV CFBs**. Stretch induced by increase in end-diastolic pressure in male RVs could indicate sex-dependent remodeling due to the contribution from RV CFBs in male rats at the cellular level inducing changes at the organ level since RV CFBs from male rats are more likely to be induced by stretch than RV CFBs from female rats.

Interestingly, *in-vitro* experiments on RV CFBs were more difficult to carry out than those on PAAFs as we found that RV CFBs were not able to be revived from frozen even when the same density of cells as PAAFs was taken from T75 flasks. Isolation of RV CFBs was adapted from a method used to isolate mouse LV CFBs, therefore time in collagenase was a variable that was iterated on until a consistent sufficient population of RV CFBs could be derived. Another crucial

difference between the two fibroblast types was in the attachment methods, as described in Section 4.1.2.7. Enough PAAFs stayed attached when using collagen I to coat the polyacrylamide gels, but many attachment methods were tested before a combination of fibronectin and sulfo-SANPAH was successful in retaining RV CFBs. Those methods included 2% gelatin, laminin, and collagen I. No sex differences were observed in revival and attachment of PAAFs.

As was applied to the PAAFs, one could use logic-based computational networks of mechanosignaling to analyze the RV CFB response to stretch and stiffness. Zeigler *et al.* have made a computational model of cardiac fibroblast response to "mechanical" signals [69] which can be iterated on using our *in-vitro* data to probe which pathways are more sensitive to stiffness or stretch, or which pathways are more likely to be upregulated by RV CFBs from male or female rats. This could result in very targeted hypothesis generation and predictions of which nodes should be inhibited to prevent deleterious RV fibrosis, especially in male RVs.

### 5.1.5 Limitations

One limitation of this work is that there is no model of RV cardiac fibroblasts that distinguishes sex differences. Work done by Zeigler *et al.* [69] has led to the creation of a mechanosignaling network of cardiac fibroblasts, but it does not separate mechanical stimuli into stretch or stiffness separately. We could use our very interesting *in-vitro* data teasing apart the mechanosignaling sex differences in RV CFBs to modify Zeigler's existing model to incorporate that CFBs from male rats were more induced by stretch. Another limitation of this work is the lack of RV CFB data from ovariectomized rats, which could give interesting information on how less circulating estrogen, but still female cells could affect profibrotic stretch induction. We would also be curious

to see if tissue from ovariectomized RVs exhibit increased fibrosis even in normotensive ovariectomized rats as seen in PAs.

**Acknowledgements**

Chapter 5 contains unpublished material coauthored with Wang, Ariel and Valdez-Jasso, Daniela. The dissertation author was the primary author of this chapter.

# CHAPTER 6: SUMMARY AND CONCLUSIONS

In this body of work, we are examining mechanisms of mechanosignaling PAH using a variety of *in-vivo, in-vitro* and *in-silico* methods that studied two tissues which become dysregulated in PAH: the pulmonary artery and right ventricle in male, female, and ovariectomized animals in a comprehensive study.

We created a novel mechanosignaling network model of the pulmonary arterial adventitial fibroblast with a model accuracy of 80% that integrates the crosstalk of signaling pathways known to be crucial to PAH, including ones involving hypoxia and pulmonary arterial fibrosis [54]. We validated this model using papers independent from model formulation, even quantitatively matching *Acta2* expression in response to ERK and p38 inhibitors found in literature. We also used sensitivity analysis to determine the important inputs of AngII, mechanical, and TGFβ. Uncertainty quantification was then used to study how robust the model was to changes in input weight and $EC_{50}$, but how important the Hill coefficient parameter $n$ was to the model accuracy. We also analyzed the epistemic uncertainty of adding literature data from fibroblasts that were not cardiovascular to the model and found that the reduced model had much lower model accuracy. This demonstrates that while there is uncertainty about adding some non-cardiovascular pathways in the PAAF model, the additional pathways deduced from these other cell types can improve prediction accuracy without significantly compromising robustness, a lesson we applied to making model inhibition simulations match better to experimental inhibtion data. The model successfully simplifies the complex relationships between pathways in PAH to make useful predictions of PAAF response to mechanical signals, stimulation, and inhibitors.

We were able to update this model by using the results of *in-vitro* experiments that separately subjected our well-characterized PAAFs to changes in substrate stiffness and stretch using tunable hydrogels and a custom equibiaxial stretcher [53]. We found that PAAFs derived from male Sprague-Dawley rats significantly responded to stretch and stiffness in all genes studied: *Co11a1, Col3a1, Acta2, Eln,* and *Loxl1* but only to stiffness in *Fn1*. This led us to iterate the model and crucially separate the input node of 'mechanical' into 'stretch' and 'stiffness' so that we could identify which pathways are more significant in upregulation due to stretch and which to stiffness. We found that stiffness activated integrin β3, the MST1/2 kinases, angiotensin II, TGFβ, and syndecan-4, and stretch regulated integrin β3, MST1/2, Ang II, and the transient receptor potential (TRP) channel. There were no interaction effects between stretch and stiffness for the six gene outputs of the model we studied. We found that protein expression of Collagen III and Fibronectin matched the trends of the RNA expression data. The results also showed that *Acta2* and *Loxl1* expression were non-monotonic, increasing at stiffnesses representing mild PAH but decreasing at stiffnesses representing severe PAH. This suggests the expression of *Col1a1*, *Col3a1*, and *Eln* might rise early *in-vivo* as the increased pulmonary arterial pressure in PAH increases vascular wall strain and stays elevated as fibrosis increases ECM stiffness, but *Loxl1* and *Acta2* expression may rise at first but eventually returns to baseline as wall stiffening becomes severe, while *Fn1* may be induced after the stiffening of the ECM has already occurred.

Our model predictions of which receptors would be most influential of AT1R or TGFβ in stretch and stiffness led us to do *in-vitro* experiments into how PAAFs would respond to inhibiting these important nodes. Without any modifications, model was able to qualitatively predict 70% of the inhibition experiment results and quantitatively match *Col3a1* response to TGFβRI and the *Loxl1* response to TGFβRI and AT1R. As stated a few paragraphs above, the sensitivity analysis

of the model indicates, AngII, TGFβ and stiffness and stretch were important drivers in PAH disease pathology. We are testing this through *in-vitro* experiments to inhibit the AngII receptor AT1R and the TGFβ receptor TGFβR. Through this analysis, we were able to determine the important pathways regulating the profibrotic gene expression of the six candidate genes *Co11a1, Col3a1, Acta2, Fn1, Loxl1,* and *Eln*. These pathways were stiffness and stretch upregulation of AngII, TGFβ and the Hippo pathway, stretch activating TRP, AngII activating MAPK and AP1 leading to latent TGFβ, and TGFβ activation through smad2/3 phosphorylation and TAK1 activation of p38.

By analyzing the quantitative differences between the predicted model response and experimental data, we were able to make model modifications to try to explain these differences. Experimental results indicated that *Col1a1* requires AngII and TGFβ to respond to stiffness and stretch, but *Col3a1* only requires AngII. *Col1a1* and *Col3a1* did not respond to TGFβRI in the same way, so positing ET1 and PPARγ both being necessary for *Col1a1* induction alone based on work in PAECs was used to explain this phenomenon [181]. Smad2/3 and YAP/TAZ being cotranscriptional regulators as in cardiomyocytes was a way to explain the more dramatic effect of AT1R on collagen expression experimentally [201]. Previously, the model had no difference in the regulation of *Col1a1* and *Col3a1,* but this experimental result and importance of the Collagen I / Collagen III ratio in pulmonary hypertension indicates this should not be the case [202]. Based on the difference between *Col1a1* and *Col3a1* regulation, *Col3a1* induction via stiffness or stretch would be more difficult to block than *Col1a1* induction since it only requires AngII signaling.

Similar dramatic effects on *Acta2* TGFβ and AngII inhibition led us to test p38 and PKCα both being necessary as in atherosclerotic response to AT1R, while *Fn1* inhibition was more notable in the model predictions than in the experiments which indicates the need for more

pathways regulating *Fn1* expression, such as stretch regulating STAT3 and stiffness regulating Piezo1 [183, 18h]. *Acta2* requires both AngII and TGFβ for response to stretch and stiffness, while *Fn1* requires AngII and TGFβ for response to stiffness. This work has indicated an interesting target to block to reduce fibroblast to myofibroblast transition induced by *Acta2* [63], since blocking PKCα would theoretically block *Acta2* stiffness and stretch induction without knocking out important pathways to adaptive remodeling downstream of TGFβ and AngII. *Fn1* expression, on the other hand, demonstrates why epistemic uncertainty of adding non-PAAF and non-cardiovascular pathways to the model can still benefit model formulation [53].

Our work to elucidate mechanisms by which regulation of these profibrotic genes occurs is crucial to understanding which cytokines are necessary in profibrotic response. Since we surmise, for example, that ET1 and PPAR signaling are both necessary for induction of *Col1a1* but not *Col3a1* we can reach a specificity of targeting these specific nodes to inhibit specific profibrotic genes that could not have been achieved without simulating this with a complex model. This makes the model more useful as a high-throughput predictive screening tool that can identify which nodes to target to decrease profibrotic signaling.

Since we learned that stretch is an important regulator, we examined gene expression of the six profibrotic genes in response to stretch after 4 hours, 8 hours, and 24 hours. In doing this we found that *Col1a1* increases monotonically and has the highest expression at 24 hours, *Fn1* is most upregulated at 4 and 8 hours then returns to baseline, and the other four genes are upregulated at 8 hours and then decreases. When examining the role of stretch alone, *Col1a1* is the only gene that increases in expression throughout time, while male PAAFs subjected to stiffness *and* stretch indicated that *Col1a1, Col3a1* and *Eln* were all observed to increase and continue increasing. This shows that *Col3a1* and *Eln* possibly require the feedback of increased ECM stiffness to continue

to increase in relative expression but *Col1a1* induction by stretch is sufficient to increase its expression. Interestingly, *Col3a1, Eln, Acta2,* and *Loxl1* were significantly increased at 8 hours of stretch and then dropped, while *Acta2* and *Loxl1* were increased due to stretch and stiffness but decreased to baseline at severe PAH stiffnesses. This indicates that stretch may be the main inducer of *Acta2* and *Loxl1* in male PAAFs since the same response occurs with and without stiffness, and as wall stiffness becomes severe the effects of stretch fall off in these two genes. *Fn1* levels were significantly induced by increased substrate stiffness and transiently upregulated by stretch at 4 hours, but returned to baseline, while there was no significant upregulation of *Fn1* by stretch at 24 hours. This leads us to conclude that there is only a transient *Fn1* response to stretch, possibly at the initial adaptive remodeling step.

In addition to studying how PAAFs respond to stretch and stiffness, a crucial aspect of PAH we studied was sex differences at the *in-vivo* and *in-vitro* level in the pulmonary artery, the vascular remodeling of which is a major hallmark of PAH pathobiology and can lead to the observed sex differences in outcome. *In-vivo* data from pulmonary arteries isolated from rats treated with sugen-hypoxia allows us to examine how the vessel responds to simulated PAH conditions. The pulmonary artery tissue data indicates that sugen-hypoxia treatment for six to ten weeks after treatment with hypoxia significantly upregulates expression of all six genes in PAs from male rats, but only significant increases in *Col1a1, Fn1*, *Loxl1*, and *Eln* expression in PAs from female pulmonary arteries, and PAs from ovariectomized females only exhibited increased *Col1a1*. Pulmonary arteries isolated from normotensive ovariectomized rats had a higher relative expression than ones isolated from normotensive male and female rats. Since PAAFs are a major regulator of response to factors in PAH such as increased vascular wall stiffness and wall strain, we examined the induction of the same six genes in cells from male, female, and ovariectomized

rats. These *in-vitro* experiments allowed us to tease apart how cells differ in their response to stiffness, stretch, and sex separately. In PAAFs, we found that male-derived cells generally responded to stretch and stiffness, but female cells required a higher stiffness representing severe PAH before responding to changes in stiffness and exhibited no response to stretch except in *Acta2*. This aligns well with work by Chaudhury *et al.* that indicates female sex hormones are no longer protective for female patients experiencing severe PAH, suggesting early intervention would be more effective in treating women before increased stiffening of the PAs occurs [197]. On the other hand, PAAFs from ovariectomized female rats had an overall higher relative expression even at stiffnesses representing normotensive and mild PAH conditions, upregulation in stiffness only in *Col1a1* and *Eln*, and response to stretch in *Acta2*. This is similar to how PAAFs derived from ovariectomized female rats exhibited increased relative expression at stiffnesses representing normotensive and mild PAH conditions as compared to PAAFs derived from male and female rats. Cells and tissue derived from normotensive ovariectomized rats thus already seem to have high profibrotic responses from the procedure alone. This aligns well with studies done by Hussien *et al*. on ovariectomy in rats causing fibrosis because of activation of the renin-angiotensin system, and as we have already established, angiotensin is an important inducer of four of the six profibrotic genes (*Col1a1, Col3a1, Acta2, Fn1*) [198].

This leads us to conclude that there is higher induction of profibrotic genes in both PAAFs and PAs from male rats, lower induction of PAAFs and PAs from female rats, and a higher baseline induction in PAAFs and PAs from ovariectomized rats, which could be a reason for the worse PAH survival rates in male patients as this induction can lead to increased PA stiffening and fibrosis seen in male rats [179] which can in turn lead to RV failure via pressure overload.

This increased vascular load on the RV leads to RV wall thickening, and then dilation and dysfunction [203]. RV tissue from normotensive and SuHx treated male Sprague-Dawley rats showed that some genes were upregulated by SuHx at the 4-week timepoint and then returned to baseline by 9-10 weeks: *Col1a1, Fn1, Eln*, while some increase to their highest point after 9-10 weeks of SuHx treatment: *Col3a1, Loxl1, Acta2*. Our group has found that this 4-week timepoint is a turning point in the RV hypertrophy from the early stage of PAH, leading to a late-stage increase in end-systolic and end-diastolic elastance after that [177]. The induction of *Col1a1* and *Fn1* at 4 weeks indicates these matrix proteins may be upregulated during the adaptive RV wall thickening and then decrease, while *Eln* which is a primary responder to stretch may also increase initially when the vascular load induces a pressure which stretches the RV cells but then decrease as wall stiffening compensates and decreases the stretch induction. *Col3a1* in another example of being differentially expressed from *Col1a1*, increases monotonically, and may feed back into increasing more as the RV stiffens in week 9 and 10. *Loxl1* as it increases will crosslink collagen and cause even more RV stiffening. *Acta2* induction will increase transition of RV CFBs into myofibroblasts, which will put down excess ECM and further increase this stiffening process. The turn from 4 week to 9- and 10-week PAH is not the only interesting results in RV tissue, however, since we also examined the difference in male and female RV tissue after 6 weeks of sugen-hypoxia treatment.

The six profibrotic genes we examined at week 4 and weeks 9 and 10 were probed for in male and female RV tissue. By two-way ANOVA, sugen-hypoxia significantly upregulated male RV tissue in these six profibrotic genes while female RV tissue was not significantly upregulated. Since RV stiffness by measure of end diastolic elastance and RV fibrosis by measure of collagen:myocyte ratio was all significantly increased in RV tissue from male rats but not in RVs

from female rats, this increase in profibrotic response in male RVs was not altogether unexpected based on previous data from our lab. As a main regulator of the RV response to PAH conditions such as stiffness and stretch, it is important to determine the mechanism by which this profibrotic activation occurred by studying RV CFBs *in-vitro*.

*In-vitro* experiments allow us to study RV CFBs in response to stiffness, stretch and sex separately. We found sex differences in the RV CFBs isolated from male and female rats, which could play a role in why outcomes from PAH manifests distinctly in male versus female patients. RV CFBs from male rats were found to respond primarily to stretch while RV CFBs from female rats were not as induced by stretch. As important regulators of heart function, ventricular fibroblasts have been proven to have inherent sex differences that lead to sexual dimorphism in presentation and outcome of cardiac diseases [180]. The proposed mechanism by which this could occur is that increased end diastolic pressure in RVs from male rats induces stretch activation of the RV CFBs from male rats that does not occur in RV CFBs from female rats since there is no significant increase in end diastolic pressure due to sugen-hypoxia treatment in female rats (Figure 5.4). This stretch induction leads to excessive ECM deposition via *Acta2* leading to RV CFB transition into myofibroblasts, as well as induction of *Col1a1*, a matrix protein, and *Eln*, a matrix protein that responds to increases in stretch in the male RVs that ultimately leads to a stiffer RV, through induction of *Loxl1* which crosslinks collagen, that in turn feeds back into even more ECM remodeling. Our discovery of this possible mechanism of maladaptive remodeling in the male RV goes a long way to explaining why being male is an independent predictor of death in regard to PAH, as RV dysfunction is the main cause of death in PAH [204]. RV CFBs from female rats do not show this increase in stiffening or fibrosis in data from our lab, which explains why female

patients are more likely to survive PAH. Targeting this maladaptive remodeling process in male RVs could do much to treat PAH patients before RV dilatation causes death.

We have created the first model of PAAFs which we iteratively improved using our own *in-vitro* stiffness, stretch, and inhibition data. We have also demonstrated that we can separate the mechanical stimuli of stretch and stiffness to improve the model and understand the intricacies of upregulation of stiffness and stretch in six profibrotic genes in isolated PAAFs. We also uniquely demonstrated sex differences in male, female, and ovariectomized -derived fibroblasts and PA and RV tissue that could explain the PAH sex paradox. In studying as complex of a disease as PAH, we have used computational models and *in-vivo* and *in-vitro* experiments in both organ systems to study many facets of its pathobiology in response to abnormal mechanical environments. This has allowed us to conclude that the variables of stretch, stiffness, and sex all play crucial roles and interplay with each other in understanding PAH disease pathology.

Stretch and stiffness affect male PAAF induction at 24 hours after stretch similarly to how PAs from male rats are activated after six to ten weeks of sugen-hypoxia treatment but changing the variable of sex to female rats leads to decreased PAAF induction by stretch and PA induction in general, while ovariectomized rats are even less induced because of a high baseline of expression in normotensive rat PAAFs and PAs. In male PAAFs, changing the harvest time after stretch by itself illuminates the role of *Col1a1* in increasing fibrosis in response to stretch while the other five genes have a more transient response to stretch alone. Stiffness alone, on the other hand, induces all six profibrotic genes in male-derived PAAFs, all except *Acta2* in female-derived PAAFs, and only *Col1a1* and *Eln* in ovariectomized-derived PAAFs. All of these important conclusions tell us how complex PAH is to understand and our ability to isolate variables to study allows us to pinpoint which genes are more important at which timepoint in what sex animal, or

which mechanical stimulus is more crucial to induction of which gene. These conclusions indicate the need for sex-specific treatments in PAH that can target upregulation by stiffness which induces more profibrotic genes in female fibroblasts or stretch which induces more profibrotic genes in male fibroblasts. This is an important step in discovering new treatments for PAH and delving into the mechanisms by which profibrotic genes are upregulated inherently differently in male and female cells.

## 6.2 Limitations

While we have made many strides to understanding PAH at many levels with our current work, there are many limitations of our work that should be addressed.

### 6.2.1 *In-vivo* Limitations

Only six profibrotic genes were studied in PAs from male, female, and ovariectomized rats, a comprehensive RNA-Seq of the differences between normotensive and sugen-hypoxia PAs and PAs from different sex animals could give a more comprehensive view of what is upregulated, downregulated, or not changed in response to treatment and sex.

The sugen-hypoxia model, while good at replicating vascular remodeling, right heart failure, and sexual dimorphism in PAH, the mechanisms of sugen-hypoxia are not well understood, and it is not able to recapitulate a model of severe PAH [205].

The ovariectomy rat model is not a translational model of menopause but can mimic estrogen deficiency. It can also induce the renin-angeiotensin system which can conflate profibrotic results since baseline relative expression may be inherently high in cells derived from ovariectomized rats [198].

### 6.2.2 *In-vitro* Limitations

While our work has explored inherent sex differences in male, female, and ovariectomized PAAFs, it is a limitation that we have not studied the effects of growing these cells in hormone-free media or added estrogen to the male and ovariectomized cells which could illuminate the role of sex hormones in stiffness and stretch induction. In female PAAFs, we have not tested stimulation with testosterone.

We study static stretch as a measure of hemodynamic load rather than the cyclic stretch that pulmonary arteries experience because the frequency of cyclic stretch is not high enough but this is a limitation of our stretch system. The harvest time after stretch being 4, 8, and 24 hours leading to different induction of specific genes indicates that 24 hours is only able to capture the stretch and stiffness induction in male PAAFs, we did not test different times for PAAFs from female and ovariectomized animals and may have missed their stretch and stiffness induction.

We used rat PAAFs because of the detailed laboratory hemodynamic data and biomechanical measurements of ECM stiffness in the sugen-hypoxia rat model of PAH and normotensive control rats. However, human PAAFs have been used to study fibrotic signaling in response to matrix stiffness by Bertero *et al.* and we have been able to order human PAAFs from different sex donors [11]. We have determined human normotensive PA stiffness to be 2 kPa and PAH stiffness to be 4 kPa but have not yet successfully gotten RT-PCR data from our stretchers.

Another limitation of this study is that most of our data is relative expression, aside from collagen III and smooth muscle actin protein quantities being qualitatively consistent with their corresponding changes in mRNA expression. Actual protein expression reflects changes in ECM

from MMPs, degradation, and responses to post-translational modifications which could drastically change relative amounts [82].

We never tested combinations of inhibitor TGFβRI and AT1RI, which could tell us if certain profibrotic genes such as *Loxl1* and *Eln* were not regulated by either cytokine.

### 6.2.3 *In-silico* Limitations

The limitations of our model currently are that we can make predictions of changing different nodes to the network with some accuracy, but the model only extends to six profibrotic genes. It is also a logic-based set of ordinary differential equations and does not reflect the complexity of biochemical signaling. It can be extended to include a mass-action component equation with kinetic rates to create a more quantitative and predictive model of matrix remodeling

The network model also uses default parameters due to the dearth of literature data in PAAFs, but is still able to predict 80% of input-node experiments in the literature by capturing the important network topology [54]. The model has many OR reactions that could be ANDs if given enough literature support and experimental evidence for, such as smad2/3 and YAP/TAZ signaling.

The model does not include paracrine signaling from other cell types such as the PASMCs and PAECs that are also present in the pulmonary artery, along with macrophages that are upregulated by inflammation [13].

The PAAF model does not have sex differences included and would need to be restructured based on our work to reflect important induction of fibroblasts from male animals by stretch and lack of induction of fibroblasts from female animals by stretch [199].

### 6.3 Future Directions

A lot has been done to understand profibrotic responses to stiffness and stretch, but there is much future work that needs to be done to elucidate those mechanisms and ones governing sex differences in PAAFs and RV CFBs. In the future, we can use RNA-Seq to extend the model to many different genes to get a better picture of which genes are important in the regulation of PAH.

We can also add more detail in specific parameters of the model to improve the predictive capabilities of the model aside from those regulating JNK1/2 inhibition of *Eln* [173]. The model is also not currently able to replicate sex differences, which can be done through adding estrogen and other hormone receptors to the model and iterating upon its effects to better recapitulate our interesting *in-vitro* sex difference results in PAAFs [64]. The model can be tuned through different stimulations to upregulate certain stretch induced pathways in male PAAFs as opposed to female PAAFs, for example.

Since a model of cardiac fibroblasts was already made by Ziegler *et al*., an interesting future direction would be to iterate upon that model to separate the effects of stiffness and stretch using our *in-vitro* RV CFB data [69]. We can also modify the CFB model to better reflect demonstrated sex differences such as CFBs from male rats being more induced by stretch [199].

We also have done many of our *in-vitro* studies in rat PAAFs, which is not necessarily fully reflective of the changes we see in human patients. In the future, it would be very interesting to see if these *in-vitro* studies can be recapitulated using cultured human PAAFs, especially from cells isolated from patients of different genders [11].

In the future, an in-depth study of how estrogen or testosterone stimulation affects PAAF and CFB induction by stiffness and stretch using hormone-free fetal bovine serum would also be interesting.

# REFERENCES


[1] Ogata T, Iijima T. 1993 Structure and pathogenesis of plexiform lesion in pulmonary hypertension. Chin Med J (Engl). 106(1):45-8. PMID: 8504682.

[2] Sun W, Chan SY. 2018 Pulmonary arterial stiffness: An early and pervasive driver of pulmonary arterial hypertension. Front Med. doi:10.3389/fmed.2018.00204

[3] Hemnes AR, Humbert M. 2017 Pathobiology of pulmonary arterial hypertension: understanding the roads less travelled. Eur Respir Rev 26(146):170093. doi:10.1183/16000617.0093-201713

[4] Sommer N, Ghofrani HA, Pak O, Bonnet S, Provencher S, Sitbon O, Rosenkranz S, Hoeper MM, Kiely DG. 2021 Current and future treatments of pulmonary arterial hypertension. Br J Pharmacol 178(1):6-30. doi: 10.1111/bph.15016.

[5] Sitbon O, Gomberg-Maitland M, Granton J, Lewis MI, Mathai SC, Rainisio M, Stockbridge NL, Wilkins MR, Zamanian RT, Rubin LJ. 2019 Clinical trial design and new therapies for pulmonary arterial hypertension. Eur Respir J. 53(1):1801908. doi: 10.1183/13993003.01908-2018.

[6] Dannewitz Prosseda S, Ali MK, Spiekerkoetter E. 2020 Novel Advances in Modifying BMPR2 Signaling in PAH. Genes (Basel). 12(1):8. doi:10.3390/genes12010008.

[7] Shimoda LA, Laurie SS. 2013 Vascular remodeling in pulmonary hypertension. J Mol Med 91: 297-309.

[8] Tuder RM, Archer SL, Dorfmuller P, Erzurum SC, Guignabert C, Michelakis E, Rabinovitch M, Schermuly R, Stenmark KR, Morrell NW. 2013 Relevant issues in the pathology and pathobiology of pulmonary hypertension. J Am Coll Cardiol 62:D4-12.

[9] Good RB, Gilbane AJ, Trinder SL, Denton CP, Coghlan G, Abraham DJ, Holmes AM. 2015 Endothelial to Mesenchymal Transition Contributes to Endothelial Dysfunction in Pulmonary Arterial Hypertension. Am J Pathol 185(7):1850-8. doi: 10.1016/j.ajpath.2015.03.019.

[10] Kumar S, Sud N, Fonseca FV, Hou Y, Black SM. 2010 Shear stress stimulates nitric oxide signaling in pulmonary arterial endothelial cells via a reduction in catalase activity: role of protein kinase C delta. Am J Physiol Lung Cell Mol Physiol 298(1):L105-16. doi: 10.1152/ajplung.00290.2009.

[11] Bertero T, Handen AL, Chan SY. 2018 Factors associated with heritable pulmonary arterial hypertension exert convergent actions on the miR-130/301-vascular matrix feedback loop. Int J Mol Sci. doi:10.3390/ijms19082289

[12] Dieffenbach PB, Maracle M, Tschumperlin DJ, Fredenburgh LE. 2018 Mechanobiological feedback in pulmonary vascular disease. Front Physiol. doi:10.3389/fphys.2018.00951

[13] Thenappan T, Chan SY, Weir EK. 2018 Role of extracellular matrix in the pathogenesis of pulmonary arterial hypertension. Am J Physiol – Hear Circ Physiol doi:10.1152/ajpheart.00136.201814

[14] Gomez-Arroyo JG, Farkas L, Alhussaini AA, Farkas D, Kraskauskas D, Voelkel NF, Bogaard HJ. 2012 The monocrotaline model of pulmonary hypertension in perspective. Am J Physiol Lung Cell Mol Physiol. 302(4):L363-9. doi: 10.1152/ajplung.00212.2011.

[15] Zhu G, Zhang W, Liu Y, Wang S. 2018 miR-371b-5p inhibits endothelial cell apoptosis in monocrotaline-induced pulmonary arterial hypertension via PTEN/PI3K/Akt signaling pathways. Mol Med Rep. 18(6):5489-5501. doi: 10.3892/mmr.2018.9614.

[16] Temple IP, Quigley GM, Schneider H, Monfredi O, Cartwright EJ, Zi M, Yamanushi TT, Mahadevan VS, Hart G, Dobrzynski H, Boyett MR. 2014 Pulmonary hypertension leads to dysfunction and widespread ion channel remodelling within the atrioventricular node in the monocrotaline rat model. EP Europace. 16:iii6. doi: 10.1093/europace/euu237.7

[17] Liang S, Yu H, Chen X, Shen T, Cui Z, Si G, Zhang J, Cheng Y, Jia S, Song S, Zhang X, Yu X. 2017 PDGF-BB/KLF4/VEGF Signaling Axis in Pulmonary Artery Endothelial Cell Angiogenesis. Cell Physiol Biochem. 41(6):2333-2349. doi: 10.1159/000475652.

[18] Taraseviciene-Stewart L, Kasahara Y, Alger L, Hirth P, Mc Mahon G, Waltenberger J, Voelkel NF, Tuder RM. 2001 Inhibition of the VEGF receptor 2 combined with chronic hypoxia causes cell death-dependent pulmonary endothelial cell proliferation and severe pulmonary hypertension. FASEB J. 2001 Feb;15(2):427-38. doi: 10.1096/fj.00-0343com.

[19] Woodcock CC, Hafeez N, Handen A, Tang Y, Harvey LD, Estephan LE, Speyer G, Kim S, Bertero T, Chan SY. 2021 Matrix stiffening induces a pathogenic QKI-miR-7-SRSF1 signaling axis in pulmonary arterial endothelial cells. Am J Physiol Lung Cell Mol Physiol. 320(5):L726-L738. doi: 10.1152/ajplung.00407.2020.15

[20] Nickel NP, Spiekerkoetter E, Gu M, Li CG, Li H, Kaschwich M, Diebold I, Hennigs JK, Kim KY, Miyagawa K, Wang L, Cao A, Sa S, Jiang X, Stockstill RW, Nicolls MR, Zamanian RT, Bland RD, Rabinovitch M. 2015 Elafin Reverses Pulmonary Hypertension via Caveolin-1-Dependent Bone Morphogenetic Protein Signaling. Am J Respir Crit Care Med 191(11):1273-86. doi: 10.1164/rccm.201412-2291OC.

[21] Ranchoux B, Harvey LD, Ayon RJ, Babicheva A, Bonnet S, Chan SY, Yuan JX, Perez VJ. 2017 Endothelial dysfunction in pulmonary arterial hypertension: an evolving landscape. Pulm Circ 8(1):2045893217752912. doi: 10.1177/2045893217752912

[22] Welsh DJ, Peacock AJ. 2013 Cellular responses to hypoxia in the pulmonary circulation. High Alt Med Biol 14(2):111-6. doi:10.1089/ham.2013.1016

[23] Kang BY, Park KK, Kleinhenz JM, Murphy TC, Green DE, Bijli KM, Yeligar SM, Carthan KA, Searles CD, Sutliff RL, Hart CM. 2016 Peroxisome Proliferator-Activated Receptor γ and microRNA 98 in Hypoxia-Induced Endothelin-1 Signaling. Am J Respir Cell Mol Biol. 54(1):136-46. doi: 10.1165/rcmb.2014-0337OC.

[24] Bertero T, Oldham WM, Cottrill KA, Pisano S, Vanderpool RR, Yu Q, Zhao J, Tai Y, Tang Y, Zhang YY, Rehman S, Sugahara M, Qi Z, Gorcsan J 3rd, Vargas SO, Saggar R, Saggar R, Wallace WD, Ross DJ, Haley KJ, Waxman AB, Parikh VN, De Marco T, Hsue PY, Morris A, Simon MA, Norris KA, Gaggioli C, Loscalzo J, Fessel J, Chan SY. 2016 Vascular stiffness mechanoactivates YAP/TAZ-dependent glutaminolysis to drive pulmonary hypertension. J Clin Invest. 126(9):3313-35. doi: 10.1172/JCI86387.

[25] Lyle MA, Davis JP, Brozovich FV. 2017 Regulation of Pulmonary Vascular Smooth Muscle Contractility in Pulmonary Arterial Hypertension: Implications for Therapy. Front Physiol. 8:614. doi:10.3389/fphys.2017.00614.

[26] Stenmark KR, Frid MG, Graham BB, Tuder RM. 2018 Dynamic and diverse changes in the functional properties of vascular smooth muscle cells in pulmonary hypertension. Cardiovasc Res. Mar 15;114(4):551-564. doi: 10.1093/cvr/cvy004.

[27] He RL, Wu ZJ, Liu XR, Gui LX, Wang RX, Lin MJ. 2018 Calcineurin/NFAT Signaling Modulates Pulmonary Artery Smooth Muscle Cell Proliferation, Migration and Apoptosis in Monocrotaline-Induced Pulmonary Arterial Hypertension Rats. Cell Physiol Biochem 49(1):172-189. doi: 10.1159/000492852.

[28] Li X, Zhang X, Leathers R, Makino A, Huang C, Parsa P, Macias J, Yuan JX, Jamieson SW, Thistlethwaite PA. 2009 Notch3 signaling promotes the development of pulmonary arterial hypertension. Nat Med. 15(11):1289-97. doi: 10.1038/nm.2021.

[29] Wang Y, Dai S, Cheng X, Prado E, Yan L, Hu J, He Q, Lv Y, Lv Y, Du L. 2019 Notch3 signaling activation in smooth muscle cells promotes extrauterine growth restriction-induced pulmonary hypertension. Nutr Metab Cardiovasc Dis 29(6):639-651. doi: 10.1016/j.numecd.2019.03.004.

[30] Zhang Q, Cao Y, Luo Q, Wang P, Shi P, Song C, E M, Ren J, Fu B, Sun H. 2018 The transient receptor potential vanilloid-3 regulates hypoxia-mediated pulmonary artery smooth muscle cells proliferation via PI3K/AKT signaling pathway. Cell Prolif 51(3):e12436. doi:10.1111/cpr.12436.

[31] Tao W, Sun W, Zhu H, Zhang J. 2019 miR-205-5p suppresses pulmonary vascular smooth muscle cell proliferation by targeting 16 MICAL2-mediated Erk1/2 signaling. Microvasc Res 124:43-50. doi:10.1016/j.mvr.2019.03.001.

[32] Wei H, Zhang D, Liu L, Xia W, Li F. 2019 Rho signaling pathway enhances proliferation of PASMCs by suppressing nuclear translocation of Smad1 in PAH. Exp Ther Med. 2019 Jan;17(1):71-78. doi: 10.3892/etm.2018.6942.

[33] Calvier L, Chouvarine P, Legchenko E, Kokeny G, Mozes MM, Hansmann G. 2019 Chronic TGF-β1 Signaling in Pulmonary Arterial Hypertension Induces Sustained Canonical Smad3 Pathways in Vascular Smooth Muscle Cells. Am J Respir Cell Mol Bio 61(1):121-123. doi: 10.1165/rcmb.2018-0275LE.

[34] Wang T, Li Y, Chen J, Xie L, Xiao T. 2018 TGF-β1/Smad3 signaling promotes collagen synthesis in pulmonary artery smooth muscle by down-regulating miR-29b. Int J Clin Exp Pathol. 11(12):5592-5601.

[35] Lei S, Peng F, Li ML, Duan WB, Peng CQ, Wu SJ. 2020 LncRNA-SMILR modulates RhoA/ROCK signaling by targeting miR-141 to regulate vascular remodeling in pulmonary arterial hypertension. Am J Physiol Heart Circ Physiol 319(2):H377-H391. doi: 10.1152/ajpheart.00717.2019.

[36] Sun Z, Nie X, Sun S, Dong S, Yuan C, Li Y, Xiao B, Jie D, Liu Y. 2017 Long Non-Coding RNA MEG3 Downregulation Triggers Human Pulmonary Artery Smooth Muscle Cell Proliferation and Migration via the p53 Signaling Pathway. Cell Physiol Biochem. 42(6):2569-2581. doi:10.1159/000480218.

[37] Huang LJ, Zhang CC, Zhao MP, Zheng MX, Ying L, Chen XW, Wang WT. 2017 The regulation of MAPK signaling pathway on cell proliferation and apoptosis in hypoxic PASMCs of rats. Zhongguo Ying Yong Sheng Li Xue Za Zhi. 33(3):226-230. Chinese. doi: 10.12047/j.cjap.5422.2017.056.

[38] Yadav VR, Song T, Mei L, Joseph L, Zheng YM, Wang YX. 2018 PLCγ1-PKCε-IP3R1 signaling plays an important role in hypoxia-induced calcium response in pulmonary artery smooth muscle cells. Am J Physiol Lung Cell Mol Physiol 314(5):L724-L735. doi: 10.1152/ajplung.00243.2017.

[39] Wang J, Tian XT, Peng Z, Li WQ, Cao YY, Li Y, Li XH. 2019 HMGB1/TLR4 promotes hypoxic pulmonary hypertension via suppressing BMPR2 signaling. Vascul Pharmacol. 2019 Jun;117:35-44. doi:10.1016/j.vph.2018.12.006.

[40] Song S, Carr SG, McDermott KM, Rodriguez M, Babicheva A, Balistrieri A, Ayon RJ, Wang J, Makino A, Yuan JX. 2018 STIM2 (Stromal Interaction Molecule 2)-Mediated Increase in Resting Cytosolic Free Ca2+ Concentration Stimulates PASMC Proliferation in Pulmonary Arterial Hypertension. Hypertension. 71(3):518-529. doi: 10.1161/HYPERTENSIONAHA.117.10503.17

[41] Yan X, Wang J, Zhu Y, Feng W, Zhai C, Liu L, Shi W, Wang Q, Zhang Q, Chai L, Li M. 2019 S1P induces pulmonary artery smooth muscle cell proliferation by activating calcineurin/NFAT/OPN signaling pathway. Biochemical and biophysical research communications 516, 921-927. doi:10.1016/j.bbrc.2019.06.160

[42] Chen T, Huang JB, Dai J, Zhou Q, Raj JU, Zhou G. 2018 PAI-1 is a novel component of the miR-17 92 signaling that regulates pulmonary artery smooth muscle cell phenotypes. Am J Physiol Lung Cell Mol Physiol 315(2):L149-L161. doi: 10.1152/ajplung.00137.2017

[43] Stenmark KR, Davie N, Frid M, Gerasimovskaya E, Das M. 2006 Role of the adventitia in pulmonary vascular remodeling. Physiology. doi:10.1152/physiol.00053.2005

[44] Dieffenbach PB, Haeger CM, Coronata AMF, Choi KM, Varelas X, Tschumperlin DJ, Fredenburgh LE. 2017 Arterial stiffness induces remodeling phenotypes in pulmonary

artery smooth muscle cells via YAP/TAZ-mediated repression of cyclooxygenase-2. Am J Physiol - Lung Cell Mol Physiol. doi:10.1152/ajplung.00173.2017

[45] Strauss BH, Rabinovitch M. 2000 Adventitial fibroblasts: Defining a role in vessel wall remodeling. Am J Respir Cell Mol Biol. doi:10.1165/ajrcmb.22.1.f172

[46] Scott NA, Cipolla GD, Ross CE, Dunn B, Martin FH, Simonet L, Wilcox JN. 1996 Identification of a potential role for the adventitia in vascular lesion formation after balloon overstretch injury of porcine coronary arteries. Circulation. doi:10.1161/01.CIR.93.12.2178

[47] Mallawaarachchi CM, Weissberg PL, Siow RCM. 2005 Smad7 gene transfer attenuates adventitial cell migration and vascular remodeling after balloon injury. Arterioscler Thromb Vasc Biol. doi:10.1161/01.ATV.0000168415.33812.51

[48] Barman SA, Chen F, Su Y, Dimitropoulou C, Wang Y, Catravas JD, Han W, Orfi L, Szantai Kis C, Keri G, Szabadkai I, Barabutis N, Rafikova O, Rafikov R, Black SM, Jonigk D, Giannis A, Asmis R, Stepp DW, Ramesh G, Fulton DJ. NADPH oxidase 4 is expressed in pulmonary artery adventitia and contributes to hypertensive vascular remodeling. Arterioscler Thromb Vasc Biol. 2014 Aug;34(8):1704-15. doi: 10.1161/ATVBAHA.114.303848. Epub 2014 Jun 19. PMID:24947524; PMCID: PMC4228789.

[49] Chai X, Sun D, Han Q, Yi L, Wu Y, Liu X. 2018 Hypoxia induces pulmonary arterial fibroblast proliferation, migration, differentiation and vascular remodeling via the PI3K/Akt/p70S6K signaling pathway. Int J Mol Med. 41(5):2461-2472. doi:10.3892/ijmm.2018.3462

[50] Cussac LA, Cardouat G, Tiruchellvam Pillai N, Campagnac M, Robillard P, Montillaud A, Guibert C, Gailly P, Marthan R, Quignard JF, Savineau JP, Ducret T. 2020 TRPV4 channel mediates adventitial fibroblast activation and adventitial remodeling in pulmonary hypertension. Am J Physiol Lung Cell Mol Physiol. 318(1):L135-L146. doi: 10.1152/ajplung.00084.201918

[51] Bertero T, Cottrill KA, Lu Y, Haeger CM, Dieffenbach P, Annis S, Hale A, Bhat B, Kaimal V, Zhang YY, Graham BB, Kumar R, Saggar R, Saggar R, Wallace WD, Ross DJ, Black SM, Fratz S, Fineman JR, Vargas SO, Haley KJ, Waxman AB, Chau BN, Fredenburgh LE, Chan SY. 2015 Matrix Remodeling Promotes Pulmonary Hypertension through Feedback Mechanoactivation of the YAP/TAZ-miR-130/301 Circuit. Cell Rep. doi:10.1016/j.celrep.2015.09.049

[52] Boyd R, Rätsep MT, Ding LL, Wang H Di. 2011 ETA and ETB receptors are expressed in vascular adventitial fibroblasts. Am J Physiol - Hear Circ Physiol. doi:10.1152/ajpheart.00869.2010

[53] Wang A, Cao S, Stowe JC, Valdez-Jasso D. 2021 Substrate Stiffness and Stretch Regulate Profibrotic Mechanosignaling in Pulmonary Arterial Adventitial Fibroblasts. Cells. 10(5):1000. doi: 10.3390/cells10051000.

[54] Wang A, Cao S, Aboelkassem Y, Valdez-Jasso D. 2020 Quantification of uncertainty in a new network model of pulmonary arterial adventitial fibroblast pro-fibrotic signalling. Philos Trans A Math Phys Eng Sci. 12;378(2173):20190338. doi: 10.1098/rsta.2019.0338.

[55] Makino A, Firth AL, Yuan JX. 2011 Endothelial and smooth muscle cell ion channels in pulmonary vasoconstriction and vascular remodeling. Compr Physiol. 1(3):1555-602. doi: 10.1002/cphy.c100023.

[56] Gairhe S, Bauer NN, Gebb SA, McMurtry IF. 2011 Myoendothelial gap junctional signaling induces differentiation of pulmonary arterial smooth muscle cells. Am J Physiol Lung Cell Mol Physiol. 301(4):L527-35. doi:10.1152/ajplung.00091.2011.

[57] Gairhe S, Bauer NN, Gebb SA, McMurtry IF. 2012 Serotonin passes through myoendothelial gap junctions to promote pulmonary arterial smooth muscle cell differentiation. Am J Physiol Lung Cell Mol Physiol. 303(9):L767-77. doi: 10.1152/ajplung.00183.2012.

[58] Weinstein N, Mendoza L, ´Alvarez-Buylla ER. 2020 A Computational Model of the Endothelial to Mesenchymal Transition. Front Genet. 11:40. doi: 10.3389/fgene.2020.00040.

[59] Kraeutler MJ, Soltis AR, Saucerman JJ. 2010 Modeling cardiac β-adrenergic signaling with normalized-Hill differential equations: comparison with a biochemical model. BMC Syst Biol 4, 157. https://doi.org/10.1186/1752-0509-4-157

[60] Cao S, Aboelkassem Y, Wang A, Valdez-Jasso D, Saucerman JJ, Omens JH, McCulloch AD. 2020 Quantification of model and data uncertainty in a network analysis of cardiac myocyte mechanosignalling. Philos Trans A Math Phys Eng Sci. 378(2173), 20190336. https://doi.org/10.1098/rsta.2019.0336

[61] Liu F, Haeger CM, Dieffenbach PB, Sicard D, Chrobak I, Coronata AM, Suárez Velandia MM, Vitali S, Colas RA, Norris PC, Marinković A, Liu X, Ma J, Rose CD, Lee SJ, Comhair SA, Erzurum SC, McDonald JD, Serhan CN, Walsh SR, Tschumperlin DJ, Fredenburgh LE. 2016 Distal vessel stiffening is an early and pivotal mechanobiological regulator of vascular remodeling and pulmonary hypertension. JCI Insight. 1(8):e86987. doi: 10.1172/jci.insight.86987. PMID: 27347562; PMCID: PMC4918638.

[62] Tse JR, Engler AJ. 2010 Preparation of hydrogel substrates with tunable mechanical properties. Curr Protoc Cell Biol. Chapter 10:Unit 10.16. doi: 10.1002/0471143030.cb1016s47. PMID: 20521229.

[63] Herum KM, Choppe J, Kumar A, Engler AJ, McCulloch AD. 2017 Mechanical regulation of cardiac fibroblast profibrotic phenotypes. Mol Biol Cell. 28(14):1871-1882. doi: 10.1091/mbc.E17-01-0014. Epub 2017 May 3. PMID: 28468977; PMCID: PMC5541838.

[64] Morris H, Denver N, Gaw R, Labazi H, Mair K, MacLean MR. 2021 Sex Differences in Pulmonary Hypertension. Clin Chest Med. 42(1):217-228. doi: 10.1016/j.ccm.2020.10.005. Epub 2021 Jan 13. PMID: 33541615.

[65] Fernandez RA, Sundivakkam P, Smith KA, Zeifman AS, Drennan AR, Yuan JX. 2012 Pathogenic role of store-operated and receptor-operated Ca(2+) channels in pulmonary arterial hypertension. J Signal Transduct. 2012:951497. doi:10.1155/2012/951497

[66] Vélez-Rendón D, Pursell ER, Shieh J, Valdez-Jasso D. 2019 Relative Contributions of Matrix and Myocytes to Biaxial Mechanics of the Right Ventricle in Pulmonary Arterial Hypertension. J Biomech Eng. 141(9): 091011. https://doi.org/10.1115/1.4044225

[67] Grieb M, Burkovski A, Sträng JE, Kraus JM, Groß A, Palm G, Kühl M, Kestler HA. 2015 Predicting variabilities in cardiac gene expression with a boolean network incorporating uncertainty. PLoS ONE 10, e0131832. (doi:10.1371/journal.pone.0131832)

[68] Mirams GR, Pathmanathan P, Gray RA, Challenor P, Clayton RH. 2016 Uncertainty and variability in computational and mathematical models of cardiac physiology. J. Physiol. 594, 6833–6847. (doi:10.1113/JP271671)

[69] Zeigler AC, Richardson WJ, Holmes JW, Saucerman JJ. 2016 A computational model of cardiac fibroblast signaling predicts context-dependent drivers of myofibroblast differentiation. J. Mol. Cell Cardiol. 94, 72–81. (doi:10.1016/j.yjmcc.2016.03.008)

[70] El Kasmi KC, Pugliese SC, Riddle SR, Poth JM, Anderson AL, Frid MG, Li M, Pullamsetti SS, Savai R, Nagel MA, Fini MA, Graham BB, Tuder RM, Friedman JE, Eltzschig HK, Sokol RJ, Stenmark KR. 2014 Adventitial fibroblasts induce a distinct proinflammatory/profibrotic macrophage phenotype in pulmonary hypertension. J Immunol. Jul 15;193(2):597-609. doi:10.4049/jimmunol.1303048. Epub 2014 Jun 13. PMID: 24928992; PMCID: PMC4100597.

[71] Misra S, Fu AA, Misra KD, Shergill UM, Leof EB, Mukhopadhyay D. 2010 Hypoxia induced phenotypic switch of fibroblasts to myofibroblasts through a matrix metalloproteinase 2/tissue inhibitor of metalloproteinase-mediated pathway: implications for venous neointimal hyperplasia in hemodialysis access. J. Vasc. Interv. Radiol. 21, 896–902.(doi:10.1016/j.jvir.2010.02.030)

[72] Reddy VS, Harskamp RE, van Ginkel MW, Calhoon J, Baisden CE, Kim IS, Valente AJ, Chandrasekar B (2008) Interleukin-18 stimulates fibronectin expression in primary human cardiac fibroblasts via PI3K-Akt-dependent NF-κ B activation. J. Cell Physiol. 215, 697–707. (doi:10.1002/jcp.21348)

[73] Zhang J, Lo CS. 1995 Regulation of fibronectin expression by PDGF-BB And IGF-I in cultured rat thoracic aortic adventitial fibroblasts. Cell Biol. Int. 19, 517–526. (doi:10.1006/cbir.1995.1096)

[74] Lin S, Ma S, Lu P, Cai W, Chen Y, Sheng J. 2014 Effect of CTRP3 on activation of adventitial fibroblasts induced by TGF-β1 from rat aorta *in-vitro*. Int. J. Clin. Exp. Pathol. 7, 2199–2208.

[75] Zalewski A, Shi Y. 1997 Vascular myofibroblasts: lessons from coronary repair and

remodeling. Arterioscler. Thromb. Vasc. Biol. 17, 417–422. (doi:10.1161/01.ATV.17.3.417)

[76] Zhou HY, Chen WD, Zhu DL, Wu LY, Zhang J, Han WQ, Li JD, Yan C, Gao PJ. 2009 The PDE1A-PKCα signaling pathway is involved in the upregulation of α-smooth muscle actin by TGF-β1 in adventitial fibroblasts. J. Vasc. Res. 47, 9–15. (doi:10.1159/000231716)

[77] Zhang J, Tang L, Dai F, Qi Y, Yang L, Liu Z, Deng L, Yao W. 2019 ROCK inhibitors alleviate myofibroblast transdifferentiation and vascular remodeling via decreasing TGFβ1-mediated RhoGDI expression. Gen. Physiol. Biophys. 38, 271–280. (doi:10.4149/gpb_2019017)

[78] Liu P, Zhang C, Feng JB, Zhao YX, Wang XP, Yang JM, Zhang MX, Wang XL, Zhang Y. 2008 Cross talk among Smad, MAPK, and integrin signaling pathways enhances adventitial fibroblast functions activated by transforming growth factor-β1 and inhibited by Gax. Arterioscler. Thromb. Vasc. Biol. 28, 725–731. (doi:10.1161/ATVBAHA.107.159889)

[79] Ren M, Wang B, Zhang J, Liu P, Lv Y, Liu G, Jiang H, Liu F. 2011 Smad2 and Smad3 as mediators of the response of adventitial fibroblasts induced by transforming growth factor β1. Mol. Med. Rep. 4, 561–567. (doi:10.3892/mmr.2011.458)

[80] Wang B, Omar A, Angelovska T, Drobic V, Rattan SG, Jones SC, Dixon IM. 2007 Regulation of collagen synthesis by inhibitory Smad7 in cardiac myofibroblasts. Am. J. Physiol.- Heart Circ. Physiol. 293, H1282–H1290. (doi:10.1152/ajpheart.00910.2006)

[81] Khalil N, Xu YD, OConnor R, Duronio V. 2005 Proliferation of pulmonary interstitial fibroblasts is mediated by transforming growth factor-β1-induced release of extracellular fibroblast growth factor-2 and phosphorylation of p38 MAPK and JNK. J. Biol. Chem. 30, 43 000–43 009. (doi:10.1074/jbc.M510441200)

[82] Kucich U, Rosenbloom JC, Abrams WR, Rosenbloom J. 2002 Transforming growth factor-β stabilizes elastin mRNA by a pathway requiring active smads, protein kinase c-δ, and p38. Am. J. Respir Cell Mol. Biol. 26, 183–188. (doi:10.1165/ajrcmb.26.2.4666)

[83] Sullivan DE, Ferris M, Nguyen H, Abboud E, Brody AR. 2009 TNF-α induces TGFβ1 expression in lung fibroblasts at the transcriptional level via AP1 activation. J. Cell Mol. Med. 13, 1866–1876. (doi:10.1111/j.1582-4934.2008.00647.x)

[84] Li L, Fan D, Wang C, Wang JY, Cui XB, Wu D, Zhou Y, Wu LL. 2011 Angiotensin II Increases periostin expression via Ras/p38 MAPK/CREB and ERK1/2/TGF-β1 pathways in cardiac fibroblasts. Cardiovasc. Res. 91, 80–89. (doi:10.1093/cvr/cvr067)

[85] Qiao L, Xie L, Shi K, Zhou T, Hua Y, Liu H. 2012 Notch signaling change in pulmonary vascular remodeling in rats with pulmonary hypertension and its implication for therapeutic

intervention. PLoS ONE 7, e51514. (doi:10.1371/journal.pone.0051514)

[86] Csányi G, Taylor WR, Pagano PJ. 2009 NOX and inflammation in the vascular adventitia. Free Radic. Biol. Med. 47, 1254–1266. (doi:10.1016/j.freeradbiomed.2009.07.022)

[87] Ji J, Xu F, Li L, Chen R, Wang J, Hu WC. 2010 Activation of adventitial fibroblasts in the early stage of the aortic transplant vasculopathy in rat. Transplantation 89, 945–953. (doi:10.1097/TP.0b013e3181d05aa7)

[88] Budas GR, Boehm M, Kojonazarov B, Viswanathan G, Tian X, Veeroju S, Novoyatleva T, Grimminger F, Hinojosa-Kirschenbaum F, Ghofrani HA, Weissmann N, Seeger W, Liles JT, Schermuly RT. ASK1 Inhibition Halts Disease Progression in Preclinical Models of Pulmonary Arterial Hypertension. Am J Respir Crit Care Med. 2018 Feb 1;197(3):373-385. doi:10.1164/rccm.201703-0502OC. PMID: 28910144.

[89] Panzhinskiy E, Zawada WM, Stenmark KR, Das M. 2012 Hypoxia induces unique proliferative response in adventitial fibroblasts by activating PDGFβ receptor-JNK1 signalling. Cardiovasc. Res. 95, 356–365. (doi:10.1093/cvr/cvs194)

[90] Chandel NS, McClintock DS, Feliciano CE, Wood TM, Melendez JA, Rodriguez AM, Schumacker PT. 2000 Reactive oxygen species generated at mitochondrial Complex III stabilize hypoxia-inducible factor-1α during hypoxia: a mechanism of O2 sensing. J. Biol. Chem. 275, 25 130–25 138. (doi:10.1074/jbc.M001914200)

[91] Yang W, Zhang J, Wang H, Gao P, Singh M, Shen K, Fang N. 2011 Angiotensin II downregulates catalase expression and activity in vascular adventitial fibroblasts through an AT1R/ERK1/2-dependent pathway. Mol. Cell Biochem. 358, 21–29. (doi:10.1007/s11010-011-0915-1)

[92] Siques P, López De Pablo ÁL, Brito J, Arribas SM, Flores K, Arriaza K, Naveas N, González MC, Hoorntje A, León-Velarde F, López MR. 2014 Nitric oxide and superoxide anion balance in rats exposed to chronic and long term intermittent hypoxia. Biomed. Res. Int. 2014, 610474. (doi:10.1155/2014/610474)

[93] Tieu BC, Ju X, Lee C, Sun H, Lejeune W, Recinos 3rd A, Brasier AR, Tilton RG. 2011 Aortic adventitial fibroblasts participate in angiotensin-induced vascular wall inflammation and remodeling. J. Vasc. Res. 48, 261–272. (doi:10.1159/000320358)

[94] Stenmark KR, Nozik-Grayck E, Gerasimovskaya E, Anwar A, Li M, Riddle S, Frid M. 2011 The adventitia: essential role in pulmonary vascular remodeling. Compr. Physiol. 1, 141–161. (doi:10.1002/cphy.c090017)

[95] He RQ, Tang XF, Zhang BL, Li XD, Hong MN, Chen QZ, Han WQ, Gao PJ. 2016 Proteaseactivated receptor 1 and 2 contribute to angiotensin II-induced activation of adventitial fibroblasts from rat aorta. Biochem. Biophys. Res. Commun. 473, 517–523. (doi:10.1016/j.bbrc.2016.03.094)

[96] Shen WL, Gao PJ, Che ZQ, Ji KD, Yin M, Yan C, Berk BC, Zhu DL. 2006 NAD(P)H oxidase-derived reactive oxygen species regulate angiotensin-II induced adventitial fibroblast phenotypic differentiation. Biochem. Biophys. Res. Commun. 339, 337–343. (doi:10.1016/j.bbrc.2005.10.207)

[97] Jin X, Fu G xiang, Li X dong, Zhu D liang, Gao P. 2011 Expression and function of Osteopontin in vascular adventitial fibroblasts and pathological vascular remodeling. PLoS ONE 6, e23558. (doi:10.1371/journal.pone.0023558)

[98] Short M, Nemenoff RA, Zawada WM, Stenmark KR, Das M. 2004 Hypoxia induces differentiation of pulmonary artery adventitial fibroblasts into myofibroblasts. Am. J. Physiol. Cell Physiol. 286, C416–C425. (doi:10.1152/ajpcell.00169.2003)

[99] Hall MC, Young DA, Waters JG, Rowan AD, Chantry A, Edwards DR, Clark IM. 2003 The comparative role of activator protein 1 and Smad factors in the regulation of Timp-1 and MMP-1 gene expression by transforming growth factor-β1. J. Biol. Chem. 278, 10 304–10 313. (doi:10.1074/jbc.M212334200)

[100] Zhang H, Bajraszewski N, Wu E, Wang H, Moseman AP, Dabora SL, Griffin JD, Kwiatkowski DJ. 2007 PDGFRs are critical for PI3K/Akt activation and negatively regulated by mTOR. J. Clin. Invest. 117, 730–738. (doi:10.1172/JCI28984)

[101] Fei J, Viedt C, Soto U, Elsing C, Jahn L, Kreuzer J. 2000 Endothelin-1 and smooth muscle cells: induction of jun amino-terminal kinase through an oxygen radical - sensitive mechanism. Arterioscler. Thromb. Vasc. Biol. 20, 1244–1249. (doi:10.1161/01.ATV.20.5.1244)

[102] Wu J, Thabet SR, Kirabo A, Trott DW, Saleh MA, Xiao L, Madhur MS, Chen W, Harrison DG. 2014 Inflammation and mechanical stretch promote aortic stiffening in hypertension through activation of p38 mitogen-activated protein kinase. Circ. Res. 14, 616–625. (doi:10.1161/CIRCRESAHA.114.302157)

[103] Fleenor BS, Marshall KD, Durrant JR, Lesniewski LA, Seals DR. 2010 Arterial stiffening with ageing is associated with transforming growth factor-β1-related changes in adventitial collagen: reversal by aerobic exercise. J. Physiol. 588, 3971–3982. (doi:10.1113/jphysiol.2010.194753)

[104] Chen J, Wu J, Li L, Zou YZ, Zhu DL, Gao PJ. 2011 Effect of an acute mechanical stimulus on aortic structure in the transverse aortic constriction mouse model. Clin. Exp. Pharmacol. Physiol. 38, 570–576. (doi:10.1111/j.1440-1681.2011.05544.x)

[105] Liu G, Eskin SG, Mikos AG. 2001 Integrin alpha(v)beta(3) is involved in stimulated migration of vascular adventitial fibroblasts by basic fibroblast growth factor but not platelet-derived growth factor. J. Cell Biochem. 83, 129–135. (doi:10.1002/jcb.1208)

[106] Li G, Oparil S, Kelpke SS, Chen YF, Thompson JA. 2002 Fibroblast growth factor receptor-1 signaling induces osteopontin expression and vascular smooth muscle cell dependent adventitial fibroblast migration *in-vitro*. Circulation 106, 854–859. (doi:10.1161/01.CIR.0000024113.26985.CC)

[107] Anwar A, Li M, Frid MG, Kumar B, Gerasimovskaya EV, Riddle SR, McKeon BA, Thukaram R, Meyrick BO, Fini MA, Stenmark KR. Osteopontin is an endogenous modulator of the constitutively activated phenotype of pulmonary adventitial fibroblasts in hypoxic pulmonary hypertension. Am J Physiol Lung Cell Mol Physiol. 2012 Jul 1;303(1):L1-L11. doi:10.1152/ajplung.00050.2012. Epub 2012 May 11. PMID: 22582113; PMCID: PMC3426432.

[108] Li G, Chen YF, Kelpke SS, Oparil S, Thompson JA. 2000 Estrogen attenuates integrinβ3-dependent adventitial fibroblast migration after inhibition of osteopontin production in vascular smooth muscle cells. Circulation 101, 2949–2955. (doi:10.1161/01.CIR.101.25.2949)

[109] Herum KM, Lunde IG, Skrbic B, Florholmen G, Behmen D, Sjaastad I, Carlson CR, Gomez MF, Christensen G. 2013 Syndecan-4 signaling via NFAT regulates extracellular matrix production and cardiac myofibroblast differentiation in response to mechanical stress. J. Mol. Cell Cardiol.54, 73–81. (doi:10.1016/j.yjmcc.2012.11.006)

[110] Li L, Couse TL, DeLeon H, Xu CP, Wilcox JN, Chaikof EL. 2002 Regulation of syndecan 4 expression with mechanical stress during the development of angioplasty-induced intimal thickening. J. Vasc. Surg. 36, 361–370. (doi:10.1067/mva.2002.124364)

[111] Gerasimovskaya EV, Tucker DA, Stenmark KR. 2005 Activation of phosphatidylinositol 3-kinase, Akt, and mammalian target of rapamycin is necessary for hypoxia-induced pulmonary artery adventitial fibroblast proliferation. J. Appl. Physiol. 98, 722–731. (doi:10.1152/japplphysiol.00715.2004)

[112] Dupont S, Morsut L, Aragona M, Enzo E, Giulitti S, Cordenonsi M, Zanconato F, Le Digabel J, Forcato M, Bicciato S, Elvassore N, Piccolo S. Role of YAP/TAZ in mechanotransduction. Nature. 2011 Jun 8;474(7350):179-83. doi: 10.1038/nature10137. PMID: 21654799.

[113] McGrath JC, Deighan C, Briones AM, Shafaroudi MM, McBride M, Adler J, Arribas SM, Vila E, Daly CJ. 2005 New aspects of vascular remodelling: the involvement of all vascular cell types. Exp. Physiol. 90, 469–475. (doi:10.1113/expphysiol.2005.030130)

[114] Schulze-Bauer CAJ, Regitnig P, Holzapfel GA. 2002 Mechanics of the human femoral adventitia including the high-pressure response. Am. J. Physiol.- Heart Circ. Physiol. 282, H2427–H2440. (doi:10.1152/ajpheart.00397.2001)

[115] Lee SJ, Bae SS, Kim KH, Lee WS, Rhim BY, Hong KW, Kim CD. 2007 High glucose

enhances MMP-2 production in adventitial fibroblasts via Akt1-dependent NF-κ B pathway. FEBS Lett. 581, 4189–4194. (doi:10.1016/j.febslet.2007.07.058)

[116] Liu Y, Liang C, Liu X, Liao B, Pan X, Ren Y, Fan M, Li M, He Z, Wu J, Wu Z. AGEs Increased migration and inflammatory responses of adventitial fibroblasts via RAGE, MAPK and NF kappaB pathways. Atherosclerosis. 2010 Jan;208(1):34-42. doi: 10.1016/j.atherosclerosis.2009.06.007. Epub 2009 Jun 17. PMID: 19959167.

[117] Brasier AR. 2010 The nuclear factor-B-interleukin-6 signalling pathway mediating vascular inflammation. Cardiovasc. Res. 86, 211–218. (doi:10.1093/cvr/cvq076)

[118] Tan PM, Buchholz KS, Omens JH, McCulloch AD, Saucerman JJ. 2017 Predictive model identifies key network regulators of cardiomyocyte mechano-signaling. PLoS Comput. Biol. 13, e1005854. (doi:10.1371/journal.pcbi.1005854)

[119] Liu X, Kelm RJ, Strauch AR. 2009 Transforming growth factor β1-mediated activation of the smooth muscle α-actin gene in human pulmonary myofibroblasts is inhibited by tumor necrosis factor-α via mitogen-activated protein kinase 1-dependent induction of the Egr-1 transcriptional repressor. Mol. Biol. Cell 20, 2174–2185. (doi:10.1091/mbc.e08-10-0994)

[120] Scott RA, Kharkar PM, Kiick KL, Akins RE. 2017 Aortic adventitial fibroblast sensitivity to mitogen activated protein kinase inhibitors depends on substrate stiffness. Biomaterials 137,1–10. (doi:10.1016/j.biomaterials.2017.05.010)

[121] Zhang L, Li Y, Liu Y, Wang X, Chen M, Xing Y, Zhu D. 2015 STAT3-mediated MMP2 expression is required for 15-HETE-induced vascular adventitial fibroblast migration. J. Steroid Biochem. Mol. Biol. 149, 106–117. (doi:10.1016/j.jsbmb.2015.01.015)

[122] Chen WD, Chu YF, Liu JJ, Hong MN, Gao PJ. 2013 RhoA-Rho kinase signaling pathway mediates adventitial fibroblasts differentiation to myofibroblasts induced by TGF-β1. Sheng Li Xue Bao 65, 113–121.

[123] Robinson KG, Nie T, Baldwin AD, Yang EC, Kiick KL, Akins RE. 2012 Differential effects of substrate modulus on human vascular endothelial, smooth muscle, and fibroblastic cells. J. Biomed. Mater. Res.- Part A 100A, 1356–1367. (doi:10.1002/jbm.a.34075)

[124] Eul B, Rose F, Krick S, Savai R, Goyal P, Klepetko W, Grimminger F, Weissmann N, Seeger W, Hänze J. Impact of HIF-1alpha and HIF-2alpha on proliferation and migration of human pulmonary artery fibroblasts in hypoxia. FASEB J. 2006 Jan;20(1):163-5. doi: 10.1096/fj.054104fje. Epub 2005 Nov 1. PMID: 16263938.

[125] Frisdal E, Gest V, Vieillard-Baron A, Levame M, Lepetit H, Eddahibi S, Lafuma C, Harf A, Adnot S, Dortho MP. Gelatinase expression in pulmonary arteries during experimental pulmonary hypertension. Eur Respir J. 2001 Nov;18(5):838-45. doi: 10.1183/09031936.01.00084601. PMID: 11757635.

[126] Krick S, Hänze J, Eul B, Savai R, Seay U, Grimminger F, Lohmeyer J, Klepetko W, Seeger W, Rose F. Hypoxia-driven proliferation of human pulmonary artery fibroblasts: cross-talk between HIF-1alpha and an autocrine angiotensin system. FASEB J. 2005 May;19(7):857-9. doi:10.1096/fj.04-2890fje. Epub 2005 Feb 17. PMID: 15718424.

[127] Sauvage M, Hinglais N, Mandet C, Badier C, Deslandes F, Michel JB, Jacob MP. 1998 Localization of elastin mRNA and TGF-β1 in rat aorta and caudal artery as a function of age. Cell Tissue Res. 291, 305–314. (doi:10.1007/s004410051000)

[128] An SJ, Liu P, Shao TM, Wang ZJ, Lu HG, Jiao Z, Li X, Fu JQ. 2015 Characterization and functions of vascular adventitial fibroblast subpopulations. Cell Physiol. Biochem. 35, 1137–1150. (doi:10.1159/000373939)

[129] Haurani MJ, Cifuentes ME, Shepard AD, Pagano PJ. 2008 Nox4 oxidase overexpression specifically decreases endogenous Nox4 mRNA and inhibits angiotensin IIinduced adventitial myofibroblast migration. Hypertension 52, 143–149. (doi:10.1161/HYPERTENSIONAHA.107.101667)

[130] Smith JD, Bryant SR, Couper LL, Vary CP, Gotwals PJ, Koteliansky VE, Lindner V. 1999 Soluble transforming growth factor-β type II receptor inhibits negative remodeling, fibroblast transdifferentiation, and intimal lesion formation but not endothelial growth. Circ. Res. 84, 1212–1222. (doi:10.1161/01.RES.84.10.1212)

[131] Zhang L, Li Y, Chen M, Su X, Yi D, Lu P, Zhu D. 2014 15-LO 15-HETE Mediated Vascular Adventitia Fibrosis via p38 MARK Dependent TGF-β. J. Cell Physiol. 229, 245–257. (doi:10.1002/jcp.24443)

[132] He Y, Xiao Y, Yang X, Li Y, Wang B, Yao F, Lin R. 2017 SIRT6 inhibits TNF-α-induced inflammation of vascular adventitial fibroblasts through ROS and Akt signaling pathway. Exp. Cell Res. 357, 88–97. (doi:10.1016/j.yexcr.2017.05.001)

[133] Zhang L, Chen Y, Li G, Chen M, Huang W, Liu Y, Li Y. 2016 TGF−β1/FGF-2 signaling mediates the 15-HETE-induced differentiation of adventitial fibroblasts into myofibroblasts. Lipids Health Dis. 15, 2. (doi:10.1186/s12944-015-0174-3)

[134] Li S, Tabar SS, Malec V, Eul BG, Klepetko W, Weissmann N, Grimminger F, Seeger W, Rose F, Hänze J. 2008 NOX4 regulates ROS levels under normoxic and hypoxic conditions, triggers proliferation, and inhibits apoptosis in pulmonary artery adventitial fibroblasts. Antioxid. Redox Signal 10, 1687–1698. (doi:10.1089/ars.2008.2035)

[135] Nave AH, Mižíková I, Niess G, Steenbock H, Reichenberger F, Talavera ML, Veit F, Herold S, Mayer K, Vadász I, Weissmann N, Seeger W, Brinckmann J, Morty RE. Lysyl oxidases play a causal role in vascular remodeling in clinical and experimental pulmonary arterial hypertension. Arterioscler Thromb Vasc Biol. 2014 Jul;34(7):1446-58. doi: 10.1161/ATVBAHA.114.303534. Epub 2014 May 15. PMID: 24833797.

[136] Marino S, Hogue IB, Ray CJ, Kirschner DE. 2008 A methodology for performing global uncertainty and sensitivity analysis in systems biology. J. Theor. Biol. 254, 178–196. (doi:10.1016/j.jtbi.2008.04.011)

[137] Tennøe S, Halnes G, Einevoll GT. 2018 Uncertainpy: a Python toolbox for uncertainty quantification and sensitivity analysis in computational neuroscience. Front. Neuroinform. 14, 49. (doi:10.3389/fninf.2018.00049)

[138] Cohen TS, Lawrence GG, Khasgiwala A, Margulies SS. 2010 MAPK activation modulates permeability of isolated rat alveolar epithelial cell monolayers following cyclic stretch. PLoS ONE 5, e10385. (doi:10.1371/journal.pone.0010385)

[139] Cuenda A, Rouse J, Doza YN, Meier R, Cohen P, Gallagher TF, Young PR, Lee JC. 1995 SB 203580 is a specific inhibitor of a MAP kinase homologue which is stimulated by cellular stresses and interleukin-1. FEBS Lett. 364, 229–233. (doi:10.1016/0014-5793(95)00357-F)

[140] Sun W, Chan SY. 2018 Pulmonary arterial stiffness: An early and pervasive driver of pulmonary arterial hypertension. *Front. Med, 5*.

[141] Kolpakov,V, Rekhter MD, Gordon D, Wang WH, Kulik TJ. Effect of mechanical forces on growth and matrix protein synthesis in the *in-vitro* pulmonary artery: Analysis of the role of individual cell types. *Circ. Res.* 1995, *77*, 823–831.

[142] Bishop JE, Butt R, Dawes K, Laurent G. 1998 Mechanical load enhances the stimulatory effect of PDGF on pulmonary artery fibroblast procollagen synthesis. *Chest*, *114*, S25.

[143] Scott NA, Cipolla GD, Ross CE, Dunn B, Martin FH, Simonet L, Wilcox JN. 1996 Identification of a potential role for the adventitia in vascular lesion formation after balloon overstretch injury of porcine coronary arteries. *Circulation, 93*, 2178–2187.

[144] Camelliti P, Gallagher JO, Kohl P, McCulloch AD. 2006 Micropatterned cell cultures on elastic membranes as an *in-vitro* model of myocardium. *Nat. Protoc. 1*, 1379–1391.

[145] Simmons CS, Ribeiro AJS, Pruitt BL. 2013 Formation of composite polyacrylamide and silicone substrates for independent control of stiffness and strain. *Lab Chip, 13*, 646–649.

[146] Kim DK, Huh JE, Lee SH, Hong KP, Park JE, Seo JD, Lee WR. 1999 Angiotensin II stimulates proliferation of adventitial fibroblasts cultured from rat aortic explants. *J. Korean Med. Sci., 14*, 487–496.

[147] Rakugi H, Jacob HJ, Krieger JE, Ingelfinger JR, Pratt RE. 1993 Vascular injury induces angiotensinogen gene expression in the media and neointima. *Circulation, 87*, 283–290.

[148] Zhou HY, Chen WD, Zhu DL, Wu LY, Zhang J, Han WQ, Li JD,

Yan C, Gao PJ. 2010 The PDE1A-PKCalpha signaling pathway is involved in the upregulation of alpha-smooth muscle actin by TGF-beta1 in adventitial fibroblasts. *J. Vasc. Res.*, *47*, 9–15.

[149] Lin S, Ma S, Lu P, Cai W, Chen Y, Sheng J. 2014 Effect of CTRP3 on activation of adventitial fibroblasts induced by TGF-β1 from rat aorta *in-vitro*. *Int. J. Clin. Exp. Pathol*, *7*, 2199–2208.

[150] Tobiume K, Matsuzawa A, Takahashi T, Nishitoh H, Morita K, Takeda K, Minowa O, Miyazono K, Noda T, Ichijo H. 2001 ASK1 is required for sustained activations of JNK/p38 MAP kinases and apoptosis. *EMBO Rep. 2*, 222–228.

[151] Yu CC, Hsu MJ, Kuo ML, Chen RF, Chen MC, Bai KJ, Yu M.C, Chen BC, Lin CH. 2009 Thrombin-induced connective tissue growth factor expression in human lung fibroblasts requires the ASK1/JNK/AP-1 pathway. *J. Immunol. 182*, 7916–7927.

[152] Gana-Weisz M, Haklai R, Marciano D, Egozi, Y, Ben-Baruch G, Kloog Y. 1997 The Ras antagonist S-farnesylthiosalicylic acid induces inhibition of MAPK activation. *Biochem. Biophys. Res. Commun.*, *239*, 900–904.

[153] Lang YD, Hung CL, Wu TY, Wang LF, Chen CM. 2010 The renin-angiotensin system mediates hyperoxia-induced collagen production in human lung fibroblasts. *Free Radic. Biol. Med.*, *49*, 88–95.

[154] Xie Z, Singh M, Singh K. 2004 ERK1/2 and JNKs, but not p38 kinase, are involved in reactive oxygen species-mediated induction of osteopontin gene expression by angiotensin II and interleukin-1beta in adult rat cardiac fibroblasts. *J. Cell Physiol. 198*, 399–407.

[155] Kucich U, Rosenbloom JC, Abrams WR, Rosenbloom J. 2002 Transforming growth factor-β stabilizes elastin mRNA by a pathway requiring active Smads, protein kinase C-δ, and p38. *Am. J. Respir. Cell Mol. Biol.*, *26*, 183–188.

[156] Sano M, Fukuda K, Sato T, Kawaguchi H, Suematsu M, Matsuda S, Koyasu S, Matsui H, Yamauchi-Takihara K, Harada M, Saito Y, Ogawa S. 2001 ERK and p38 MAPK, but not NF-kappaB, are critically involved in reactive oxygen species-mediated induction of IL-6 by angiotensin II in cardiac fibroblasts. Circ Res. Oct 12;89(8):661-9. doi: 10.1161/hh2001.098873. PMID: 11597988.

[157] Lu H, Tian A, Wu J, Yang C, Xing R, Jia P, Yang L, Zhang Y, Zheng X, Li Z. 2014 Danshensu inhibits β-adrenergic receptors-mediated cardiac fibrosis by ROS/p38 MAPK axis. *Biol. Pharm. Bull.*, *37*, 961–967.

[158] Tojais NF, Cao A, Lai YJ, Wang L, Chen PI, Alcazar MAA, de Jesus Perez VA, Hopper RK, Rhodes CJ, Bill MA, Sakai LY, Rabinovitch M. 2017 Codependence of Bone Morphogenetic Protein Receptor 2 and Transforming Growth Factor-β in Elastic Fiber Assembly and Its Perturbation in Pulmonary Arterial Hypertension. Arterioscler Thromb

Vasc Biol. Aug;37(8):1559-1569. doi: 10.1161/ATVBAHA.117.309696. Epub 2017 Jun 15. PMID: 28619995; PMCID: PMC5593082.

[159] Cao S, Aboelkassem Y, Wang, A, Valdez-Jasso D, Saucerman JJ, Omens JH, McCulloch AD. 2020 Quantification of model and data uncertainty in a network analysis of cardiac myocyte mechanosignalling. *Philos. Trans. A Math. Phys. Eng. Sci., 12*, 2173.

[160] Yue Z, Xie J, Yu AS, Stock J, Du J, Yue L. 2015 Role of TRP channels in the cardiovascular system. *Am. J. Physiol. Heart Circ. Physiol.* 2015, *308*, 157–182.

[161] Suzuma I, Suzuma K, Ueki K, Hata Y, Feener EP, King GL, Aiello L.P. 2002 Stretch-induced retinal vascular endothelial growth factor expression is mediated by phosphatidylinositol 3-kinase and protein kinase C (PKC)-zeta but not by stretch-induced ERK1/2, Akt, Ras, or classical/novel PKC pathways. *J. Biol. Chem., 277*, 1047–1057.

[162] Blatti SP, Foster DN, Ranganathan G, Moses HL, Getz MJ. 1988 Induction of fibronectin gene transcription and mRNA is a primary response to growth-factor stimulation of AKR-2B cells. *Proc. Natl. Acad. Sci. USA, 85*, 1119–1123.

[163] Liu S, Parameswaran H, Young SM, Varisco BM. 2014 JNK suppresses pulmonary fibroblast elastogenesis during alveolar development. *Resp. Res., 15*, 34.

[164] Layland J, Young IS, Altringham JD. 1995 The effect of cycle frequency on the power output of rat papillary muscles *in-vitro*. *J. Exp. Biol., 198*, 1035–1043.

[165] Froese AR, Shimbori C, Bellaye PS, Inman M, Obex S, Fatima S, Jenkins G, Gauldie J, Ask K, Kolb M. 2016 Stretch-induced Activation of Transforming Growth Factor-β1 in Pulmonary Fibrosis. *Am. J. Respir. Crit. Care Med., 194*, 84–96.

[166] Lee AA, Dillmann WH, McCulloch AD, Villarreal FJ. 1995 Angiotensin II stimulates the autocrine production of transforming growth factor-beta 1 in adult rat cardiac fibroblasts. *J. Mol. Cell Cardiol. 27*, 2347–2357.

[167] Fisher SA, Absher M. 1995 Norepinephrine and ANG II stimulate secretion of TGF-beta By neonatal rat cardiac fibroblasts *in-vitro*. *Am. J. Physiol., 268*, 910–917.

[168] Galie PA, Russell MW, Westfall MV, Stegemann JP. 2012 Interstitial fluid flow and cyclic strain differentially regulate cardiac fibroblast activation via AT1R and TGF-β1. *Exp. Cell Res., 318*, 75–84.

[169] Hamzeh MT, Sridhara R, Alexander LD. 2015 Cyclic stretch-induced TGF-β1 and fibronectin expression is mediated by β1-integrin through c-Src- and STAT3-dependent pathways in renal epithelial cells. *Am. J. Physiol. Renal Physiol., 308*, 425–436.

[170] Humbert M, Gerry Coghlan J, Khanna D. 2012 Early detection and management of

Pulmonary arterial hypertension. Eur Respir Rev. Dec 1;21(126):306-12. doi: 10.1183/09059180.00005112. PMID: 23204118

[171] Rafikova O, Al Ghouleh I, Rafikov R. 2019 Focus on Early Events: Pathogenesis of Pulmonary Arterial Hypertension Development. Antioxid Redox Signal. 2019 Nov 1;31(13):933-953. doi: 10.1089/ars.2018.7673. Epub Jul 2. PMID: 31169021; PMCID: PMC6765063.

[172] Vonk Noordegraaf A, Westerhof BE, Westerhof N. 2017 The Relationship Between the Right Ventricle and its Load in Pulmonary Hypertension. J Am Coll Cardiol. Jan 17;69(2):236-243. doi: 10.1016/j.jacc.2016.10.047. PMID: 28081831.

[173] Campo A, Mathai SC, Le Pavec J, Zaiman AL, Hummers LK, Boyce D, Housten T, Champion HC, Lechtzin N, Wigley FM, Girgis RE, Hassoun PM. 2010 Hemodynamic predictors of survival in scleroderma-related pulmonary arterial hypertension. Am J Respir Crit Care Med. 2010 Jul 15;182(2):252-60. doi: 10.1164/rccm.200912-1820OC. Epub Mar 25. PMID: 20339143; PMCID: PMC2913238.

[174] Rain S, Rain S, Handoko ML, Trip P, Gan CT, Westerhof N, Stienen GJ, Paulus WJ, Ottenheijm CA, Marcus JT, Dorfmüller P, Guignabert C, Humbert M, Macdonald P, Dos Remedios C, Postmus PE, Saripalli C, Hidalgo CG, Granzier HL, Vonk-Noordegraaf A, van der Velden J, de Man FS. 2013 Right ventricular diastolic impairment in patients with pulmonary arterial hypertension. Circulation. Oct 29;128(18):2016-25, 1-10. doi: 10.1161/CIRCULATIONAHA.113.001873. Epub 2013 Sep 20. PMID: 24056688.

[175] Souders CA, Bowers SL, Baudino TA. 2009 Cardiac fibroblast: the renaissance cell. Circ Res. Dec 4;105(12):1164-76. doi: 10.1161/CIRCRESAHA.109.209809. PMID: 19959782; PMCID: PMC3345531.

[176] Hinz B, Phan SH, Thannickal VJ, Galli A, Bochaton-Piallat ML, Gabbiani G. 2007 The myofibroblast: one function, multiple origins. Am J Pathol. Jun;170(6):1807-16. doi: 10.2353/ajpath.2007.070112. PMID: 17525249; PMCID: PMC1899462.

[177] Kwan ED, Vélez-Rendón D, Zhang X, Mu H, Patel M, Pursell E, Stowe J, Valdez-Jasso D. 2021 Distinct time courses and mechanics of right ventricular hypertrophy and diastolic stiffening in a male rat model of pulmonary arterial hypertension. Am J Physiol Heart Circ Physiol. Oct 1;321(4):H702-H715. doi: 10.1152/ajpheart.00046.2021. Epub 2021 Aug 27. PMID: 34448637; PMCID: PMC8794227.

[178] Jang S, Vanderpool RR, Avazmohammadi R, Lapshin E, Timothy N, Bachman MS, Sacks M, Simon MA. 2017 Biomechanical and Hemodynamic Measures of Right Ventricular Diastolic Function: Translating Tissue Biomechanics to Clinical Relevance. *J Am Heart Assoc*. 2017;6(9):e006084. 12. doi:10.1161/JAHA.117.006084

[179] Rafikova O, Rafikov R, Meadows ML, Kangath A, Jonigk D, Black SM. 2015 The sexual dimorphism associated with pulmonary hypertension corresponds to a fibrotic phenotype.

*Pulm Circ*. 2015 Mar;5(1):184-97. doi: 10.1086/679724. PMID: 25992281; PMCID: PMC4405725.

[180] Walker CJ, Schroeder ME, Aguado BA, Anseth KS, Leinwand LA. 2021 Matters of the heart: Cellular sex differences. *J Mol Cell Cardiol*. 2021 Nov;160:42-55. doi: 10.1016/j.yjmcc.2021.04.010. Epub 2021 Jun 22. PMID: 34166708; PMCID: PMC8571046.

[181] Kang BY, Park KK, Green DE, Bijli KM, Searles CD, Sutliff RL, Hart CM. 2013 Hypoxia mediates mutual repression between microRNA-27a and PPARγ in the pulmonary vasculature. *PLoS One*. 2013 Nov 14;8(11):e79503. doi: 10.1371/journal.pone.0079503. PMID: 24244514; PMCID: PMC3828382.

[182] Savorani C, Malinverno M, Seccia R, Maderna C, Giannotta M, Terreran L, Mastrapasqua E, Campaner S, Dejana E, Giampietro C. 2021 A dual role of YAP in driving TGFβ-mediated endothelial-to-mesenchymal transition. *J Cell Sci*. 2021 Aug 1;134(15):jcs251371. doi: 10.1242/jcs.251371. Epub 2021 Aug 2. PMID: 34338295; PMCID: PMC8353525.

[183] Hamzeh MT, Sridhara R, Alexander LD. 2015 Cyclic stretch-induced TGF-β1 and fibronectin expression is mediated by β1-integrin through c-Src- and STAT3-dependent pathways in renal epithelial cells. *Am J Physiol Renal Physiol*. 2015 Mar 1;308(5):F425-36. doi: 10.1152/ajprenal.00589.2014. Epub 2014 Dec 4. PMID: 25477471; PMCID: PMC4422350.

[184] Braidotti N, Chen SN, Long CS, Cojoc D, Sbaizero O. 2022 Piezo1 Channel as a Potential Target for Hindering Cardiac Fibrotic Remodeling. *Int J Mol Sci*. 2022 Jul 22;23(15):8065. doi: 10.3390/ijms23158065. PMID: 35897650; PMCID: PMC9330509.

[185] Wolf D, Tseng N, Seedorf G, Roe G, Abman SH, Gien J. 2014 Endothelin-1 decreases endothelial PPARγ signaling and impairs angiogenesis after chronic intrauterine pulmonary hypertension. *Am J Physiol Lung Cell Mol Physiol*. 2014 Feb 15;306(4):L361-71. doi: 10.1152/ajplung.00277.2013. Epub 2013 Dec 13. PMID: 24337925; PMCID: PMC3920227.

[186] Montezano AC, Amiri F, Tostes RC, Touyz RM, Schiffrin EL. 2007 Inhibitory effects of PPAR-gamma on endothelin-1-induced inflammatory pathways in vascular smooth muscle cells from normotensive and hypertensive rats. *J Am Soc Hypertens*. 2007 Mar-Apr;1(2):150-60. doi: 10.1016/j.jash.2007.01.005. PMID: 20409845.

[187] Tang M, Zhong M, Shang Y, Lin H, Deng J, Jiang H, Lu H, Zhang Y, Zhang W. 2008 Differential regulation of collagen types I and III expression in cardiac fibroblasts by AGEs through TRB3/MAPK signaling pathway. *Cell Mol Life Sci*. 2008 Sep;65(18):2924-32. doi: 10.1007/s00018-008-8255-3. PMID: 18726071.

[188] Millar NL, Gilchrist DS, Akbar M, Reilly JH, Kerr SC, Campbell AL, Murrell GAC, Liew FY, Kurowska-Stolarska M, McInnes IB. 2015 MicroRNA29a regulates IL-33-mediated tissue remodelling in tendon disease. *Nat Commun*. 2015 Apr 10;6:6774. doi: 10.1038/ncomms7774. PMID: 25857925; PMCID: PMC4403384.

[189] Jeong J, Lee J, Lim J, Cho S, An S, Lee M, Yoon N, Seo M, Lim S, Park S. 2019 Soluble RAGE attenuates AngII-induced endothelial hyperpermeability by disrupting HMGB1-mediated crosstalk between AT1R and RAGE. *Exp Mol Med*. 2019 Sep 27;51(9):1-15. doi: 10.1038/s12276-019-0312-5. PMID: 31562296; PMCID: PMC6802637.

[190] Chichger H, Vang A, O'Connell KA, Zhang P, Mende U, Harrington EO, Choudhary G. 2015 PKC δ and βII regulate angiotensin II-mediated fibrosis through p38: a mechanism of RV fibrosis in pulmonary hypertension. *Am J Physiol Lung Cell Mol Physiol*. 2015 Apr 15;308(8):L827-36. doi: 10.1152/ajplung.00184.2014. Epub 2015 Feb 6. PMID: 25659900; PMCID: PMC4398873.

[191] Legchenko E, Chouvarine P, Borchert P, Fernandez-Gonzalez A, Snay E, Meier M, Maegel L, Mitsialis SA, Rog-Zielinska EA, Kourembanas S, Jonigk D, Hansmann G. 2018 PPARγ agonist pioglitazone reverses pulmonary hypertension and prevents right heart failure via fatty acid oxidation. *Sci Transl Med*. 2018 Apr 25;10(438):eaao0303. doi: 10.1126/scitranslmed.aao0303. PMID: 29695452.

[192] Austin ED, Hamid R. 2018 Y Not? Sex Chromosomes May Modify Sexual Dimorphism in Pulmonary Hypertension. *Am J Respir Crit Care Med*. 2018 Apr 1;197(7):858-859. doi: 10.1164/rccm.201709-1865ED. PMID: 28968140; PMCID: PMC6020416.

[193] DuPont JJ, Kenney RM, Patel AR, Jaffe IZ. 2019 Sex differences in mechanisms of arterial stiffness. *Br J Pharmacol*. 2019 Nov;176(21):4208-4225. doi: 10.1111/bph.14624. Epub 2019 May 11. PMID: 30767200; PMCID: PMC6877796.

[194] de Jesus Perez VA. 2011 Making sense of the estrogen paradox in pulmonary arterial hypertension. *Am J Respir Crit Care Med*. 2011 Sep 15;184(6):629-30. doi: 10.1164/rccm.201107-1184ED. PMID: 21920924.

[195] Philip JL, Tabima DM, Wolf GD, Frump AL, Cheng TC, Schreier DA, Hacker TA, Lahm T, Chesler NC. 2020 Exogenous Estrogen Preserves Distal Pulmonary Arterial Mechanics and Prevents Pulmonary Hypertension in Rats. *Am J Respir Crit Care Med*. 2020 Feb 1;201(3):371-374. doi: 10.1164/rccm.201906-1217LE. PMID: 31661294; PMCID: PMC6999110.

[196] Zemskova M, McClain N, Niihori M, Varghese MV, James J, Rafikov R, Rafikova O. 2020 Necrosis-Released HMGB1 (High Mobility Group Box 1) in the Progressive Pulmonary Arterial Hypertension Associated With Male Sex. *Hypertension*. 2020 Dec;76(6):1787-1799. doi: 10.1161/HYPERTENSIONAHA.120.16118. Epub 2020 Oct 5. PMID: 33012199; PMCID: PMC7666015.

[197] Chaudhary KR, Deng Y, Yang A, Cober ND, Stewart DJ. 2021 Penetrance of Severe Pulmonary Arterial Hypertension in Response to Vascular Endothelial Growth Factor Receptor 2 Blockade in a Genetically Prone Rat Model Is Reduced by Female Sex. *J Am Heart Assoc*. 2021 Aug 3;10(15):e019488. doi: 10.1161/JAHA.120.019488. Epub 2021 Jul 28. PMID: 34315227; PMCID: PMC8475703.

[198] Hussien NI, El-Kerdasy HI, Sorour SM, Shoman AA. 2019 Chronic oestrogen deficiency induced by ovariectomy may cause lung fibrosis through activation of the renin-angiotensin system in rats. *Arch Physiol Biochem*. 2022 Apr;128(2):290-299. doi: 10.1080/13813455.2019.1676262. Epub 2019 Oct 12. PMID: 31608713.

[199] Frump AL, Albrecht M, Yakubov B, Breuils-Bonnet S, Nadeau V, Tremblay E, Potus F, Omura J, Cook T, Fisher A, Rodriguez B, Brown RD, Stenmark KR, Rubinstein CD, Krentz K, Tabima DM, Li R, Sun X, Chesler NC, Provencher S, Bonnet S, Lahm T. 2021 17β-Estradiol and estrogen receptor α protect right ventricular function in pulmonary hypertension via BMPR2 and apelin. *J Clin Invest*. 2021 Mar 15;131(6):e129433. Doi: 10.1172/JCI129433. PMID: 33497359; PMCID: PMC7968046.

[200] Tello K, Dalmer A, Axmann J, Vanderpool R, Ghofrani HA, Naeije R, Roller F, Seeger W, Sommer N, Wilhelm J, Gall H, Richter MJ. 2019 Reserve of Right Ventricular-Arterial Coupling in the Setting of Chronic Overload. *Circ Heart Fail*. 2019 Jan;12(1):e005512. doi: 10.1161/CIRCHEARTFAILURE.118.005512. PMID: 30616360.

[201] Wang J, Liu S, Heallen T, Martin JF. 2018 The Hippo pathway in the heart: pivotal roles in development, disease, and regeneration. *Nat Rev Cardiol*. 2018 Nov;15(11):672-684. doi: 10.1038/s41569-018-0063-3. PMID: 30111784.

[202] Golob MJ, Wang Z, Prostrollo AJ, Hacker TA, Chesler NC. 2016 Limiting collagen turnover via collagenase-resistance attenuates right ventricular dysfunction and fibrosis in pulmonary arterial hypertension. *Physiol Rep*. 2016 Jun;4(11):e12815. doi: 10.14814/phy2.12815. PMID: 27252252; PMCID: PMC4908492.

[203] Vonk Noordegraaf A, Galiè N. 2011 The role of the right ventricle in pulmonary arterial hypertension. *Eur Respir Rev*. 2011 Dec;20(122):243-53. doi: 10.1183/09059180.00006511. PMID: 22130817.

[204] Keen J, Prisco SZ, Prins KW. 2021 Sex Differences in Right Ventricular Dysfunction: Insights From the Bench to Bedside. *Front Physiol*. 2021 Jan 18;11:623129. doi: 10.3389/fphys.2020.623129. PMID: 33536939; PMCID: PMC7848185.

[205] Voelkel NF, Bogaard HJ. 2021 Sugen, hypoxia and the lung circulation. *Pulm Circ*. 2021 Oct 4;11(4):20458940211051188. doi: 10.1177/20458940211051188. PMID: 34631012; PMCID: PMC8493318.